UNIVERSITY OF CALIFORNIA

Santa Barbara

Rates and mechanics of fold uplift and lateral bedrock planation in convergent foreland basins

A dissertation submitted in partial satisfaction of the

requirements for the degree Doctor of Philosophy

in Earth Science

by

Nel Aaron Bufe

Committee in charge:

Professor Douglas W. Burbank, Chair

Professor Bodo Bookhagen, University of Potsdam

Professor Thomas Dunne

March 2017

The dissertation of Nel Aaron Bufe is approved.

_____

Bodo Bookhagen

_____

Thomas Dunne

_____

Douglas W. Burbank, Committee Chair

December 2016

Rates and mechanics of fold uplift and lateral bedrock planation in convergent foreland basins

by

Nel Aaron Bufe

ACKNOWLEDGEMENTS

Five years and three months ago, Beach-Boys on my lips, I stepped on a plane and embarked on an adventure to this land so far, and yet so familiar from Hollywood movies, world news, and McDonald restaurants. A field trip to the Mohave Desert and my first night sleeping out under the stars marked the beginning of a wondrous journey across the surface of the Earth. I will forever remain indebted to UC Santa Barbara, the Earth Science department, and particularly my advisor Douglas Burbank for bringing me across the pond and supporting me throughout my PhD. Thank you, Doug, for your insights, the training, and the formative discussions. Your key impulses at the right times opened avenues that I never could have imagined taking. I hope that some of your intuition for important problems, your skill of asking the right questions, and your mastery of communicating science through text and illustrations will remain with me. Alongside Doug, Bodo Bookhagen got me through countless hours of labwork and introduced me to a number of analytical tools. Thank you, Bodo, for your advice and your infectious can-do attitude about any problem.

Alternative realities will, for the foreseeable future, remain within the realm of Science Fiction tales. Nevertheless, I am certain that without the inspiring surface processes class taught by Niels Hovius at Cambridge University and his list of potential advisors, I would have rolled down an entirely different slope.

The completion of this thesis would not have been possible without a number of collaborators. First and foremost, I want to thank my Chinese colleagues Chen Jie, Liu Langtao, Li Tao, Qin Jintang, Yang Xiaodong, Yang Huili, and driver Lau Li. Thank you for the countless hours of applying for permits, organizing travel and lodging, for all the great

fun in the field, and for the tasty dinners (ohhh those “big pan chicken”). I am grateful to David Bekaert and Ekbal Hussain for a stimulating research visit in Leeds and for jumping on the boat (or rather on the satellite) to get the InSAR right. A one-months visit in Socorro, New Mexico will stay particularly dear to my heart and, whereas the results from this work are forthcoming, I acknowledge Fred Phillips for opening the doors to his chlorine lab, David Parmelee and Shasta Marrero for their guidance through the processing, and Daisy Morgan and Stas Edel for the music and the jam sessions. Chris Paola generously provided me with the exceptional opportunity of spending three formative months at Saint Anthony Falls Laboratory in Minneapolis, MN. Discussions with Jean-Louis Grimaud, Sara Baumgardner, Andrew Wickert, Kristen Sweeney, Colin Phillips, and Crystal Ng and the tireless help in setting up and carrying out the experiments from Richard Christopher, James Mullin, Ben Erickson, Sara Mielke, and Erik Steen, will never be forgotten. I am sorry that I left you behind at the first sign of snow after a beautiful autumn to drive back to sunny Santa Barbara.

Back at UCSB, I want to thank my dear friend Jon Harvey for the talk, the laughs, the waves, and for his inspiring façon de vivre et d’enseigner. Thanks to Jessica Thompson for her friendship and her invaluable aid with every aspect of my work in China, and a big yuhey to the Burbanker’s Eric Shoettle, Al Neely, and Rebecca Streit for holding up the office morale. There is truth to be found outside the Burbank lab, and I would like to thank Phil Gans, Alexander Simms, and Thomas Dunne for their insights as committee members at different stages of my work. I am infinitely grateful for Hannah Smit, Yann Ricard, Kris Ducket, Jeri O’Mahoney, Yvette Howze, Kate Lima, Vivian Stopple, Patricia Machuca, and Cecilia Sousa for their incessant assistance in finding the correct shore to land on in the

confusing archipelago of administration. Finally, I want to thank the friendship and help of the UCSB family and particularly Forrest Horton, Graham Lederer, Graham Hagen-Peter, Jeffrey Creamer, Joshua Garber, Laura Reynolds, Jorge Crempien, Beau Gentry, Brenna Quigley, Adam Guinsburg, Susannah Porter, John Cottle, Andrew Kylander-Clark, and the members of the ginger support team (I have official permission to use this term) Elisabeth Steel, Sophie Briggs, and Mary Kate Fidler.

Being part of a community with an exhilarating enthusiasm that allows for thought-provoking discussion on every aspect of science and life has been a great privilege. For the ideas, the beers, and the encouragements, I want to thank Joel Pederson, Kristen Cook, Luca Malatesta, Joel Scheingross, Miriam Dühnforth, Taylor Schildgen, Vaughan Voller, Ryan Gold, Jens Turowski, Kerry Johnson, Anke Friedrich, Michael Lamb, Kelin Whipple, Markus Hoffmann, Aradhna Tripati, Efi Foufoula-Georgiou, Ajay Limaye, Dan Cazanacli, Anthony Longjas, Alejandro Tejedor, Antoinette Abeyta, Steffi Tofelde, Simon Kübler, Steffanie Rieger, and Cengiz Zabci.

Very special thanks go to Gesine, Abbi, Till, Niko, Béla, their partners and kids, as well as to Mark Hoggard, Paul van Houtem, Eike Imping, Esther Kaufmann and the friends and extended family that have been a constant anchor at home, while maintaining my sanity, and accompanying me through many worlds outside of Geology. Finally, Sophie Gruber, your understanding, love, and constant support has been the greatest gift of all! Thank you so very much for being there!

This research was funded by the National Science Foundation (NSF), UC-Santa Barbara, the German Academic Exchange Service (DAAD), The Geologic Society of America (GSA), and the Lloyd and & Mary Edwards Field Studies Fellowship.

VITA OF NEL AARON BUFE

EDUCATION

2011 - 2017:	Ph.D., University of California, Santa Barbara
2007 - 2011:	B.A. & M.Sci., King's College, University of Cambridge
2003 - 2006:	French Baccalaureate & German Abitur; Lycée International de St Germain en Laye

PROFESSIONAL APPOINTMENTS

2011 - 2016:	Researcher at the University of California Santa Barbara
2015:	Intern at ConocoPhillips, Houston
2015:	Associate at University of California, Santa Barbara
2012 - 2015:	Teaching assistant at University of California, Santa Barbara

RESEARCH AND EDUCATIONAL GRANTS

2015:	Earthscope Geochronology Award
2014:	GSA Graduate Student Research Grant
2014:	Earth Research Institute Summer Fellowship
2013:	UCSB Dep. of Earth Sciences-Graduate Opportunity Award
2012:	DAAD-Doktorandenstipendium
2011:	UCSB Regents Special Fellowship

PRIZES AND HONORS

2015:	UCSB Alumni Graduate Award for Research Excellence
2013:	Lloyd and & Mary Edwards Field Studies Fellowship
2010:	Scholarship of King's College, Cambridge
2009:	Scholarship of King's College, Cambridge
2009:	BP scholarship

INVITED TALKS

2016	Caltech (Group seminar)
2016	UCLA (Group seminar)
2016	GFZ Potsdam (Group seminar)
2016	University of Potsdam (Group seminar)
2015	Ludwig Maximilian University, Munich (Group seminar)
2013	China Earthquake Administration, Beijing (Group seminar)

RESEARCH AND TECHNICAL SKILLS

<u>Laboratory skills</u>

- Optically Stimulated Luminescence dating
- Cosmogenic Nuclide dating of ^{10}Be in quartz and ^{36}Cl in carbonates
- Physical experiment of geomorphic and hydrologic processes
- Inductively coupled plasma mass-spectrometry for U-Pb dating of zircons
- Optical microscopy
- Cathodoluminescence

Field, mapping and remote sensing skills

- Topographic analysis and metrics
- Structural, lithologic, and geomorphic mapping
- GPS Surveying
- Mapping and interpretation of seismic data
- Application of InSAR

IT skills

MATLAB	data visualization, topographic analysis, image analysis, statistics, modeling
ArcGIS	mapping, topographic analysis, data visualization, geo-statistics
Adobe Illustrator	Illustration and presentation of scientific material
Stereonet	Structural analysis
Decision Space	Seismic interpretation
Petrosys	Seismic interpretation

Language skills

German	native
English	proficient
French	advanced

Further training

2016: **OSL short course** (2 weeks), Utah State University.
2013: **Introduction to salt tectonics** (1 day), Exxon Mobile short course, UC Santa Barbara.
2012: **Integrated basin analysis and hydrocarbon systems** (1 day), Exxon Mobile short course, UC Santa Barbara.
2012: **Summer Institute on Earth-surface Dynamic** (10 days), Future Earth: Interactions of Climate and Earth-surface Processes, St. Anthony Falls Laboratory, Minneapolis.
2011: **LIDAR short course** (2 days), UC Davis.

Projects & collaborators

Quaternary landscape evolution around the Yellowstone hotspot.

- With Joel Pederson (USU)

Quaternary to decadal uplift rates in the eastern Pamir-Tian Shan collision zone.

- With David Bekaert (JPL), Ekbal Hussain (U. Leeds), Bodo Bookhagen (U Potsdam), Douglas Burbank (UCSB)

Planation surfaces on actively uplifting anticlines in the foreland of the Tian Shan.

- With Douglas Burbank (UCSB), Bodo Bookhagen (U. Potsdam), Chen Jie (China Earthquake Administration)

Physical experiments of fluvially created lateral planation surfaces on active folds

- With Chris Paola (UMN), Douglas Burbank (UCSB)

Geomorphic analysis of active faulting along the Akşehir normal fault, SW Turkey

- With Ed Keller (UCSB), Savaş Topal (Pamukkale University, Denizli)

The metamorphic aureole of the Skaergaard intrusion, Greenland.

- With Marian Holness (U of Cambridge), Madeleine Humphreys (U. of Durham)

TEACHING EXPERIENCE

Instructor

Spring 2015:	Geological Applications of GIS

Teaching Assistant

Winter 2015	Geological Catastrophes
Spring 2014	Geological Applications of GIS
Winter 2014	Structural Geology
Winter 2012	Structural Geology

OUTREACH AND COMMUNITY SERVICES

2015-2016:	UCSB Science Line participant
2015:	Participation in Science Nights at elementary schools
2014:	UCSB Graduate Student Representative
2013:	UCSB Graduate Alumni Career Panel organizing committee
2012-2013:	UCSB Speakers Club organizing committee
2008-2009:	Univ. of Cambridge Teaching Committee representative

PUBLICATIONS

Manuscripts

Bufe, A., Burbank, D.W., Liu, L., Bookhagen, B., Chen, J., Qin, J., Li, T., Thompson Jobe, J.A., Yang, H. *Variations of lateral bedrock erosion rates control planation of uplifting folds in the foreland of the Tian Shan, NW China*. (in review at JGR-Earth Surface)

Bufe, A., Bekaert, D., Hussain, E., Bookhagen, B., Burbank, D.W., Thompson, J.A., Chen, J., Li, T., Langtao, L., Gan, W. *Spatial and temporal dynamics of folds in the foreland of the Tian Shan, revealed through geodetic and geologic rock-uplift rates.* (in preparation)

Peer reviewed publications

Bufe, A., Paola, C., Burbank, D.W. (2016). *Fluvial bevelling of topography controlled by lateral channel mobility and uplift rate*. Nature Geoscience, *9*(9), 706-710.

Topal, S., Keller, E., **Bufe, A**., Koçyiğit, A. (2016). *Tectonic geomorphology of a large normal fault: Akşehir fault, SW Turkey*. Geomorphology, 259, 55-69.

Bufe, N. A., Holness, M. B., Humphreys, M. C. S. (2014). *Contact Metamorphism of Precambrian Gneiss by the Skaergaard Intrusion.* Journal of Petrology, 55, 1595-1617.

Selected conference proceedings

Bufe A., Pederson J., Tuzlack D. (2016). *Insights into the Quaternary tectonics of the Yellowstone hotspot from a terrace record along the Hoback and Snake rivers*. AGU Fall Meeting Abstracts. San Francisco, CA, USA.

Bufe, A., Bookhagen, B., Bekaert, D., Hussain, E., Burbank, D. W. (2016). *Rapid deformation in the foreland of the Pamir and Tian Shan, western China, revealed by Envisat-ASAR radar interferometry*. TerraSAR-X/TanDEM-X Science Team Meeting. Oberpfaffenhofen, Germany.

Bufe A., Pederson J., Tuzlack D. (2016). *Quaternary tectonics along the flanks of Yellowstone from terraces along the Hoback and Snake River.* GSA Annual Meeting. Denver, CO, USA.

Bufe, A., Paola, C., Burbank, D.W., Thompson, J.A. (2016). *Experimental evidence for climatically controlled changes between lateral erosion and incision of actively uplifting folds.* EGU General Assembly. Vienna, Austria.

Lavier, L., Ball, P.J., Manatschal, G., Heumann, M., Macdonald, J.D., Matt, V.J., **Bufe, A**. (2016). *Deciphering the rheological, stratigraphic and thermal evolution of magma-poor rifted margins: coupling thermo mechanical models with observations and interpretations from seismic reflection data*. Rifts III: Catching the Wave. London, UK.

Thompson, J.A., Chen, J., Yang, H., Li, T., Bookhagen, B., Burbank, D.W., **Bufe, A**. (2015). *OSL and cosmogenic 10Be dating of fluvial terraces on the northeast Pamir margin, northwest China*. AGU Fall Meeting Abstracts. San Francisco, CA, USA.

Bufe, A., Paola, C., Burbank, D.W. (2015). *Controls on lateral erosion of an active uplift by antecedent streams: An Experimental Study.* Binghamton Symposium on Experimental Geomorphology. Buffalo NY, USA.

Thompson, J., Li, T., Burbank, D., Chen, J., Bookhagen, B., **Bufe, A**., Yang, H. (2014). *Late Quaternary deformation rates in the Pamir-Tian Shan collision zone, NW China*. AGU Fall Meeting Abstracts. San Francisco, CA, USA.

Bufe, A., Burbank, D.W., Chen, J., Liu, L., Li, T., Thompson, J. (2014). *Constraints on timing and rates of strath terrace formation on actively uplifting anticlines in the foreland of the Chinese Tien Shan*. AGU Fall Meeting Abstracts. San Francisco, CA, USA.

Liu, L., **Bufe, A**., Chen, J., Burbank, D.W., Li, T., Thompson, J. (2014). *Detrital zircon U-Pb provenance study in Cenozoic strata of the Pamir-Tianshan collision zone*. AGU Fall Meeting Abstracts. San Francisco, CA, USA.

Bufe, N., Bookhagen, B., Burbank, D.W., Bekaert, D., Hussain, D. (2013). *Active deformation in the Pamir–Tian Shan collision zone, NW China*. Himalayan Karakorum Tibet Workshop & International Symposium on Tibetan Plateau. Tübingen, Germany.

Bufe, A., Burbank, D.W., Bookhagen, B. (2012). *Decadal deformation rates from SAR interferometry in the eastern Pamir-Tian Shan collision zone and implication for the growth and erosion of detachment folds*. AGU Fall Meeting Abstracts. San Francisco, CA, USA.

ABSTRACT

Rates and mechanics of fold uplift and lateral bedrock planation in convergent foreland basins.

by

Nel Aaron Bufe

Tectonic uplift and subsidence of rocks, together with their erosion, redistribution, and deposition by atmospheric, biologic, and gravitational processes shapes the topography of Earth's surface. Studying the rates and mechanics of such processes and how they vary in space and time is critical to understanding the dynamic environment in which we live.

Topographic change is most dramatic along convergent plate boundaries in continental settings. Here, single faults and folds can uplift at rates of several millimeters per year and can present a significant seismic hazard. Understanding the rates of growth and propagation of contractional structures is integral to an assessment of such hazards, as well as to modeling the development of continental collision zones. Whereas point measurements of deformation rates are commonly possible, constraining the full temporal and spatial evolution of structures remains challenging.

Competing with rock-uplift that elevates Earth's surface, landscape lowering is driven by the incision of rivers into bedrock. Rivers can also bevel laterally into bedrock, thereby planating topography and creating topographic markers, such as fluvial strath terraces, which are commonly used to infer climatic and tectonic changes. Significant uncertainties

remain in understanding the mechanics of such lateral erosion by rivers and of strath-terrace formation in uplifting landscapes.

Three studies in this thesis address the competition between surface uplift and lateral erosion, as well as the temporal and spatial patterns of fold growth. Chapter 1 presents results from physical experiments on the interactions between alluvial rivers with a zone of uplift. From these experiments, a simple parameter emerges that predicts the width of active beveling as a function of the uplift rate and the mobility of channels. Chapter 2 describes a field-study of the extensive lateral planation of actively uplifting folds by rivers in the foreland of the Tian Shan, northwestern China. Here, geomorphic mapping and dating of Late Quaternary terraces reveals that, contrary to existing models of strath-terrace formation, changes in lateral erosion rates of 1-3 orders of magnitude strongly control formation of planation surfaces. The dated fluvial terraces presented in this chapter do not only constrain rates of bedrock erosion, but also add to the growing database of Quaternary shortening and rock-uplift rates of contractional structures along the deforming eastern Pamir-Tian Shan collision zone. In order to explore how these rapidly deforming structures evolve both in time- and space, new decadal uplift rates obtained from interferometric synthetic aperture radar time-series analyses are presented in Chapter 3. These data place constraints on the spatial patterns of surface- and rock-uplift rates. In combination with rock-uplift rates measured over geologic timescales, a probabilistic model shows that, where significant (mm/y) changes in peak rock-uplift rate occurred across the Quaternary, gradual variations in those rates are more likely than sudden, step-like changes.

TABLE OF CONTENTS

Introduction

High mountain ranges, wide alluvial plains, and steep coastal cliffs might appear to be built for eternity, but every earthquake, landslide, or flood is a dramatic reminder that Earth's surface changes on timescales as short as a second. The most rapidly evolving regions are arguably those of steep topography, with rates of surface change of several millimeters per year (Burbank and Anderson, 2011). Here, topography is controlled by a fundamental competition between relief creation through relative rock uplift versus landscape flattening through erosional or depositional processes (Burbank et al., 1996; Kim et al., 2010; Kirby and Whipple, 2012; Straub et al., 2009). Because the relief of a landscape controls the potential energy available to erosional processes (DiBiase and Whipple, 2011; Sklar et al., 2016), more than half of the total mass eroded is derived from the steepest 10% of the global landmass (Larsen et al., 2014; Willenbring et al., 2014). Fluxes of sediment from upland settings, in turn, strongly control the dynamics of alluvial rivers (Ashworth et al., 2004; Bryant et al., 1995; Constantine et al., 2014; Wickert et al., 2013) and the construction of the sedimentary stratigraphic record (Paola, 2000; Tucker and Slingerland, 1996). Moreover, rapid physical erosion drives chemical weathering (West et al., 2005) and, therefore, potentially Earth's climate (Raymo and Ruddiman, 1992; Walker et al., 1981). Understanding the rates and processes of rock uplift and erosion in active tectonic settings has, therefore, far-reaching implications ranging from quantifying natural hazards to understanding the complex interaction that drive the evolution of Earth's surface.

The advent of methods to place absolute ages on structures in landscapes offers an unprecedented opportunity to obtain temporal constraints on some of the fundamental processes of landscape evolution. Moreover, land- and satellite-based remote sensing

techniques provide a wealth of topographic data that can be used to search for topographic and sedimentary signatures of climatic and tectonic processes (Bull, 1990; Clubb et al., 2016; Hancock and Anderson, 2002; Kirby and Whipple, 2012; Mudd, 2016; Roberts and White, 2010; Willett et al., 2014). The studies in this thesis address some of the knowledge gaps in understanding the interactions between erosion and uplift processes in convergent tectonic settings.

Using a set of physical experiments, a theoretical background for the competition between river planation and rock-uplift is developed in Chapter 1. A specially designed experimental basin allows the structural growth of a single fold crossed by antecedent rivers with precise control of uplift rate, as well as of sediment and water fluxes. These experiments reveal that a competition between the lateral mobility of channels and the uplift rate predicts > 95% of the extent of bedrock planation in weak bedrock. The channel mobility, in turn, is strongly controlled by sediment and water fluxes (Constantine et al., 2014; Wickert et al., 2013), and, therefore, presents a direct link between climatic forcing and bedrock erosion.

The experiments presented in Chapter 1 were motivated by an example of extensive beveling of actively uplifting anticlines in the rapidly deforming foreland of the southeastern Tian Shan, NW China. Chapter 2 applies the theoretical framework developed in Chapter 1 to this spectacular example of strath cutting. Such straths are commonly used as markers for tectonic, climatic, or sea-level changes in landscapes (Bull, 1990; Hancock and Anderson, 2002; Pazzaglia et al., 1998). A combination of field mapping, optically stimulated luminescence dating, and cosmogenic nuclide geochronology of fluvial deposits preserved on planation surfaces shows that order-of-magnitude changes in the lateral erosion rate drive

the cutting and abandonment of planation surfaces in this setting. These findings offer an alternative mechanism for the formation of planation surfaces, which have commonly been linked to pauses in the vertical incision of rivers (Finnegan and Balco, 2013; Hancock and Anderson, 2002; Langston et al., 2015).

Chapter 3 shifts the focus to the spatial and temporal evolution of uplift rates along the northeastern Pamir-Tian Shan collision zone − one of the fastest deforming regions on Earth. A new, high-resolution dataset of decadal uplift rates from a decomposition of interferometric synthetic aperture radar time-series and GPS data constrains the spatial pattern of surface- and rock-uplift rates on a series of folds and faults. These decadal rates are combined with a compilation of published Quaternary rock-uplift rates in the foreland (including rates presented in Chapter 2) to constrain simple models of the lifecycle of a fold and show that commonly, gradual changes in peak rock-uplift rates are more likely than step-wise, sudden changes in the growth of the folds.

References for the Introduction

Ashworth, P. J., Best, J. L., and Jones, M., 2004, Relationship between sediment supply and avulsion frequency in braided rivers: Geology, v. 32, no. 1, p. 21-24.

Bryant, M., Falk, P., and Paola, C., 1995, Experimental study of avulsion frequency and rate of deposition: Geology, v. 23, no. 4, p. 365-368.

Bull, W. B., 1990, Stream-terrace genesis: implications for soil development: Geomorphology, v. 3, no. 3–4, p. 351-367.

Burbank, D. W., and Anderson, R. S., 2011, Tectonic geomorphology, John Wiley & Sons.

Burbank, D. W., Leland, J., Fielding, E., Anderson, R. S., Brozovic, N., Reid, M. R., and Duncan, C., 1996, Bedrock incision, rock uplift and threshold hillslopes in the northwestern Himalayas: Nature, v. 379, no. 6565, p. 505-510.

Clubb, F. J., Mudd, S. M., Attal, M., Milodowski, D. T., and Grieve, S. W. D., 2016, The relationship between drainage density, erosion rate, and hilltop curvature: Implications for sediment transport processes: Journal of Geophysical Research: Earth Surface, p. n/a-n/a.

Constantine, J. A., Dunne, T., Ahmed, J., Legleiter, C., and Lazarus, E. D., 2014, Sediment supply as a driver of river meandering and floodplain evolution in the Amazon Basin: Nature Geoscience, v. 7, no. 12, p. 899-903.

DiBiase, R. A., and Whipple, K. X., 2011, The influence of erosion thresholds and runoff variability on the relationships among topography, climate, and erosion rate: Journal of Geophysical Research: Earth Surface, v. 116, no. F4, p. F04036.

Finnegan, N. J., and Balco, G., 2013, Sediment supply, base level, braiding, and bedrock river terrace formation: Arroyo Seco, California, USA: Geological Society of America Bulletin, v. 125, no. 7-8, p. 1114-1124.

Hancock, G. S., and Anderson, R. S., 2002, Numerical modeling of fluvial strath-terrace formation in response to oscillating climate: Geological Society of America Bulletin, v. 114, no. 9, p. 1131-1142.

Kim, W., Sheets, B. A., and Paola, C., 2010, Steering of experimental channels by lateral basin tilting: Basin Research, v. 22, no. 3, p. 286-301.

Kirby, E., and Whipple, K. X., 2012, Expression of active tectonics in erosional landscapes: Journal of Structural Geology, v. 44, no. 0, p. 54-75.

Langston, A. L., Tucker, G. E., and Anderson, R. S., 2015, Interpreting climate-modulated processes of terrace development along the Colorado Front Range using a landscape evolution model: Journal of Geophysical Research: Earth Surface, p. 2121–2138.

Larsen, I. J., Montgomery, D. R., and Greenberg, H. M., 2014, The contribution of mountains to global denudation: Geology, v. 42, no. 6, p. 527-530.

Mudd, S. M., 2016, Detection of transience in eroding landscapes: Earth Surface Processes and Landforms, p. n/a-n/a.

Paola, C., 2000, Quantitative models of sedimentary basin filling: Sedimentology, v. 47, p. 121-178.

Pazzaglia, F. J., Gardner, T. W., and Merritts, D. J., 1998, Bedrock Fluvial Incision and Longitudinal Profile Development Over Geologic Time Scales Determined by Fluvial Terraces, Rivers Over Rock: Fluvial Processes in Bedrock Channels, American Geophysical Union, p. 207-235.

Raymo, M. E., and Ruddiman, W. F., 1992, Tectonic forcing of late Cenozoic climate: Nature, v. 359, no. 6391, p. 117-122.
Roberts, G. G., and White, N., 2010, Estimating uplift rate histories from river profiles using African examples: Journal of Geophysical Research: Solid Earth, v. 115, no. B2, p. B02406.
Sklar, L. S., Riebe, C. S., Lukens, C. E., and Bellugi, D., 2016, Catchment power and the joint distribution of elevation and travel distance to the outlet: Earth Surface Dynamics, v. 4, no. 4, p. 799-818.
Straub, K. M., Paola, C., Mohrig, D., Wolinsky, M. A., and George, T., 2009, Compensational Stacking of Channelized Sedimentary Deposits: Journal of Sedimentary Research, v. 79, no. 9, p. 673-688.
Tucker, G. E., and Slingerland, R., 1996, Predicting sediment flux from fold and thrust belts: Basin Research, v. 8, no. 3, p. 329-349.
Walker, J. C. G., Hays, P. B., and Kasting, J. F., 1981, A negative feedback mechanism for the long-term stabilization of Earth's surface temperature: Journal of Geophysical Research: Oceans, v. 86, no. C10, p. 9776-9782.
West, A. J., Galy, A., and Bickle, M., 2005, Tectonic and climatic controls on silicate weathering: Earth and Planetary Science Letters, v. 235, no. 1–2, p. 211-228.
Wickert, A. D., Martin, J. M., Tal, M., Kim, W., Sheets, B., and Paola, C., 2013, River channel lateral mobility: metrics, time scales, and controls: Journal of Geophysical Research: Earth Surface, v. 118, no. 2, p. 396-412.
Willenbring, J. K., Codilean, A. T., Ferrier, K. L., McElroy, B., and Kirchner, J. W., 2014, Short Communication: Earth is (mostly) flat, but mountains dominate global denudation: apportionment of the continental mass flux over millennial time scales, revisited: Earth Surface Dynamics Discussions, v. 2014, p. 1-17.
Willett, S. D., McCoy, S. W., Perron, J. T., Goren, L., and Chen, C.-Y., 2014, Dynamic Reorganization of River Basins: Science, v. 343, no. 6175.

Chapter 1: Fluvial beveling of topography controlled by lateral channel mobility and uplift rate[a]

Aaron Bufe[1*], Chris Paola[2] and Douglas W. Burbank[1]

1 Department of Earth Sciences, University of California, Santa Barbara, California, 93106, USA

2 Department of Earth Sciences, University of Minnesota, Twin Cities, Minnesota, 55455, USA

Abstract

Valley morphologies of rivers crossing zones of active uplift range from narrow canyons to broad alluvial surfaces. They provide illuminating examples of the fundamental, but poorly understood competition between relief creation and landscape flattening. Motivated by field examples of abandoned kilometer-wide, fluvially eroded platforms on active detachment folds in the Tian Shan foreland, we present physical experiments investigating the controls on the area of a growing fold that is reworked by antecedent rivers. These experiments reproduce the range of observed field morphologies, varying from wholesale beveling of the uplifting fold to the formation of narrow, steep-walled canyons. A log-linear fit to a simple dimensionless parameter shows that the competition between lateral channel mobility and rock-uplift rate explains > 95% of the variation in the beveled fraction of the folds. Our data suggest that lateral bedrock erosion rates of 0.5-40 m/yr are required to explain the formation of extensive platforms in the Tian Shan foreland and imply that

[a]Adapted from: Bufe et al., (2016), Fluvial bevelling of topography controlled by lateral channel mobility and uplift rate: Nature Geoscience, v. 9, no. 9, p. 706-710.

varying water and sediment fluxes can cause striking changes in the degree of landscape flattening by influencing the lateral erosion rate.

1 Introduction

Much of the topography on Earth's surface is built by the interaction between rock uplift and erosion. Whereas rivers can create relief by incising into uplifting bedrock, they also flatten it by lateral planation. Currently, much remains to be learned about this fundamental competition, despite its importance for explaining many landscape features and interpreting them in terms of climatic, tectonic, or autogenic processes. A single stream, flowing perpendicular to an uplifting fold, provides a simple natural laboratory in which to study links among uplift, erosion, sediment and water fluxes, and the erodibility of the uplifting material. Whereas transverse streams generally narrow across a zone of uplift (Amos and Burbank, 2007; Duvall et al., 2004; Harbor, 1998; Lavé and Avouac, 2001; Whittaker et al., 2007), in some cases, valleys preserve evidence of efficient lateral planation -- beveling -- of actively uplifting rock (Lavé and Avouac, 2001; Scharer et al., 2006). A striking example of extremely efficient lateral planation occurs in the foreland of the Tian Shan (Fig. 1). Here, a series of active detachment folds with 2-5 km of structural relief and uplifting at 1–3 mm/y (Chen et al., 2007; Heermance et al., 2008; Li et al., 2013; Scharer et al., 2004) preserves extensive low-relief surfaces interpreted as having been beveled by transverse drainages (Fig. 1). A combination of weak bedrock in the core of the folds (Chen et al., 2007; Heermance et al., 2007), abundant, coarse bedload, and the presence of upstream-aggrading alluvial fans likely promotes efficient lateral erosion (Cook et al., 2014; Johnson and Finnegan, 2015). Obvious differences in the magnitude of beveling between folds (Fig. 1b)

and changes from beveling to incision (Fig. 1c) raise questions about what controls the erosion of these uplifts.

Inspired by these observations, we present results from a simple experiment investigating the controls on the width of valleys across active uplifts, focusing on the formation of wide, beveled platforms versus incised canyons. We explore general behaviors and system-scale variables that we interpret as relatively independent of scale (Paola et al., 2009). Previous experiments investigating transverse drainage development have successfully reproduced river antecedence, stream piracy, and lake overflow (Douglass and Schmeeckle, 2007), and demonstrated how planforms of meandering and braided streams are affected by even small amounts of uplift (Ouchi, 1985). We build upon these previous studies by using a basin designed to allow precise control and reproducibility of uplift rates, sediment flux, and water flux, as well as collection of high-resolution topographic and photographic data. The experiments test the hypothesis that the extent of beveling of an uplift is controlled by a competition between the uplift rate and the mobility of channels. Traditionally, planation surfaces formed by rivers incising into uplifting bedrock have been attributed to a slowing of vertical incision through either changes in local base level (Castillo et al., 2013; Finnegan and Balco, 2013; Pazzaglia and Gardner, 1993; Whittaker et al., 2007) or high sediment loads shielding the river bed (Bull, 1990; DeVecchio et al., 2012; Fuller et al., 2009; Hancock and Anderson, 2002; Molnar et al., 1994). Here, we explicitly consider the importance of changes in the lateral erosion rate in explaining the competition between relief creation and flattening (Fuller et al., 2016; Lavé and Avouac, 2001; Limaye and Lamb, 2016).

2 Theoretical and experimental framework

Consider a simple fold that grows across the width of an active alluvial fan (Fig. 1). We show here that the fraction of the uplifting material that can be reworked by rivers can be predicted by a simple dimensionless parameter describing the competition between the time it takes to uplift a fixed volume of material and the time to rework a fixed volume of the alluvial fan surface (Fig. 2)

$$F_b \sim \frac{Q_f}{Q_u} \quad (1),$$

where Q_u is the flux of "rock" uplifted above the base level across the entire fold and Q_f is the flux of material reworked by rivers on the alluvial fans upstream of the uplift defined as:

$$Q_f = \frac{A_f H}{T_f} \quad (2),$$

where A_f is the area of the actively reworked alluvial fan upstream of the fold, H is the flow depth, and T_f is the lateral channel mobility timescale. Similar to previous studies, the channel mobility timescale (T_f) is defined as an e-folding timescale of surface reworking, i.e., the time required to rework 63% of the active fluvial surface (Cazanacli et al., 2002; Kim et al., 2010; Wickert et al., 2013) which has been shown to be strongly affected by sediment flux (Constantine et al., 2014; Wickert et al., 2013).

We performed six experiments in a specially designed stream table with dimensions of 4.8x3.0x0.6 m and allowing a total of 0.14 m of surface uplift across a ~0.50 m wide zone spanning the table's width (Fig. 3a). The basin was filled with very well sorted silica sand (D_{50} = 0.52 mm), and we supplied a constant flux of water and the same sand through a single U-shaped inlet at the top of the flume (Fig. 3). All experiments started with a phase of rapid aggradation, because initial slopes were set below the equilibrium slope for the fluxes

of sediment and water. Once the net surface change oscillated around zero, the uplift was imposed through 47 regularly spaced increments of ~3 mm of surface uplift at the fold's apex.

3 Results

With a steady water discharge, our experiments encompass a 100-fold range in uplift rates, a 6- to 7-fold range in sediment flux, and a 4-fold range of upstream active fluvial surface width. With this range of explored parameters, we reproduce a range of morphologies observed on folds in the foreland of the Tian Shan (Fig. 1): from near-complete beveling of the uplift in which emergent topography is continuously reworked, to the formation of a narrow canyon through the fold (Fig. 4). As is typical for experiments with steep slopes and a coarse sediment load (Cazanacli et al., 2002; Kim et al., 2010; Whipple et al., 1998; Wickert et al., 2013), a self-organized braided channel pattern rapidly evolved (Fig. 3b). Undercutting of steep channel walls by a laterally migrating stream and subsequent collapse of the wet sand were common across the uplift, and was probably the most efficient process by which the emerging fold was eroded. This channel migration was highly stochastic and commonly occurred in rapid lateral sweeps as a combination of (1) erosion along the walls of a "canyon" by migration of the river in a direction parallel to the fold axis and (2) erosion focused on the upstream side of the fold by rivers being deflected laterally as they impinged on the structure (similar to sweeps described in the field (Cook et al., 2014)).

Across the experimental series, the most important observation is that high fractions of beveling are associated with low uplift rates, low channel-mobility timescales, i.e., rapidly migrating streams, and wide upstream alluvial fans (Fig. 5). The data are regressed with Q_f

calculated during ongoing uplift, but we find that the upstream channel mobility in these experiments is not significantly affected by the uplift and is instead dominantly controlled by the imposed boundary conditions and the sediment and water fluxes (Fig. 5). The beveled fraction decreases log-linearly as the ratio of mobility-to-uplifted volume (Eq. 1) decreases (Fig. 5). Although these data display no evidence for a threshold behavior, we stress that the relationship has to break down at very high or very low beveled areas, because the beveled fraction cannot be higher than 100% or lower than 0%. In the absence of evidence for how the system behaves at these limits, the log-linear fit provides the simplest description of the available data.

With sufficiently high channel mobility (resulting here from high sediment fluxes) or sufficiently low uplift rates, mobile channels can erode sediment laterally at rates equivalent to the rate at which fold growth is feeding sediment mass into the system (Fig. 5). Our results suggest that, for complete beveling of the uplift, the rate of volumetric reworking upstream of the uplift has to be ~20-60 times higher than the rate of volumetric addition by fold uplift (Fig. 5). Thus, lateral erosion across the uplift is ~20-60 times slower than the corresponding channel mobility on an aggrading alluvial plain.

With less mobile channels, only a fraction of the uplifting fold can be eroded, and rivers become confined into a zone across the uplift that they continuously rework, leading to an emergent fold that is traversed by valley-confined channels (Fig. 4). We note that channel mobility in braided rivers is the product of both avulsions and lateral channel migration (Wickert et al., 2013). Because our method of calculating channel mobility is independent of the detailed processes controlling the mobility, these results should in principle apply to a range of river types.

4 Discussion

4.1 Changes between incision and beveling

When comparing two systems in equilibrium, order-of-magnitude differences in the uplift rate, channel mobility timescales, or the area of the active fluvial area upstream of the uplift are necessary to explain significant (> 25%) differences in the beveled fraction (Fig. 5). Furthermore, as expected, equilibrium slopes and channel mobilities are consistent for experiments with similar water and sediment inputs, but vary strongly with the sediment supply rate (Constantine et al., 2014; Wickert et al., 2013) (Table S2).

When considering a particular system in equilibrium, small (<< order-of magnitude) perturbations in the sediment and water balance can have striking impacts on the channel mobility and the width of the active upstream fluvial surface: enough to cause large differences in the beveled fraction. This effect is demonstrated by Run 6. In this experiment, the initial inlet geometry (cf. Fig. 3) was V-shaped and changed to a U-shape only after 2.5 h of runtime. As expected from theoretical considerations of sediment transport (Parker et al., 1998), the increased focusing of the water flux through the U-shaped inlet led to a higher transport capacity and lower equilibrium slope, and thus to the incision of a canyon *prior* to the onset of uplift at 8 h of runtime. This incision caused a striking reduction of the width of both the active area upstream and the beveled area of the fold (Fig. 5). Notably, the input parameters for Run 6 are the same as for Run 3, but the beveled fraction is only about half of that run. However, by taking into account the width of the active fluvial surface and the channel mobility upstream of the uplift, the beveled area can still be predicted. This finding emphasizes how small perturbations of the upstream boundary condition or changes in the inputs can trigger a significant response, leading to a new state of equilibrium. Importantly,

this result illustrates how channel mobility can be influenced by processes other than the sediment flux and explains why the ratio of sediment flux to uplift flux is not sufficient to predict lateral planation by rivers when departures from equilibrium are considered (Fig. 6). Thus, a small decrease in sediment flux or increase in water flux is expected to increase the transport capacity (Metivier and Meunier, 2003) and to cause 1) a decrease in channel mobility and 2) a phase of incision accompanied by a notable decrease in the area of the active fluvial surface (Fig. 6). Together, these two processes can trigger large changes in the extent of beveling in response to quite modest changes in sediment or water flux. These observations raise questions concerning which mechanistic processes control the width changes of the active fluvial surface following a change in sediment flux, and how fast the system recovers from, or responds to, a phase of incision.

As an alternative to variations in inputs, autogenic cycles could cause changes between incision and lateral erosion of the folds (Finnegan and Dietrich, 2011; Kim et al., 2014; Limaye and Lamb, 2016). Indeed, we observe two major autogenic cycles in the experiments. First, several minute-long sweeps of rapid lateral erosion occur in all runs, but their time scales are short enough not to cause significant changes in the beveled area. Second, in the long, slow uplift experiment (Run 4), we observe five 10- to 20-hour-long cycles in which topography can build along the flanks of the basin before being removed in rapid lateral sweeps. Whereas the proportion of the beveled area of the fold during these periods can be reduced from 100% to 80% (Fig. S5), these cycles cannot explain changes between narrow canyons and wide platforms, such as those seen in the foreland of the Tian Shan (Fig. 1). Thus, we suggest that persistent changes between beveling and incision, with

major changes in the extent of beveling, have to be driven by external factors such as changes in water and sediment flux.

4.2 Lateral channel mobility in the field

The use of unconsolidated sand as experimental substrate means that no detachment limit exists, rivers are always at transport capacity, and the effect of tools in detaching grains (Sklar and Dietrich, 2004) becomes unimportant. Therefore, our experiments are most applicable to weakly consolidated uplifted material. We do not know if the presence of a detachment limit simply shifts or steepens the log-linear fit (Fig. 5) or if sufficient rock strength could qualitatively change the observed dependence of valley width on the uplift/mobility ratio. However, the experiments successfully reproduce the general range of morphologies seen in the field for rivers crossing folds that are uplifting easily erodible bedrock (Fig. 1). Thus, we suggest that the general concept of a competition between channel mobility and uplift rates (corrected for base-level changes) that controls how rivers create or destroy relief is largely scale independent and could apply, with modification, to account for bedrock strength in detachment-limited systems.

Therefore, making assumptions about steady fold-uplift rates relative to base level, and some representative flow depth, we can use the fit to the experimental data to estimate the channel mobilities necessary to bevel the detachment folds in the foreland of the Tian Shan. Sudden deformation by earthquakes in which rock uplift is significantly greater than flow depths could potentially complicate field applications of the experimental data. However, deformation of detachment folds is likely to be dominated by slow creep. Moreover, rapid lateral bedrock erosion has been shown to occur subsequent to major earthquakes after just a short period of adjustment (Cook et al., 2014).

The Kashi and Atushi folds have the same weakly consolidated sand and siltstones exposed in their cores and have been uplifting at 1-3 mm/y over the last 1-2.4 My (Chen et al., 2007; Heermance et al., 2008; Heermance et al., 2007; Scharer et al., 2006; Scharer et al., 2004). Neogene sediment-accumulation rates in the foreland and thus rates of base-level rise have been up to 0.8 mm/y (Heermance et al., 2007). Whereas the eastern part of the Atushi fold was beveled entirely across much of its length (Fig. 1), only ~20% of the Kashi fold preserves clear topographic evidence for lateral erosion. Using a block uplift at a rate of 1.5 ± 0.5 mm/y, a characteristic flow depth of 0.75 ± 0.25 m, and assuming that the entire 200 ± 40 km^2 of the upstream alluvial fan were being actively reworked at the time of beveling, we find that channel mobility timescales on the order of ~40 ± 30 years are necessary to explain beveling of 95 ± 5% of 100 km^2 of the Atushi fold. Given that major rivers (with drainage areas > 1 km^2) on the alluvial fans upstream of the Atushi fold are spaced 2-8 km apart, we predict that effective lateral migration rates on the alluvial fans of 30–800 m/y and corresponding lateral bedrock erosion rates of 0.5–40 m/y (20-60 times slower) would be necessary for near-complete beveling of that fold. Such high lateral migration rates -- tens to hundreds of meters per year -- may seem unlikely in today's arid climate. Yet, even now, summer thunderstorms drive flash floods, and snowmelt feeds high spring discharges that cause significant erosion and mobile channels. Similarly high lateral migration rates have been reported on other fans, alluvial plains, and deltas, such as the Emerald Lake Fan, B.C., the Yellow River Delta, and the Lower Mississippi alluvial plain (Jerolmack and Mohrig, 2007). In Taiwan, lateral bedrock erosion rates of up to 5.1 m/y, comparable to our estimate of 0.5-40 m/y, have been reported (Cook et al., 2014). These locations all have wetter climates than the modern foreland of the Tian Shan, but there is

evidence for episodes of wetter climate in the Tarim basin throughout the late Pleistocene (Yang and Scuderi, 2010). These wet episodes most likely coincide with times of beveling of the folds.

Beveled platforms on the Atushi fold (Fig. 1) are now uplifted, and modern streams are incising 20- to 200-m-deep canyons into the folds. Thus, a change from beveling to incision has occurred. It appears unlikely that large variations in rock-uplift rates caused incision to begin, given the equivalence of decadal (geodetic) and Late Pleistocene shortening rates (Li et al., 2012). Order-of-magnitude decreases in the ratio of sediment flux to water flux also seem unlikely considering that deep incision of the fan heads is uncommon. Given the ubiquitous, Late Pleistocene terraces along channels entering the Tarim Basin (Li et al., 2013) and evidence for several episodes of much wetter climates in the area (Yang and Scuderi, 2010), we suggest that climatically controlled changes in sediment and water fluxes caused repeated, synchronous episodes of beveling and incision of folds in the Tian Shan foreland.

In summary, our experiments demonstrate that a simple competition between lateral channel mobility and rock-uplift rate can explain a range of topographies from narrow, steep-walled canyons to wide, beveled platforms and thus illuminate one of the fundamental competitions that drive relief creation and destruction on Earth's surface. Similarities in the morphologies between the experiments and the field suggest that these findings are largely scale-independent and applicable to detachment-limited systems, at least where bedrock is relatively weak. Whereas in a simple equilibrium case, channel mobility is controlled by sediment flux, perturbations of the equilibrium can cause striking changes in both mobility and active fluvial area and, thus, in the morphologies of valleys crossing growing folds.

References

Amos, C. B., and Burbank, D. W., 2007, Channel width response to differential uplift: Journal of Geophysical Research: Earth Surface, v. 112, no. F2, p. F02010.

Bull, W. B., 1990, Stream-terrace genesis: implications for soil development: Geomorphology, v. 3, no. 3–4, p. 351-367.

Castillo, M., Bishop, P., and Jansen, J. D., 2013, Knickpoint retreat and transient bedrock channel morphology triggered by base-level fall in small bedrock river catchments: The case of the Isle of Jura, Scotland: Geomorphology, v. 180, no. 0, p. 1-9.

Cazanacli, D., Paola, C., and Parker, G., 2002, Experimental steep, braided flow: application to flooding risk on fans: Journal of Hydraulic Engineering, v. 128, no. 3, p. 322-330.

Chen, J., Heermance, R., Burbank, D. W., Scharer, K. M., Miao, J., and Wang, C., 2007, Quantification of growth and lateral propagation of the Kashi anticline, southwest Chinese Tian Shan: Journal of Geophysical Research: Solid Earth, v. 112, no. B3, p. B03S16.

Constantine, J. A., Dunne, T., Ahmed, J., Legleiter, C., and Lazarus, E. D., 2014, Sediment supply as a driver of river meandering and floodplain evolution in the Amazon Basin: Nature Geoscience, v. 7, no. 12, p. 899-903.

Cook, K. L., Turowski, J. M., and Hovius, N., 2014, River gorge eradication by downstream sweep erosion: Nature Geoscience, v. 7, no. 9, p. 682-686.

DeVecchio, D. E., Heermance, R. V., Fuchs, M., and Owen, L. A., 2012, Climate-controlled landscape evolution in the Western Transverse Ranges, California: Insights from Quaternary geochronology of the Saugus Formation and strath terrace flights: Lithosphere, v. 4, no. 2, p. 110-130.

Douglass, J., and Schmeeckle, M., 2007, Analogue modeling of transverse drainage mechanisms: Geomorphology, v. 84, no. 1–2, p. 22-43.

Duvall, A., Kirby, E., and Burbank, D., 2004, Tectonic and lithologic controls on bedrock channel profiles and processes in coastal California: Journal of Geophysical Research: Earth Surface, v. 109, no. F3, p. F03002.

Finnegan, N. J., and Balco, G., 2013, Sediment supply, base level, braiding, and bedrock river terrace formation: Arroyo Seco, California, USA: Geological Society of America Bulletin, v. 125, no. 7-8, p. 1114-1124.

Finnegan, N. J., and Dietrich, W. E., 2011, Episodic bedrock strath terrace formation due to meander migration and cutoff: Geology, v. 39, no. 2, p. 143-146.

Fuller, T. K., Gran, K. B., Sklar, L. S., and Paola, C., 2016, Lateral erosion in an experimental bedrock channel: the influence of bed roughness on erosion by bed-load impacts: Journal of Geophysical Research: Earth Surface, v. 121, p. 1084-1105.

Fuller, T. K., Perg, L. A., Willenbring, J. K., and Lepper, K., 2009, Field evidence for climate-driven changes in sediment supply leading to strath terrace formation: Geology, v. 37, no. 5, p. 467-470.

Hancock, G. S., and Anderson, R. S., 2002, Numerical modeling of fluvial strath-terrace formation in response to oscillating climate: Geological Society of America Bulletin, v. 114, no. 9, p. 1131-1142.

Harbor, D. J., 1998, Dynamic Equilibrium between an Active Uplift and the Sevier River, Utah: The Journal of Geology, v. 106, no. 2, p. 181-194.

Heermance, R. V., Chen, J., Burbank, D. W., and Miao, J., 2008, Temporal constraints and pulsed Late Cenozoic deformation during the structural disruption of the active Kashi foreland, northwest China: Tectonics, v. 27, no. 6, p. TC6012.

Heermance, R. V., Chen, J., Burbank, D. W., and Wang, C., 2007, Chronology and tectonic controls of Late Tertiary deposition in the southwestern Tian Shan foreland, NW China: Basin Research, v. 19, no. 4, p. 599-632.

Jerolmack, D. J., and Mohrig, D., 2007, Conditions for branching in depositional rivers: Geology, v. 35, no. 5, p. 463-466.

Johnson, K. N., and Finnegan, N. J., 2015, A lithologic control on active meandering in bedrock channels: Geological Society of America Bulletin, v. 127, no. 11-12, p. 1766-1776.

Kim, W., Petter, A., Straub, K., and Mohrig, D., 2014, Investigating the autogenic process response to allogenic forcing, *in* Martinius, A. W., Ravnas, R., Howell, J. A., Steel, R. J., and Wonham, J. P., eds., From Depositional Systems to Sedimentary Successions on the Norwegian Continental Margin: Hoboken, NJ, USA, John Wiley & Sons, Ltd., p. 127-138.

Kim, W., Sheets, B. A., and Paola, C., 2010, Steering of experimental channels by lateral basin tilting: Basin Research, v. 22, no. 3, p. 286-301.

Lavé, J., and Avouac, J. P., 2001, Fluvial incision and tectonic uplift across the Himalayas of central Nepal: Journal of Geophysical Research: Solid Earth, v. 106, no. B11, p. 26561-26591.

Li, T., Chen, J., Thompson, J. A., Burbank, D. W., and Xiao, W., 2012, Equivalency of geologic and geodetic rates in contractional orogens: New insights from the Pamir Frontal Thrust: Geophysical Research Letters, v. 39, no. 15, p. L15305.

Li, T., Chen, J., Thompson, J. A., Burbank, D. W., and Yang, X., 2013, Quantification of three-dimensional folding using fluvial terraces: A case study from the Mushi anticline, northern margin of the Chinese Pamir: Journal of Geophysical Research: Solid Earth, v. 118, no. 8, p. 4628-4647.

Limaye, A. B. S., and Lamb, M. P., 2016, Numerical model predictions of autogenic fluvial terraces and comparison to climate change expectations: Journal of Geophysical Research: Earth Surface, v. 121, p. 512-544.

Metivier, F., and Meunier, P., 2003, Input and output mass flux correlations in an experimental braided stream. Implications on the dynamics of bed load transport: Journal of Hydrology, v. 271, no. 1–4, p. 22-38.

Molnar, P., Erik Thorson, B., Burchfiel, B. C., Deng, Q., Feng, X., Li, J., Raisbeck, G. M., Shi, J., Zhangming, W., Yiou, F., and You, H., 1994, Quaternary climate change and the formation of river terraces across growing anticlines on the north flank of the Tien Shan, China: The Journal of Geology, v. 102, no. 5, p. 583-602.

Ouchi, S., 1985, Response of alluvial rivers to slow active tectonic movement: Geological Society of America Bulletin, v. 96, no. 4, p. 504-515.

Paola, C., Straub, K., Mohrig, D., and Reinhardt, L., 2009, The “unreasonable effectiveness” of stratigraphic and geomorphic experiments: Earth-Science Reviews, v. 97, no. 1–4, p. 1-43.

Parker, G., Paola, C., Whipple, K., and Mohrig, D., 1998, Alluvial fans formed by channelized fluvial and sheet flow. I: Theory: Journal of Hydraulic Engineering, v. 124, no. 10, p. 985-995.

Pazzaglia, F. J., and Gardner, T. W., 1993, Fluvial terraces of the lower Susquehanna River: Geomorphology, v. 8, no. 2–3, p. 83-113.
Scharer, K. M., Burbank, D. W., Chen, J., and Weldon, R. J., 2006, Kinematic models of fluvial terraces over active detachment folds: Constraints on the growth mechanism of the Kashi-Atushi fold system, Chinese Tian Shan: Geological Society of America Bulletin, v. 118, no. 7-8, p. 1006-1021.
Scharer, K. M., Burbank, D. W., Chen, J., Weldon, R. J., Rubin, C., Zhao, R., and Shen, J., 2004, Detachment folding in the Southwestern Tian Shan–Tarim foreland, China: shortening estimates and rates: Journal of Structural Geology, v. 26, no. 11, p. 2119-2137.
Sklar, L. S., and Dietrich, W. E., 2004, A mechanistic model for river incision into bedrock by saltating bed load: Water Resources Research, v. 40, no. 6, p. W06301.
Whipple, K., Parker, G., Paola, C., and Mohrig, D., 1998, Channel Dynamics, Sediment Transport, and the Slope of Alluvial Fans: Experimental Study: The Journal of Geology, v. 106, no. 6, p. 677-694.
Whittaker, A. C., Cowie, P. A., Attal, M., Tucker, G. E., and Roberts, G. P., 2007, Bedrock channel adjustment to tectonic forcing: Implications for predicting river incision rates: Geology, v. 35, no. 2, p. 103-106.
Wickert, A. D., Martin, J. M., Tal, M., Kim, W., Sheets, B., and Paola, C., 2013, River channel lateral mobility: metrics, time scales, and controls: Journal of Geophysical Research: Earth Surface, v. 118, no. 2, p. 396-412.
Yang, X., and Scuderi, L. A., 2010, Hydrological and climatic changes in deserts of China since the late Pleistocene: Quaternary Research, v. 73, no. 1, p. 1-9.

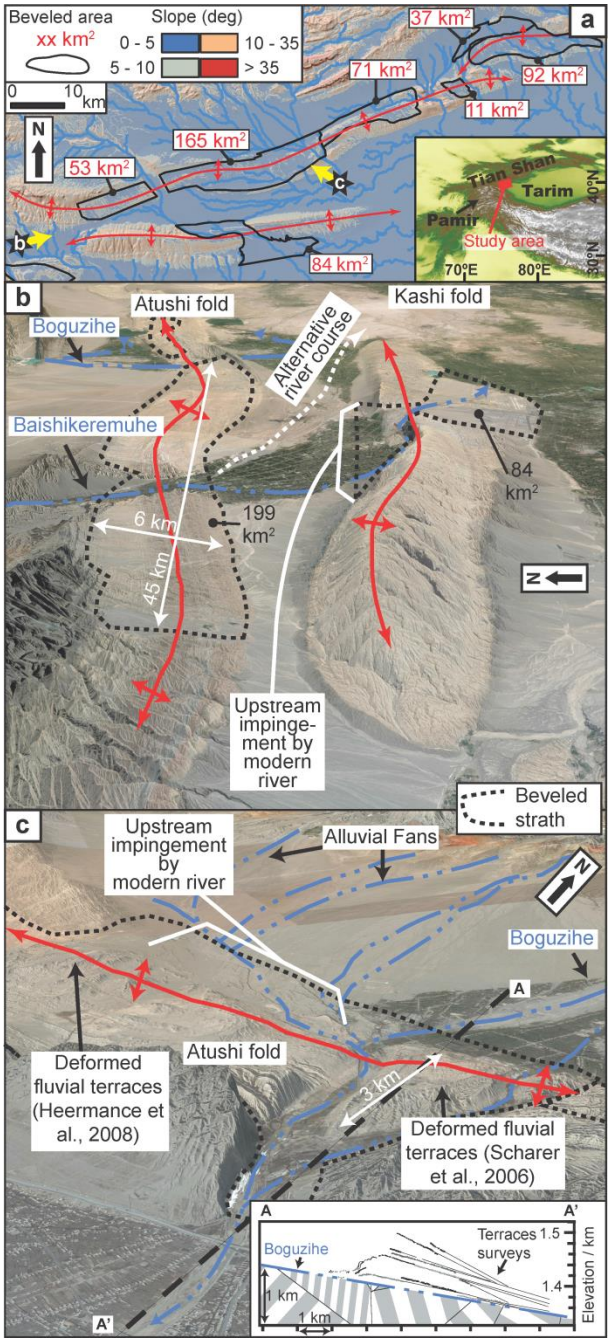

Figure 1: Extensively beveled surfaces in the foreland of the Tian Shan. (a) Slope map showing the extent of beveling on selected folds in the foreland of the Tian Shan. Yellow arrows indicate the look directions of b and c. (b) Oblique Google Earth view showing the mostly unbeveled Kashi fold and the beveled Atushi fold. (c) View of Boguzihe water gap on the Atushi fold showing incision of the modern river into the beveled fold. Remnant fluvial terraces are being uplifted and deformed as shown on the inset graph of terrace surveys (Scharer et al., 2006).

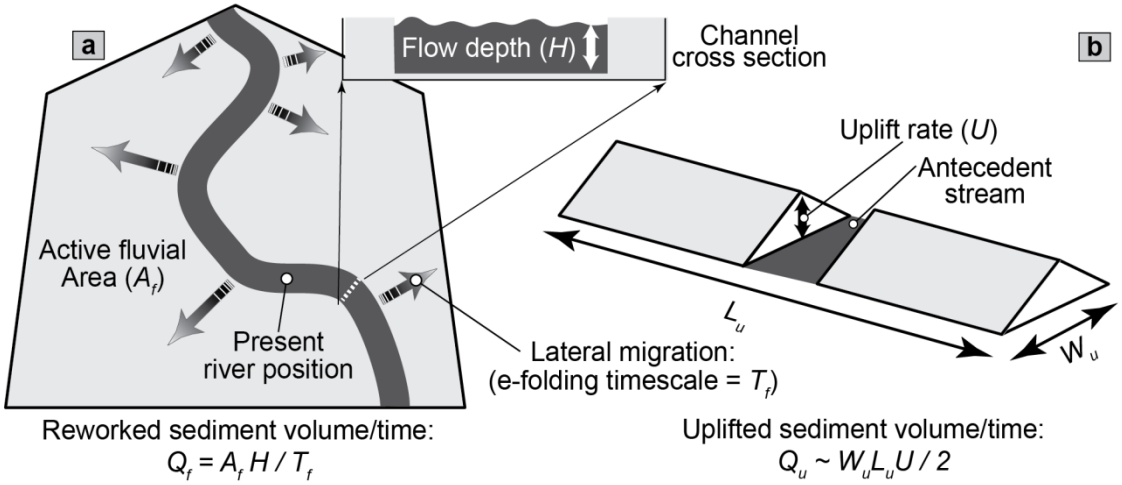

Figure 2: Sketch of the two competing "fluxes" hypothesized to predict the extent of beveling and lateral erosion rate of the uplift. (a) Rate of sediment reworking on an intermittently wetted and reworked active fluvial surface A_f by a series of streams with representative depth H reworking the surface at a rate described by timescale T_f. The rate of reworking Q_f is measured before the start of uplift. (b) Aerially integrated "rock" uplift rate. Volume calculation in the sketch assumes a triangular fold. In the experiments, the uplifted volume is measured directly from topographic scans.

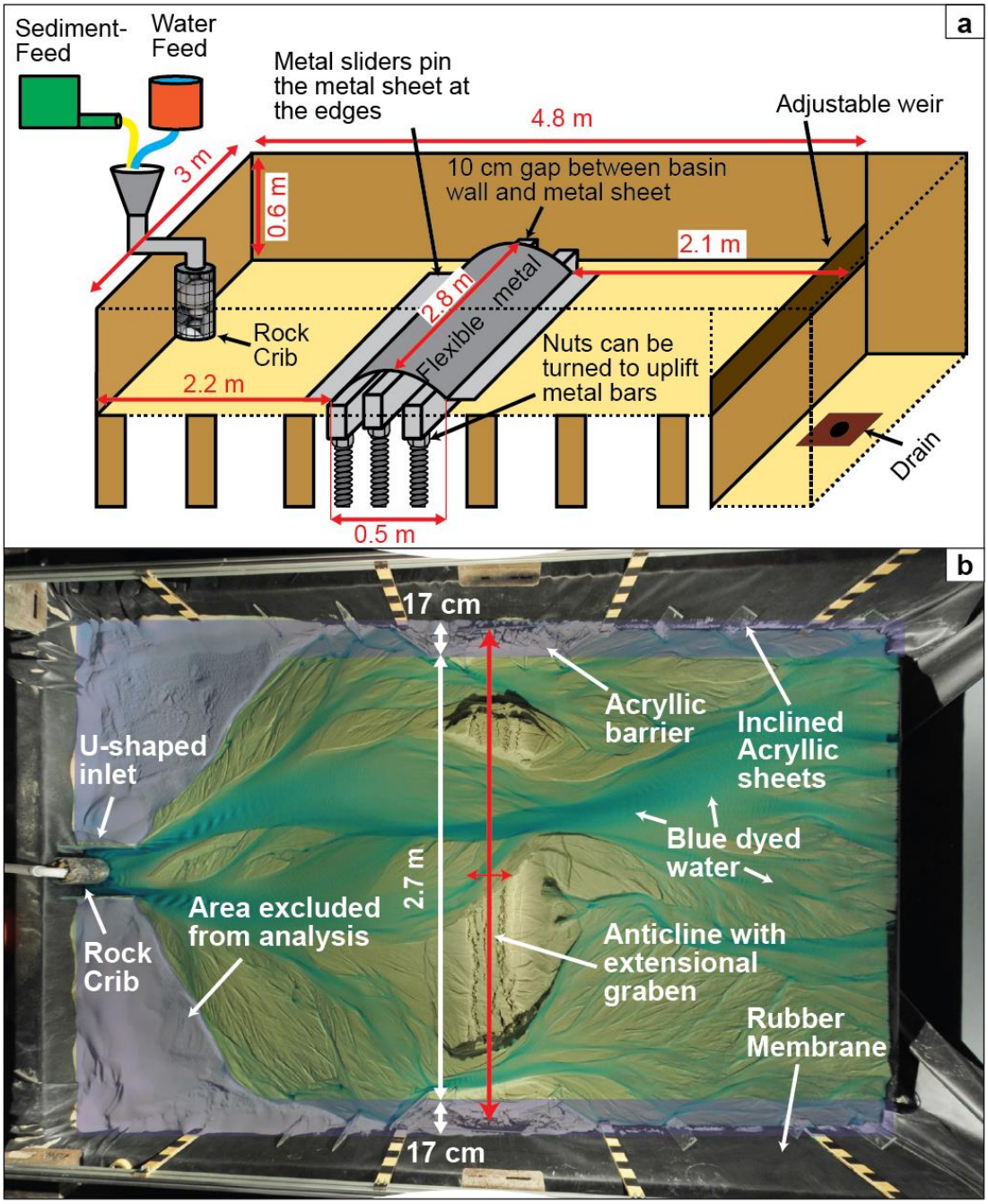

Figure 3: The experimental setup. (a) Sketch of the experimental setup. (b) Look-down photo of the basin showing Run 3 in the final stages.

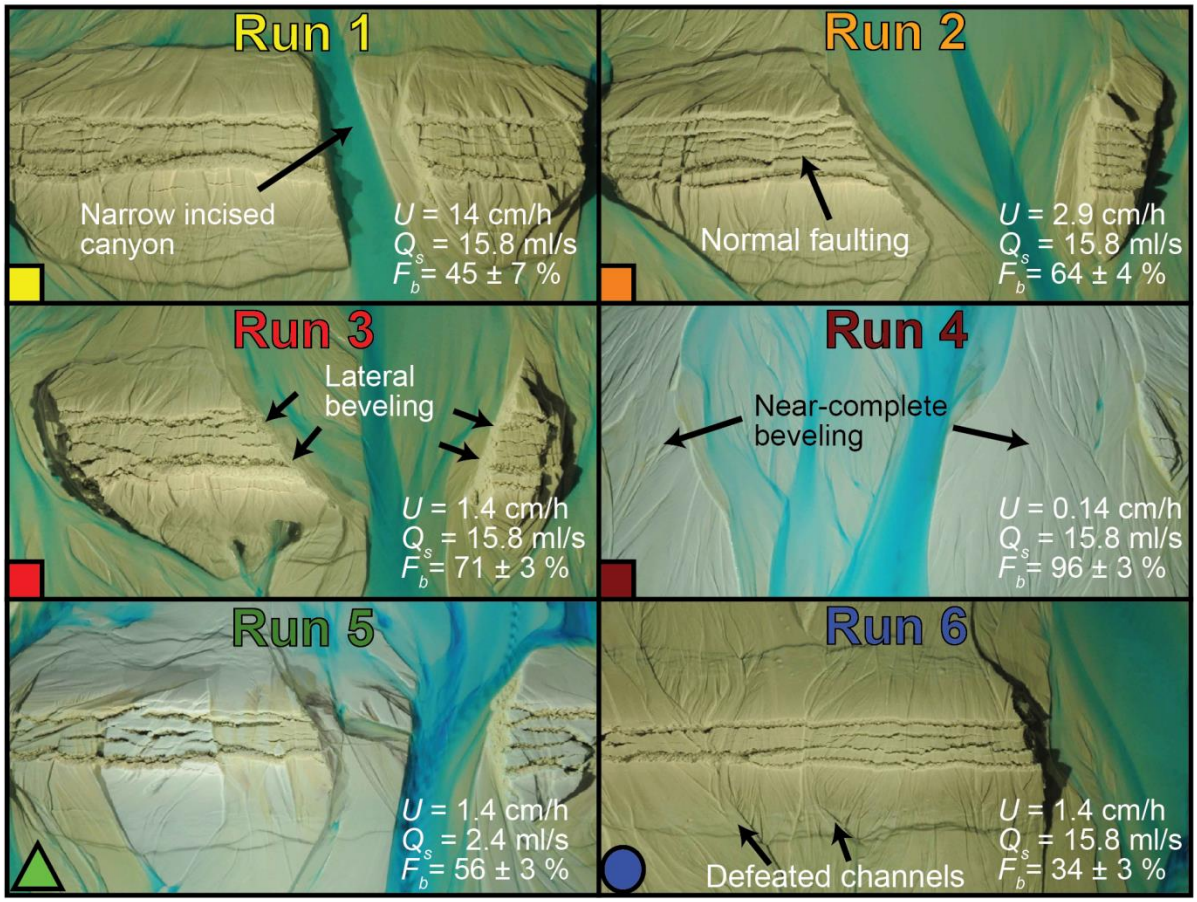

Figure 4: Photographs of the zone of uplift at the end of Runs 1-6. The final stage of each experimental run is shown together with the main input parameters and the percentage of the beveled area. The colored geometric shapes mark the color scheme adopted for the runs in Figs. 5, 6, S3-S6.

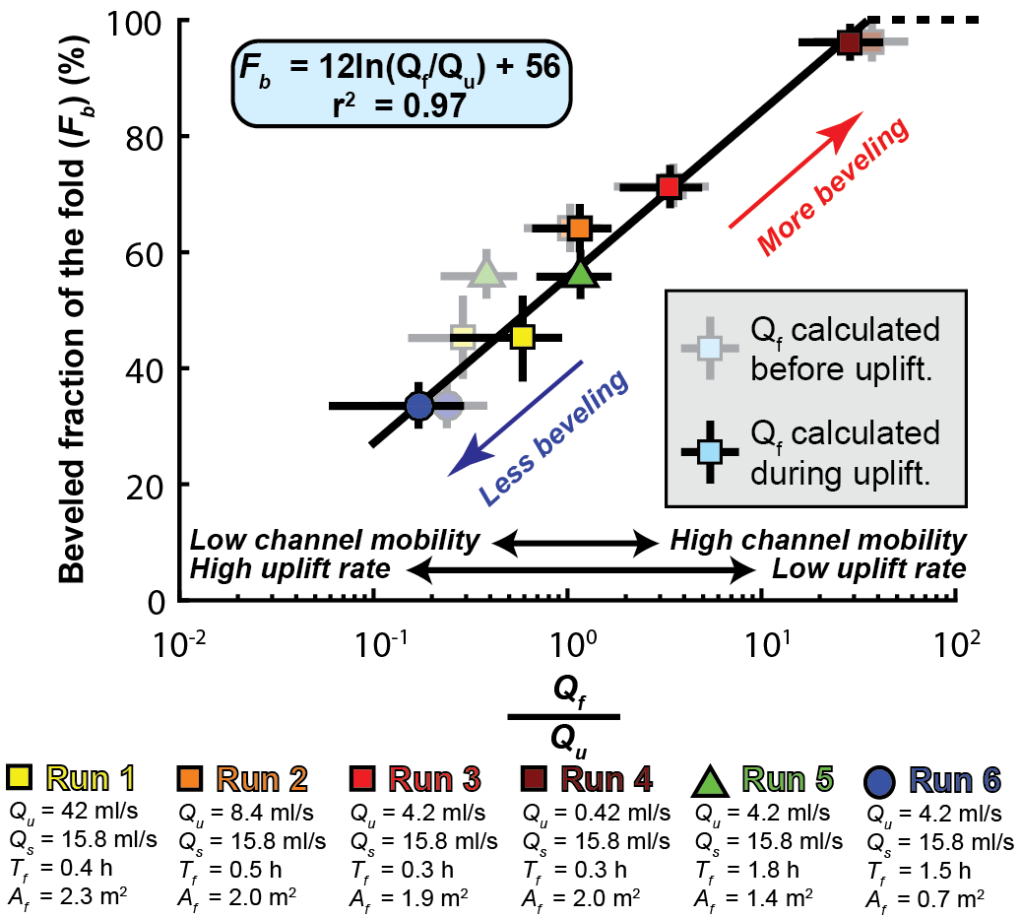

Figure 5: Percent of the area of uplift that is continuously reworked as a function of channel lateral mobility and uplift rate. The fraction of the fold that is beveled at the end of the run is plotted against the flux of sediment reworked upstream of the fold (Q_f) and the flux of uplifted sediment (Q_u). The plotted regression is for Q_f calculated during uplift. Note that the apparent log-linear trend has to plateau at 100% and 0% and that beveled areas for Run 1 and Run 5 represent maxima (Fig. S5). See methods section for treatments of the uncertainty.

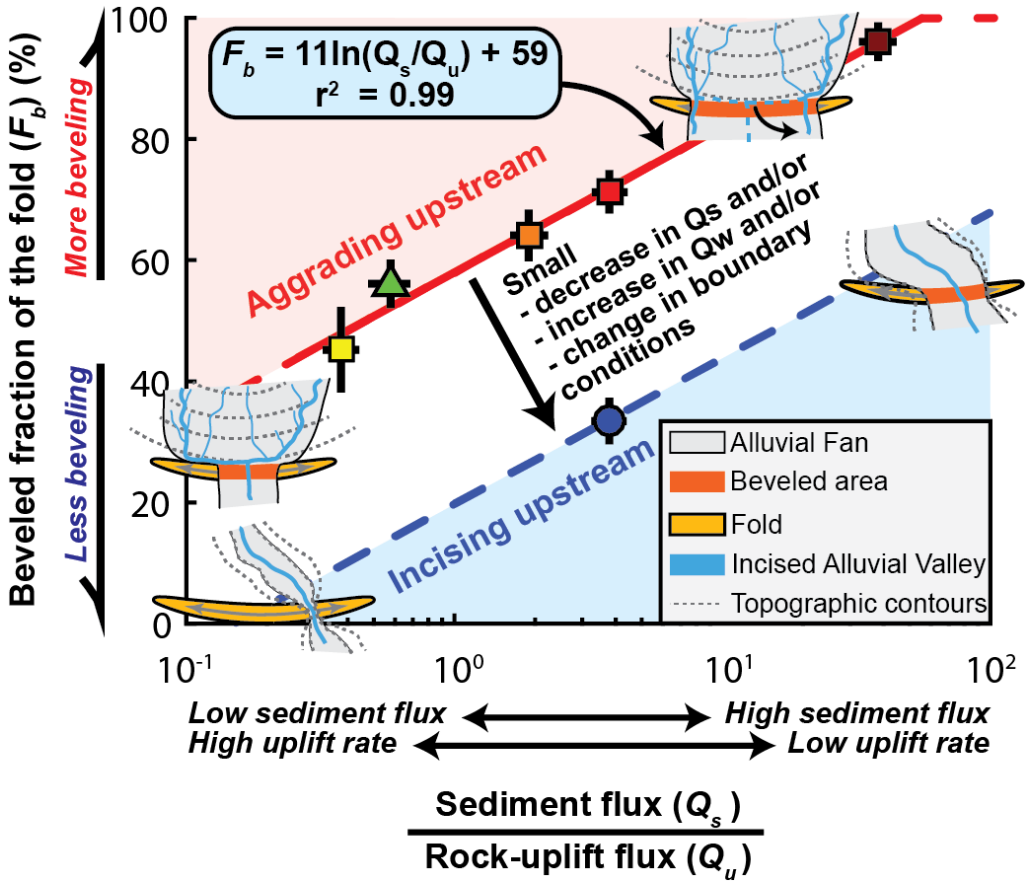

Figure 6: Beveled fraction as a function of relative sediment-to-uplift flux and conceptual sketch of the influence of perturbations to equilibrium. The conceptual sketch illustrates that, in equilibrium, the competition between sediment flux and uplift flux predicts the beveled area well. However, relatively small perturbations to the equilibrium can trigger switches between aggradation and incision and induce striking variations in channel mobility and beveled area, e.g., Run 6: blue circle. Qw is the waterflux. All other symbols are the same as in Fig. 5. See methods section for treatments of the uncertainty.

Supporting material for Chapter 1

1 Methods

1.1 Experimental setup

The uplift basin used for the experiment was built at the St Anthony Falls Laboratory, University of Minnesota, Minneapolis, in 2014 and is a wooden box with dimensions of 4.8x3.0x0.6 m, raised about one meter above the floor (Fig. 3a). Located 2.2 m down-basin, a 51-cm-wide slot accommodates the uplift mechanism. This mechanism comprises three metal beams that span the width of the basin and that are inset into the slot next to each other with a spacing of 13 cm. Mounted onto threaded rods, these metal beams can be raised a total of 20 cm by turning a hexagonal nut. One entire revolution of the nut raises the metal beam by 4.2 mm. A thin piece of flexible sheet metal covers the beams with its edges inset in sliders. Thus when the beams are uplifted, the sheet is pinned at the edge of the slider and flexes into a fold shape. There are 10-cm gaps between the metal sheet and the edges of the basin on either side (Fig. 3a). These zones on the edges do not produce constant uplift and are, therefore, excluded from the experimental space as described below. In all experiments, the entire basin was covered with a thick (~5 mm) rubber membrane and filled with well-sorted silica sand (D_{50} = 0.52 mm) at a slope less than the equilibrium slope for the imposed sediment and water flux. A constant flux of that same sand, water, and blue dye was fed from upstream into a funnel using an automatic sediment feeder, two constant-head tanks, and a small pump, respectively. The mixture of sand, water, and dye flowed into a wire mesh filled with pebbles and cobbles (the rock crib), thus diffusing the distribution of the inputs (Fig. 3). Acrylic sheets ~10 cm wide were placed at regular intervals at an angle of

~45° facing downstream along the wall in order to limit edge effects (Fig. 3b). Moreover, barriers 15 cm off the wall around the zone of uplift diverted water around the zone where the flexing metal sheet (and thus the uplift) did not extend to the edges of the basin. Finally, two plates were inserted on either side of the rock crib at the inlet to form a U-shape and to direct the flow straight down the basin (Fig. 3b). This "channeling" greatly reduced the amount of flow along the fold's edges and allowed for most of the water to be routed across the center of the basin. Moreover, it simulates the narrow outlet of a canyon onto an alluvial fan.

1.2 Data Collection

Sediment and water feeds were calibrated with a stopwatch and a 1-L graduated cylinder. Dye feed was gauged by eye. A DSLR camera with a 10.5-mm, f/2.8 fisheye lens was mounted over the center of the basin and remotely controlled. Topographic data of the basin were acquired using a laser scanner that was programmed to cover the entire basin except for its upper ~5% (~25 cm) in six swaths. Prior to each scan, the water, sediment, and dye feeds were turned off, and the surface water was allowed to drain for 10 minutes, after which time, all of the surface water had infiltrated into the sloping fan and drained downstream. Thus, except within scours on the far downstream of the basin, no standing water was present when the surface was scanned, but the sand was still damp. The resulting digital elevation model acquired from the scans has a 1-mm horizontal and sub-millimeter vertical precision. Some near-vertical faces have an uncertainty in the elevation > 1 mm or returned no data.

1.3 Experimental protocol

After an initial test run, seven experiments were performed over a two-month interval. The main variables in each run were the sediment discharge, the water discharge, and the fold uplift rate (Table S1). The weir height at the toe of the table was set to allow for a thickness of sand that exceeded the maximum uplift of the fold, while assuring that, in its upper reaches, a sloping fan would not build above the basin walls. Photos were taken every 60 seconds, and topographic scans made every hour. All experiments started with a phase of rapid aggradation as the system built a slope adjusted to the imposed sediment/water ratio. Subsequently, aggradation rates slowed down until the system alternated between hours of overall aggradation and hours of overall erosion (Fig. S1). This surface change was estimated hourly by differencing the digital elevation models from the scans. Once the surface change was within 10-20% of the input sediment flux, the system was considered in equilibrium, and uplift was started (Fig. S1). The time to equilibrium depended on how well the equilibrium slope was estimated at the setup of the experiment and was typically within 4-10 hours but reached 45 h in Run 5. In all experiments, the 47 increments of uplift were performed by raising the center beam on both sides of the stream table by 4.2 mm and then each side beam by 2.1 mm. The center beam at the end of the experiment was thus raised a total of 20 cm, which resulted in a maximum surface uplift of 14 cm at the crest of the fold. The difference between the beam uplift and surface uplift arises from spreading and collapse of the non-cohesive sand. Temporal spacing of the 47 uplift increments was chosen according to the desired uplift rate. Between successive experiments, the metal beams creating the fold shape were lowered, the weir height adjusted if necessary, and the slope reset to slightly below equilibrium using a broom and shovel. Any sand that was below the

adjusted surface layer was left untouched except for the area directly above the fold, which was entirely dug out and stirred in order to avoid biases due to pre-existing structures.

In Run 6, during the initial setup of the experiment, the acrylic plates around the water feed were arranged in a V-shape and were changed to a U-shape (as in Fig. 1b) after 2.5 h. As expected from theoretical considerations of sediment transport (Parker et al., 1998), the increased focusing of the water flux at the table's inlet led to a higher transport capacity and lower equilibrium slope, and thus to the incision of a canyon. For calculations of the equilibrium slope and channel mobility, the experiment was, therefore, separated into discrete intervals before and after the change to a U-shaped inlet and incision of the canyon (Table S2).

1.4 Image and Scan processing

The digital elevation scans were brought into MATLAB as 4672 by 3001 matrices. Each pixel corresponds to a square millimeter of basin area. To remove boundary effects, we cropped the area by 70 cm at the upstream end (in addition to the ~25 cm not covered by the scanner), 17 cm at the downstream end and 17 cm on each side of the basin (Fig. S2). The crop on the sides excludes all acrylic barriers except for the inclined sheets around the zone of uplift.

Photos were post-processed in Photoshop CS6. Fisheye distortion was removed using the inbuilt lens correction and photos were tilted such that the average slope of the alluvial fan was horizontal. Images were resampled to 1 pixel/mm^2, and major dark areas were brightened. Finally, the corrected images were cropped in MATLAB to match the extent of the topographic scans. We estimate measurement errors on the length or area measurements

to be ~1%. Errors are largest for pixels elevated highest above the basin and closest to the camera. None of these errors are large enough to significantly affect our results.

1.5 Volumetric uplift rate (Q_u)

In Runs 4 and 5, the topography was scanned every 63.5 minutes, instead of 60 minutes, in order to make some (Run 5) or all (Run 4) of the scans coincide with times in which one uplift increment was due to happen. Those uplift increments were performed when the experiment was not running, and the topography was scanned before and after the uplift increment. This procedure allowed us to sum up the surface change due to the uplift alone for all 47 increments in Run 4 and ten of the 47 increments in Run 5. Summing all uplift increments from Run 4 yields the expected total uplift volumes at each stage of the experiment (Fig. S3a). This ideal uplift record was used to convert the imposed rate of uplift of the metal bars to volumetric uplift rates on the surface of the experiments. Note that the base level is constant in these experiments, but would have to be taken into account if this work were applied to areas where base level is changing. A similar uplift model was constructed from the ten increments of Run 5 (Fig. S3b). Despite differences in equilibrium slopes and sand-layer thicknesses, the volume uplifted per increment is similar in both runs (Fig. S3c). Thus, we conclude that the thickness of the sand layer does not affect the pattern and volume of uplift significantly and that effects, such as compaction of the sand or stretching of the membrane, are insignificant.

One complication in the comparison between folds from different experiments is that surface faulting and outward spreading of the uplift occurs in areas that experienced 5-6 increments of uplift without erosion. Thus, in experiments in which the fold is continuously eroded, limited surface faulting develops, and the fold shape is narrower and more

symmetrical. In experiments in which the fold is not fully eroded, the uplift spreads out. The analysis of the uplift increments in Run 4 and 5 (Fig. S3) shows, however, that the overall uplifted volume is not affected by this process and that the final heights of the peaks on the fold are not influenced significantly. Thus, we use the uplift data from Run 4 to estimate both a peak surface-uplift rate, as well as a volumetric uplift rate for each increment of uplift with associated uncertainty (Table S2).

1.6 Beveled fraction (F_b)

In each experiment, the actively beveled area can be recognized by multiple active channels and recently abandoned, undeformed, or weakly deformed terraces less than a few centimeters above the thalweg (the lowest height) of the current stream. In order to estimate the height above the thalweg based on the scanned topography, we calculate, for each across-basin row, the height of each pixel above the minimum height (thalweg) in that row. Plots of the proportion of pixels at or below any given height above this estimated thalweg (essentially a hypsometry) typically show 30-100% of pixels ≤ 3-4 cm above the thalweg (Fig. S4). This clustering indicates low-elevation, relatively flat areas that have been recently beveled. The more distributed pixel heights within 3-15 cm above the thalweg are expected for the steeply dipping limbs of a fold (Fig. S4). We note that the rollover between the actively reworked and the strongly folded area occurs ubiquitously at a similar height range (2.8 to 3.6 cm). We therefore consider pixels below the cut-off of 3.2 ± 0.4 cm to be part of the active beveled area (Table S2).

The beveled fraction typically decreases from 100% at the beginning of each experiment toward some equilibrium value. A time-series of the beveled area reveals that equilibrium was reached for the experiments with low fold-uplift rates (Fig. S5). Thus, Runs 3, 4, and 6

can be considered in equilibrium. Run 2 is close to equilibrium, but for Runs 1 and 5, the beveled fraction we calculate is a maximum estimate − had the uplift continued, the beveled fraction might have decreased more.

1.7 Channel mobility timescale (T_f)

Similar to previous work (Cazanacli et al., 2002; Kim et al., 2010; Wickert et al., 2013), we define an e-folding channel mobility timescale as the time necessary for a river to visit 63% of the dry area within the active floodplain (Fig. S6a) (Cazanacli et al., 2002; Kim et al., 2010; Wickert et al., 2013). The use of blue dye allows pixel tracking of wet and dry areas (Cazanacli et al., 2002; Kim et al., 2010; Wickert et al., 2013). We converted photos from a 'red-green-blue' (RGB) to a 'hue-saturation-value' (HSV) color space, and set a characteristic cut-off between wet and dry images using a combination of hue and saturation values. After parts of the image outside the active floodplain were masked out, the photos were converted to binary maps of wet and dry pixels. We then smoothed the maps with a 9x9-mm window. To calculate the characteristic time scale of channel reworking, we used the method outlined in previous publications (Wickert et al., 2013): One photo is taken as a base image, and the dry area is identified. The reworking of this dry area is then tracked by looking at each subsequent photo and recording the number of pixels that have remained dry over the entire time since the base image. Each image is chosen as a base image in turn and compared with subsequent photos. We chose to interrupt the series of photos where gaps in our photographic record exceeded 6 min (for example, due to problems with the dye pump or after day-long breaks within one experimental run). These series of the area remaining dry since some arbitrary start can be fitted with a harmonic function (Cazanacli et al., 2002; Kim et al., 2010) or an exponential function (Wickert et al., 2013) (Fig. S6). We chose an

exponential fit to allow for a non-zero asymptote, which occurs when parts of the fluvial surface are abandoned for extended periods of time (several hours). The best-fit e-folding timescale is the channel-mobility time scale, T_f (Table S2). For the final regression (Fig. 5), we used T_f calculated during the uplift phase. We find, however, that ongoing uplift does not influence channel-mobility time scales in a systematic way (Fig. 5, Table S2) and that the Q_f/Q_u ratios are within error for all experiments, except for Run 5 (Fig. 5). The reason for the higher Q_f/Q_u value of Run 5 when calculated during uplift is likely the development of small ponds behind parts of the fold that remained stable for several hours before draining. Despite this complication, the regression is not affected significantly by the variations in the channel mobility (Fig. 5).

1.8 Area of the active alluvial surface (A_f)

The active fluvial area upstream of the uplift (A_f) was calculated from the topographic scans of the basin after masking out the un-reworked surfaces that define the rims of the upstream part of the basin (Fig. 3). The value was then corrected for areas that stay inactive for extended periods of time using the asymptote of the exponential fit to the remaining dry area (Fig. S6).

1.9 Flow depth (H)

Flow depth varied throughout the course of an experiment and between different channels. Therefore, some representative value of the flow depth that reflects the amount of water influx had to be chosen. The main channel through the fold typically had flow depths of 5–10 mm, and we use 7.5 ± 2.5 mm as a characteristic value. Because the water flux was not varied between experiments, this parameter is treated as a constant for all runs.

1.10 Data Availability

Photographic and topographic data for all experiments, as well as timelapse videos are stored on the SEAD repository and can be accessed through the SEN knowledge base at sedexp.net.

2 Additional Discussion

2.1 Influence of sediment flux

Because lateral channel mobility is strongly dependent on the relative sediment and water flux, one could hypothesize that, in the absence of changes in the water flux, a dimensionless parameter of the form:

$$F_b \propto \frac{Q_s}{Q_u} \tag{1}$$

where Q_s is the influx of sediment upstream of the fold, could predict the beveled area similarly to the dimensionless parameter proposed in the main text. This ratio compares the rate of mass (sediment) input into the system from upstream with the rate of mass input by the uplifting fold. The rational is that, in equilibrium, the shape and slope of a river or an alluvial fan is adjusted to transporting the amount of sediment that is input into the river (Q_s) (Mackin, 1948; Whipple et al., 1998). Thus, one could imagine that if the rate of mass flux by the active uplift is insignificant with respect to Q_s, the entire fold can be reworked. If the uplift is significant, the river adjusts its geometry and bevels only a proportion of the uplift. However, we show in this work that processes other than the sediment-to-water flux ratio control the channel mobility and the width of the active alluvial surface. For example, the change in the upstream boundary condition (as defined by the U- or V-shape of the inlet) of Run 6 is independent of the sediment flux which causes Equation 1 to provide a poor

prediction of the beveled area for Run 6 (Fig. 6). The channel mobility timescale, however, accounts for this upstream boundary effect (Fig. 5). We hypothesize that the reason why the Q_s-Q_u regression is a good predictor for all runs except Run 6 is that in each experiment, the system was brought to an equilibrium starting with a fan slope that was lower than the equilibrium slope. Therefore, the rivers always aggraded prior to uplift and covered nearly the entire available basin area (Figs. 6, S6b–g, S6i). Such boundary conditions are comparable to previous experimental studies that established the link between sediment flux and lateral channel mobility (Wickert et al., 2013). The results from Run 6 demonstrate that the link between channel mobility and sediment flux can be subject to complications when these boundary conditions are changed (Fig. S6h). Introducing initial topographies that are steeper than the equilibrium slopes for the input water and sediment fluxes, or changing sediment and water flux during the experiment could yield more data that falls off of the Q_s-Q_u regression. The power of casting the efficiency of lateral beveling as a function of channel mobility rather than sediment flux lies in the result that the channel mobility is affected by a suite of boundary conditions that are independent of the sediment flux (for example, the water flux or the initial slope of the upstream fan, changes in the shape of the inlet etc.). Thus, using the Q_s-Q_u regression, one could think that order of magnitude changes in Q_s or Q_u are required to explain dramatic changes in the beveled area. However, as we showed through Run 6, small perturbations (such as a small change in Q_s or Q_w, or a change in the inlet geometry) can have large effects on the beveled area that are not predicted by the Q_s-Q_u regression. Therefore, the Q_f-$Q_u$regression provides the more general mechanistic framework for describing the lateral erosion of an active uplift.

2.2 Influence of water flux

The uniform, steady, relatively high water flux leads, in effect, to an artificial state of constant flooding which precludes the possibility of investigating the influence of high-frequency changes in water flux, including extreme events. However, recent work suggests that total sediment transport depends mainly on the integrated flow above the threshold of transport, rather than the details of how the flow is delivered (Phillips and Jerolmack, 2016). Variations in water flux change both the transport capacity and possibly the channel mobility through the change in the sediment/water ratio. The transport capacity is also modified via slope changes across the fold, such that predictions about the influence of water are not trivial. Further experiments on the relative influence of water and sediment fluxes on the channel mobility are necessary to illuminate the influence of changes in water flux. However, whereas Q_w will influence the factor of Q_f, we hypothesise that the parameter $\frac{Q_f}{Q_u}$ remains a good predictor of the beveled fraction of the fold.

References for supporting material of Chapter 1

Cazanacli, D., Paola, C., and Parker, G., 2002, Experimental steep, braided flow: application to flooding risk on fans: Journal of Hydraulic Engineering, v. 128, no. 3, p. 322-330.

Kim, W., Sheets, B. A., and Paola, C., 2010, Steering of experimental channels by lateral basin tilting: Basin Research, v. 22, no. 3, p. 286-301.

Mackin, H. J., 1948, Concept of the Graded River: Geological Society of America Bulletin, v. 59, no. 5, p. 463-512.

Parker, G., Paola, C., Whipple, K., and Mohrig, D., 1998, Alluvial fans formed by channelized fluvial and sheet flow. I: Theory: Journal of Hydraulic Engineering, v. 124, no. 10, p. 985-995.

Phillips, C. B., and Jerolmack, D. J., 2016, Self-organization of river channels as a critical filter on climate signals: Science, v. 352, no. 6286, p. 694-697.

Whipple, K., Parker, G., Paola, C., and Mohrig, D., 1998, Channel Dynamics, Sediment Transport, and the Slope of Alluvial Fans: Experimental Study: The Journal of Geology, v. 106, no. 6, p. 677-694.

Wickert, A. D., Martin, J. M., Tal, M., Kim, W., Sheets, B., and Paola, C., 2013, River channel lateral mobility: metrics, time scales, and controls: Journal of Geophysical Research: Earth Surface, v. 118, no. 2, p. 396-412.

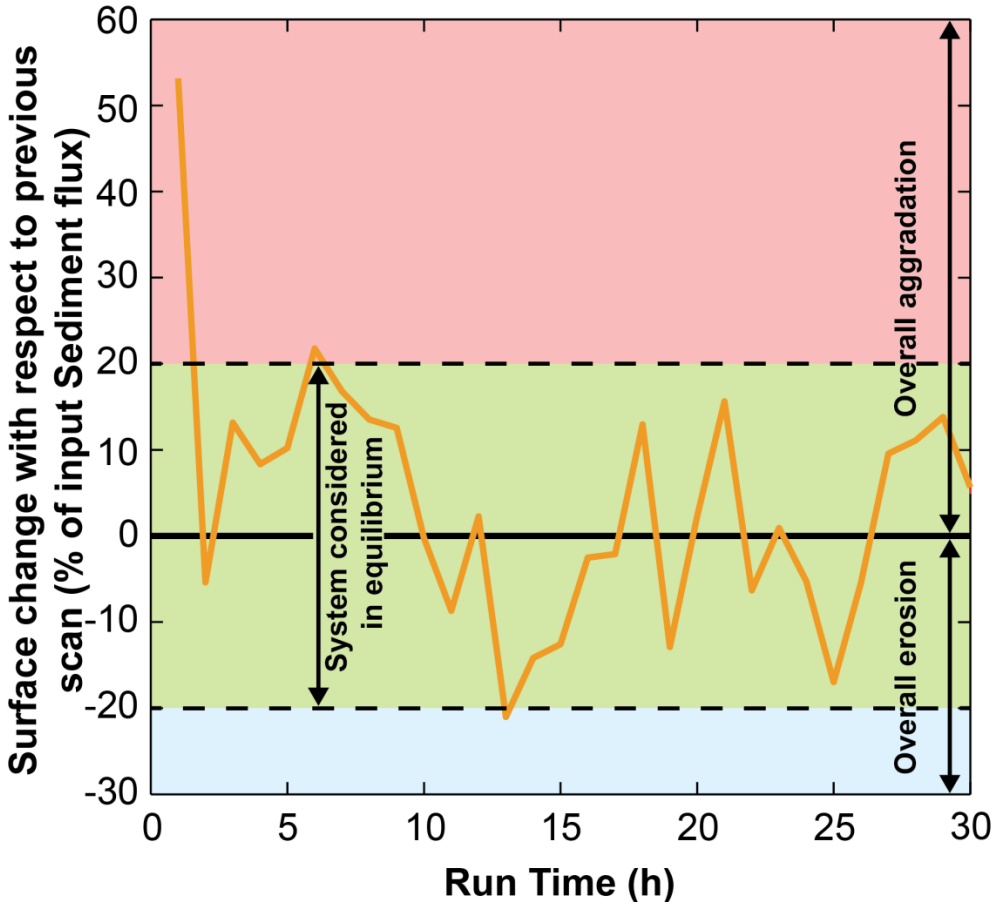

Figure S1: Plot of total volumetric surface change in the basin between two sequential scans as a function of the run time. Shown here are the first 30 h of Run 7 which did not have any uplift. After 2 h of run time, the system reaches an equilibrium in which the sediment influx into the basin and the sediment outflow are balanced. Between any sequential scans (spaced ~1 h apart) the total amount of aggradation or erosion oscillates around that equilibrium and stays within 20% of the volume of sediment input. For any run with uplift (Runs 1-6), the uplift was started when the surface change remained below the 20% mark. For most experiments, this cut-off was reached within 4-10 hours of runtime.

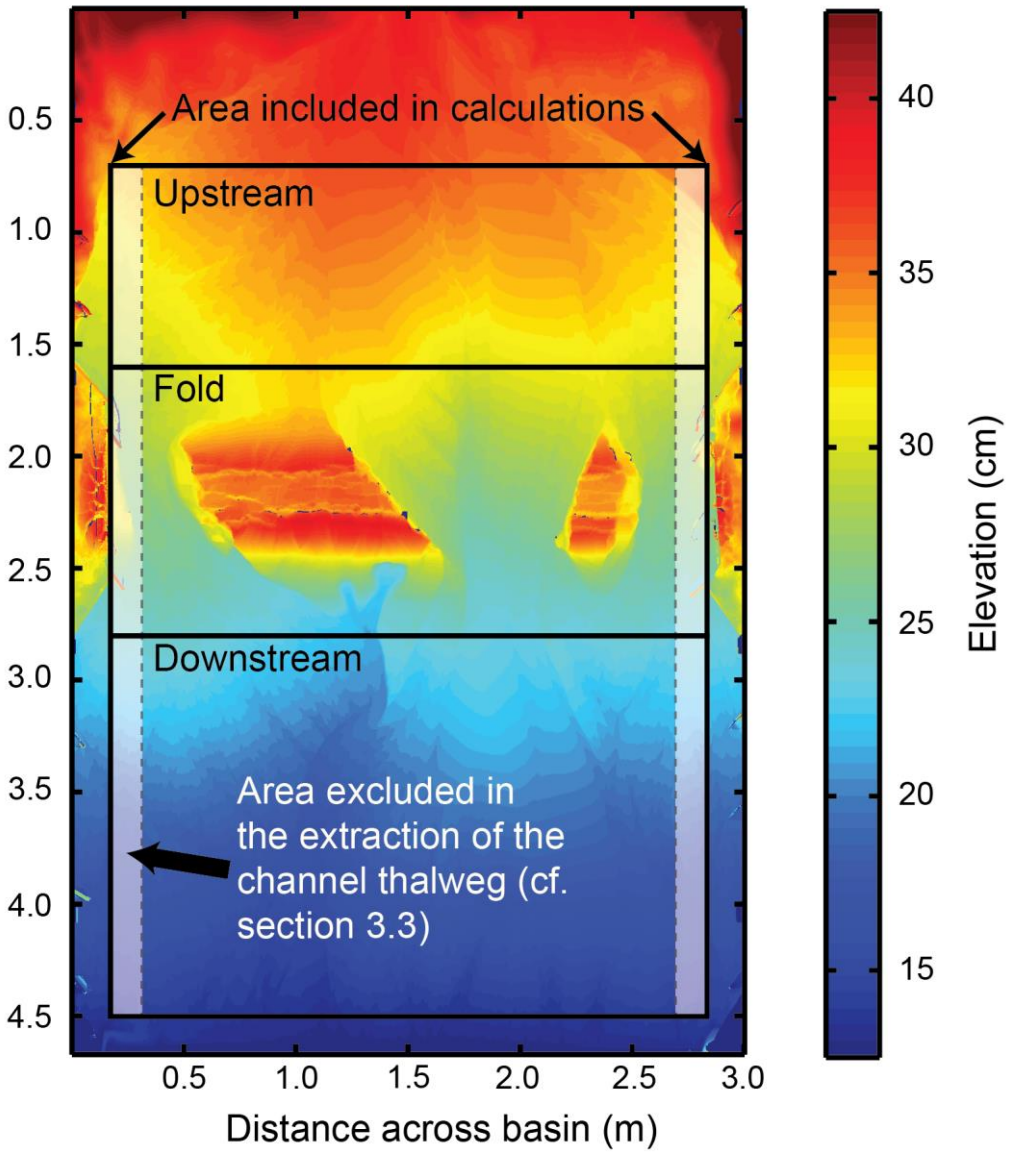

Figure S2: Scan of the final stages of Run 3 showing the different domains that were used in the analyses of this study.

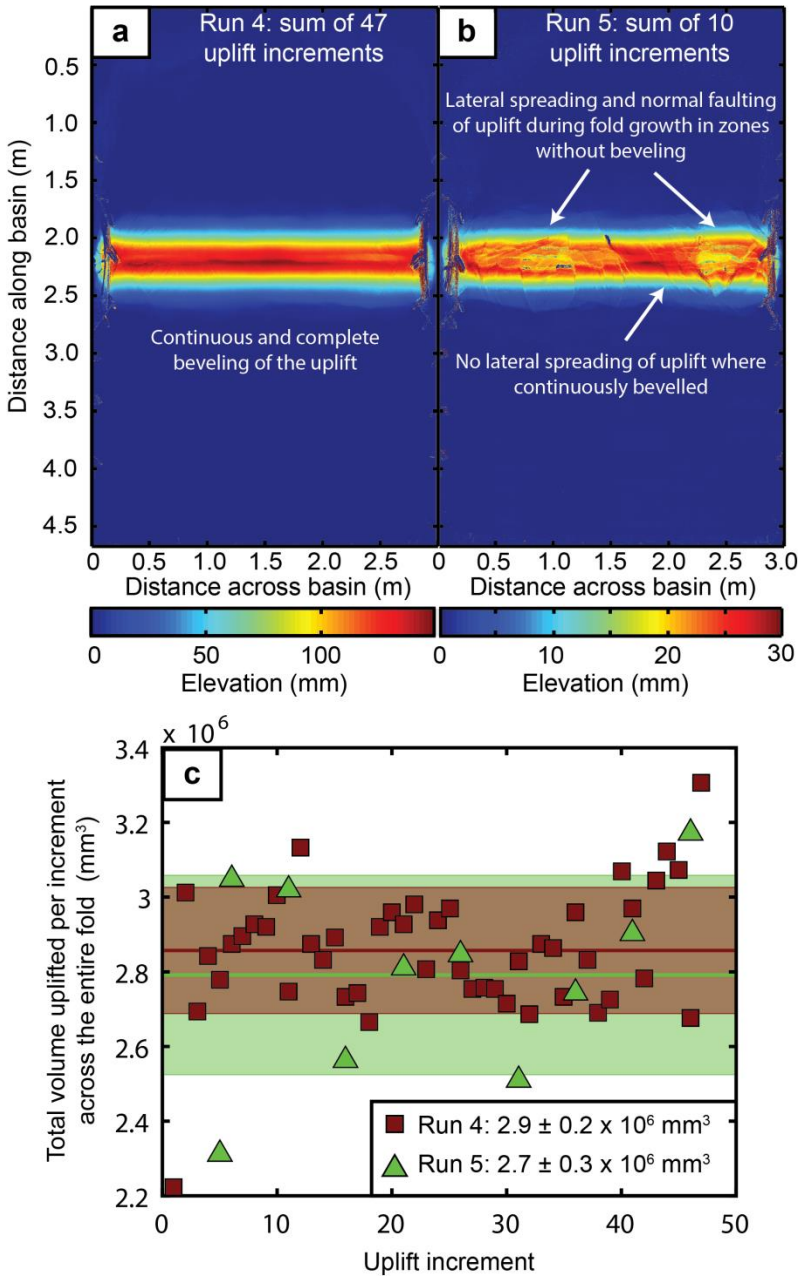

Figure S3: Ideal fold model. (a) Sum of the surface uplift in from all increments of uplift in Run 4. (b) Sum of the surface uplift for 10 increments of uplift in Run 5. Only every 5th uplift increment was recorded using the scanner so the fold model is not complete. The reason for the different uplift pattern in Run 5 is that the uplift was not continuously eroded everywhere so that normal faulting developed within the emergent terrain. The areas of uplift that show a "smoother" uplift pattern are the locations that the river beveled. (c) Plot showing the total volume of uplifted sediment during each increment in the entire basin area. The thick solid lines in green and red show the mean of each distribution with one standard deviation marked with the colored area. Note that despite differences in slope, degree of beveling, and sand thickness, the uplift during each increment in Run 4 and 5 show scatter around the same narrowly distributed values with standard deviations of 7-11%.

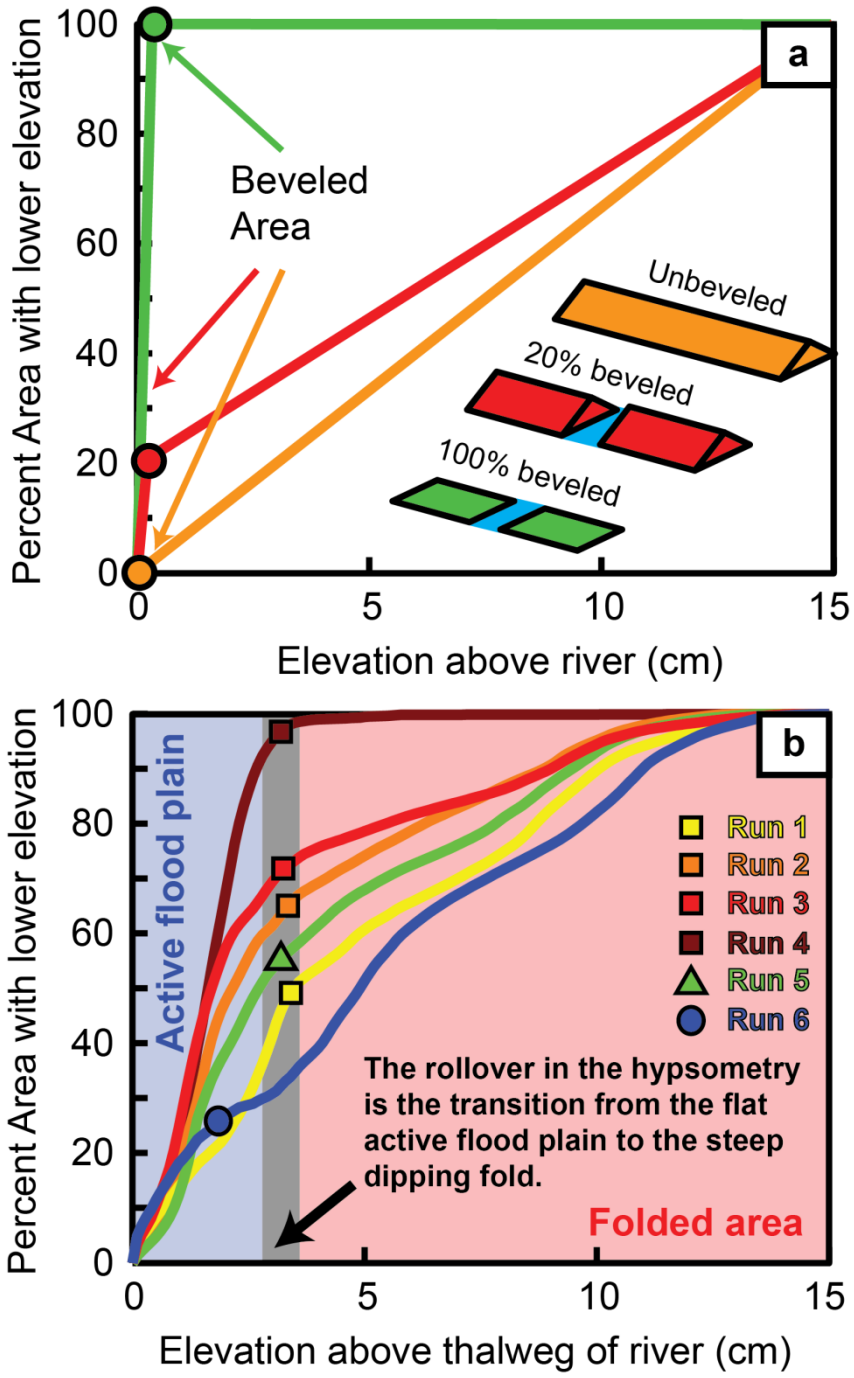

Figure S4: Illustration of how the beveled area was extracted from the experiments. **(**a) Conceptual sketch showing hypsometries expected for the ideal fold-river geometries marked in the in the inset cartoons. **(**b) Hypsometries from the fold areas (cf. Fig. **S**2) of the final scans of all experiments showing a prominent rollover point which marks the boundary between the flat recently beveled area and the inclined folded area. For all runs except Run 6, the rollover point occurs in a narrow band marked with a grey background. The percent area with lower elevation that corresponds to the rollover in the curves was taken as the beveled area with a range marked by the width of the grey band.

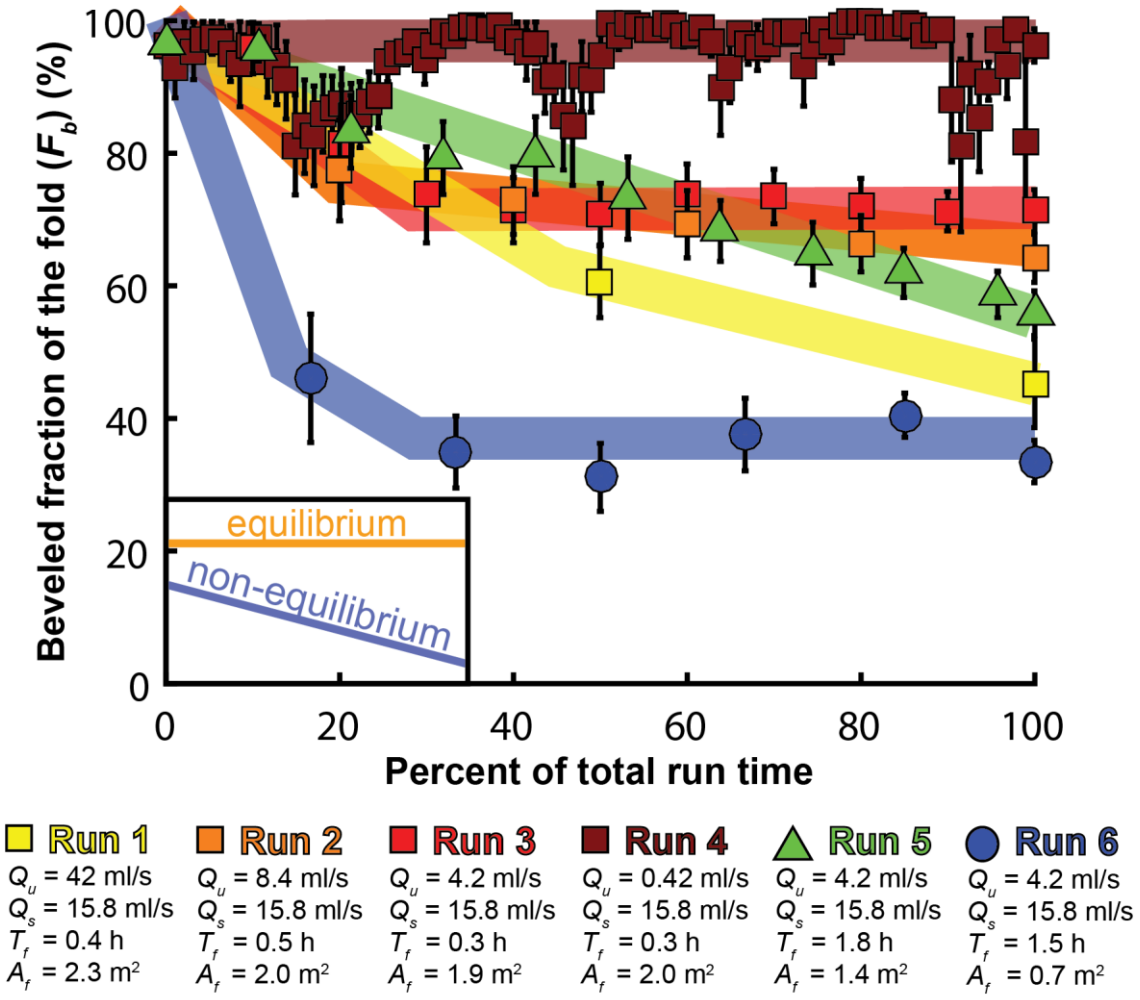

Figure S5: Plot of the evolution of beveled area over the time of the experiment. The colored bars mark the approximate trend of the data. At the start of the experiment, the beveled area is higher and starts to plateau after some time. This plateau might not be reached in Run 1 and Run 5 whereas the other experiments seem to be close to equilibrium. Therefore, the beveled area estimates for Run 1&5 present maxima. Note the autogenic periods in Run 4 during which stream flow was focused in one part of the basin allowing some topography to build up and dropping the beveled area to < 85%.

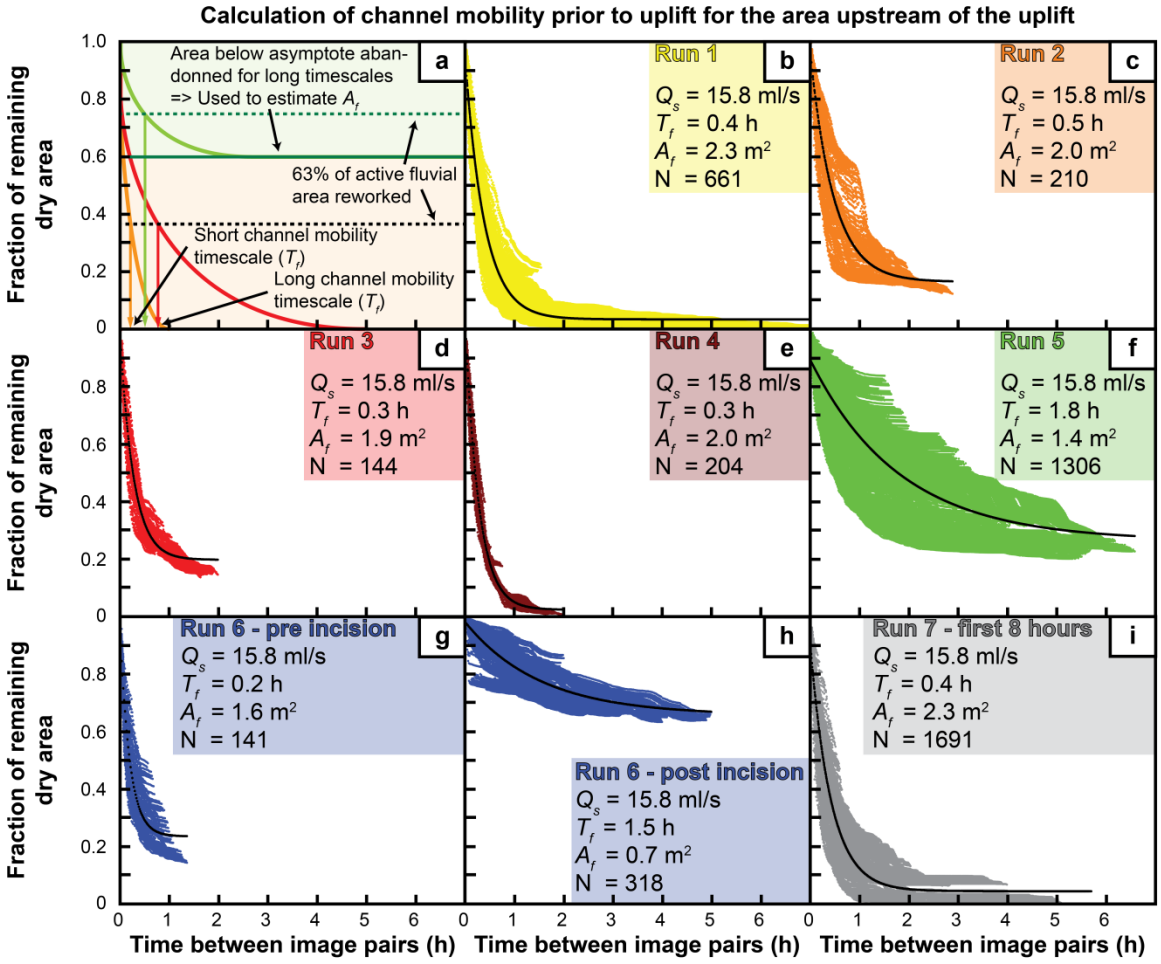

Q_s = Sediment flux; T_f = Channel mobility timescale; A_f = Active upstream fluvial area; N = Number of images in analysis;

Figure S6: Figure showing the remaining dry area upstream of the uplift as a function of time between image pairs. An exponential fit to the data yields a characteristic e-folding timescale of channel reworking (T_f). The area of the active upstream fluvial area (A_f) can be estimated from the asymptote of the exponential fit to the data where an asymptote of 0 implies that the entire upstream area is being actively reworked (as in runs 1, 4, and 7) and higher asymptotes imply that only a part of the upstream area is actively reworked. (a) Conceptual sketch showing curves expected for differently mobile channels. (b-i) Analyses for all experiments using pairs from a total of N images (as shown in the figure). Only images taken prior to the onset of uplift are used. The black lines show the exponential fit to the data that was used to calculate the channel mobility and the active upstream fluvial area. We note that the pattern and resulting channel mobility timescales are similar when the entire basin area is considered.

Table S1: Input parameters for all experiments

Run Number	Peak uplift rate ±2σ (m/s) 10^{-6}	Volumetric uplift rate ±2σ (m^3/s)* 10^{-6}	Sediment Flux ±2σ (ml/s)	Water Flux ±2σ (ml/s)	Weir Height (cm)	Total Run time after start of uplift (h)
1	40 ± 3.7	42 ± 4.9	15.8 ± 0.2	790 ± 10	12	1
2	8.0 ± 0.7	8.4 ± 1.0	15.8 ± 0.2	790 ± 10	12	5
3	4.0 ± 0.4	4.2 ± 0.5	15.8 ± 0.2	790 ± 10	12	10
4	0.40 ± 0.04	0.42 ± 0.05	15.8 ± 0.2	790 ± 10	12	100
5	4.0 ± 0.4	4.2 ± 0.5	2.4 ± 0.2	790 ± 10	16	10
6	4.0 ± 0.4	4.2 ± 0.5	15.8 ± 0.2	790 ± 10	4	6[a]
7	-[b]	-[b]	15.8 ± 0.2	790 ± 10	12	-

[a]in Run 6 the planned run time was 10 h but the experiment had to be stopped (cf. text for details)
[b]This experiment was performed without uplift

Table S2: Results for all experiments. Flow depth H was estimated as 7.5 ± 2.5 (±2σ) mm in all experiments

Run Number	Q_u ±2σ (m^3/s)* 10^{-6}	Q_s ±2σ (ml/s)	Q_w ±2σ (ml/s)	Equilibrium basin slope before start of uplift ±2σ (°)	F_b ±2σ (% of entire fold)	T_f upstream of the fold before uplift ±2σ (h)	A_f upstream before uplift ±2σ (m^2)	T_f upstream of the fold during uplift ±2σ (h)	A_f upstream during uplift ±2σ (m^2)
1	42 ± 4.9	15.8 ± 0.2	790 ± 10	5.4 ± 0.2	45 ± 7	0.4 ± 0.1	2.3 ± 0.2	0.2 ± 0.1[d]	2.3 ± 0.2
2	8.4 ± 1.0	15.8 ± 0.3	791 ± 10	5.5 ± 0.2	64 ± 4	0.5 ± 0.1	2.0 ± 0.2	0.5 ± 0.1	2.3 ± 0.2
3	4.2 ± 0.5	15.8 ± 0.4	792 ± 10	5.5 ± 0.2	71 ± 3	0.3 ± 0.1[d]	1.9 ± 0.2	0.3 ± 0.1	2.3 ± 0.2
4	0.42 ± 0.05	15.8 ± 0.5	793 ± 10	5.4 ± 0.2	96 ± 3	0.3 ± 0.1[d]	2.0 ± 0.2	0.4 ± 0.1[d]	2.1 ± 0.2
5	4.2 ± 0.5	2.4 ± 0.2	794 ± 10	2.5 ± 0.2	56 ± 3	1.8 ± 0.6	1.4 ± 0.2	0.8 ± 0.1	1.8 ± 0.2
6 V-shaped inlet (pre-incision)	4.2 ± 0.5	15.8 ± 0.2	795 ± 10	6.2 ± 0.2	-	0.2 ± 0.1[d]	1.6 ± 0.2	-	-
6 U-shaped inlet (post-incision)	4.2 ± 0.5	15.8 ± 0.3	796 ± 10	5.0 ± 0.4[b]	34 ± 3	1.5 ± 0.4	0.7 ± 0.2	1.3 ± 0.4	0.5 ± 0.2
7[a]	-	15.8 ± 0.4	797 ± 10	5.0 ± 0.2[c]	-	0.4 ± 0.1	2.3 ± 0.2	0.4 ± 0.1	2.3 ± 0.2

[a]Calculated for the first 7 h after uplift. After that a ~20 h period of more confined flows and lower beveled area occurs (see Fig. S5)
[b]Channel slope was taken as a proxy for the basin slope
[c]Only the first 8 h of the experiment are reported because of autogenic incision and aggradation cycles after that time. The slope was calculated at the end of the experiment.
[d]Channel mobility timescales are likely underestimated where the data series does not extend much beyond 1-2 h.

Chapter 2: Variations of lateral bedrock erosion rates control planation of uplifting folds in the foreland of the Tian Shan, NW China[b]

Aaron Bufe[1,2], Douglas W. Burbank[1,2], Liu Langtao [3], Bodo Bookhagen[2,4], Qin Jintang[5], Chen Jie[5], Li Tao[6], Jessica A. Thompson Jobe[7], Yang Huili[5]

[1]Department of Earth Sciences, University of California, Santa Barbara, California, 93106, USA

[2]Earth Research Institute, University of California, Santa Barbara, California, 93106, USA

[3]Department of Earth Science and Engineering, Hebei University of Engineering, Handan, China

[4]Institute of Earth and Environmental Science, University of Potsdam, Potsdam-Golm, Germany

[5]State Key Laboratory of Earthquake Dynamics, Institute of Geology, China Earthquake Administration, Beijing, 100081, China

[6]Department of Earth Sciences, San Yat-Sen University, Guangzhou, 510275, China

[7]Institute of Tectonic Studies, Department of Geological Sciences, University of Texas, El Paso, Texas, 79902, USA

[b]Adapted from: Bufe et al., (in review at JGR: Earth Surface), Variations of lateral bedrock erosion rates control planation of uplifting folds in the foreland of the Tian Shan, NW China

Abstract

Fluvial planation surfaces, such as straths, commonly serve as recorders of climatic and tectonic changes and are the product of the lateral erosion by rivers-a process that remains poorly understood. Here we present a study of a suite of kilometer-wide, fluvially eroded, low-relief surfaces on rapidly uplifting folds in the arid foreland of the southwestern Tian Shan. A combination of field work, digital elevation model analysis, and dating of fluvial deposits reveals that, despite an overall arid climate and rapid rock-uplift rates of 1-3 mm/y, rivers laterally 'bevel' or 'cut' extensive (> 1-2 km-wide) surfaces with vertical relief of ~6 m. The extent of this 'beveling' varies in space and time such, that different episodes of beveling affect individual active structures. Between times of planation, the beveled surfaces are abandoned, incised, and passively deformed across the folds. In a challenge to models that link strath cutting and abandonment primarily to changes in the vertical rates of river incision, we demonstrate that lateral erosion rates of antecedent streams crossing the folds have to change by orders of magnitude to explain both the creation of wide beveled platforms in the past and their incision at the present day. We hypothesize that significant changes in the lateral bedrock erosion rate of rivers are common and that variations in both vertical incision rates and lateral beveling rates should be taken into account when studying strath-terrace formation in rivers.

1 Introduction

Bedrock rivers commonly record a complex history of aggradation, vertical incision, and lateral migration that can be interpreted as a result of environmental, tectonic, and autogenic changes. Understanding the formation of landscapes and predicting their evolution under

changing climatic and tectonic forcing require knowledge of these river dynamics. Given an available discharge, rivers tend to adjust their geometry to the supply of sediment and, in the case of bedrock rivers, to the bedrock-uplift rate (Dietrich et al., 2003; Hack, 1957; Kirby and Whipple, 2012; Lague, 2014; Lague et al., 2003; Mackin, 1948; Sklar and Dietrich, 2001, 2004, 2006; Turowski et al., 2008; Turowski et al., 2006; Turowski et al., 2009; Whipple and Tucker, 2002; Wobus et al., 2006; Yanites and Tucker, 2010). This response of the river to external influences allows the interpretation of fluvial landscapes as a function of tectonic and climatic drivers (DiBiase and Whipple, 2011; Lague et al., 2003; Langston et al., 2015; Turowski et al., 2006). Ranging from narrow bedrock benches to wider strath terraces and regional planation surfaces, river terraces cut into bedrock are commonly used markers for assessing climatic and tectonic changes in landscapes (Amos et al., 2007; Bookhagen et al., 2006; Calvet et al., 2015; Fuller et al., 2009; Hancock and Anderson, 2002; Langston et al., 2015; Lavé and Avouac, 2001; Pazzaglia and Gardner, 1993; Pazzaglia et al., 1998; Pratt-Sitaula et al., 2004). Moreover, in order for those planar surfaces to develop, processes that reduce landscape relief, such as hillslope erosion, weathering, diffusion of regolith, or lateral erosion by rivers, have to balance or outpace rock uplift and vertical river incision (Fig. 1). We note here that most studies of extensive strath terrace formation have been done in weakly consolidated lithologies (Allen et al., 2013; Collins et al., 2016; Cook et al., 2014; Fuller et al., 2009; Hancock et al., 1999; Langston et al., 2015; Lavé and Avouac, 2001; Molnar et al., 1994; Montgomery, 2004; Schanz and Montgomery, 2016), and that the width of planation surfaces has been linked to the strength of the bedrock (Allen et al., 2013; Montgomery, 2004; Römer, 2010; Schanz

and Montgomery, 2016). However, strath terraces also form in resistant lithologies, such as granites and quartzite (Burbank et al., 1996; Pratt-Sitaula et al., 2004).

Changes in the relative rates of lateral and vertical erosion by rivers in tectonically active regions have commonly been linked to periods of low incision rates during which bedrock is planed off, alternating with periods of rapid vertical incision and the abandonment of terraces (Castillo et al., 2013; Gilbert, 1877; Hancock and Anderson, 2002; Langston et al., 2015; Merritts et al., 1994; Molnar et al., 1994; Zaprowski et al., 2001). Exploiting results from physical experiments and stream-power theory, several studies propose that decreases in incision rates occur at times when sediment flux overwhelms the transport capacity of the river. Thus, the deposited sediment shields the river bed from incision, whereas lateral erosion continues (Fig. 1) (Hancock and Anderson, 2002; Johnson and Whipple, 2007; Langston et al., 2015; Sklar and Dietrich, 2001, 2004; Turowski et al., 2007). Such changes in the ratio of transport capacity to sediment flux have been suggested to occur due to climatically controlled increases in sediment fluxes (Bookhagen et al., 2006; Bull, 1990; DeVecchio et al., 2012; Dey et al., 2016; Formento-Trigilio et al., 2003; Fuller et al., 2009; Hancock and Anderson, 2002; Jansen et al., 2011; Molnar et al., 1994; Pan et al., 2003; Pazzaglia and Brandon, 2001; Wegmann and Pazzaglia, 2002), changes in the water flux (Hanson et al., 2006), changes in vegetation density (Collins et al., 2016) or a combination of the above (Schildgen et al., 2016). Other possible processes controlling the stream power and, thus, the transport capacity and the rate of channel incision include downstream changes in base level due, for example, to sea-level changes, to downstream aggradation or degradation (Castillo et al., 2013; Finnegan and Balco, 2013; Merritts et al., 1994; Pazzaglia and Gardner, 1993), or to changes in tectonic forcing (Cook et al., 2013; Grimaud et al.,

2016; Yanites et al., 2010). More recent work has shown that rapid changes in incision rate can also happen autogenically without changes in external forcing, such as in meandering bedrock rivers with autogenic bedrock-meander formation and cutoff (Finnegan and Dietrich, 2011).

Apart from variations in vertical incision rates, changes in the lateral erosion rate can also influence terrace formation, and such changes should be influenced by the same external forcings that modulate incision rates. Whereas the concept of terrace formation with a constant vertical incision rate and varying lateral erosion rates has been proposed in the past (Davis, 1902; Lavé and Avouac, 2001; Merritts et al., 1994; Pazzaglia and Gardner, 1993; Pazzaglia et al., 1998), it is only recently that numerical and physical models have explored this concept, both for autogenically formed terraces in a meandering river (Limaye and Lamb, 2014, 2016) and for the erosion of a fold by antecedent braided streams (Bufe et al., 2016; Chapter 1). The latter experiments showed that the area of an uplift that gets actively beveled by a river, A_b, can be expressed as a balance between the upward tectonic flux of rock and the rate of lateral sediment reworking:

$$A_b = A_u\left(a\ ln\left(\frac{Q_f}{Q_u}\right) + b\right) \quad (1),$$

where A_u is the total area of the uplift, Q_u is the flux of rock uplifted above the base level across the entire fold and Q_f is the flux of material reworked by an equivalent unconfined alluvial river that is not flowing across an active uplift (Fig. 2) (Bufe et al., 2016). This flux, Q_f, can be expressed as a function of the lateral channel mobility timescale, T_f, such that:

$$Q_f = \frac{A_f H}{T_f} \quad (2).$$

where, A_f is the area that is actively reworked by the unconfined river and *H* is some metric of the river size and geometry, e.g., the flow depth (Bufe et al., 2016). For the case of a fold that is crossed by antecedent rivers, the "unconfined" channel dynamics can be estimated just upstream of the fold. Here, both the lateral channel mobility timescale, T_f, and the fluvially reworked area, A_f, can be derived from a series of observations of river positions over time. T_f is defined as the time required to rework 63% of the active fluvial surface, A_f (Cazanacli et al., 2002; Kim et al., 2010; Wickert et al., 2013). The values of a and b in equation 1 likely depend on the rock strength and factors such as the presence or absence of an alluvial surface upstream of the active structure. For a fold composed of weakly consolidated rock and crossed by antecedent rivers (Fig. 2), $a{\sim}12$ and $b{\sim}56$ (Bufe et al., 2016). Independently of the setting and the value of a and b, a key finding is that the lateral channel mobility measured in a river unconfined by any bedrock directly scales with the lateral bedrock erosion of that same river as it crosses a growing fold. In other words, processes that control the channel mobility timescale, T_f, or the area over which a river actively migrates, A_f, also control the extent of beveled area of an uplifting zone of bedrock, A_b. In alluvial rivers, the lateral channel mobility can vary significantly in different settings (Jerolmack and Mohrig, 2007) and parameterizing the controls on this channel mobility is an important subject of active research. So far, we understand qualitatively that the mobility timescale, T_f, and the area of active migration, A_f, depend on some combination of sediment and water fluxes (Bufe et al., 2016; Constantine et al., 2014; Wickert et al., 2013), bed roughness (Fuller et al., 2016), and changes in the boundary conditions, such as the confinement of the flow (Bufe et al., 2016). The "size" and geometry of gravel bedded rivers, in turn, are fairly well understood and essentially a function of the sediment size and

a representative water discharge (Parker, 1978; Parker et al., 2007; Phillips and Jerolmack, 2016).

Although the interplay between the parameters in equations 1 and 2 can be complex, the analysis above suggests that changes in the ratio of transport capacity to sediment flux commonly have two effects. First, an increased load can cause aggradation and shielding of the bed, thereby decreasing vertical incision rates (Hancock and Anderson, 2002; Johnson and Whipple, 2007; Langston et al., 2015; Sklar and Dietrich, 2001, 2004; Turowski et al., 2007). Second, an increased sediment flux typically increases the lateral mobility of alluvial rivers (Bufe et al., 2016; Constantine et al., 2014; Wickert et al., 2013). Thus, higher sediment fluxes should augment the rate of bedrock planation due to the enhanced frequency and/or persistence of contact between a river and the walls that bound it (Bufe et al., 2016). Understanding the relative magnitudes of changes in vertical and lateral erosion rates as a response to a change in the ratio of transport capacity to sediment flux has important implications for interpreting the timing and rate of strath formation, as well as the response of rivers to climatic changes.

Changes in lateral bedrock erosion have rarely been documented in the field. Here, we document extensive planation surfaces formed on rapidly uplifting anticlines in the foreland of the Tian Shan with a combination of field mapping and analysis of a digital elevation model (DEM). We combine mapping and survey data with optically stimulated luminescence (OSL) dating and cosmogenic radionuclide (CRN) dating to establish the active rock-uplift rates of these folds during Late Quaternary times and to show that striking changes in the lateral erosion rate must be invoked to explain the presence of extensive planation surfaces, now-abandoned and dissected by narrow canyons. We suggest that these

changes occur as a result of shifts in the balance between sediment and water flux and/or changes in the flood frequency.

2 Geological setting

The Tian Shan is a major intracontinental mountain range, running east-west from Tajikistan to northwest China (Fig. 3). It has been formed by the collision and accretion of northward drifting island arcs in the Palaeozoic and Mesozoic (Bazhenov et al., 2003; Carroll et al., 1995) and the reactivation of old structures around 35-25 Ma due to the Indo-Asian collision (Abdrakhmatov et al., 1996; Coutand et al., 2002; Hendrix et al., 1992; Molnar and Tapponnier, 1975; Scharer et al., 2004; Sobel and Dumitru, 1997; Yin et al., 1998). Geodetic studies show that a current total of 20-25 mm/y of convergence between India and stable Eurasia is accommodated across the Tian Shan; a rate representing 40-60% of the total Indo-Eurasian convergence across this orogen (Abdrakhmatov et al., 1996; Zhang et al., 2004; Zubovich et al., 2016; Zubovich et al., 2010). In westernmost China, at the junction of the Tian Shan, the Tarim Basin, and the Pamir, deformation has stepped southwards from the Tian Shan front into the foreland over the last 25 Ma (Heermance et al., 2008). The most recent phase of this southward migration is the growth of three anticlines: the Kashi, Atushi, and Mutule anticlines (Figs. 3, 4) (Heermance et al., 2008). Other active folds to the west, notably the Mingyaole and Mushi anticline (Fig. 4), are interpreted to be structures resulting directly from the collision between the Pamir and the Tian Shan (Li et al., 2012; Li et al., 2015a; Li et al., 2013, 2015b) and are not considered in this study. However, the erosion processes described here also affected parts of these structures.

The Kashi fold (Fig. 4) extends east to west for ~60 km and is a doubly plunging detachment anticline with a tight, box-like shape and steeply dipping limbs. Kashi's

elongate, tapered nose is propagating eastward into the Tarim Basin at rates of ~40 mm/y (Chen et al., 2007; Scharer et al., 2004). An eastward decreasing structural relief of > 2.5 km (Fig. 5a) and two paleomagnetic ages constrain average rock-uplift rates over the last 0.8-1.4 My to be 2.2 ± 0.5 mm/y in the west and < 1.9 mm/y in the east (Chen et al., 2007; Scharer et al., 2004). The 100-km-long and ~10- to 15-km-wide Atushi anticline (Fig. 4) is similarly interpreted as a rapidly eastward propagating, box-like, near-isoclinal detachment anticline with structural relief in the west of ~4 km (Fig. 5b) decreasing eastward to < 2 km (Heermance et al., 2008; Scharer et al., 2006; Scharer et al., 2004). Average rock-uplift rates since fold initiation are on the order of ~3.0 ± 0.8 mm/y (Heermance et al., 2008; Scharer et al., 2004). As the Atushi fold propagated eastward, it interfered with the westward propagating Mutule fold (Scharer et al., 2004) (Fig. 4). The westernmost tip of the Mutule fold is interpreted as a detachment fold with a likely initiation age of 0.8-1 My and a structural relief of < 2 km (Scharer et al., 2004), implying average rock-uplift rates of ~2 mm/y. About 10 km east of Mutule's western tip, the fold's structural relief rapidly increases to nearly 6 km (Fig. 5c) implying uplift rates exceeding 3 mm/y. Here, a southward-dipping thrust fault controls the uplift of the structure (Figs. 4, 5c).

Over 6 km of Tertiary strata fill the Kashi Basin and record sedimentation from the early Paleogene to today (Heermance et al., 2007). Early to mid-Paleogene marine sediments (including evaporites) are unconformably overlain by fluvial and lacustrine sandstones, siltstones, and shales of the Miocene Wuqia Group (Fig. 4). The Plio-Pleistocene Atushi Formation conformably overlies the Wuqia Group and features mostly low-energy fluvial sediments composed of weakly-to-moderately cemented, sand-, silt- and mudstones with uncommon pebble conglomerates (Fig. 4). The cores of the Atushi, Kashi, Mutule, and

Mingyaole anticlines all expose this easily erodible Atushi Formation and only in the westernmost part of the Atushi fold are older units exposed (Fig. 4). Throughout the western Tarim Basin, the time-transgressive, moderately cemented, pebble-to-boulder conglomerate of the Xiyu Formation overlies the Tertiary strata (Charreau et al., 2009) (Fig. 4). The unit has varying stratigraphic thickness, is laterally discontinuous and youngs basinward, thus recording the southward advance of both deformation and the gravel front over the last 25 Ma (Heermance et al., 2007). Rapid foreland sedimentation rates throughout the Neogene of up to 0.8 mm/y (Heermance et al., 2007) imply that (given some isostatic compensation and sediment compaction), structures have to uplift rock at rates exceeding ~0.3 mm/y for topography to emerge.

All folds in the foreland are crossed by braided, commonly ephemeral rivers with a coarse bedload (pebble to cobbles with a small boulder fraction), but also a high sand, silt, and clay content. In between the folds, large alluvial fans are built by streams emerging from the Tian Shan mountain front to the north (Figs. 3, 4). Catchment areas of antecedent streams range from < 100 km^2 to nearly 4000 km^2 (Fig. 3), and their headwater geomorphology shows that the catchments have been largely unglaciated (Stroeven et al., 2013). Notably, the western Mutule fold is crossed by very small streams draining the faulted ridge to the north of the fold (typical catchment areas of 50-80 km^2), whereas antecedent drainages of the Atushi and Kashi folds have large catchment areas (Fig. 3). All streams of the smaller (< 1000 km^2) catchments are currently ephemeral, but even the largest drainages have a highly variable streamflow with only small discharges outside the snow-melt season and between major thunderstorms.

The northwestern Tarim Basin (Fig. 3) is characterized by an arid desert climate (< 70 mm/y precipitation), such that the major rivers are fed by meltwater from the high peaks of the Tian Shan, whereas cloudbursts drive ephemeral discharge on many alluvial fan systems. However, the region has been wetter in the past (Yang et al., 2008; Yang and Scuderi, 2010). The base-level evolution in the Tarim Basin is poorly known. For the antecedent streams crossing the Atushi, Kashi, and Mutule folds (Figs 3, 4), the base level downstream of the folds is most likely slowly rising due to aggradation by antecedent rivers, as well as by the major eastward-draining Kezilesu river just south of the study area (Fig. 3). Clearly, the rates of aggradation are lower than the uplift rates of most of each fold's length, but some structures, such as the easternmost Kashi fold, are buried beneath the alluvial plain (Chen et al., 2002; Chen et al., 2007). Little evidence exists for major lakes just south of the Kashi and Atushi folds that might have caused rapid changes in the base level.

3 Methods

3.1 Mapping and sedimentology

Topographic analysis and terrace mapping was done using the 90-m SRTMv 4.1 DEM (Jarvis et al., 2008) and using satellite imagery in Google Earth® followed by ground truthing in the field. Selected terraces on Mutule and Kashi, as well as the river crossing the Mutule fold, were surveyed using differential GPS. Thicknesses of strath-covering sediments on central Atushi and central Mutule were measured using a laser rangefinder along gullies that clearly expose the base of the strath. Given some surface modification by deflation, inflation, and surface erosion, we identified largely unmodified terrace surfaces

from their restricted surface relief and the presence of desert pavement. Uncertainties in the thickness measurements are in the range of ± 0.3 to ± 0.7 m.

Clast imbrications (n > 650) in 14 locations were measured based on multiple exposure surfaces with diverse orientations and depth beneath the terrace surface in order to limit the bias related to oversampling of a particular orientation. Orientation and depth below the terrace surface were recorded with a compass and a laser rangefinder, respectively. Changes in source areas between the terrace deposits and the modern river channels were assessed using lithologic clast counts along 9 surface transects in modern river beds and 4 depth transects on exposures of fluvial terraces. In each location, 100-140 clasts with b-axes > 1 cm were sampled every 20 cm and were classified as carbonate-rich or silicic on the basis of presence of calcium carbonate. In addition, we separately identified an easily recognized, dark-grey to white, weakly metamorphosed microcrystalline limestone that occurred in various proportions along all streams. In a separate suite of measurements on the central Mutule fold, we measured clast sizes along 3 surface transects in modern river beds and 7 depth transects on fluvial terrace outcrops (Wolman, 1954). Grains with b-axes < 5 mm were counted either as fine pebbles and sand (< 5 mm, but visible to the eye) or as fine silt and clay (not visible to the eye). At each of the three river transects, 124 greater-than-silt-sized counts were obtained. For each of the 7 terrace locations, 26-60 clasts were counted. In the data analysis, we assigned an uncertainty of 10% (1σ confidence level) to each count (Whittaker et al., 2011) and ignored any clasts with b-axes < 0.5 mm.

3.2 Optically stimulated luminescence dating

Sand lenses within gravelly deposits covering bedrock straths were sampled for OSL dating on the three upper terraces of the Mutule fold, at two locations on the western and

eastern Atushi fold, as well as on the highest terrace on the Kashi fold. The samples were processed and measured in the Laboratory of Luminescence Research at the Institute of Geology, China Earthquake Administration, Beijing, following standard techniques and a single-aliquot regenerative dose protocol (Murray and Wintle, 2000; Wintle and Murray, 2006). Dose rates were estimated by measuring activities of ^{238}U, ^{226}Ra, ^{228}Ra, ^{228}Th, and ^{40}K in sediment collected within a 15-cm radius around the tube around the OSL sample. We note that samples CK-1 and WCA-3 have exceptionally high U-series disequilibria, and their ages are reported, but not used in the analysis. The distribution of measured D_e values for the aliquots of each sample was modeled using a three-parameter minimum age model (MAM) (Galbraith and Roberts, 2012; Galbraith et al., 1999) and a central age model (CAM) (Galbraith and Roberts, 2012; Galbraith et al., 1999). We calculated the skew, kurtosis, and overdispersion and used the criteria by Arnold et al. (2007) to choose the most appropriate age model. Finally, we doubled the standard errors from the MAM and CAM models to obtain ages at the 2σ confidence level. See Text S1.4 for more detail on the methodology.

3.3 Cosmogenic nuclide dating

Eight samples were collected from a 3-m deep profile (Anderson et al., 1996; Hancock et al., 1999; Repka et al., 1997) on the highest, most extensive Atushi terrace for ^{10}Be cosmogenic radionuclide (CRN) dating. The site lies ~60 m away from the terrace edge, with relief of < 20 cm within a radius of several meters, and with a weakly developed desert pavement. Seven sand samples were collected from stratigraphic intervals each less than 10 cm thick and spaced 30-100 cm apart and one sample consisting of 1- to 4-cm-diameter quartz clasts was collected on the terrace surface within 3 m of the depth profile site. The

samples were processed at the cosmogenic nuclide preparation laboratory at UC Santa Barbara following standard procedures (Bookhagen and Strecker, 2012), measured at the Purdue Rare Isotope Measurement (PRIME) Laboratory, and analyzed using a Monte Carlo depth-profile simulator (Hidy et al., 2010) and the CRONUS-Earth-2008-v2.3 exposure age calculator (Balco et al., 2008). See Text S1.5 for more detail on the methodology.

4 Results

4.1 Planation surfaces in the foreland of the Tian Shan

The Kashi, Atushi, and Mutule folds have uplifted 2-5 km of rock over the past 1-2 My (Figs. 5a-c) (Chen et al., 2007; Heermance et al., 2008; Scharer et al., 2004). Despite this large structural relief, the present-day surface of the folds lies only 100-800 m above the surrounding alluvial fans, thereby attesting to efficient fluvial and hillslope erosion that approximately matches the rock-uplift rates (Fig. 5). All three folds (Kashi, Atushi, Mutule), expose a variably thick, outer rim of more resistant Xiyu conglomerates (Neogene to Quaternary in age) surrounding a core of weakly cemented, quite readily eroded sand- and siltstones of the Pliocene Atushi Formation (Figs. 4, 5). Furthermore, extensive areas with mean slopes < 5° exist on the studied structures, where relief within a radius of 1 km is < 100-200 m (Fig. 6). Steeply inclined beds of the folds (Scharer et al., 2004) are clearly visible both on satellite imagery (Fig. 7) and in the field (Fig. 8) and demonstrate the erosional nature of these nearly planar topographic surfaces that truncate the underlying beds. The rims of the fold composed of the resistant Xiyu conglomerate commonly stand above the Atushi Formation and attest to their slightly greater resistance to erosion (Fig. 5). Nonetheless, the Xiyu commonly is largely planed off as well (Figs. 5e, g, h). Parts of the

planar surfaces are covered by alluvial and fluvial gravels that unconformably overlie the steep bedding and attest to the role of fluvial erosion in creating these surfaces (Figs. 6, 7, 8) (Chen et al., 2007; Heermance et al., 2008; Scharer et al., 2006). Hereafter, the planar surfaces will be termed “beveled” or “planated” surfaces or areas. Many of the beveled areas are currently incised by major antecedent streams and smaller consequent streams, leaving fluvial terraces behind (Table 1, Figs. 6, 7, 8). Many of these abandoned terraces have been progressively tilted and, thus, record continued uplift by the folds since the terraces were abandoned (Heermance et al., 2008; Scharer et al., 2006) (Fig. 9a). Despite similar uplift rates, bedrock lithologies, and local climate, a detailed consideration of each structure reveals that not all folds exhibit a similar distribution of beveled areas.

4.1.1 Beveling of the Kashi fold

The western Kashi fold initiated 1.4 ± 0.3 My ago and has a typical convex-up topography with a steep, highly dissected, short northern limb and a gentler sloping, dissected southern limb. These flanks bound a crest rising up to 800 m above the modern depositional plain (Figs. 5d, 7b). The eastern part of the Kashi fold also shows an emergent fold nose (Fig. 5f), but one that has seen more limited erosion (Scharer et al., 2004). This part of the fold is younger: folding began < 1 My ago, and topographic emergence occurred much later than on the western tip of the fold (Chen et al., 2007). Both, the western and the eastern parts have not experienced efficient lateral beveling. Where the Baishikeremuhe river (Fig. 3b) impinges obliquely onto the Kashi fold, it is deflected eastwards down a topographic ramp that broadly parallels the fold flank (Fig. 7b). Eventually, the Baishikeremuhe crosses the fold at an oblique angle of ~0-70°, but prior to being trapped in the current watergap, this river was deflected around the eastern nose of the fold (Chen et

al., 2007). During times of active aggradation, the river may still flow around the fold's eastern nose, as suggested by well-preserved abandoned channels on the alluvial fan surface north of Kashi (Chen et al., 2007; Scharer et al., 2006). Where the modern river impinges onto the upstream flank of the fold, it has beveled a cusp-shaped indentation across the northern ~2 km of Kashi's northern limb (Figs. 7b, 9a). Downstream, on the southern limb of the fold, a series of tilted strath terraces with thick, near-complete fluvial cover document the anticlockwise rotation of the river and the uplift of the Kashi fold (Fig. 9a) (Table 1).

4.1.2 Beveling of the Atushi fold

In contrast to the Kashi fold, the west-central part of the Atushi fold to Kashi's north lacks a convex-up topographic profile, and instead forms a wide, planar platform with slopes commonly < 5° and a mean 500-m-radius relief of < 50 to 100 m (Figs. 5g, 6, 7c). The WSW-ENE slope of ~0.7°along this 15- to 20-km-long platform that both spans and trends parallel to the fold's axis is notably similar to the slope of a parallel topographic swath across the modern alluvial fans that impinge on the fold's upstream flank (Fig. 10). This parallelism suggests that the west-central Atushi fold has not been differential tilted since its beveling. Only ~16 % of the beveled area of western-central Atushi is currently covered by fluvial deposits (Table 1, Fig. 6). However, on the basis of localized, beveled "plateaus" of remnant incised topography, two extensively beveled areas, each ~10 km long and separated vertically by ~30-60 m, can be identified (Fig. 10). The more eastern surface is incised 70-90 m by the modern Boguzihe river, whereas the preserved incision depth further west is 25-45 m (Fig. 10). We note that ~1-1.5 km of the northern limb (10-20% of the total fold width) of the Atushi fold is buried beneath unincised gravels and is likely being actively beveled (Fig. 6). Contrary to Atushi's western and central segments, the eastern part of the Atushi

fold rises to a height of > 200 m with respect to the flanking basin (Figs 5h-k). Here, incision of antecedent rivers forms canyons, tens to hundreds of meters deep, and the limbs of the folds are steep and highly dissected by gullies (Table 1, Fig. 7d): similar to the flanks of the western Kashi fold (Fig. 7b). However, despite this surface uplift, two prominent, planar areas are preserved on the eastern Atushi fold (Figs. 5i-k, 7d).

4.1.3 Beveling of the Mutule fold

Further east, the Mutule fold has the most extensive low-lying beveled surface in the area (Figs. 5m-o). In fact, the northern limb of the fold (~30% of the total fold width) is nearly completely buried under modern alluvial fans with rare bedrock outcrops beneath a slightly raised strath terrace that shows < 5-10 m of incision down to local base level (Table 1, Figs. 6, 7e). Greater surface uplift of strath terraces or less efficient recent erosion of the southern limb of the Mutule fold has led to 10-50 m of incision by modern channels (Table 1, Figs. 7e, 9b). The fluvial gravels in this location are still extensively preserved in the north, but preservation decreases southward (Fig. 9b). These fluvial gravels on the southern limb reveal a somewhat complex geometry. Rather than a flight of clearly defined river terraces separated by sharp risers, the T1-T3 surfaces are present at a nearly continuous range of elevations above the modern river (Fig. S2). Hence, correlating terraces across a several-kilometer-wide fold poses a challenge, because antecedent rivers sweep from southward flow directions in the west to southeastward in the east, and the appropriate local base-level is not always clear (Fig. S2). Nevertheless, well-preserved terrace risers are present, and four major terrace levels can be identified (Fig. 9b).

In summary, the three folds described here record erosional geometries ranging from steep limbs eroded by gullying and hillslope erosion to aerially extensive, beveled surfaces

that are preserved at heights ranging from 0 to 280 m above the modern rivers and are covered by varying amounts of fluvial sediments (Table 1). On western-central Atushi and Mutule folds, between 50-90% of the fold is beveled and lies < 50-100 m above the current base level, whereas on eastern Atushi, the beveled areas are raised to nearly 300 m, and on the Kashi fold, less than 20% of the fold has been planated (Table 1). Thus, the extent of planation varies spatially across the Tian Shan foreland.

4.2 Fluvial terraces

4.2.1 Sedimentology

All beveled surfaces, except the highest ones on the eastern parts of the Atushi fold, preserve some fluvial deposits. These deposits are typically moderately sorted, granule-to-cobble conglomerates, with uncommon sand and silt lenses of up to 30-40 cm thickness, as well as rare boulders (Figs. 8, S3). Considerable grain-size variations between moderately- to well-bedded horizons occur. Generally, beds are sub-meter thick and planar, but meter-scale channels and scours are common. Even within the thickest cover sequences, no clear evidence for major cut-and-fill events or hiatuses could be found (with one exception cf. Fig. S4c). Clasts are typically sub-rounded to rounded (similar to the modern river) and imbricated, non-spherical clasts are abundant (Figs. 8b, S3a). Note that in the case of the Mutule fold, despite the short travel distance (< 10 km), clasts are still rounded because the catchment drains a ridge of Xiyu conglomerate (Fig. 4) comprising rounded clasts. The deposits are matrix- to clast-supported with sandy or less commonly silty matrices. A mud fraction is present and drapes all grains, but thick deposits of clay-to-sand sizes only occur in rare lenses and pockets that likely represent slackwater deposits or minor channels (Fig. S3a). On all folds, the surface of the fluvial cover sequences is generally smooth with a

relief of < 1 m (Fig. 8). Undulations with amplitudes of tens of centimeters across several meters are interpreted as primary alluvial fan structures, whereas relief of several meters typically occurs only along terrace scarps or where flexural-slip scarps offset the strath surfaces, e.g., Li et al. (2015b). Modifications to the primary topography of the terrace surface are observed where fines collect in deflation hollows and where relative coarsening of the surface occurs around small gullies (Fig. S3c). We estimate that these surface modifications have magnitudes of < 10 cm.

4.2.2 Terrace-cover thickness

We mapped the thickness of two major preserved deposits on the Atushi and Mutule fold (Fig. 11). With respect to the planar preserved character of the abandoned, upper alluvial surface, we find that most of the cover sequences are between 1-6 m thick with uncommon deposits > 10 m thick. In comparison to rather planar, upper terrace surfaces, the gravel thickness above a strath may vary by several meters across distances of a few meters and reveals a complex strath surface topography with meter-scale relief (Fig. 11). The flat-lying terrace gravels are observed to buttress against steeply dipping bedrock (Figs. 8c, S4d). Thus, the strath surface was not entirely flat, but has topography with commonly 6 ± 2 m and up to 20 m of relief.

4.2.3 Imbrication measurements

Imbrication measurements on terraces of Atushi and Mutule show moderately dispersive flows consistent with a braided river system flowing on a gently inclined alluvial surface (Fig. 11). On Mutule, the mean flow direction is ~113° from north, which is indistinguishable from the general flow direction of the modern river (Fig. 11a). On Atushi,

mean flow directions are generally southeastward, with a mean of ~135°, similar to the modern Boguzihe river. Thus, in general, imbrications reveal a pattern of flow directions similar to the modern day.

4.2.4 Lithological clast counts

Based on catchment areas (Fig. 3) and lithological clast counts (Table 2), 3-5 different source areas of streams crossing the folds in the study area can be defined (Fig. 12, Table A2). It is obvious from these counts that the Mutule terraces have been deposited by local rivers draining the 60-km^2 catchment to its north (MUT R1, R2: Fig. 12), rather than the larger (1070 km^2) Bapanshuimogou river on eastern Mutule (MUT R3) (cf. Fig. 3). Moreover, it is clear that Baishikeremuhe has not had any major influence in depositing the Atushi terraces (Fig. 12). Although the Boguzihe upstream of the Atushi fold (Fig. 3) comprises three major drainages, clast compositions of the terrace deposits most closely mimic the two westernmost tributaries (Bog3, Bog2), thereby suggesting that the current tributary geometry persisted during times of beveling and aggradation on the terraces (Fig. 12, Table 2). Finally, negligible differences exist when comparing terraces at different levels from the same fold, e.g., SMT_north vs. SMT_south (Fig. 12), or the bottom, top, and surface of one thick deposit, e.g., a 12- to 13-m-thick terrace on south Mutule (Table A2). We conclude that efficient planation of folds that are being uplifted rapidly can occur by streams with catchment areas ranging from < 100 km^2 to 4000 km^2.

4.2.5 Clast-size counts

We measured clast sizes along three locations of a river crossing the Mutule fold, as well as seven terrace locations (Fig. 13, Table 3). The D_{50} and D_{84} values of amalgamated terrace

deposits are lower than those of the modern river, but both lie within the 20% uncertainty bounds (2σ confidence level). Thus, in this location, a slight coarsening during times of incision may have occurred, but the data are inconclusive.

4.3 Timing of terrace formation and planation episodes

The timing of beveling and the rate of uplift is estimated using 14 optically stimulated luminescence (OSL) ages and one cosmogenic depth profile on terraces of the Kashi, Atushi, and Mutule folds. Measured ^{10}Be concentrations in the depth profile on the central Atushi fold decrease exponentially with depth (Table 4, Fig. S5). This observation is consistent with the absence of significant post-depositional sediment mixing and with a rapid and fairly steady sediment-accumulation rate compared to the age of the terrace. The age calculation requires some assumptions about the surface erosion or inflation rate of the terrace since abandonment. Judging from the development of desert pavement (Fig. S3c) and the preservation of primary fluvial topography on the terrace surface, we argue that erosion is limited. The presence of a ~30-cm-thick horizon with an estimated 50% silt-and-gypsum, (Fig. S3b) suggests that surface inflation of ~15 cm by windblown dust (Kurth et al., 2011; Wells et al., 1995) is likely more important than deflation by erosion. Hence, in our cosmogenic analysis, we allow an inflation of 15 cm, an erosion of 10 cm, and erosion/inflation rates of ± 1 cm/ky. We further assign a range of terrace densities of 1.4-2.3 g/cm^3 and a neutron attenuation length of 160 ± 5 g/cm^2 (Gosse and Phillips, 2001; Hidy et al., 2010). We calculate the most probable age after 2 x 10^5 iterations using a Monte Carlo simulator (Hidy et al., 2010) (Table A4). Ages using either a time-independent or time-dependent scaling scheme and either including or excluding the surface sample vary between 74 ± 17 ka (±2σ) and 89 ± 21 ka, respectively (Table A8). Any surface erosion or

disintegration of larger pebbles into smaller pieces will cause underestimates of the surface age. Therefore, given uncertainties in the surface age, we use a mean age of 82 ± 19 ka and suggest excluding the surface sample entirely for the inheritance estimate.

Equivalent dose distributions for single aliquots of our OSL samples generally have a high overdispersion (36-67 %), and are significantly skewed (Table 5). These characteristics are commonly interpreted as signs of partial bleaching of the grains (Arnold et al., 2007; Bailey and Arnold, 2006; Kenworthy et al., 2014; Olley et al., 1998; Olley et al., 1999; Olley et al., 2004; Rhodes, 2011; Rittenour, 2008) (Table 5). Ages deduced from OSL dating vary depending on the age model used (Table 5). Based on the skewness and the overdispersion values, the minimum age model (MAM) is the most appropriate for all but two samples (Arnold et al., 2007) (Table 5). With three exceptions (Figs. S6, S7), samples from different terraces are in stratigraphic order with respect to the base-level of the modern river (Fig. 14).

Our dates (all reported at a 2σ–confidence interval) reveal that the three studied structures are affected by different major beveling episodes. The high surface of the eastern Atushi fold that lies > 200 m above local base level (Figs. 5i, 5k, 7d) remains undated, but is likely older than 100 ka (Fig. 15a). One terrace on western Atushi is dated to 35 ± 7 ka (Fig. 15a, Table 5), whereas the fluvial gravels on western-central Atushi yield an age of 82 ± 22 ka (Fig. 15c). The highest terrace (T4) on the Kashi fold was formed at 48 ± 10 ka (Fig. 15b) and terraces on Mutule are dated to respectively 11 ± 3 (±2σ) ka, 21 ± 7 ka, and 28 ± 7 ka (Fig. 15d, Table 5). Finally, modern-day lateral planation can be observed most clearly on northern Mutule (Fig. 15a), in the divot carved into the northern side of the Kashi fold (Figs. 7, 9), and across a ~ 20-km-wide zone on the northern limb of western-central Atushi (Fig.

6). It is particularly striking that the Mutule fold, despite a recent episode of major beveling, is eroded by the smallest antecedent rivers (Fig. 3) and that the youngest part of the eastward propagating Atushi fold (Chen et al., 2002) has been abandoned for the longest time.

5 Discussion

The most significant finding of this work is that kilometer-wide, low-relief surfaces partly covered with fluvial deposits and preserved on the Kashi, Atushi and Mutule folds provide evidence for intermittent periods of very efficient lateral erosion of these rapidly uplifting anticlines by rivers with catchment areas ranging in size from < 100 km^2 to 4000 km^2. Together with Late Quaternary terrace ages, our mapping provides constraints on the uplift rates of the folds and on the rates and mechanism of river planation. We first discuss evidence for repeated changes between planation and incision of the folds by the local antecedent drainages. Then, we explore the timing of Quaternary fold growth and fold planation. These results underpin a discussion about strath-formation models.

5.1 Intermittent periods of incision and planation by antecedent drainages

Two lines of evidence suggest repeated alternations of efficient lateral planation of the folds with vertical incision that creates narrow canyons. First, the height of beveled surfaces above the modern base level and the depth of incision into them varies greatly along the folds (Table 1). In most cases, variations in rock-uplift rate cannot explain the height differences, but instead, the beveled surfaces are clearly of different ages. This temporal difference is most convincingly shown by progressive tilting of terraces at different heights (Fig. 9a) (Heermance et al., 2008; Scharer et al., 2006). Another striking example is the contrast between western and eastern Atushi. Whereas the beveled areas on western-central

Atushi are > 100 m lower than surfaces in the east (Figs. 5g-k, 7c-d), western Atushi began to be uplifted earlier, has a generally higher structural relief, and is inferred to have experienced higher or similar rates of shortening and rock-uplift than eastern Atushi (Chen et al., 2007; Scharer et al., 2004). Thus, this fold preserves several beveling episodes that affected only parts of the structure. Planation surfaces preserved at different elevations, therefore, imply intermittent, rather than continuous beveling of the folds.

The second line of evidence for intermittent periods of beveling and incision is the meter-scale relief of the strath surface preserved beneath the fluvial deposits (Figs. 8, 11). Strath relief is typically ~6 ± 2 m and could represent topography that was formed during an episode of incision that preceded partial planation and partial infilling during a beveling episode. Alternatively, meter-scale scours could have formed at the same time as the fold was rapidly beveled. In both scenarios, the gravels (except for the lowest few centimeters to meters) would be coeval with the planation episode. Where gravel thickness exceeds 5-10 m, scouring of the strath during the time of fold planation seems unlikely. Thus, a stringer of 10- to 20-m-thick gravel (T4) that extends nearly 6 km downslope across the Mutule fold and is buttressed against the bedrock (Fig. 8b, Fig. 11a: T4) is consistent with an episode of > 10 m of incision pre-dating the T4-planation episode. We, therefore, conclude that episodes of beveling and incision have likely alternated on these folds for an extended period of time – possibly across the entire time of their emergence above the depositional surface.

We argue that transitions between beveling and incision periods are not commonly accompanied by major drainage reorganization events. First, based on lithologic clast counts, source areas of the gravels covering planation surfaces are similar to source areas of

modern antecedent drainages (Fig. 12). Second, average imbrication directions of terrace deposits are close to the flow directions of modern streams (Fig. 11). Finally, the imbrication, moderate grain size, significant rounding, and presence of planar beds and channels observed in the fluvial terraces (Figs. 8, S3, S4) are comparable to the modern alluvial fan and river deposits and are consistent with a braided channel facies (Labourdette and Jones, 2007; Miall, 1977). Moreover, despite some modification, the surfaces of fluvial deposits show primary structures similar to channels traversing the modern alluvial fans. Therefore, during a time of planation, a thin ($< 6 \pm 2$ m) alluvial fan-type deposit likely covered the entire beveled surface, such as is preserved on the very recently beveled area on northern Mutule (Figs. 6, 7e), and the folds were eroded by multiple, rapidly migrating braided rivers.

5.2 Rates of rock uplift in the foreland of the Tian Shan

In order to constrain rates of lateral planation, the rates of rock uplift on the folds over the past 10-100 ky are a key input. Since initiation of fold growth, as determined by the first appearance of growth strata 1-2.5 million-years ago, average rock-uplift rates of the Kashi and Atushi folds have been constrained to 1-3 mm/y (Chen et al., 2007; Heermance et al., 2008). However, uplift rates over the past 10-100 ky, the time of most recent fold planation that is recorded by a series of strath terraces, remain quite poorly constrained. Here, we complement terrace surveys from previous studies showing that abandoned terraces on the Mushi, Mingyaole, Kashi, and Atushi folds are commonly tilted or otherwise deformed by increasing amounts with age due to the ongoing growth and uplift by the folds (Fig. 9) (Fig. 13 in Heermance et al., 2008; Fig. 8 in Li et al., 2013; Fig. 8, 9, 11 in Scharer et al., 2006). In the absence of significant incision of the modern alluvial fans in the foreland of the Tian

Shan, we interpret the incised and tilted terraces as recording average rock-uplift rates of the folds (relative to the slowly rising base level resulting from foreland aggradation) throughout the late Quaternary. On the western Mutule fold, tilting with respect to the modern river is not clear (Fig. 9b), likely because total uplift since terrace abandonment (deduced from the depth of incision) is small compared to the other folds (Table 1) and because terraces on this fold are relatively short, are not preserved across much of the fold limb, and largely occur within the bounds of a single dip domain (Fig. 9). Moreover, if the fold deforms primarily by hinge migration (Li et al., 2015a), rather than limb rotation, differential rotation is not expected except for the outer hinge (Scharer et al., 2006). Evidence for continued uplift on Mutule is, nonetheless, strong, because 1) alluvial fans upstream of Mutule are not incised, 2) strath terraces sit as much as 50 m above modern base level across the fold, and 3) aggradation by > 50 m (the height of T4 on Mutule) of the entire area north of Mutule and subsequent stripping by a similar amount without leaving erosional remnants seems unlikely. Thus, the Late Quaternary ages of the terraces dated in this study imply that the folds in the foreland of the Tian Shan have been actively uplifting during the Quaternary. Terrace ages on Kashi, Atushi, and Mutule define a trend of increasing ages with height above the modern river (Fig. 14). Rock-uplift rates were estimated by dividing the difference in height between the highest and lowest terraces by their age difference (Table 6). Where only one terrace level was dated (Atushi and Kashi), we used the age and the height above the modern river to estimate uplift rates (Table 6). Note that in case of the Kashi fold, we projected the tilted T4 terrace (Fig. 9) to the core of the anticline to estimate a peak uplift rate (Table 6). We disregard samples WCA-1, and WCA-3 in this analysis, because the terrace on western Atushi was not clearly deposited by

a river crossing the fold, but was probably created by fold-internal drainage, thereby complicating the interpretation of the base level. Using the preferred OSL age models, we estimate uplift rates of ~2.7 ± 0.7 mm/y (±2σ) for Kashi, ~1.0 ± 0.3 mm/y for Atushi and ~1.9 ± 0.5 mm/y for Mutule since between ~80 and ~30 ka (Fig. 14). These rates are similar to the million-year uplift rates calculated for these folds (Chen et al., 2007; Heermance et al., 2008; Scharer et al., 2004). We note that this range of incision/uplift rates is decreased by ~ 0.5 mm/y for Mutule if the central age model is used for all samples (Fig. 14). We conclude that the terraces in the foreland of the Tian Shan record Late Quaternary uplift of the folds at rates that are comparable to million-year average rates and that evidence for large temporal variations in rock-uplift rates over the last 80 ky is sparse.

5.3 Rates of lateral erosion and duration of beveling episodes

In the context of quasi-steady rock uplift at multi-millennial time scales, one major implication of the presence of extensive beveled platforms, on the one hand, and incised channels, on the other, is that large changes in lateral bedrock erosion rates are necessary to explain the extensive beveled surfaces. Commonly, strath-terrace formation has been interpreted to be driven by changes in vertical incision rates, whereas lateral erosion rates are assumed constant or changes in them are not addressed (DeVecchio et al., 2012; Fuller et al., 2009; Gilbert, 1877; Hancock and Anderson, 2002; Langston et al., 2015; Merritts et al., 1994; Molnar et al., 1994; Pan et al., 2003; Zaprowski et al., 2001). In the Tian Shan foreland, vertical incision rates likely vary, but their variation is not necessary to explain the beveled platforms. In order to support this argument, we estimate lateral erosion rates during beveling episodes using the area, relief, and age of strath surfaces together with the uplift rates of the folds (Table 7, Fig. 15). In order to estimate how planation rates have changed

through time, we then compare those planation rates with "modern" lateral erosion rates constrained by the area of current canyons created by incised, antecedent streams since abandonment of the planation surfaces (Table 7, Fig. 15).

Given the area of an incised valley (A_v) that was created during an episode of incision with duration (Δt_i), an average areal planation rate of the stream in this valley during the incision period (P_i) can be estimated as:

$$P_i = \frac{A_v}{\Delta t_i} \quad (3),$$

(Fig. 16). For the planation of a bedrock strath with area (A_s) that is beveled during a time-interval (Δt_b), an equivalent lateral rate (P_b) can be estimated:

$$P_b = \frac{A_s}{\Delta t_b} \quad (4),$$

(Fig. 16). Such average planation rates are maximum rates, because some of the eroded area is created through vertical incision of bedrock by channels and through hillslope erosion. Moreover, it is unlikely that the rate of planation is constant, as assumed by equations 3-4, but rather the rate should decrease with a growing beveled surface and with a declining frequency of contacts between the channel and the valley walls (Hancock and Anderson, 2002). Because similar caveats apply to both valley and strath planation, rates derived from equations 3-4, nonetheless, provide a useful comparison between planation rates during incision versus beveling episodes. We note that equations 3-4 are independent of the number of streams that laterally cut the valley or strath.

As discussed above, we assume that streams incise into a fold at an average rate equivalent to the uplift rate of the structure. Therefore, the duration of an incision episode (Δt_i) can be estimated as:

$$\Delta t_i = \frac{D_v}{U} \quad (5),$$

with D_v being the depth of the incised valley and U the uplift rate of the fold (Fig. 16). Equivalently, where fluvial gravels mantle and preserve the topography of the strath surface, we can estimate the duration of the time within which each point on the strath surface has to be visited by beveling rivers (Δt_b) as:

$$\Delta t_b \leq \frac{R_s}{U} \quad (6),$$

*w*ith R_s being the maximum relief of the bedrock strath surface and U being the uplift rate. In other words, lateral planation must happen at a rate higher than or equal to the time necessary to uplift a height equal to the strath relief R_s (Fig. 16). The planation surface could be actively beveled for a duration longer than Δt_b, but each point on the planation surface has to be revisited within a time < Δt_b in order to maintain a relief smaller than R_s.

Using above analysis on the Kashi (Fig. 15b), Atushi (Fig. 15c), and Mutule (Fig. 15d) folds, we find that order of magnitude changes (20-50 fold) in areal planation rates are necessary to explain the contrast between eroded areas of valleys and strath surfaces (Table 7).

In addition to the areal planation rate, we can estimate a rate of lateral bedrock erosion for the incision episode equivalent to a single straight river moving laterally in one direction:

$$E_{hi} = \frac{A_v L}{\Delta t_i} \quad (7),$$

and for the beveling episode:

$$E_{hb} = \frac{A_s L}{\Delta t_b} \quad (8),$$

with L being the length of the eroded surface in the average flow-direction (Figs. 15,16). The length L is estimated by the orientation of channels, terraces and measured imbrication directions (Fig. 11). These lateral bedrock erosion rates of a single hypothetical straight river likely do not correspond to real measurable bank erosion rates because channels are sinuous, and planation surfaces were cut by multithreaded, braided streams. However, the rates serve as an estimate for the order of magnitude of lateral bedrock erosion rates in the Tian Shan foreland.

Inferred minimum lateral bedrock erosion rates of 0.2-0.6 m/y (P_b) during at least 2-6 ky-long beveling episodes (Δt_b) (Table 7) are more than an order-of-magnitude higher than maximum planation rates (P_i) during the 10- to 50-ky-long episodes (Δt_i) when incision of the folds dominated (Table 7). Notably, planation rates during beveling episodes are more than two orders-of-magnitude larger than incision rates. We reiterate that Δt_b merely represents the time during which each point on the planation surface has to be revisited, and that the duration of the beveling episodes could have been much longer than Δt_b. Moreover, planation rates during beveling episodes (P_b) are likely to have been much higher than estimated here, because the measured extent of strath surfaces used in this calculation is limited to the area where fluvial gravels are preserved (Fig. 17). In support of planation rates exceeding 0.2 m/y during beveling episodes, analogue experiments have shown that, in order to explain the wholesale beveling observed on the Atushi fold ($A_b = A_u$ in equation 1), lateral bedrock erosion rates of several meters per year are necessary (Bufe et al., 2016).

Above analysis relies on the assumption that uplift rates are constant through time. If fold uplift and river incision ceases, planation rates necessary to explain the formation of wide beveled surfaces would be smaller, and the existence of strath terrace formation could

potentially be explained with changes in the incision rates alone. However, in order to cut the strath surfaces preserved on northern Kashi, southern Kashi, Atushi, and Mutule with planation rates equivalent to the rates measured during incision periods, fold incision would have to cease for respectively > 42 ± 28 ky, 28 ± 9 ky, 141 ± 66 ky, and 54 ± 22 ky. Given the occurrence of uplifted terraces with age ranges of 10-80 ky, such pauses in fold incision appear impossible. Therefore, order-of-magnitude changes in the lateral erosion rate are necessary to explain the coexistence of wide planation surfaces and narrow canyons on the same active structure.

Caution has to be taken when extending these results to different settings. Bedrock strength has a significant effect on the lateral erosion rates, and the size of planation surfaces has been linked to bedrock lithology (Allen et al., 2013; Montgomery, 2004; Römer, 2010; Schanz and Montgomery, 2016). Whereas narrow strath terraces have been documented in more resistant lithologies, such as granites and quartzite (Burbank et al., 1996; Pratt-Sitaula et al., 2004), most wide planation surfaces form in weak or weathered lithologies (Allen et al., 2013; Collins et al., 2016; Cook et al., 2014; Fuller et al., 2009; Hancock et al., 1999; Langston et al., 2015; Lavé and Avouac, 2001; Molnar et al., 1994; Montgomery, 2004; Schanz and Montgomery, 2016). As a perturbed fluvial system adjusts towards a new equilibrium, lateral erosion rates of bedrock topography can reach 10s of meters per year (Bufe et al., 2016; Collins et al., 2016; Cook et al., 2014), even in resistant lithologies, such as unweathered granite (Anton et al., 2015) and, thus, can match river migration rates on alluvial plains (Jerolmack and Mohrig, 2007). Hence, whereas the absolute lateral erosion rates are typically lower and planation surfaces narrower where rock-strength is high,

accelerated lateral erosion rates (with respect to vertical incision rates) can likely contribute to strath-terrace formation even in such settings.

5.4 Mechanism of beveling

The mechanism of rapid lateral beveling of the folds is likely a combination of sweep erosion upstream of a channel narrowing (Bufe et al., 2016; Cook et al., 2014) that forms features such as the "dent" in the northern Kashi fold (Figs. 7b, 9a), as well as lateral erosion of valley walls along the length of an antecedent river (Fig. 17) (Bufe et al., 2016). Both of these mechanisms are observed in analogue experiments of antecedent rivers crossing actively uplifting folds (Bufe et al., 2016; Douglass and Schmeeckle, 2007). Two questions are asked here: 1) what controls the differences in beveling history between different catchments (spatial differences); and 2) what controls the changes between planation and canyon formation within one catchment (temporal differences)?

5.4.1 Planation in different catchments: The role of channel mobility

Folds are beveled both by single large rivers, such as the Baishikeremuhe crossing the Kashi fold (Figs. 3, 7b), and by suites of braided streams migrating across the entire width of the fold, such as seen on the alluvial fans upstream of Atushi and Mutule (Fig. 7). Notably, given their similar bedrock strength, rock-uplift rates, and fairly homogeneous climatic conditions, efficient beveling of these two folds has been accomplished by rivers with >40-fold differences in drainage areas (< 100 km^2 to 4000 km^2). Therefore, similarly wide areas can be eroded, despite expected 10- to 100-fold differences in water discharges – an unexpected result. The small catchments with short (~5-6 km long), steep (2.5-3.5°), alluvial fans upstream of Mutule (Figs. 4, 5m-o) must have had channel mobilities similar to larger

streams on the longer (9- to 12-km-long), gentler (1-1.5°) alluvial fans upstream western-central Atushi (Figs. 5g-h) during times of planation. At the same time, some large catchments only bevel relatively small proportions of the structures they cross: for example, the Baishikeremuhe crossing the Kashi fold (Figs. 3, 6), although this limited beveling may be a result of diversion of the river around the fold for extended periods.

Recalling equations (1) and (2), we note that with a constant uplift rate, the lateral bedrock erosion rate of a river scales with the rate of sediment reworking of an equivalent alluvial river upstream of the uplift (Fig. 2). This rate of sediment reworking (Q_f) is dependent on the depth of the river (or some other measure of its size), *H*, the area over which the river actively migrates, A_f, and the lateral channel mobility, T_f (Fig. 2). Given the > 60-fold difference in upstream catchment area, we hypothesize that the lower discharge and, thus, smaller H (Parker, 1978; Parker et al., 2007) of the rivers draining across Mutule is compensated by a higher ratio of sediment-to-water fluxes and corresponding higher channel mobility time scale, T_f, (Bufe et al., 2016; Constantine et al., 2014; Wickert et al., 2013). The approximately two-fold steeper slope of the Mutule fans (2.5-3.5°) compared to the fans on Atushi (1-1.5°) (Figs. 5g-h v.s. 5m-o) is consistent with a higher sediment-to-water ratio in the Mutule rivers (Ashworth et al., 2004; Bryant et al., 1995; Cazanacli et al., 2002; Kim et al., 2010; Whipple et al., 1998). Moreover, differences in lateral erosion efficiency between neighboring catchments could be due to small, random (autogenic) differences in sediment- and water fluxes or to differences in the confinement of the river (Bufe et al, 2016).

The relatively small size of planation surfaces on Kashi could be attributed either to a lower mobility of the river due to some upstream boundary condition confining the flow of

the Baishikeremuhe as it is draining across the westernmost Atushi fold (Bufe et al., 2016). However, the estimated lateral erosion rates during beveling of the main T4 terrace are on the same order or even higher than those on Mutule and Atushi. Another possible explanation for the lack of more complete beveling is the episodic and perhaps quite sustained diversion of significant discharge around the nose of the eastern Kashi fold (Scharer et al., 2006; Chen et al., 2007) and/or to a relatively late capture of the Baishikeremuhe (Chen et al., 2007). If the topography of the Kashi fold had been high (> 10-100 m) at the time of capture, the presence of high walls may have slowed lateral erosion (Malatesta et al., 2016). Similar topographic thresholds could inhibit renewed planation of eastern Atushi (Fig. 7d).

5.4.2 Changes from lateral planation to incision

Let us consider one single alluvial fan that is graded to a slope set mostly by the water and sediment flux (Ashworth et al., 2004; Bryant et al., 1995; Cazanacli et al., 2002; Kim et al., 2010; Whipple et al., 1998) and that is traversed by channels migrating with some mobility that is also dependent on these fluxes (Bufe et al., 2016; Constantine et al., 2014; Wickert et al., 2013). A decrease in the sediment flux, an increase in the water flux, a change in the flood frequency, or some change to the confinement of the river, e.g., due to a landslide, can cause entrenchment of the system and a dramatic reduction of both the actively reworked fluvial area, A_f, and the channel lateral mobility, T_f (Bufe et al., 2016). Because no evidence for widespread changes in river confinement exists in the Kashi foreland, we postulate that changing water and sediment fluxes or changing flood frequencies caused alternating periods of planation and incision (Fig. 17).

Correlating the record of beveled surfaces directly with documented regional climatic changes that would explain changes in the water and sediment influxes or the flood frequency appears untenable with our data. Our terrace ages cannot be consistently correlated with trends in the marine isotope stage record (Fig. 14, S6) (Lisiecki and Raymo, 2005; Petit et al., 1999) or with clusters of terrace and alluvial fan ages from other deposits in the region (Li et al., 2012; Li et al., 2013; Thompson et al., in review; Yang and Scuderi, 2010) (Fig 14). The proliferation of terraces across a range of regional climates is consistent with experimental findings that relatively small perturbations can have large effects on the channel mobility (Bufe et al., 2016). However, the number of samples in this study is small with respect to the size of the beveled surfaces and large areas on the folds remain undated. Perhaps, a more detailed and thorough dating of planation surfaces or more extensive hydrologic data would reveal an overall climate dependency. In any case, the temporal differences in the occurrence of planation surfaces across the folds in the study area excludes a simple scenario of regional climatic changes causing coeval rapid lateral planation on all folds.

Independently of the regional climate, linking planation episodes in each catchment directly to changes in the sediment and water fluxes is difficult, especially if such changes are small, short, or infrequent. Two possible measures are clast sizes of the fluvial sediment (as recorder of water and sediment fluxes) or erosion rates in upstream catchments (as proxy for higher sediment fluxes to the basin). Clast sizes in the modern rivers are coarser than on the terraces by a factor of 1.3. However, as discussed above, D_{50} values are within 2σ uncertainties of each other (Fig. 13). Moreover, comparing bed material at the surface of the modern river with material from the subsurface of the paleo-river (the terraces) can be

inappropriate, because a coarsening of the modern surface is expected if transport capacity exceeds the sediment load (Dietrich et al., 1989; Montgomery et al., 1999). Thus, the difference in D_{50} values between river and terrace deposits (Fig. 13) could be explained without any change in the hydrology between the past and the present. Alternatively, the size of the input sediment in modern rivers could have increased due to grain-size-modulating processes in the upstream catchments, e.g., tectonic perturbations or changes in vegetation (Whittaker et al., 2010). Finally, a coarsening of modern surface deposits by a factor of 1.3 could be explained by a reduction of sediment supply of 10-80% with respect to the water supply (Dietrich et al., 1989). More clast-size data are necessary to confirm the presence or absence of a trend. Measuring changes in catchment-wide mean erosion rates, as a proxy for sediment flux (Davis et al., 2012; Hidy et al., 2014; McPhillips et al., 2013; Schaller et al., 2004; Schaller and Ehlers, 2006; Schaller et al., 2002; Wittmann et al., 2010), between times of fold planation and fold incision using cosmogenic nuclide dating is the subject of ongoing work by the authors.

6 Conclusions

Despite rapid rock-uplift rates of 1-3 mm/y, actively uplifting folds in the foreland of the Tian Shan have been efficiently and extensively beveled by antecedent rivers at least in the past 100 ky. In striking contrast, modern rivers incise narrow canyons into the uplifting structures. The kilometer-wide lateral extent of the planation surfaces and rapid rock-uplift rates of the folds imply that, during > 2- to 6-ky-long episodes of active planation of the folds, lateral bedrock erosion rates were at least 200-600 mm/y: rates 70 to 600 times higher than the average vertical incision rates. These estimates are minima and planation rates could be as high as several meters per year. In contrast to these intervals of rapid lateral

beveling, order-of-magnitude decreases in these rates are required to explain the formation of the relatively narrow bedrock canyons that dominate today. Given the relative paucity of ages of these planation surfaces, a link of the intermittent periods of planation and incision to climatic cycles is unclear, but we hypothesize that local changes in water and sediment fluxes or the frequency of flooding events control the occurrence of beveling episodes. We contend that changes in rates of lateral erosion by rivers, as opposed to changes in their vertical incision rates, are the primary controlling factor in the formation of fluvial planation surfaces in the foreland of the Tian Shan (Fig. 17). It is likely that variations in lateral channel mobilities are important in controlling strath-terrace formation in other areas – especially those with readily eroded bedrock.

References

Abdrakhmatov, K. Y., Aldazhanov, S. A., Hager, B. H., Hamburger, M. W., Herring, T. A., Kalabaev, K. B., Makarov, V. I., Molnar, P., Panasyuk, S. V., Prilepin, M. T., Reilinger, R. E., Sadybakasov, I. S., Souter, B. J., Trapeznikov, Y. A., Tsurkov, V. Y., and Zubovich, A. V., 1996, Relatively recent construction of the Tien Shan inferred from GPS measurements of present-day crustal deformation rates: Nature, v. 384, no. 6608, p. 450-453.

Allen, G. H., Barnes, J. B., Pavelsky, T. M., and Kirby, E., 2013, Lithologic and tectonic controls on bedrock channel form at the northwest Himalayan front: Journal of Geophysical Research: Earth Surface, v. 118, no. 3, p. 1806-1825.

Amos, C. B., Burbank, D. W., Nobes, D. C., and Read, S. A. L., 2007, Geomorphic constraints on listric thrust faulting: Implications for active deformation in the Mackenzie Basin, South Island, New Zealand: Journal of Geophysical Research: Solid Earth, v. 112, no. B3, p. B03S11.

Anderson, R. S., Repka, J. L., and Dick, G. S., 1996, Explicit treatment of inheritance in dating depositional surfaces using in situ 10Be and 26Al: Geology, v. 24, no. 1, p. 47-51.

Anton, L., Mather, A. E., Stokes, M., Munoz-Martin, A., and De Vicente, G., 2015, Exceptional river gorge formation from unexceptional floods: Nature Communications, v. 6.

Arnold, L. J., Bailey, R. M., and Tucker, G. E., 2007, Statistical treatment of fluvial dose distributions from southern Colorado arroyo deposits: Quaternary Geochronology, v. 2, no. 1–4, p. 162-167.

Ashworth, P. J., Best, J. L., and Jones, M., 2004, Relationship between sediment supply and avulsion frequency in braided rivers: Geology, v. 32, no. 1, p. 21-24.

Bailey, R. M., and Arnold, L. J., 2006, Statistical modelling of single grain quartz De distributions and an assessment of procedures for estimating burial dose: Quaternary Science Reviews, v. 25, no. 19–20, p. 2475-2502.

Balco, G., Stone, J. O., Lifton, N. A., and Dunai, T. J., 2008, A complete and easily accessible means of calculating surface exposure ages or erosion rates from 10Be and 26Al measurements: Quaternary Geochronology, v. 3, no. 3, p. 174-195.

Bazhenov, M. L., Collins, A. Q., Degtyarev, K. E., Levashova, N. M., Mikolaichuk, A. V., Pavlov, V. E., and Van der Voo, R., 2003, Paleozoic northward drift of the North Tien Shan (Central Asia) as revealed by Ordovician and Carboniferous paleomagnetism: Tectonophysics, v. 366, no. 1–2, p. 113-141.

Bookhagen, B., Fleitmann, D., Nishiizumi, K., Strecker, M. R., and Thiede, R. C., 2006, Holocene monsoonal dynamics and fluvial terrace formation in the northwest Himalaya, India: Geology, v. 34, no. 7, p. 601-604.

Bookhagen, B., and Strecker, M. R., 2012, Spatiotemporal trends in erosion rates across a pronounced rainfall gradient: Examples from the southern Central Andes: Earth and Planetary Science Letters, v. 327–328, p. 97-110.

Bryant, M., Falk, P., and Paola, C., 1995, Experimental study of avulsion frequency and rate of deposition: Geology, v. 23, no. 4, p. 365-368.

Bufe, A., Paola, C., and Burbank, D. W., 2016, Fluvial bevelling of topography controlled by lateral channel mobility and uplift rate: Nature Geoscience, v. 9, no. 9, p. 706-710.
Bull, W. B., 1990, Stream-terrace genesis: implications for soil development: Geomorphology, v. 3, no. 3–4, p. 351-367.
Burbank, D. W., Leland, J., Fielding, E., Anderson, R. S., Brozovic, N., Reid, M. R., and Duncan, C., 1996, Bedrock incision, rock uplift and threshold hillslopes in the northwestern Himalayas: Nature, v. 379, no. 6565, p. 505-510.
Calvet, M., Gunnell, Y., and Farines, B., 2015, Flat-topped mountain ranges: Their global distribution and value for understanding the evolution of mountain topography: Geomorphology, v. 241, p. 255-291.
Carroll, A. R., Graham, S. A., Hendrix, M. S., Ying, D., and Zhou, D., 1995, Late Paleozoic tectonic amalgamation of northwestern China: Sedimentary record of the northern Tarim, northwestern Turpan, and southern Junggar Basins: Geological Society of America Bulletin, v. 107, no. 5, p. 571-594.
Castillo, M., Bishop, P., and Jansen, J. D., 2013, Knickpoint retreat and transient bedrock channel morphology triggered by base-level fall in small bedrock river catchments: The case of the Isle of Jura, Scotland: Geomorphology, v. 180, no. 0, p. 1-9.
Cazanacli, D., Paola, C., and Parker, G., 2002, Experimental steep, braided flow: application to flooding risk on fans: Journal of Hydraulic Engineering, v. 128, no. 3, p. 322-330.
Charreau, J., Gumiaux, C., Avouac, J.-P., Augier, R., Chen, Y., Barrier, L., Gilder, S., Dominguez, S., Charles, N., and Wang, Q., 2009, The Neogene Xiyu Formation, a diachronous prograding gravel wedge at front of the Tianshan: Climatic and tectonic implications: Earth and Planetary Science Letters, v. 287, no. 3–4, p. 298-310.
Chen, J., Burbank, D. W., Scharer, K. M., Sobel, E., Yin, J., Rubin, C., and Zhao, R., 2002, Magnetochronology of the Upper Cenozoic strata in the Southwestern Chinese Tian Shan: rates of Pleistocene folding and thrusting: Earth and Planetary Science Letters, v. 195, no. 1–2, p. 113-130.
Chen, J., Heermance, R., Burbank, D. W., Scharer, K. M., Miao, J., and Wang, C., 2007, Quantification of growth and lateral propagation of the Kashi anticline, southwest Chinese Tian Shan: Journal of Geophysical Research: Solid Earth, v. 112, no. B3, p. B03S16.
Collins, B. D., Montgomery, D. R., Schanz, S. A., and Larsen, I. J., 2016, Rates and mechanisms of bedrock incision and strath terrace formation in a forested catchment, Cascade Range, Washington: Geological Society of America Bulletin, v. 128, no. 5-6, p. 926-943.
Constantine, J. A., Dunne, T., Ahmed, J., Legleiter, C., and Lazarus, E. D., 2014, Sediment supply as a driver of river meandering and floodplain evolution in the Amazon Basin: Nature Geoscience, v. 7, no. 12, p. 899-903.
Cook, K. L., Turowski, J. M., and Hovius, N., 2013, A demonstration of the importance of bedload transport for fluvial bedrock erosion and knickpoint propagation: Earth Surface Processes and Landforms, v. 38, no. 7, p. 683-695.
-, 2014, River gorge eradication by downstream sweep erosion: Nature Geoscience, v. 7, no. 9, p. 682-686.
Coutand, I., Strecker, M. R., Arrowsmith, J. R., Hilley, G., Thiede, R. C., Korjenkov, A., and Omuraliev, M., 2002, Late Cenozoic tectonic development of the intramontane

Alai Valley, (Pamir-Tien Shan region, central Asia): An example of intracontinental deformation due to the Indo-Eurasia collision: Tectonics, v. 21, no. 6, p. 1053.
Davis, M., Matmon, A., Rood, D. H., and Avnaim-Katav, S., 2012, Constant cosmogenic nuclide concentrations in sand supplied from the Nile River over the past 2.5 m.y: Geology, v. 40, no. 4, p. 359-362.
Davis, W. M., 1902, Baselevel, Grade and Peneplain: The Journal of Geology, v. 10, no. 1, p. 77-111.
DeVecchio, D. E., Heermance, R. V., Fuchs, M., and Owen, L. A., 2012, Climate-controlled landscape evolution in the Western Transverse Ranges, California: Insights from Quaternary geochronology of the Saugus Formation and strath terrace flights: Lithosphere, v. 4, no. 2, p. 110-130.
Dey, S., Thiede, R. C., Schildgen, T. F., Wittmann, H., Bookhagen, B., Scherler, D., Jain, V., and Strecker, M. R., 2016, Climate-driven sediment aggradation and incision since the late Pleistocene in the NW Himalaya, India: Earth and Planetary Science Letters, v. 449, p. 321-331.
DiBiase, R. A., and Whipple, K. X., 2011, The influence of erosion thresholds and runoff variability on the relationships among topography, climate, and erosion rate: Journal of Geophysical Research: Earth Surface, v. 116, no. F4, p. F04036.
Dietrich, W. E., Bellugi, D. G., Sklar, L. S., Stock, J. D., Heimsath, A. M., and Roering, J. J., 2003, Geomorphic Transport Laws for Predicting Landscape form and Dynamics, Prediction in Geomorphology, American Geophysical Union, p. 103-132.
Dietrich, W. E., Kirchner, J. W., Ikeda, H., and Iseya, F., 1989, Sediment supply and the development of the coarse surface layer in gravel-bedded rivers: Nature, v. 340, no. 6230, p. 215-217.
Douglass, J., and Schmeeckle, M., 2007, Analogue modeling of transverse drainage mechanisms: Geomorphology, v. 84, no. 1–2, p. 22-43.
Finnegan, N. J., and Balco, G., 2013, Sediment supply, base level, braiding, and bedrock river terrace formation: Arroyo Seco, California, USA: Geological Society of America Bulletin, v. 125, no. 7-8, p. 1114-1124.
Finnegan, N. J., and Dietrich, W. E., 2011, Episodic bedrock strath terrace formation due to meander migration and cutoff: Geology, v. 39, no. 2, p. 143-146.
Formento-Trigilio, M. L., Burbank, D. W., Nicol, A., Shulmeister, J., and Rieser, U., 2003, River response to an active fold-and-thrust belt in a convergent margin setting, North Island, New Zealand: Geomorphology, v. 49, no. 1–2, p. 125-152.
Fuller, T. K., Gran, K. B., Sklar, L. S., and Paola, C., 2016, Lateral erosion in an experimental bedrock channel: the influence of bed roughness on erosion by bed-load impacts: Journal of Geophysical Research: Earth Surface, v. 121, p. 1084-1105.
Fuller, T. K., Perg, L. A., Willenbring, J. K., and Lepper, K., 2009, Field evidence for climate-driven changes in sediment supply leading to strath terrace formation: Geology, v. 37, no. 5, p. 467-470.
Galbraith, R. F., and Roberts, R. G., 2012, Statistical aspects of equivalent dose and error calculation and display in OSL dating: An overview and some recommendations: Quaternary Geochronology, v. 11, no. 0, p. 1-27.
Galbraith, R. F., Roberts, R. G., Laslett, G. M., Yoshida, H., and Olley, J. M., 1999, Optical dating of single and multiple grains of quartz from Jinmium Rock Shelter, northern

Australia: Part I, experimental design and statistical models: Archaeometry, v. 41, no. 2, p. 339-364.
Gilbert, G. K., 1877, Report on the Geology of the Henry Mountains (Utah), Government Printing Office, v. 2029.
Gosse, J. C., and Phillips, F. M., 2001, Terrestrial in situ cosmogenic nuclides: theory and application: Quaternary Science Reviews, v. 20, no. 14, p. 1475-1560.
Grimaud, J. L., Paola, C., and Voller, V., 2016, Experimental migration of knickpoints: influence of style of base-level fall and bed lithology: Earth Surface Dynamics, v. 4, no. 1, p. 11-23.
Hack, J. T., 1957, Studies of longitudinal stream profiles in Virginia and Maryland, 294B.
Hancock, G. S., and Anderson, R. S., 2002, Numerical modeling of fluvial strath-terrace formation in response to oscillating climate: Geological Society of America Bulletin, v. 114, no. 9, p. 1131-1142.
Hancock, G. S., Anderson, R. S., Chadwick, O. A., and Finkel, R. C., 1999, Dating fluvial terraces with 10Be and 26Al profiles: application to the Wind River, Wyoming: Geomorphology, v. 27, no. 1–2, p. 41-60.
Hanson, P. R., Mason, J. A., and Goble, R. J., 2006, Fluvial terrace formation along Wyoming's Laramie Range as a response to increased late Pleistocene flood magnitudes: Geomorphology, v. 76, no. 1–2, p. 12-25.
Heermance, R. V., Chen, J., Burbank, D. W., and Miao, J., 2008, Temporal constraints and pulsed Late Cenozoic deformation during the structural disruption of the active Kashi foreland, northwest China: Tectonics, v. 27, no. 6, p. TC6012.
Heermance, R. V., Chen, J., Burbank, D. W., and Wang, C., 2007, Chronology and tectonic controls of Late Tertiary deposition in the southwestern Tian Shan foreland, NW China: Basin Research, v. 19, no. 4, p. 599-632.
Hendrix, M. S., Graham, S. A., Carroll, A. R., Sobel, E. R., Mcknight, C. L., Schulein, B. J., and Wang, Z. X., 1992, Sedimentary Record and Climatic Implications of Recurrent Deformation in the Tian-Shan - Evidence from Mesozoic Strata of the North Tarim, South Junggar, and Turpan Basins, Northwest China: Geological Society of America Bulletin, v. 104, no. 1, p. 53-79.
Hidy, A. J., Gosse, J. C., Blum, M. D., and Gibling, M. R., 2014, Glacial–interglacial variation in denudation rates from interior Texas, USA, established with cosmogenic nuclides: Earth and Planetary Science Letters, v. 390, no. 0, p. 209-221.
Hidy, A. J., Gosse, J. C., Pederson, J. L., Mattern, J. P., and Finkel, R. C., 2010, A geologically constrained Monte Carlo approach to modeling exposure ages from profiles of cosmogenic nuclides: An example from Lees Ferry, Arizona: Geochemistry, Geophysics, Geosystems, v. 11, no. 9.
Jansen, J. D., Fabel, D., Bishop, P., Xu, S., Schnabel, C., and Codilean, A. T., 2011, Does decreasing paraglacial sediment supply slow knickpoint retreat?: Geology, v. 39, no. 6, p. 543-546.
Jarvis, A., Reuter, H. I., Nelson, A., and Guevara, E., 2008, Hole-filled SRTM for the globe Version 4: available from the CGIAR-CSI SRTM 90m Database (http://srtm.csi.cgiar.org).
Jerolmack, D. J., and Mohrig, D., 2007, Conditions for branching in depositional rivers: Geology, v. 35, no. 5, p. 463-466.

Johnson, J. P., and Whipple, K. X., 2007, Feedbacks between erosion and sediment transport in experimental bedrock channels: Earth Surface Processes and Landforms, v. 32, no. 7, p. 1048-1062.
Kenworthy, M. K., Rittenour, T. M., Pierce, J. L., Sutfin, N. A., and Sharp, W. D., 2014, Luminescence dating without sand lenses: An application of OSL to coarse-grained alluvial fan deposits of the Lost River Range, Idaho, USA: Quaternary Geochronology, v. 23, no. 0, p. 9-25.
Kim, W., Sheets, B. A., and Paola, C., 2010, Steering of experimental channels by lateral basin tilting: Basin Research, v. 22, no. 3, p. 286-301.
Kirby, E., and Whipple, K. X., 2012, Expression of active tectonics in erosional landscapes: Journal of Structural Geology, v. 44, no. 0, p. 54-75.
Kurth, G., Phillips, F. M., Reheis, M. C., Redwine, J. L., and Paces, J. B., 2011, Cosmogenic nuclide and uranium-series dating of old, high shorelines in the western Great Basin, USA: Geological Society of America Bulletin, v. 123, no. 3-4, p. 744-768.
Labourdette, R., and Jones, R. R., 2007, Characterization of fluvial architectural elements using a three-dimensional outcrop data set: Escanilla braided system, South-Central Pyrenees, Spain: Geosphere, v. 3, no. 6, p. 422-434.
Lague, D., 2014, The stream power river incision model: evidence, theory and beyond: Earth Surface Processes and Landforms, v. 39, no. 1, p. 38-61.
Lague, D., Crave, A., and Davy, P., 2003, Laboratory experiments simulating the geomorphic response to tectonic uplift: Journal of Geophysical Research: Solid Earth, v. 108, no. B1.
Langston, A. L., Tucker, G. E., and Anderson, R. S., 2015, Interpreting climate-modulated processes of terrace development along the Colorado Front Range using a landscape evolution model: Journal of Geophysical Research: Earth Surface, p. 2121–2138.
Lavé, J., and Avouac, J. P., 2001, Fluvial incision and tectonic uplift across the Himalayas of central Nepal: Journal of Geophysical Research: Solid Earth, v. 106, no. B11, p. 26561-26591.
Li, T., Chen, J., Thompson, J. A., Burbank, D. W., and Xiao, W., 2012, Equivalency of geologic and geodetic rates in contractional orogens: New insights from the Pamir Frontal Thrust: Geophysical Research Letters, v. 39, no. 15, p. L15305.
Li, T., Chen, J., Thompson, J. A., Burbank, D. W., and Yang, H., 2015a, Hinge-migrated fold-scarp model based on an analysis of bed geometry: A study from the Mingyaole anticline, southern foreland of Chinese Tian Shan: Journal of Geophysical Research: Solid Earth, v. 120, no. 9, p. 6592-6613.
Li, T., Chen, J., Thompson, J. A., Burbank, D. W., and Yang, X., 2013, Quantification of three-dimensional folding using fluvial terraces: A case study from the Mushi anticline, northern margin of the Chinese Pamir: Journal of Geophysical Research: Solid Earth, v. 118, no. 8, p. 4628-4647.
-, 2015b, Active flexural-slip faulting: a study from the Pamir-Tian Shan convergent zone, NW China: Journal of Geophysical Research: Solid Earth, p. 4359–4378.
Limaye, A. B. S., and Lamb, M. P., 2014, Numerical simulations of bedrock valley evolution by meandering rivers with variable bank material: Journal of Geophysical Research: Earth Surface, v. 119, no. 4, p. 927-950.

-, 2016, Numerical model predictions of autogenic fluvial terraces and comparison to climate change expectations: Journal of Geophysical Research: Earth Surface, v. 121, p. 512-544.
Lisiecki, L. E., and Raymo, M. E., 2005, A Pliocene-Pleistocene stack of 57 globally distributed benthic δ18O records: Paleoceanography, v. 20, no. 1, p. n/a-n/a.
Mackin, H. J., 1948, Concept of the Graded River: Geological Society of America Bulletin, v. 59, no. 5, p. 463-512.
Malatesta, L. C., Prancevic, J. P., and Avouac, J.-P., 2016, Autogenic entrenchment patterns and terraces due to coupling with lateral erosion in incising alluvial channels: Journal of Geophysical Research: Earth Surface.
McPhillips, D., Bierman, P. R., Crocker, T., and Rood, D. H., 2013, Landscape response to Pleistocene-Holocene precipitation change in the Western Cordillera, Peru: 10Be concentrations in modern sediments and terrace fills: Journal of Geophysical Research: Earth Surface, v. 118, no. 4, p. 2488–2499.
Merritts, D. J., Vincent, K. R., and Wohl, E. E., 1994, Long river profiles, tectonism, and eustasy: A guide to interpreting fluvial terraces: Journal of Geophysical Research: Solid Earth, v. 99, no. B7, p. 14031-14050.
Miall, A. D., 1977, A review of the braided-river depositional environment: Earth-Science Reviews, v. 13, no. 1, p. 1-62.
Molnar, P., Erik Thorson, B., Burchfiel, B. C., Deng, Q., Feng, X., Li, J., Raisbeck, G. M., Shi, J., Zhangming, W., Yiou, F., and You, H., 1994, Quaternary climate change and the formation of river terraces across growing anticlines on the north flank of the Tien Shan, China: The Journal of Geology, v. 102, no. 5, p. 583-602.
Molnar, P., and Tapponnier, P., 1975, Cenozoic Tectonics of Asia: Effects of a Continental Collision: Science, v. 189, no. 4201, p. 419-426.
Montgomery, D. R., 2004, Observations on the role of lithology in strath terrace formation and bedrock channel width: American Journal of Science, v. 304, no. 5, p. 454-476.
Montgomery, D. R., Panfil, M. S., and Hayes, S. K., 1999, Channel-bed mobility response to extreme sediment loading at Mount Pinatubo: Geology, v. 27, no. 3, p. 271-274.
Murray, A. S., and Wintle, A. G., 2000, Luminescence dating of quartz using an improved single-aliquot regenerative-dose protocol: Radiation Measurements, v. 32, no. 1, p. 57-73.
Olley, J., Caitcheon, G., and Murray, A., 1998, The distribution of apparent dose as determined by Optically Stimulated Luminescence in small aliquots of fluvial quartz: Implications for dating young sediments: Quaternary Science Reviews, v. 17, no. 11, p. 1033-1040.
Olley, J. M., Caitcheon, G. G., and Roberts, R. G., 1999, The origin of dose distributions in fluvial sediments, and the prospect of dating single grains from fluvial deposits using optically stimulated luminescence: Radiation Measurements, v. 30, no. 2, p. 207-217.
Olley, J. M., Pietsch, T., and Roberts, R. G., 2004, Optical dating of Holocene sediments from a variety of geomorphic settings using single grains of quartz: Geomorphology, v. 60, no. 3–4, p. 337-358.
Pan, B., Burbank, D., Wang, Y., Wu, G., Li, J., and Guan, Q., 2003, A 900 k.y. record of strath terrace formation during glacial-interglacial transitions in northwest China: Geology, v. 31, no. 11, p. 957-960.

Parker, G., 1978, Self-formed straight rivers with equilibrium banks and mobile bed. Part 2. The gravel river: Journal of Fluid Mechanics, v. 89, no. 01, p. 127-146.
Parker, G., Wilcock, P. R., Paola, C., Dietrich, W. E., and Pitlick, J., 2007, Physical basis for quasi-universal relations describing bankfull hydraulic geometry of single-thread gravel bed rivers: Journal of Geophysical Research: Earth Surface, v. 112, no. F4, p. F04005.
Pazzaglia, F. J., and Brandon, M. T., 2001, A Fluvial Record of Long-term Steady-state Uplift and Erosion Across the Cascadia Forearc High, Western Washington State: American Journal of Science, v. 301, no. 4-5, p. 385-431.
Pazzaglia, F. J., and Gardner, T. W., 1993, Fluvial terraces of the lower Susquehanna River: Geomorphology, v. 8, no. 2–3, p. 83-113.
Pazzaglia, F. J., Gardner, T. W., and Merritts, D. J., 1998, Bedrock Fluvial Incision and Longitudinal Profile Development Over Geologic Time Scales Determined by Fluvial Terraces, Rivers Over Rock: Fluvial Processes in Bedrock Channels, American Geophysical Union, p. 207-235.
Petit, J. R., Jouzel, J., Raynaud, D., Barkov, N. I., Barnola, J. M., Basile, I., Bender, M., Chappellaz, J., Davis, M., Delaygue, G., Delmotte, M., Kotlyakov, V. M., Legrand, M., Lipenkov, V. Y., Lorius, C., Pepin, L., Ritz, C., Saltzman, E., and Stievenard, M., 1999, Climate and atmospheric history of the past 420,000 years from the Vostok ice core, Antarctica: Nature, v. 399, no. 6735, p. 429-436.
Phillips, C. B., and Jerolmack, D. J., 2016, Self-organization of river channels as a critical filter on climate signals: Science, v. 352, no. 6286, p. 694-697.
Pratt-Sitaula, B., Burbank, D. W., Heimsath, A., and Ojha, T., 2004, Landscape disequilibrium on 1000–10,000 year scales Marsyandi River, Nepal, central Himalaya: Geomorphology, v. 58, no. 1–4, p. 223-241.
Repka, J. L., Anderson, R. S., and Finkel, R. C., 1997, Cosmogenic dating of fluvial terraces, Fremont River, Utah: Earth and Planetary Science Letters, v. 152, no. 1–4, p. 59-73.
Rhodes, E. J., 2011, Optically Stimulated Luminescence Dating of Sediments over the Past 200,000 Years: Annual Review of Earth and Planetary Sciences, v. 39, no. 1, p. 461-488.
Rittenour, T. M., 2008, Luminescence dating of fluvial deposits: applications to geomorphic, palaeoseismic and archaeological research: Boreas, v. 37, no. 4, p. 613-635.
Römer, W., 2010, Multiple planation surfaces in basement regions: Implications for the reconstruction of periods of denudation and uplift in southern Zimbabwe: Geomorphology, v. 114, no. 3, p. 199-212.
Schaller, M., Blanckenburg, F. v., Hovius, N., Veldkamp, A., van den Berg, Meindert W., and Kubik, P. W., 2004, Paleoerosion Rates from Cosmogenic10Be in a 1.3 Ma Terrace Sequence: Response of the River Meuse to Changes in Climate and Rock Uplift: The Journal of Geology, v. 112, no. 2, p. 127-144.
Schaller, M., and Ehlers, T. A., 2006, Limits to quantifying climate driven changes in denudation rates with cosmogenic radionuclides: Earth and Planetary Science Letters, v. 248, no. 1–2, p. 153-167.
Schaller, M., von Blanckenburg, F., Veldkamp, A., Tebbens, L. A., Hovius, N., and Kubik, P. W., 2002, A 30 000 yr record of erosion rates from cosmogenic 10Be in Middle

European river terraces: Earth and Planetary Science Letters, v. 204, no. 1–2, p. 307-320.
Schanz, S. A., and Montgomery, D. R., 2016, Lithologic controls on valley width and strath terrace formation: Geomorphology, v. 258, p. 58-68.
Scharer, K. M., Burbank, D. W., Chen, J., and Weldon, R. J., 2006, Kinematic models of fluvial terraces over active detachment folds: Constraints on the growth mechanism of the Kashi-Atushi fold system, Chinese Tian Shan: Geological Society of America Bulletin, v. 118, no. 7-8, p. 1006-1021.
Scharer, K. M., Burbank, D. W., Chen, J., Weldon, R. J., Rubin, C., Zhao, R., and Shen, J., 2004, Detachment folding in the Southwestern Tian Shan–Tarim foreland, China: shortening estimates and rates: Journal of Structural Geology, v. 26, no. 11, p. 2119-2137.
Schildgen, T. F., Robinson, R. A. J., Savi, S., Phillips, W. M., Spencer, J. Q. G., Bookhagen, B., Scherler, D., Tofelde, S., Alonso, R. N., Kubik, P. W., Binnie, S. A., and Strecker, M. R., 2016, Landscape response to late Pleistocene climate change in NW Argentina: Sediment flux modulated by basin geometry and connectivity: Journal of Geophysical Research: Earth Surface, p. 392-414.
Sklar, L. S., and Dietrich, W. E., 2001, Sediment and rock strength controls on river incision into bedrock: Geology, v. 29, no. 12, p. 1087-1090.
-, 2004, A mechanistic model for river incision into bedrock by saltating bed load: Water Resources Research, v. 40, no. 6, p. W06301.
-, 2006, The role of sediment in controlling steady-state bedrock channel slope: Implications of the saltation–abrasion incision model: Geomorphology, v. 82, no. 1–2, p. 58-83.
Sobel, E. R., and Dumitru, T. A., 1997, Thrusting and exhumation around the margins of the western Tarim basin during the India-Asia collision: Journal of Geophysical Research: Solid Earth, v. 102, no. B3, p. 5043-5063.
Stroeven, A. P., Hättestrand, C., Heyman, J., Kleman, J., and Morén, B. M., 2013, Glacial geomorphology of the Tian Shan: Journal of Maps, v. 9, no. 4, p. 505-512.
Thompson, J. A., Chen, J., Yang, H., Li, T., Bookhagen, B., and Burbank, D. W., in review, Coarse- versus fine-grain OSL and cosmogenic 10Be dating of deformed fluvial terraces on the northeast Pamir margin, northwest China: Quaternary Geochronology.
Turowski, J. M., Hovius, N., Meng-Long, H., Lague, D., and Men-Chiang, C., 2008, Distribution of erosion across bedrock channels: Earth Surface Processes and Landforms, v. 33, no. 3, p. 353-363.
Turowski, J. M., Lague, D., Crave, A., and Hovius, N., 2006, Experimental channel response to tectonic uplift: Journal of Geophysical Research: Earth Surface, v. 111, no. F3, p. F03008.
Turowski, J. M., Lague, D., and Hovius, N., 2007, Cover effect in bedrock abrasion: A new derivation and its implications for the modeling of bedrock channel morphology: Journal of Geophysical Research: Earth Surface, v. 112, no. F4, p. F04006.
-, 2009, Response of bedrock channel width to tectonic forcing: Insights from a numerical model, theoretical considerations, and comparison with field data: Journal of Geophysical Research: Earth Surface, v. 114, no. F3, p. F03016.

Wegmann, K. W., and Pazzaglia, F. J., 2002, Holocene strath terraces, climate change, and active tectonics: The Clearwater River basin, Olympic Peninsula, Washington State: Geological Society of America Bulletin, v. 114, no. 6, p. 731-744.
Wells, S. G., McFadden, L. D., Poths, J., and Olinger, C. T., 1995, Cosmogenic 3He surface-exposure dating of stone pavements: Implications for landscape evolution in deserts: Geology, v. 23, no. 7, p. 613-616.
Whipple, K., Parker, G., Paola, C., and Mohrig, D., 1998, Channel Dynamics, Sediment Transport, and the Slope of Alluvial Fans: Experimental Study: The Journal of Geology, v. 106, no. 6, p. 677-694.
Whipple, K. X., and Tucker, G. E., 2002, Implications of sediment-flux-dependent river incision models for landscape evolution: Journal of Geophysical Research: Solid Earth, v. 107, no. B2, p. ETG 3-1-ETG 3-20.
Whittaker, A. C., Attal, M., and Allen, P. A., 2010, Characterising the origin, nature and fate of sediment exported from catchments perturbed by active tectonics: Basin Research, v. 22, no. 6, p. 809-828.
Whittaker, A. C., Duller, R. A., Springett, J., Smithells, R. A., Whitchurch, A. L., and Allen, P. A., 2011, Decoding downstream trends in stratigraphic grain size as a function of tectonic subsidence and sediment supply: Geological Society of America Bulletin, v. 123, no. 7-8, p. 1363-1382.
Wickert, A. D., Martin, J. M., Tal, M., Kim, W., Sheets, B., and Paola, C., 2013, River channel lateral mobility: metrics, time scales, and controls: Journal of Geophysical Research: Earth Surface, v. 118, no. 2, p. 396-412.
Wintle, A. G., and Murray, A. S., 2006, A review of quartz optically stimulated luminescence characteristics and their relevance in single-aliquot regeneration dating protocols: Radiation Measurements, v. 41, no. 4, p. 369-391.
Wittmann, H., von Blanckenburg, F., Maurice, L., Guyot, J.-L., Filizola, N., and Kubik, P. W., 2010, Sediment production and delivery in the Amazon River basin quantified by in situ—produced cosmogenic nuclides and recent river loads: Geological Society of America Bulletin.
Wobus, C. W., Tucker, G. E., and Anderson, R. S., 2006, Self-formed bedrock channels: Geophysical Research Letters, v. 33, no. 18, p. L18408.
Wolman, M. G., 1954, A method of sampling coarse river-bed material: Eos, Transactions American Geophysical Union, v. 35, no. 6, p. 951-956.
Yang, Q., Wei, W., and Li, J., 2008, Temporal and spatial variation of atmospheric water vapor in the Taklimakan Desert and its surrounding areas: Chinese Science Bulletin, v. 53, no. 2, p. 71-78.
Yang, X., and Scuderi, L. A., 2010, Hydrological and climatic changes in deserts of China since the late Pleistocene: Quaternary Research, v. 73, no. 1, p. 1-9.
Yanites, B. J., and Tucker, G. E., 2010, Controls and limits on bedrock channel geometry: Journal of Geophysical Research: Earth Surface, v. 115, no. F4, p. F04019.
Yanites, B. J., Tucker, G. E., Mueller, K. J., and Chen, Y.-G., 2010, How rivers react to large earthquakes: Evidence from central Taiwan: Geology, v. 38, no. 7, p. 639-642.
Yin, A., Nie, S., Craig, P., Harrison, T. M., Ryerson, F. J., Xianglin, Q., and Geng, Y., 1998, Late Cenozoic tectonic evolution of the southern Chinese Tian Shan: Tectonics, v. 17, no. 1, p. 1-27.

Zaprowski, B. J., Evenson, E. B., Pazzaglia, F. J., and Epstein, J. B., 2001, Knickzone propagation in the Black Hills and northern High Plains: A different perspective on the late Cenozoic exhumation of the Laramide Rocky Mountains: Geology, v. 29, no. 6, p. 547-550.

Zhang, P.-Z., Shen, Z., Wang, M., Gan, W., Bürgmann, R., Molnar, P., Wang, Q., Niu, Z., Sun, J., Wu, J., Hanrong, S., and Xinzhao, Y., 2004, Continuous deformation of the Tibetan Plateau from global positioning system data: Geology, v. 32, no. 9, p. 809-812.

Zubovich, A. V., Schöne, T., Metzger, S., Mosienko, O., Mukhamediev, S., Sharshebaev, A., and Zech, C., 2016, Tectonic interaction between the Pamir and Tien Shan observed by GPS: Tectonics, p. 283–292.

Zubovich, A. V., Wang, X.-q., Scherba, Y. G., Schelochkov, G. G., Reilinger, R., Reigber, C., Mosienko, O. I., Molnar, P., Michajljow, W., Makarov, V. I., Li, J., Kuzikov, S. I., Herring, T. A., Hamburger, M. W., Hager, B. H., Dang, Y.-m., Bragin, V. D., and Beisenbaev, R. T., 2010, GPS velocity field for the Tien Shan and surrounding regions: Tectonics, v. 29, no. 6, p. TC6014.

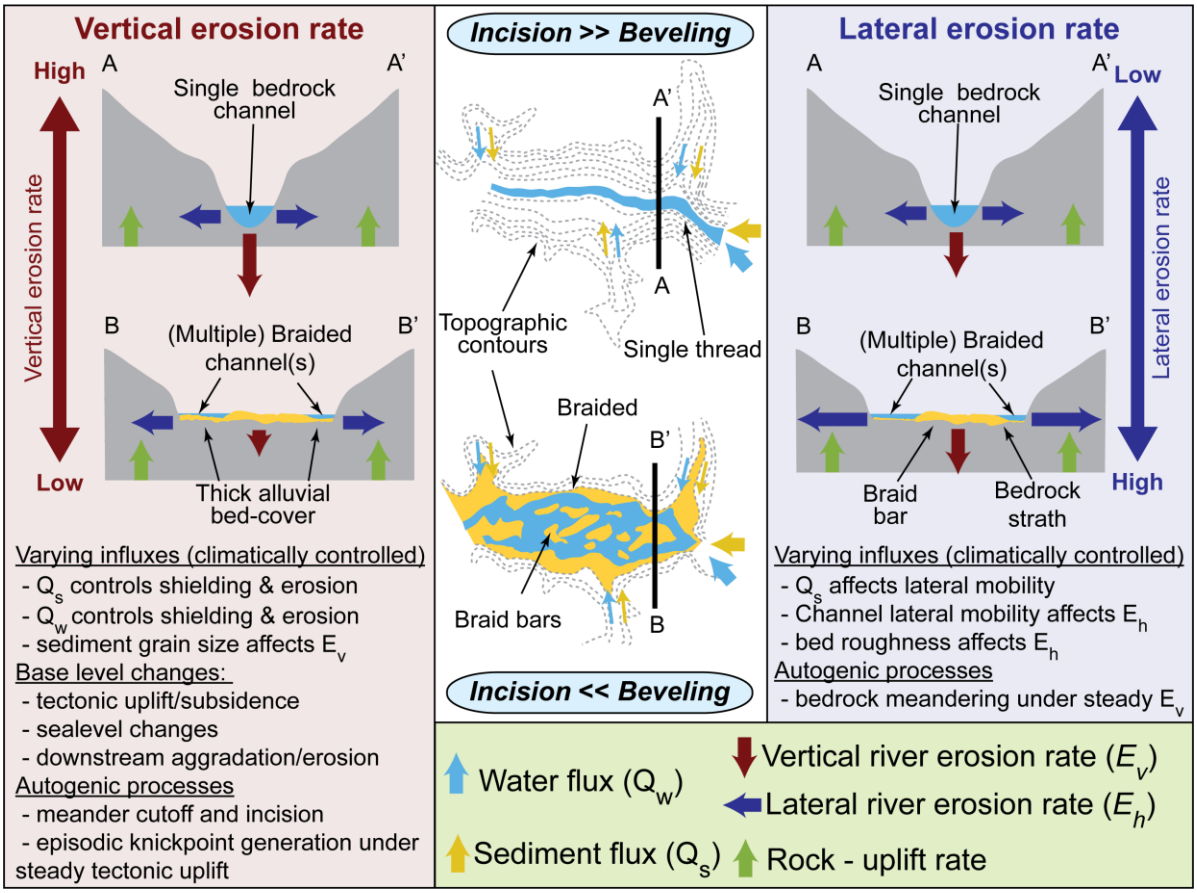

Figure 1: Conceptual sketch showing different planation surface formation models. Changes in the degree of planation can be caused by changing vertical erosion rates and/or changing lateral erosion rates. Different factors controlling lateral and vertical erosion rates are summarized below the sketches.

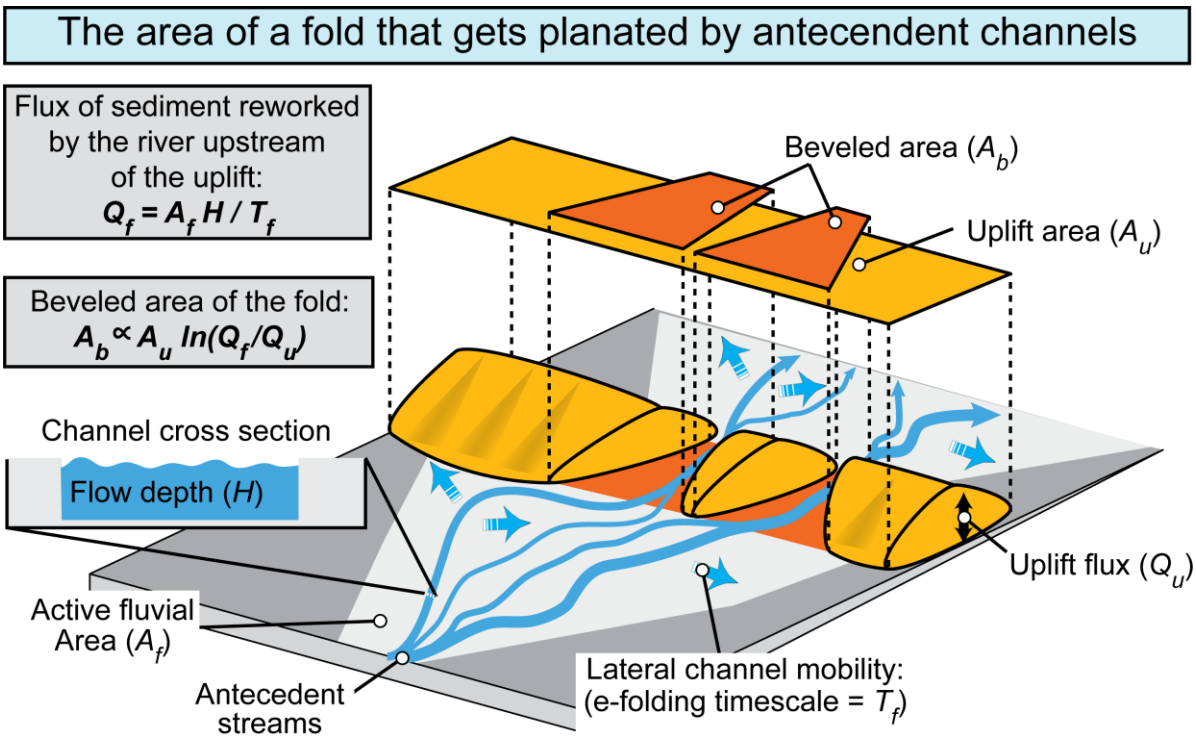

Figure 2: Conceptual sketch of the role of channel mobility in controlling the planation of a growing uplift by an alluvial river. The beveled area of the uplift can be predicted by a competition between the uplift flux (Q_u) and the flux of sediment that is reworked by an alluvial river unconfined by bedrock (Q_f) (Bufe et al., 2016).

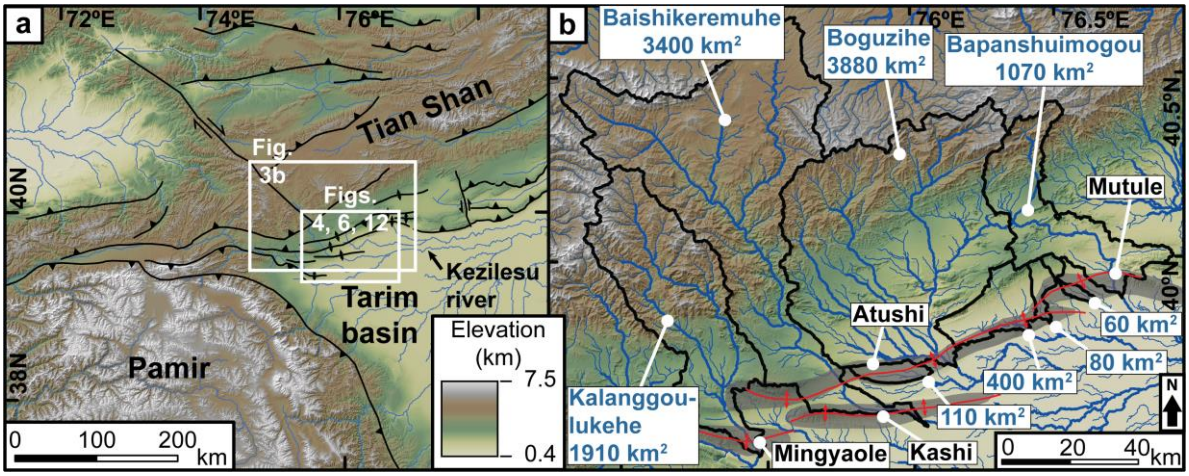

Figure 3: Topographic overview of the study area. **(**a) Inset showing the location of the study area and panels in Figs. 4, 6, and 12. (b) Watersheds of rivers draining across the studied folds in the foreland of the Tian Shan. Folds are shaded in grey and fold axes marked in red. Blue numbers denote the drainage areas of each catchment. Only major catchment names are given.

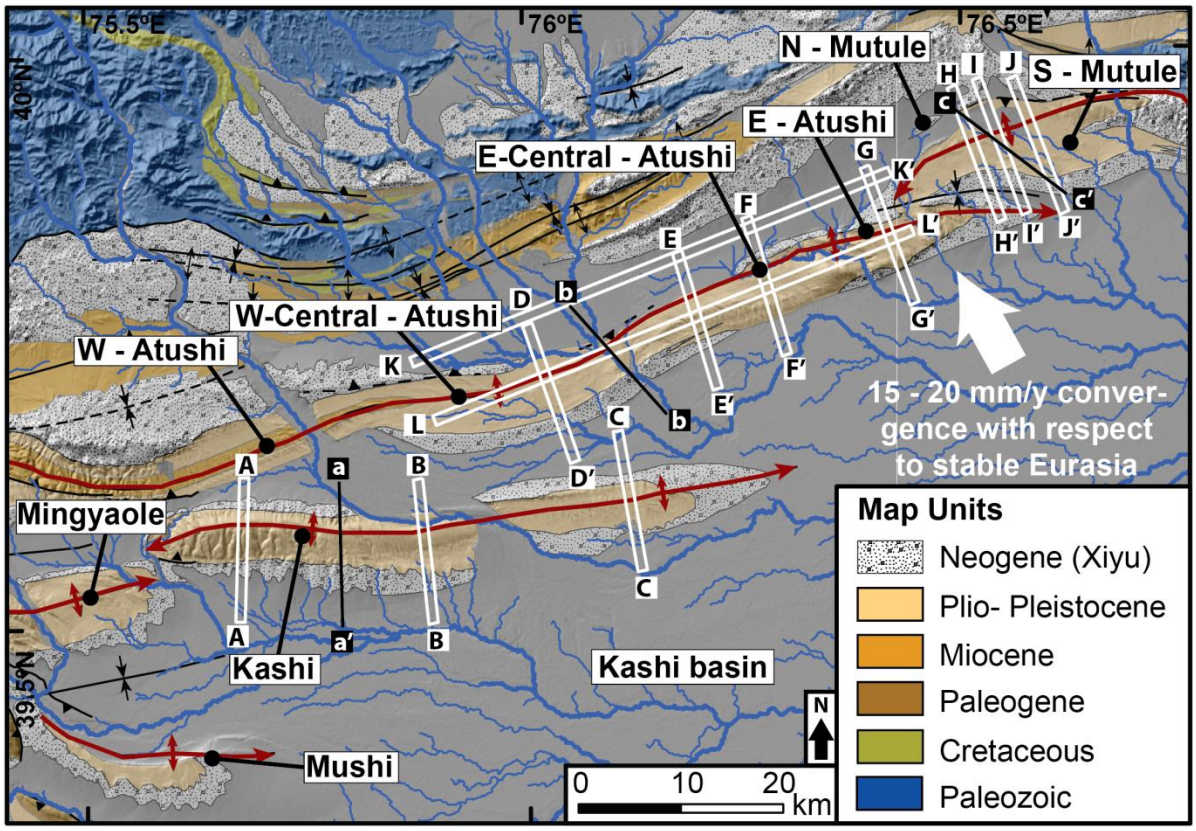

Figure 4: Simplified geologic map of the study area adapted from Heermance et al. (2007) and locations of profiles in Figs. 5 and 10.

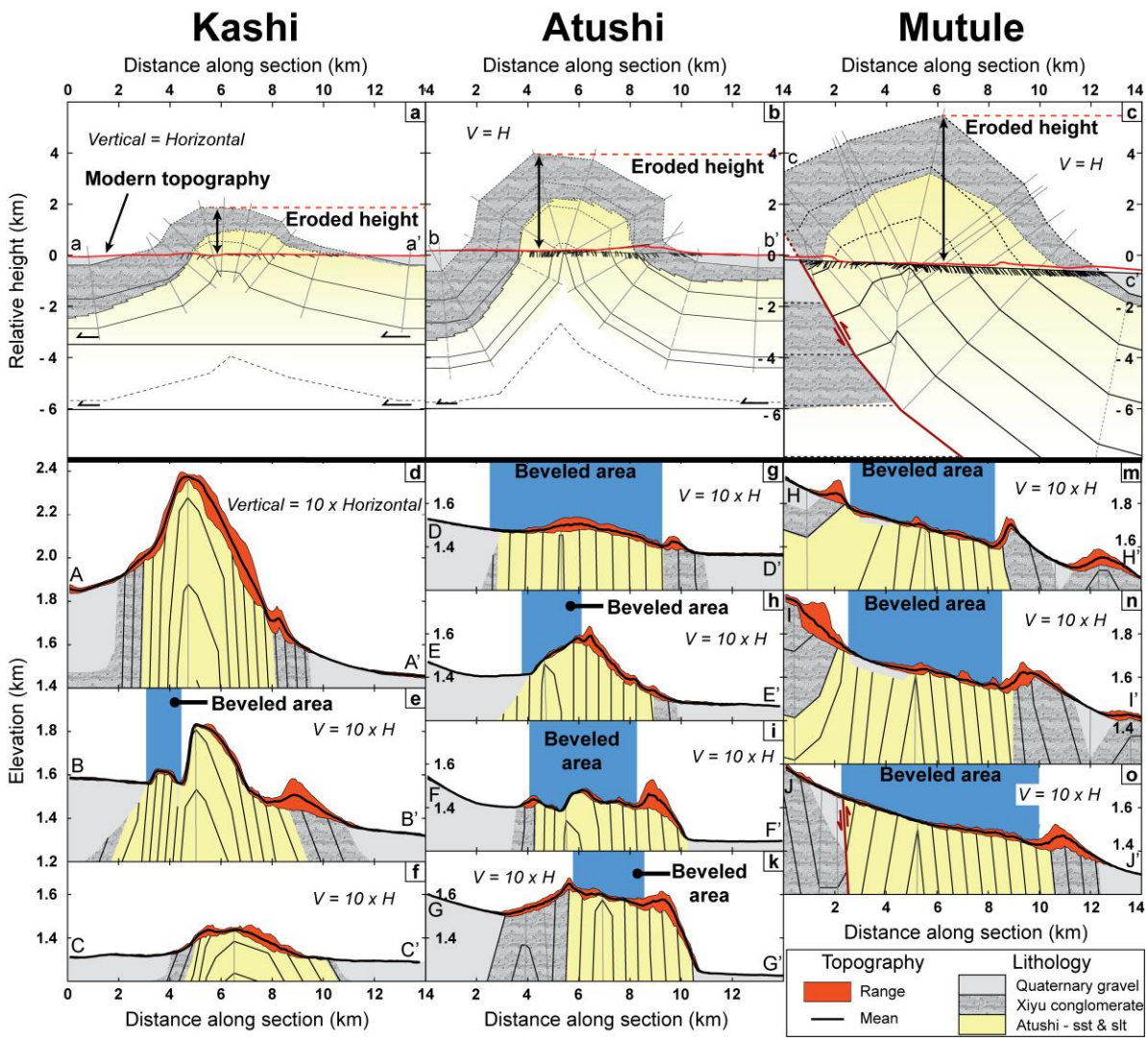

Figure 5: Profiles across the three folds in the study area. See Fig. 4 for profile locations. (a-c) Structure profiles (no vertical exaggeration) across all three folds from field mapping and analysis of seismic sections. (a-b) are adapted from (Scharer et al., 2006), (c) is from mapping by the authors (Fig. S1). (d-o) Swath profiles (1-km-wide) across Kashi, Atushi, and Mutule approximately perpendicular to the fold axes with 10-fold vertical exaggeration. The underlying lithology (colors), the bedding (thin black lines) and fold axes (thin grey lines) are sketched from published structural sections, maps close to the swath profiles (Heermance et al., 2007; Scharer et al., 2006), and mapping by the authors. Beveled surfaces are marked by blue bands.

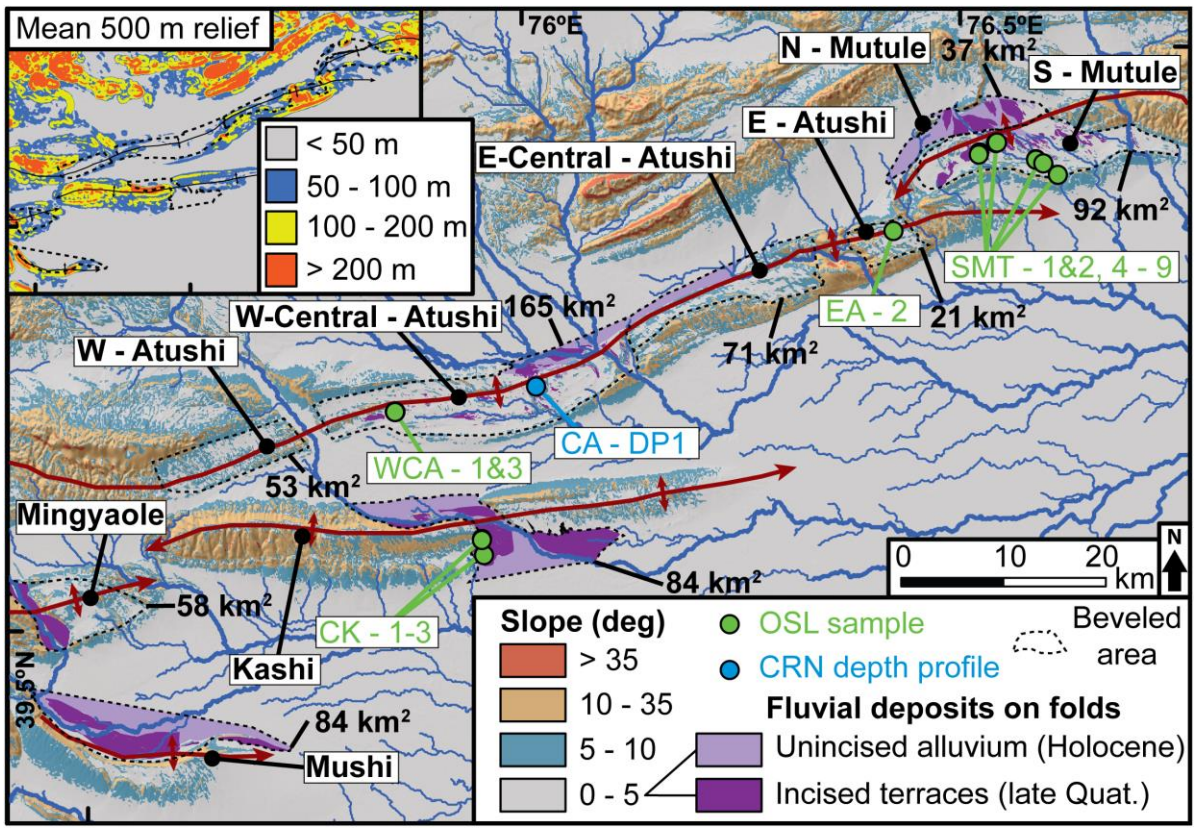

Figure 6: Map of mean slope and 500-m-radius relief across the study area calculated with the 90-m SRTM DEM. The extent of beveling (in km^2), as well as the distribution of Pleistocene and Holocene fluvial gravels across the folds, was mapped on Google Earth ® imagery and in the field. Upper surfaces of fluvial gravels have slopes << 5°, except where terrace risers or flexural-slip scarps disrupt the surface. Where fluvial gravels are absent, dissection creates a landscape of steep hills and gullies. Green and blue dots mark the location of optically stimulated luminescence (OSL) and cosmogenic radionuclide (CRN) samples; red lines mark axes of anticlines. Holocene (light purple) and Pleistocene (dark purple) gravels with slopes < 5° are shown on the folds. Other than on the folds, low-slope areas are largely formed by alluvial fans.

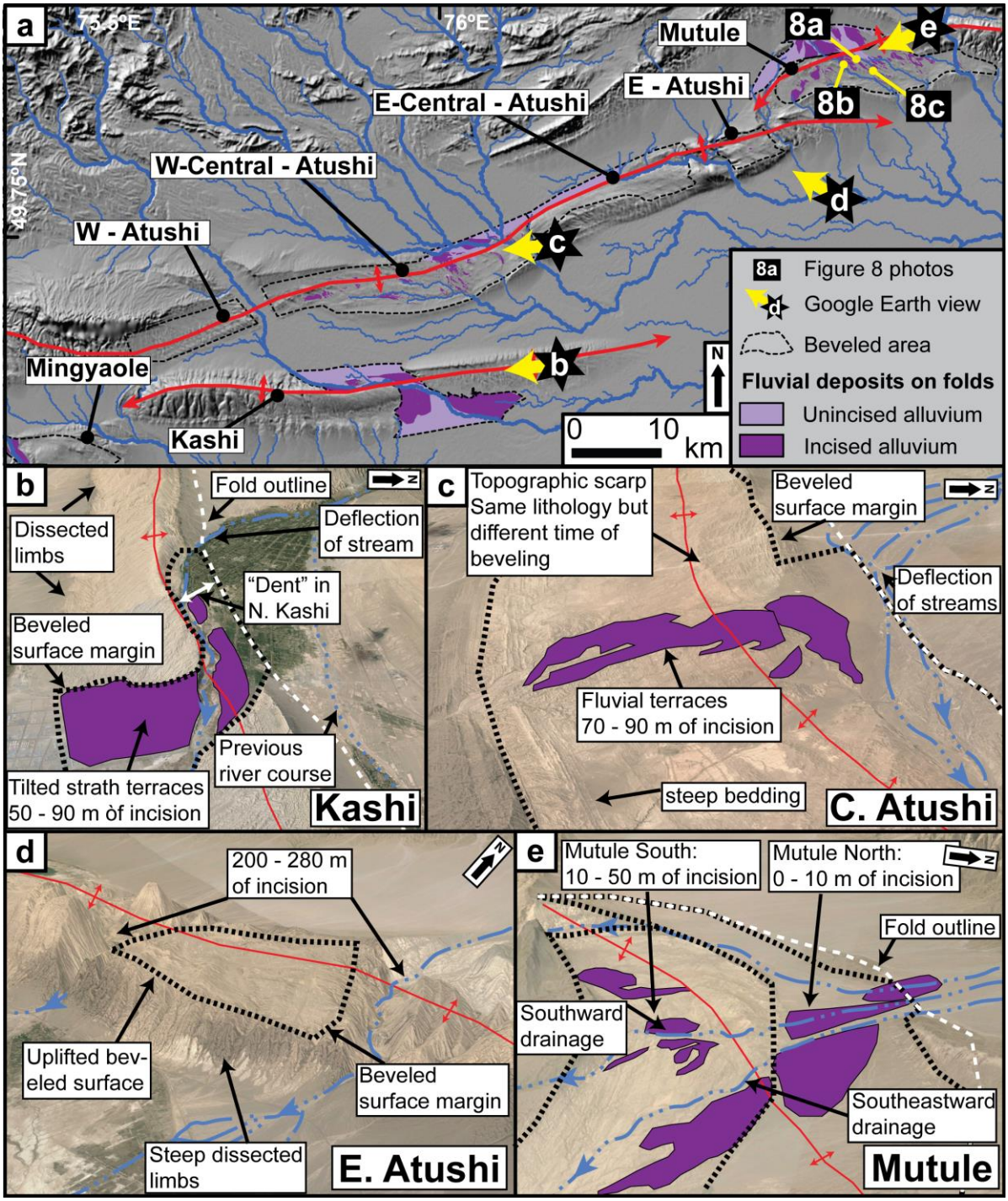

Figure 7: Google Earth views of the three studied folds. (a) Hillshade map showing the locations of panels b-e (black stars) and the photos in Fig. 8. Yellow arrows point in the direction of view. (b-d). Google Earth views of Kashi, Atushi and Mutule. Black dotted lines mark beveled areas, blue dash-dotted lines approximate locations of modern rivers, purple areas depict major incised (late Quaternary) gravels, red lines trace anticline axes, and white dashed lines outline the folds (only in b, c & e).

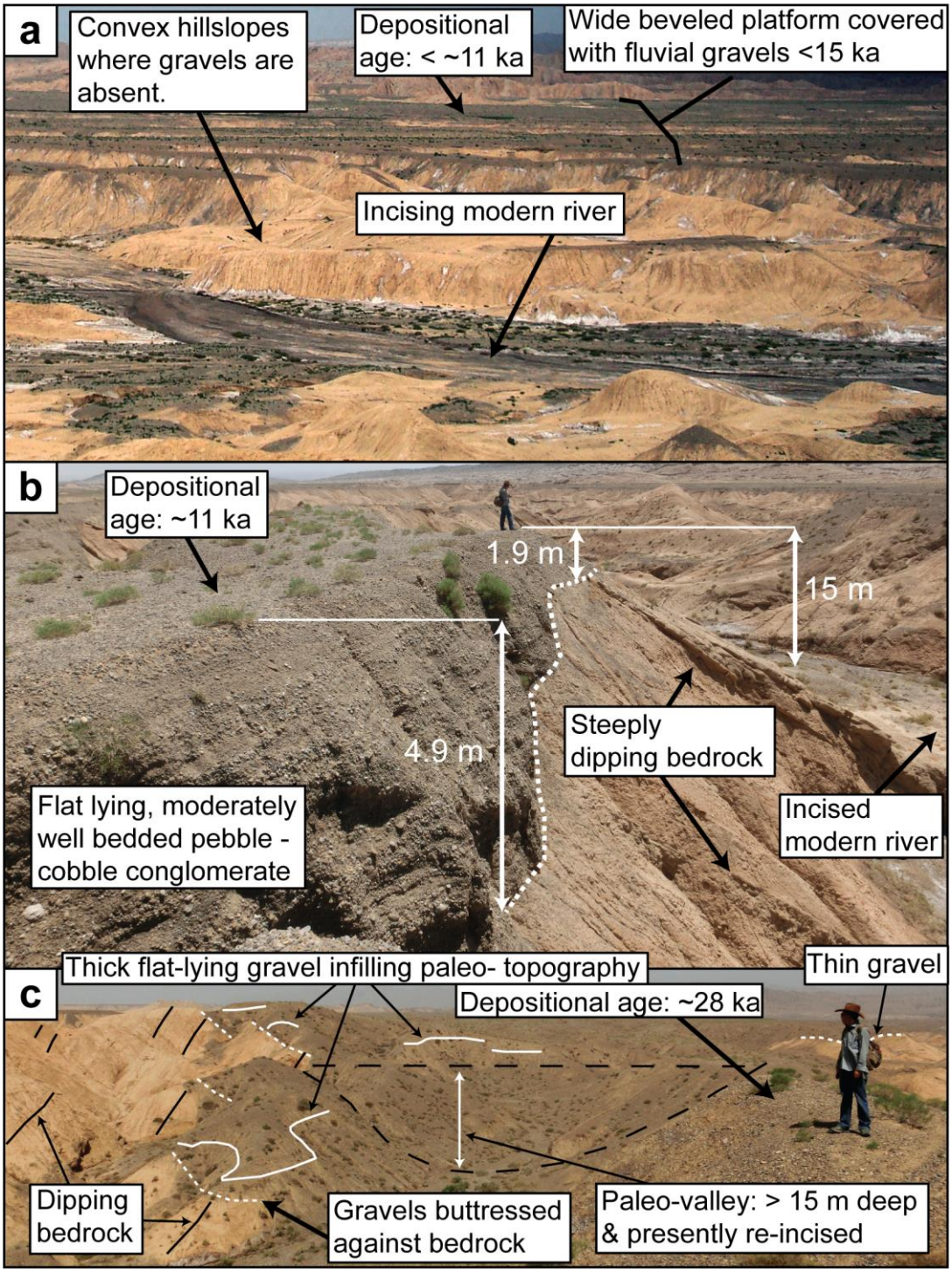

Figure 8: Field photographs of planation surfaces on Mutule. (a) Uplifted planation surfaces covered with fluvial deposits in the background and incising modern river in the foreground. Note the convex-up, steep hills that have been stripped bare of their fluvial cover. (b) Typical flat-lying gravel deposits with thicknesses of < 1-6 m and meter-scale thickness changes. (c) Anomalously thick, gravels buttressed against steeply dipping bedrock. See Fig. 7 for location of photographs.

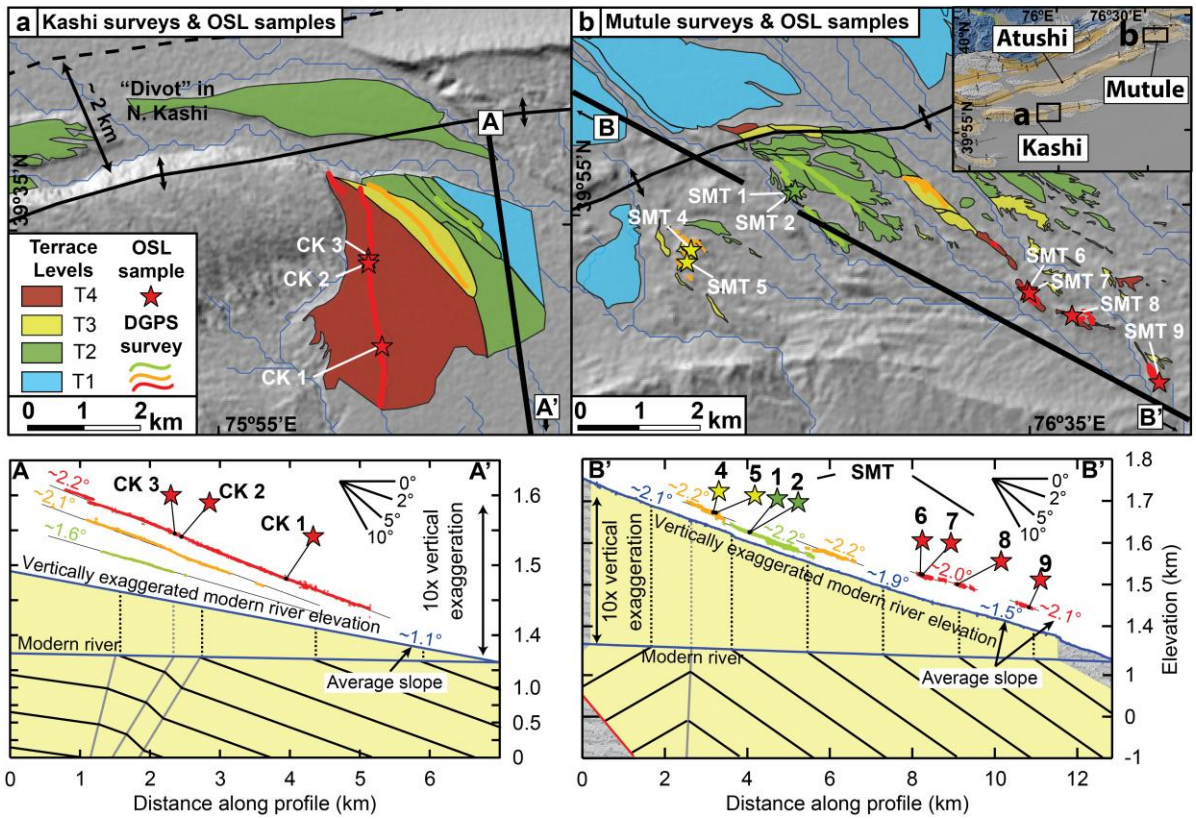

Figure 9: OSL sample locations, terrace surveys, and slopes on (a) central Kashi and (b) southern Mutule. The maps show terraces mapped using Google Earth ® and field mapping. Surveys of differential GPS are shown as bold lines. On the cross sections, the structure is simplified from sections shown in Figs. 4a-b. Results from differential GPS surveys are plotted with respect to the modern river and the locations of OSL samples are marked with stars. Note that the modern river profile on A-A' is obtained using a 90-m DEM, whereas the profile on B-B' was measured with a differential GPS.

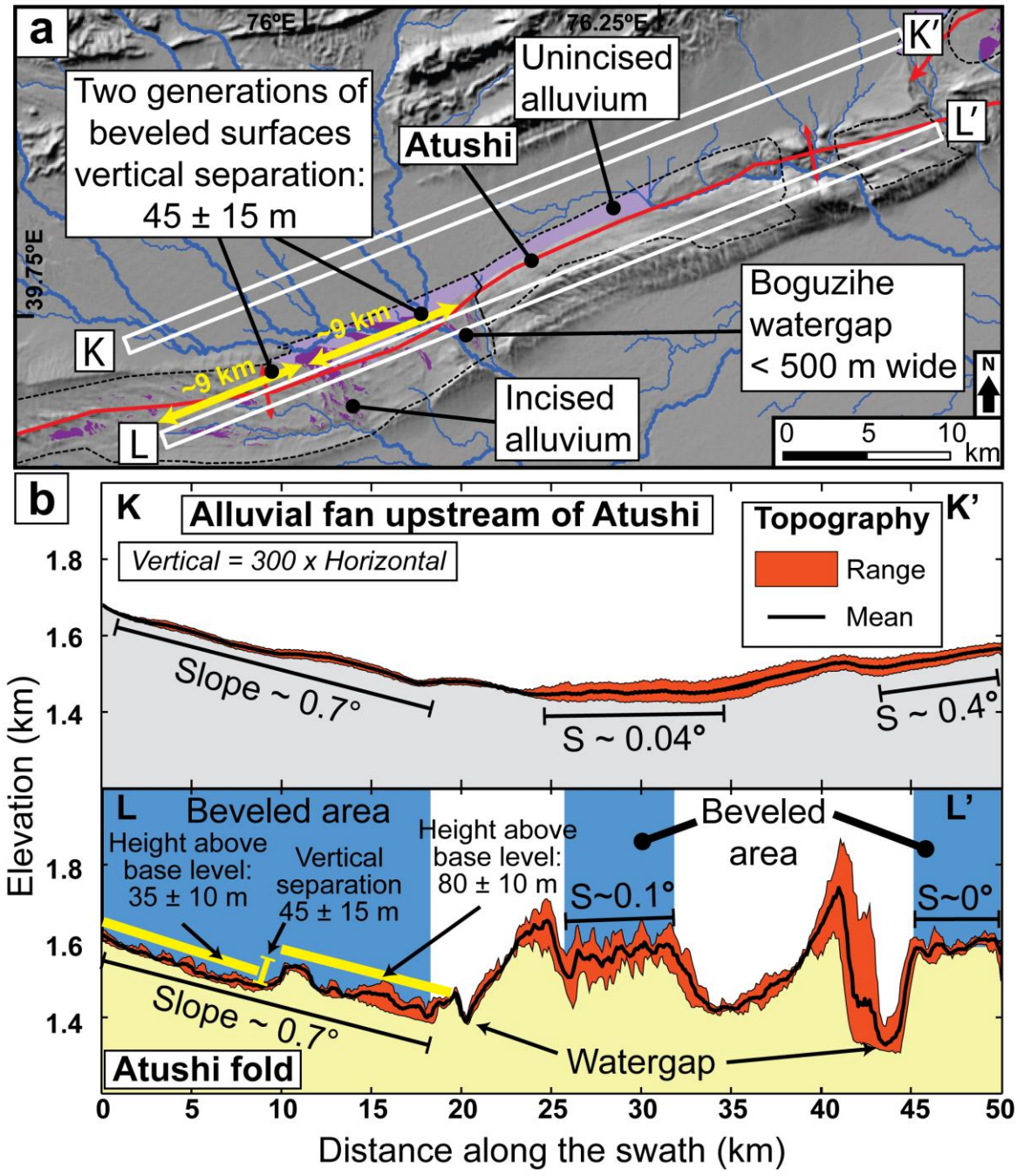

Figure 10: Comparison between the axis-parallel slope of the Atushi fold with that of the upstream alluvial fan. (a) Hillshade showing the location of swath profiles K-K' and L-L' (cf. Fig. 4 for regional context). Red lines mark the fold axis. (b) Swath profiles (1-km-wide) approximately parallel to the Atushi fold axis along the fold and the upstream alluvial fan. The color-scheme for the sections is the same as in Fig. 5. The fold profiles show beveled surfaces at 3 different heights. The base level is defined by the height of the modern river crossing the fold. Note that the axis-parallel slope (0.7°) of the beveled area on western-central Atushi is similar to the slope of the upstream fan ~7 km to its north.

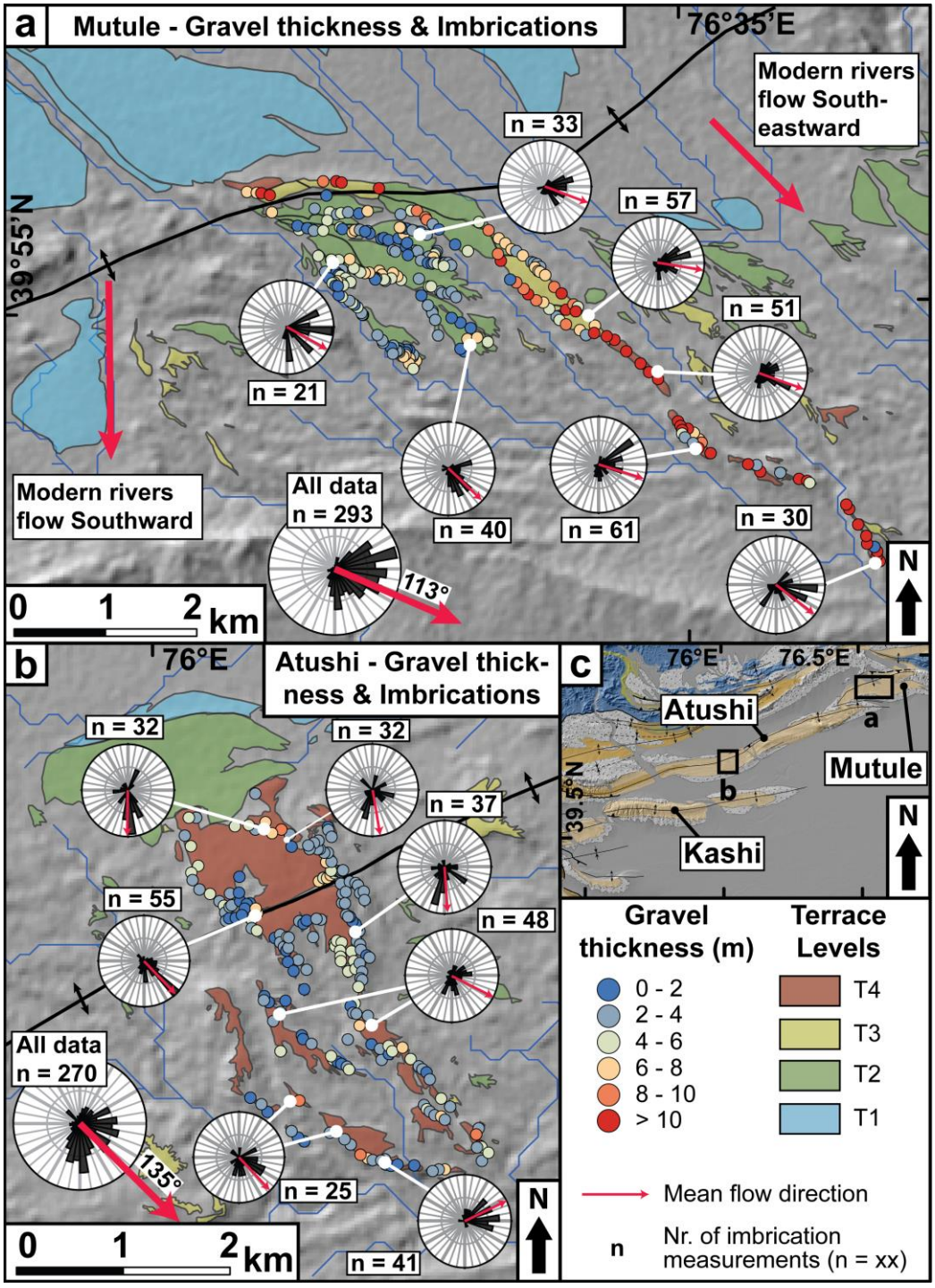

Figure 11: Imbrication direction and gravel thicknesses of the fluvial deposits on major terrace sequences of (a) central Atushi, and (b) southern Mutule. Notably, the mean paleo-flow-direction approximates that of modern rivers. Gravel thickness is mostly < 6 m, but some thicker deposits occur, especially along a narrow band on central Mutule. Because terrace surfaces are very planar with meter-scale relief of << 1 m, abrupt changes in the gravel thickness at the meter scale indicate relief on the strath surface.

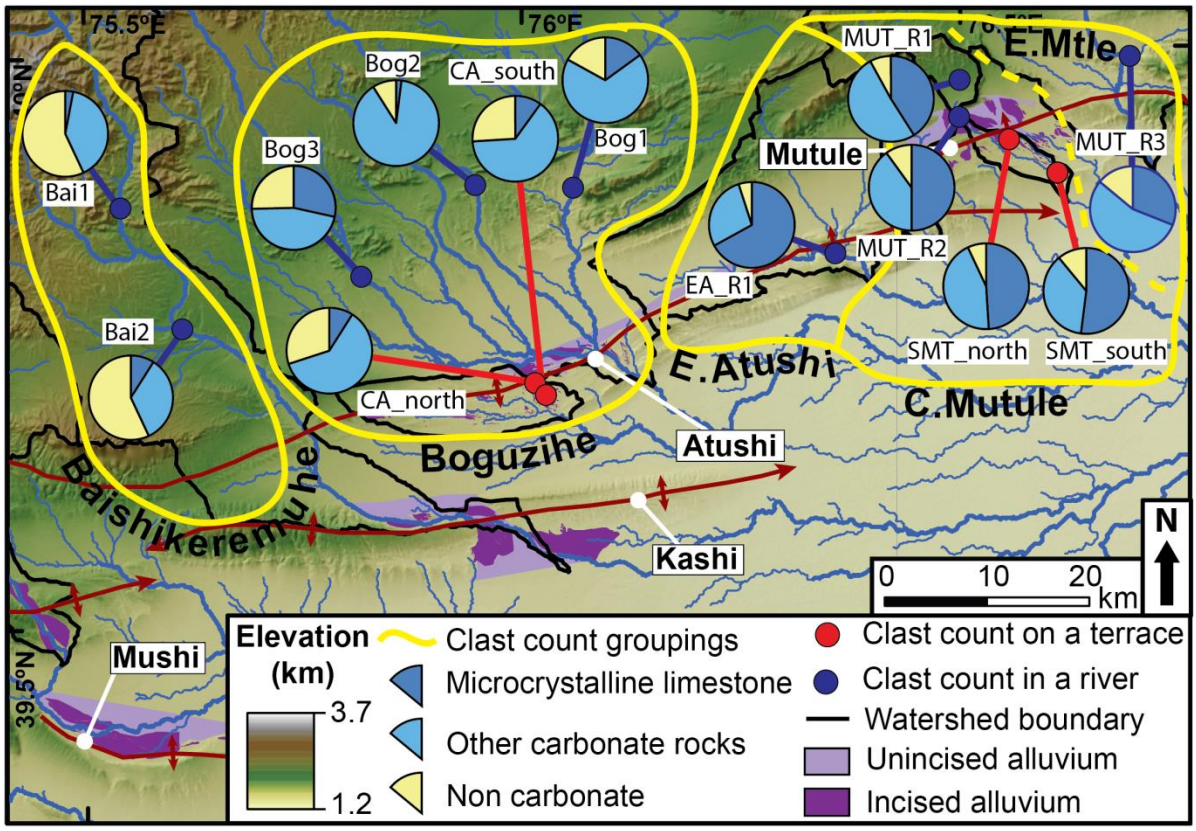

Figure 12: Lithologic clast counts in 9 river locations and 4 terrace locations. For each location, 100-140 clast counts were sorted into three groups. The groupings ("microcrystalline limestone," "carbonate rocks," or "non carbonate rocks") are interpreted to indicate common source areas, as marked by yellow boundaries (see Table A2 for the calculations underlying the groupings).

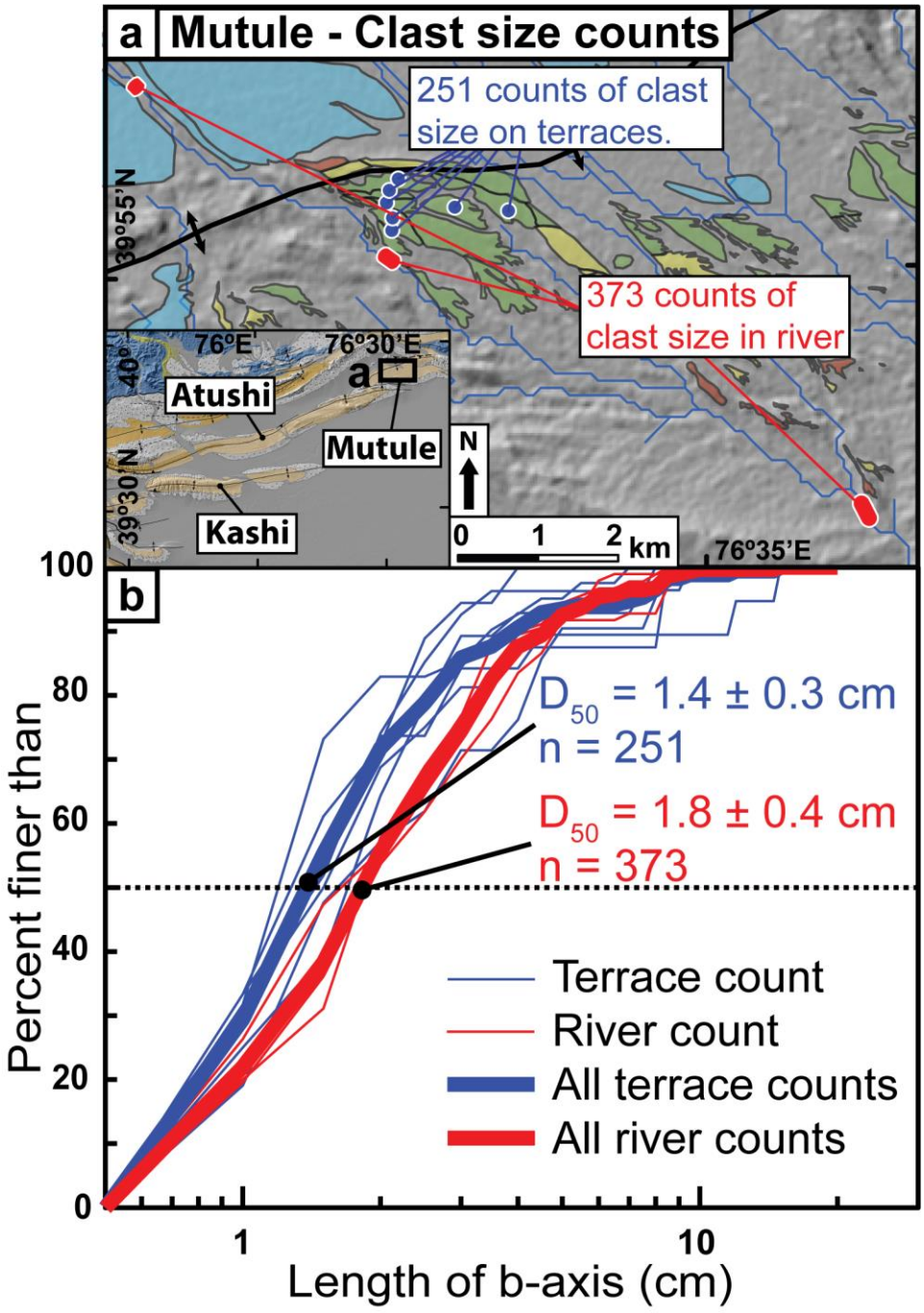

Figure 13: Counts of clast size with b-axes > 0.5 mm on Mutule fold. For each river location (red dots), ~125 clasts were counted at three nearby sites, yielding 373 counts per location. On the terraces, 20-60 clasts were counted at seven locations, totaling 251 clasts. (a) Map showing count sites on discrete terraces on central Mutule. Color scheme for the terraces mimics Figs. 9 and 11. (b) Particle-size distribution for individual terrace (blue) and river (red) counts (fine lines) and the mean of all counts (bold lines). Uncertainties in the D_{50} values are estimated as 10% following Whittaker et al. (2011) and reported at the 2σ-confidence interval in the figure.

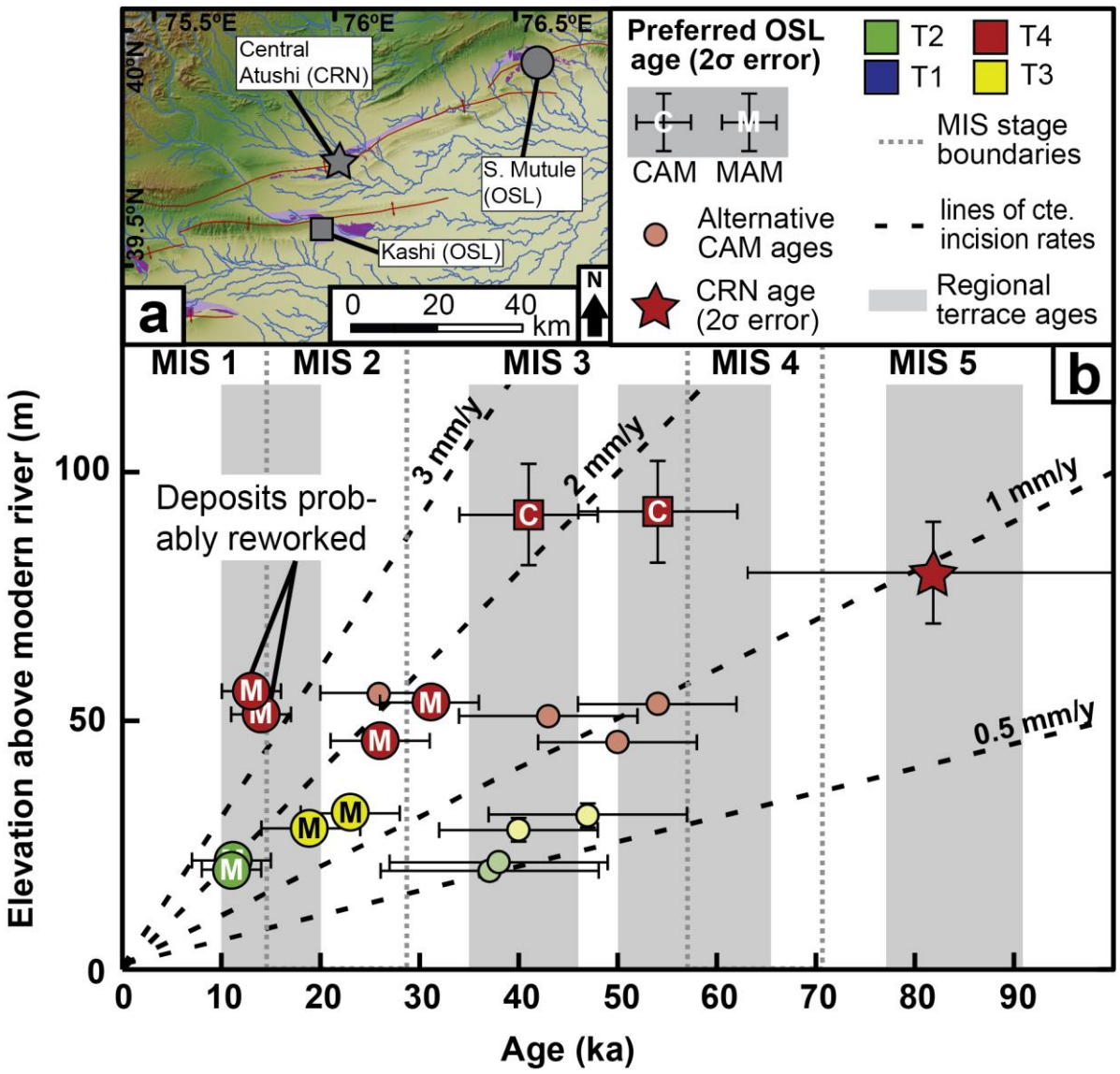

Figure 14: Terrace ages as a function of height above modern rivers. All uncertainties are reported at the 2σ-confidence level. (a) Overview map showing the location for dated surfaces in the study area and the symbology for the datapoints used in (b). See also Fig. 6 for locations. (b) Terrace ages versus height above the modern river. Preferred sample ages are marked with darker colored symbols (cf. Table 5). For samples where the minimum age model was preferred, the central age model result is plotted as a lighter-colored and smaller data point. Sample height above the modern river combines the terrace height above the modern river and the sample depth below the terrace surface. Dashed black lines mark the expected elevation as a function of age for a range of uplift/incision rates. The dotted grey lines are the boundaries of the marine isotope stages based on Lisiecki and Raymo (2005). The light grey bars mark clusters of published ages of fan, basin, and terrace gravels in the region (Li et al., 2012; Li et al., 2013; Thompson et al., in review). The outlier age on the eastern Atushi fold (EA-2: 250 m height at 15 ka) is not plotted here, but can be seen in Fig. S6.

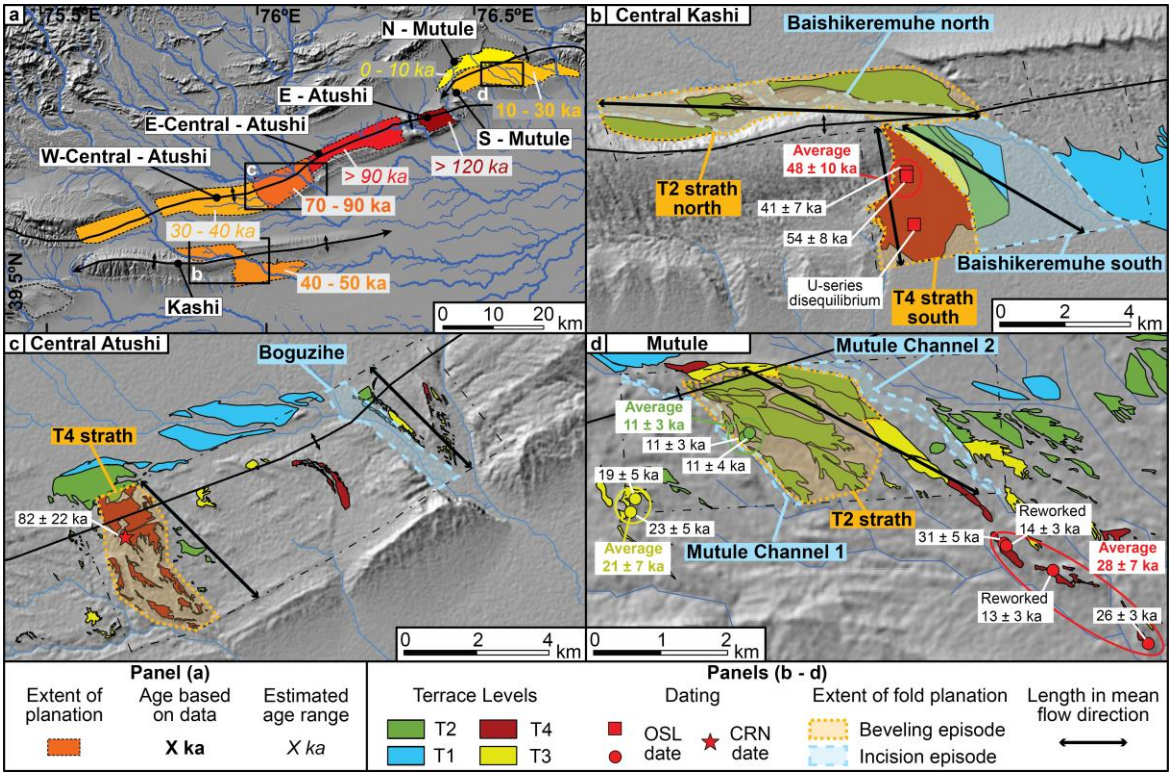

Figure 15: Summary of ages (±2σ) of beveled surfaces and areas used for the calculation of beveling rates. (a) Overview of the main beveled areas in the region with darker colors showing older surfaces. The age ranges correspond to the oldest major beveling episode preserved. Most surfaces (such as the surfaces on the Kashi fold) have been partly reworked by younger planation episodes. Black squares show the locations of panels b–d. (b-d) Terrace surfaces on Kashi, Atushi, and Mutule fold showing the dates from OSL and CRN dating. Also shown are areas of preserved strath terraces and areas of modern river valleys used for calculating beveling rates (light orange and light blue transparent areas; see Table 7 for calculations). Fine, black, dash-dot lines mark the fold-area over which these calculations were made. The mean flow direction in which the length of the beveled surface is measured is estimated on Atushi and Mutule from imbrication measurements and on Kashi from the orientation of terraces.

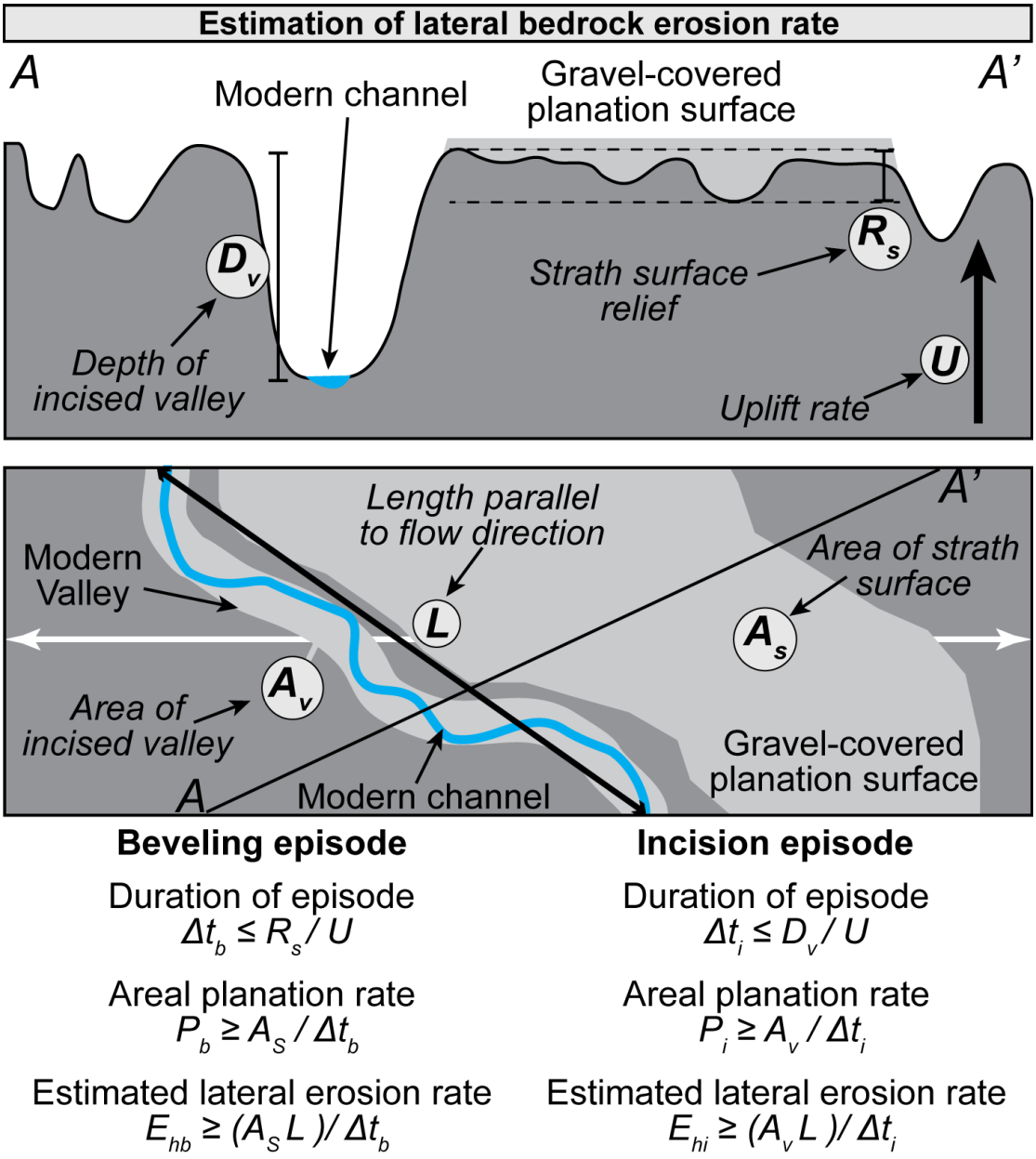

Figure 16: Conceptual sketch showing the calculation of lateral beveling rates at times of incision and planation.

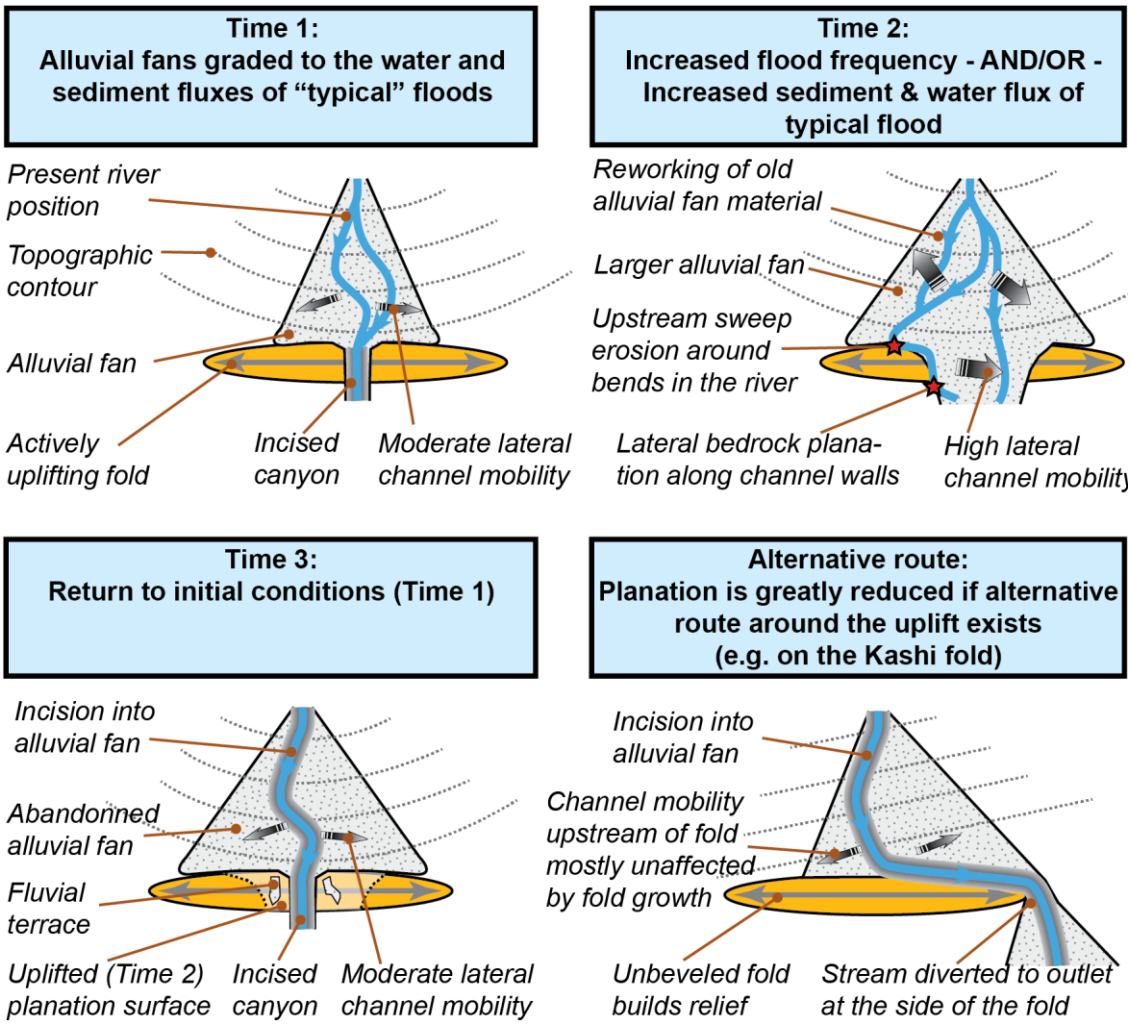

Figure 17: Conceptual sketch for a cycle of beveling and incision of an actively uplifting fold.

Table 1: Planation surfaces and depth of incision of folds in the foreland of the Tian Shan

Fold	Depth of incision into highest beveled surface (m)[a]	Approximate total area of fold (km^2)	Total beveled area (km^2)	Percent beveled area	Area covered by incised (late Quaternary) alluvium (km^2)	Area covered by unincised (Holocene) alluvium (km^2)	Percent of beveled area covered by alluvium
Mushi	30 - 60	300	84	28	29	43	86
Mingyaole	70 - 250	220	58	26	11	0	19
Kashi	50 - 90	460	84	18	36	45	96
West Atushi	30 - 70	120	53	44	0	0	0
West-Central Atushi	25 - 90	220	165	75	12	15	16
East-Central Atushi	80 - 120	150	71	48	0	11	16
East Atushi	200 - 280	70	21	31	0	0	0
North Mutule	0 - 10	40	37	91	11	21	87
South Mutule	10 - 50	180	92	51	10	2	13
Sum of all folds	NA	1760	655	37	109	137	37

[a]estimated from profiles on a 90 m SRTM

Table 2: Lithologic clast counts in the study area

Sample Name (West to East)	Location	Latitude	Longitude	Elevation (m)	Number of counts	Total carbonate Rocks (%)	Non Carbonate rocks (%)	Micro-crystalline carbonate rocks (%)
Bai1	River	39.7630	75.6106	1924	119	43	57	9
Bai2	River	39.8690	75.5411	2127	115	43	57	3
Bog3	River	39.8079	75.8146	1854	130	75	25	28
Bog2	River	39.8871	75.9450	1805	119	91	9	2
Bog1	River	39.8840	76.0563	1605	117	83	17	15
CA_north	Terrace	39.7130	76.0111	1480	111	70	30	9
CA_south	Terrace	39.7024	76.0233	1458	125	74	26	10
EA_R1	River	39.8232	76.3541	1337	125	95	5	67
MUT_R1	River	39.9410	76.4970	1721	127	90	10	50
MUT_R2	River	39.9732	76.4986	1910	124	92	8	41
SMT_north	Terrace	39.9207	76.5535	1541	131	93	7	49
SMT_south_lower 4m	Terrace	39.8907	76.6080	1380	141	88	12	56
SMT_south_upper 4m	Terrace	39.8909	76.6079	1396	139	90	10	49
SMT_south_surface	Terrace	39.8909	76.6079	1396	133	89	11	52
SMT_south_mean	Terrace	39.8909	76.6079	1396	138	89	11	52
MUT_R3	River	39.9919	76.6927	1453	119	86	14	31

Table 3: Clast-size counts on Mutule

Sample Name	Latitude	Longitude	Elevation (masl)	Number of non-silt counts	D_{50}[a] ±1σ (cm)	D_{84}[a] ±1σ (cm)
SMT_R_south (start)	39.8879	76.6073	1387	124	1.7 ± 0.2	3.5 ± 0.5
SMT_R_south (end)	39.8904	76.6058	1332			
SMT_R_north (start)	39.9384	76.5010	1747	124	1.9 ± 0.3	3.3 ± 0.5
SMT_R_north (end)	39.9378	76.5016	1740			
SMT_R_central (start)	39.9189	76.5369	1599	125	1.9 ± 0.3	4.1 ± 0.6
SMT_R_central (end)	39.9179	76.5387	1596			
SMT_Terrace_1	39.9215	76.5383	1618	27	1.5 ± 0.2	3.7 ± 0.6
SMT_Terrace_2	39.9230	76.5384	1635	26	1.3 ± 0.2	2.4 ± 0.4
SMT_Terrace_3	39.9247	76.5376	1629	60	1.2 ± 0.2	2.7 ± 0.4
SMT_Terrace_4	39.9260	76.5380	1627	36	1.7 ± 0.3	2.8 ± 0.4
SMT_Terrace_5	39.9273	76.5394	1622	32	1.6 ± 0.2	4.4 ± 0.7
SMT_Terrace_6	39.9240	76.5475	1588	28	1.4 ± 0.2	3.0 ± 0.4
SMT_Terrace_7	39.9235	76.5553	1570	42	1.5 ± 0.2	2.4 ± 0.4
Mean of terrace counts	-	-	-	251	1.4 ± 0.2	2.9 ± 0.4
Mean of river counts	-	-	-	373	1.8 ± 0.3	3.6 ± 0.5

[a]Calculated ignoring counts < 0.5 cm; Uncertainties are estimated as 10% following Whittaker et al., (2011).

Table 4: Cosmogenic nuclide dating of depth profile CA-DP1

CA - DP: Latitude: 39.7120; **Longitude:** 76.0115; **Elevation:** 1.5 km; **Height above modern river:** 80 ± 10 (±2σ) m[a]; **Be-10 Standard:** 07KNSTD[b]					
Sample name	**Depth below surface ±2σ (cm)[c]**	**Quartz weight ±1σ (g)[d]**	**Be Carrier ±1σ (mg)[d]**	**^{10}Be/^{9}Be ±1σ (10^{-14})[e]**	**^{10}Be concentration ±1σ (10^{5} atoms/g)[f]**
CA - DP1 - surf	0	118.278 ± 0.005	0.185 ± 0.001	1086 ± 23	11.37 ± 0.25
CA - DP1 - 0.3	30 ± 5	89.640 ± 0.005	0.197 ± 0.001	705 ± 12	10.37 ± 0.19
CA - DP1 - 0.6	60 ± 5	105.952 ± 0.005	0.197 ± 0.001	684 ± 20	8.49 ± 0.25
CA - DP1 - 0.9	90 ± 5	101.971 ± 0.005	0.200 ± 0.001	524 ± 16	6.86 ± 0.21
CA - DP1 - 1.2	120 ± 5	144.888 ± 0.005	0.197 ± 0.001	583 ± 11	5.30 ± 0.10
CA - DP1 - 1.6	160 ± 5	133.801 ± 0.005	0.196 ± 0.001	452 ± 11	4.42 ± 0.11
CA - DP1 - 2.0	200 ± 5	140.252 ± 0.005	0.196 ± 0.001	379 ± 7	3.54 ± 0.07
CA - DP1 - 3.0	300 ± 5	49.778 ± 0.005	0.198 ± 0.001	135 ± 4	3.61 ± 0.10

See Supplementary figure S5 for graphical profile and age analysis.

[a]Uncertainties are estimated.

[b]Samples were measured at PRIME using a standard prepared by Nishiizumi, et al (2007).

[c]CA-DP1-surf is from amalgamated pebbles spread out on the surface of the terrace. All other samples are from sand taken from 10-cm intervals within the depth profile.

[d]Uncertainties are estimated from the precision of the laboratory scale.

[e]A mean blank 10Be/9Be ratio of 13.82 ± 1.30 x10^{-15} measured from two laboratory blanks (^{10}Be/^{9}Be of 11.10 ± 1.62 x10^{-15} and 16.53 ± 2.00 x10^{-15}), was subtracted from the measured ^{10}Be/^{9}Be ratio. Uncertainties are from uncertainties in the AMS measurement of samples and blanks.

[f]Uncertainties include uncertainties in the ^{10}Be/^{9}Be ratio, the carrier mass, and the quartz weight.

Table 5: Results from optically stimulated luminescence dating of fluvial gravels

Sample Name[a]	Lat	Lon	Fold	Terrace surface	Depth of sample below surface ±2σ (m)[b]	Elev. of terrace above modern river ±2σ (m)[b]	Nr. of aliquots (accepted /total)	Dose Rate ±2σ (Gy/ky)[c]	MAM Age ±2σ (ka)[d]	CAM Age ±2σ (ka)[d]	Dispersion (%)	Skew	Kurtosis
CK-1	39.5643	75.9505	C. Kashi	T4	1.4 ± 0.2	60 ± 10	25/33	1.8 ± 0.1	15 ± 2	55 ± 14	61	0.5	-0.6
CK-2	39.5776	75.9480	C. Kashi	T4	3.3 ± 0.2	95 ± 10	22/29	1.7 ± 0.1	30 ± 4	54 ± 8	32	0.3	-0.7
CK-3	39.5785	75.9480	C. Kashi	T4	3.9 ± 0.2	95 ± 10	20/27	2.7 ± 0.1	23 ± 3	41 ± 7	36	0.4	-1.2
SMT-1	39.9195	76.5384	S. Mutule	T2	1.3 ± 0.2	21 ± 1	23/42	1.8 ± 0.1	11 ± 3	37 ± 11	67	1.1	0.6
SMT-2	39.9200	76.5393	S. Mutule	T2	1.4 ± 0.2	23 ± 1	21/35	2.2 ± 0.1	11 ± 4	38 ± 11	64	0.8	1.1
SMT-4	39.9114	76.5191	S. Mutule	T3	6.0 ± 0.2	34 ± 2	33/64	2.3 ± 0.1	19 ± 5	40 ± 8	52	1.1	0.7
SMT-5	39.9096	76.5183	S. Mutule	T3	3.0 ± 0.2	34 ± 2	23/38	2.6 ± 0.1	23 ± 5	47 ± 10	45	0.5	-0.4
SMT-6	39.9046	76.5833	S. Mutule	T4	5.7 ± 0.2	59 ± 1	33/47	2.7 ± 0.2	31 ± 5	54 ± 8	36	1.1	0.9
SMT-7	39.9043	76.5838	S. Mutule	T4	7.0 ± 0.2	58 ± 1	31/55	3.0 ± 0.2	14 ± 3	43 ± 9	56	1.4	1.8
SMT-8	39.9008	76.5918	S. Mutule	T4	1.4 ± 0.2	57 ± 1	20/27	3.0 ± 0.2	13 ± 3	26 ± 6	48	1.0	0.1
SMT-9	39.8907	76.6082	S. Mutule	T4	5.3 ± 0.2	51 ± 1	34/58	2.4 ± 0.1	26 ± 5	50 ± 8	42	1.0	0.3
EA-2	39.8439	76.4201	E. Atushi	NA	0.9 ± 0.2	240 ± 40	29/44	2.1 ± 0.1	15 ± 3	36 ± 7	48	0.8	1.1
WCA-1	39.6907	75.8513	W.-C. Atushi	NA	1.0 ± 0.2	-[e]	21/49	2.3 ± 0.1	35 ± 7	61 ± 12	40	1.4	1.9
WCA-3	39.6907	75.8513	W.-C. Atushi	NA	2.3 ± 0.2	-[e]	30/38	3.0 ± 0.2	18 ± 3	45 ± 9	49	1.4	2.5

[a]CK = central Kashi, SMT = south Mutule, EA = east Atushi, WCA = West-central Atushi.
[b]Uncertainties are estimated.
[c]The dose rate is calculated from radionuclide activities in representative samples measured through gamma ray spectroscopy and an estimated water content of 5 ± 5% (±2σ). Uncertainties are propagated from the standard deviations of radionuclide activities and the estimated uncertainties of the water contents.
[d]Ages are obtained by applying the minimum age model and the central age model (Galbraith, 2005; Galbraith and Roberts, 2012; Galbraith et al., 1999) to the single aliquot equivalent dose data. Resulting equivalent doses are divided by the dose rate to obtain an age. Uncertainties are propagated from the dose rate uncertainty and equivalent dose standard error.
Dark grey bars mark the two samples that are ignored in this study due to high U-series disequilibrium. Light grey bars mark the preferred age-model based on the skew and the dispersion values (Arnold et al., 2007).
[e]Terrace appear to have been formed by rivers that drain the fold internally. The current elevation above that river is 15 - 25 m. However, the river profiles of fold-internal rivers are likely changing more significantly with the uplift of the fold than rivers crossing the structure - we therefore ignore this datapoint.

Table 6: Average incision/uplift rates of Kashi, Atushi, and Mutule

Structure[a]	Interval considered[b]	Depth of incision ±2σ (m)[c]	Duration of incision ±2σ (ky)[d]	Average incision/uplift rate ±2σ (mm/y)
Kashi	T4 terrace peak - modern river	130 ± 20	48 ± 10	2.7 ± 0.7
Kashi	T4 sample - modern river	95 ± 10	48 ± 10	2.0 ± 0.5
Atushi	T4 peak/sample - modern river	80 ± 10	82 ± 22	1.0 ± 0.3
Mutule	T4 peak/sample - modern river	55 ± 1	28 ± 4	2.0 ± 0.2
Mutule	T3 peak/sample - modern river	34 ± 1	21 ± 4	1.6 ± 0.3
Mutule	T2 peak/sample - modern river	22 ± 1	11 ± 3	2.0 ± 0.5
Mutule	T4 peak/sample - T3 peak/sample	21 ± 2	7 ± 5	3.0 ± 2.2
Mutule	T4 peak/sample - T2 peak/sample	33 ± 1	17 ± 4	1.9 ± 0.5
Mutule	T3 peak/sample - T2 peak/sample	12 ± 2	10 ± 4	1.2 ± 0.5

[a]For each structure (except Atushi) multiple estimates of average incision rates are given. The incision rate that best estimates average uplift rates of the structure, is marked in gray.
[b]Intervals considered in the analysis are either an interval between a terrace gravel top and the bed of the modern river or between two terrace gravel tops.
[c]Terrace elevations above the modern river are taken from averages of the terrace elevation estimated at the sample sites (cf. Table 5 for Kashi & Mutule and Table 4 for Atushi). The T4 elevation on the crest of the Kashi fold (T4 peak) is estimated by extrapolating the terrace and river slopes (shown in Fig. 9) up to the fold crest.
[d]Duration of incision is estimated by assuming mean terrace ages for dated terraces represent abandonment ages.

Table 7: Calculation of planation rates for incision and planation episodes

Lateral bedrock erosion rates during planation episodes and during incision episodes								
Landform	**Fold**	**Peak uplift rate (U) ±2σ (mm/y)**	**Maximum incision depth (D_v or R_s) ±2σ (m)[a]**	**Duration of episode (Δt) ±2σ (ky)[b]**	**Planated area (A) ±2σ (km2)**	**Areal planation rate (P) ±2σ (m2/y)**	**Flow-parallel length (L) ±2σ (km)[c]**	**Lateral bedrock erosion rate (E_h) ±2σ (mm/y)[d]**
Incision episode (modern rivers)								
Baishikeremhue	North Kashi	2.7 ± 0.7	45 ± 15	17 ± 7	5.8 ± 0.3	350 ± 150	11.6 ± 0.6	30 ± 13
Baishikeremhue	Centr/South Kashi		130 ± 20	48 ± 14	14.5 ± 0.7	300 ± 90	6.3 ± 0.3	48 ± 15
Boguzihe	Atushi	1.0 ± 0.3	50 ± 10	51 ± 18	2.4 ± 0.1	47 ± 17	4.1 ± 0.2	12 ± 4
Mut Channel 1	Mutule	1.9 ± 0.5	22 ± 1	11 ± 3	0.2 ± 0.0	22 ± 6	4.3 ± 0.2	5 ± 1
Mut Channel 2			22 ± 1	11 ± 3	0.5 ± 0.0	46 ± 13	4.3 ± 0.2	11 ± 3
Beveling episodes								
T2 strath	North Kashi	2.7 ± 0.7	6 ± 2	2 ± 1	14.7 ± 7.3	6600 ± 4300	11.6 ± 0.6	570 ± 370
T4 strath	Centr/South Kashi	2.7 ± 0.7	10 ± 5	4 ± 2	8.3 ± 0.8	2300 ± 1300	4.3 ± 0.2	520 ± 300
T4 strath	Atushi	1.0 ± 0.3	6 ± 2	6 ± 3	6.7 ± 2.0	1100 ± 600	4.8 ± 0.2	230 ± 120
T2 strath	Mutule	1.9 ± 0.5	6 ± 2	3 ± 1	3.7 ± 1.1	1200 ± 600	4.3 ± 0.2	280 ± 150

[a]Incision depth for modern rivers are measured from the top of gravel covered straths to the modern river-bed and obtained from differential GPS surveys (Mutule, Baishikeremuhe south) or estimated from Google Earth (Boguzihe, Baishikeremuhe north). The incision depth for planation surfaces is estimated from measured strath relief (Mutule & Atushi) or estimated (Kashi).
[b]Calculated by assuming incision rates are equal to average uplift rates. For the sake of consistency, we propagated the errors from the peak uplift rate and the incision depth even for the Baishikeremuhe south and the Mutule channels for which the duration is known from the OSL data.
[c]The straight line length of channels and planation surfaces are measured in the (measured or estimated) average direction of flow.
[d]These lateral bedrock erosion rates are rates equivalent to one or several straight channels linearly eroding the sides of a canyon wall (see text for details).

Supporting material for Chapter 2

1 Methods

1.1 Terrace elevations above modern river

Terrace heights above the modern river were obtained by projecting the GPS survey data from terraces and rivers on a line parallel to the approximate flow direction of the modern river (Fig. 9). Where no surveys were made, river elevations were extracted from the 90-m SRTM DEM. On the western-central Atushi fold, dated terraces are located 5-9 km from the modern Boguzihe and Baishikeremuhe rivers (Fig. 6). Hence, elevations were extracted from the 90-m SRTM and detrended with an overall 0.7° east-northeastward slope of the beveled surface that dominates the western Atushi fold (Fig. 10). Corresponding uncertainties in the elevation are, therefore, higher here than for the elevations obtained through GPS surveys (Table 6).

1.2 Lithologic clast count statistics

In order to assess the difference between count locations we calculated the sum of squares of the difference in the proportions of carbonate rocks ($Carb$) and the proportion of microcrystalline carbonate ($Xtln$) (Table A2): For example for two samples Spl1 and Spl2, the calculated difference would be: $\sqrt{(Carb_{Spl1} - Carb_{Spl2})^2 + (Xtln_{Spl1} - Xtln_{Spl2})^2}$. A value of < 20 is considered similar. Source area can then be determined on the basis of this similarity factor and the geographic locations of the streams.

1 3 Structural cross section of the Mutule fold

The structural cross section of Mutule (Fig. 5c) was constructed based on mapping along a transect across the Mutule fold (Table A4, Fig. S1) as well as on Google Earth ® imagery. Strike and dip direction were measured along the main river crossing central Mutule (Fig. S1). The bedding data was projected onto a line trending 165° (approximately perpendicular to the fold-axis) and the apparent dip calculated. The cross-section was constructed analogously to (Scharer et al., 2004): the bedding data was separated into 12 dip-panels and an average dip of each panel was calculated from the bedding data. Each dip-panel was then treated as a kink-band with constant thickness and bed-length. The fault in the cross section was inferred from surface mapping and unpublished seismic data.

Seismic data shows the depth of detachment at approximately 5.6 seconds two-way-travel-time. Using a velocity model for sections to the east of the Mutule fold (Heermance et al., 2008), we infer a depth of the detachment at ~11 ± 3 km. This depth is consistent with a possible eastward deepening of the detachment level from 3-6 km at Kashi (Heermance et al., 2008) to 9-12 km on eastern Atushi (Scharer et al., 2004). The data suggests a total uplift since initiation of ~6.9 km and an excess area of ~67 km^2, implying ~6.0-6.1 km of shortening. If we consider only the topography above the modern river, total uplift is ~5.8 km, the excess area is ~50 km, and total shortening 4.6-4.8 km.

1.4 Optically Stimulated Luminescence (OSL) sampling and analysis

OSL field sampling followed standard procedures (Nelson et al., 2015). A ~25-cm-long metal tube was pounded into the sand parallel to bedding and sealed on both ends for transportation. In addition, a sample of ~1-1.5 kg of sediment was collected in a 30-cm radius around the tube for dose-rate calculations. The tubes were opened in a dark room and

the sand was wet-sieved to 90-180 μm. Then, samples were leached first in 30% H_2O_2 followed by 40% HCl and further cleaned through magnetic separation. Finally, samples were leached in 10 % HF for 10 min, 40% HF for 40 min, and 10% HCl for 40 min. Aliquots of clean sand were mounted onto 9.7-mm steel discs using silica paste and a 2-mm mask. The samples were measured on a Risø Reader TL/OSL-DA-20. The measurement followed the standard single-aliquot regenerative dose protocol (Murray and Wintle, 2000; Wintle and Murray, 2006). We chose a pre-heat temperature of 260°C, a cut-heat temperature of 220°C, and a measurement temperature of 125°C following previous protocols established for samples from the area (Thompson et al., in review). For each sample 25-65 aliquots were measured and retained if recycling ratios were within 0.9-1.1, recuperation < 5% of the natural luminescence, IR depletion ratios between 0.9-1.1, and the signal intensities 3σ above the background (Table A5).

In order to estimate the dose rate, activities of ^{238}U, ^{226}Ra, ^{228}Ra, ^{228}Th, and ^{40}K in the sediment collected around the OSL sample were measured using gamma ray spectrometry. Dose rates for the measured nuclides and their daughters were then calculated using the activity to dose rate conversion of Nathan (2010) and assuming a $^{235}U/^{238}U$ activity ratio of 0.04605. The cosmogenic nuclide contribution was estimated using standard corrections (Prescott and Hutton, 1988; Prescott and Hutton, 1994). Water contents measured in the collected samples range from 0.1-10%. Since water contents varied from saturation at deposition to at least the modern water content with likely wetter and drier episodes in the past, we chose a mean water content of 5 ± 5% for all samples. We assessed potential disequilibrium in the ^{238}U decay chain, which is common in soils and fluvial sediments (Olley et al., 1996; Olley et al., 1997), by calculating the $^{238}U/^{226}Ra$ ratio with corresponding

uncertainty. Seven of the 14 samples have values that are not within error of unity (Table A6). However, all of the ratios are at least within 60% of unity and within 20% of unity if we consider the uncertainty in the measurement (Table A6). With the high ^{40}K content in our samples (Table A6), the ^{238}U and ^{235}U decay chains account for < 20 % of the total dose rate. Thus, the minor U-series disequilibrium is expected to introduce uncertainties of << 10% (Olley et al., 1996; Olley et al., 1997). These uncertainties are well within the range of uncertainties introduced by varying water contents and make us believe that exploring detailed U-series loss and gain scenarios (e.g. Zander et al., 2007) will not change our uncertainty estimate significantly.

1.5 Cosmogenic Nuclide dating sample preparation and analysis

The sand samples from the depth profile were sieved in the field into fractions of 250-800 μm, whereas the surface pebble sample was crushed and sieved to 200-800 μm in facilities at the UC Santa Barbara. Quartz was separated and purified by density and magnetic separation followed by leaching in hydrochloric acid and at least three 24 h leaches in 1 or 2% HF solutions. 30-150 g of pure quartz was digested in concentrated HF after addition if a pure ^{9}Be carrier. Fe was removed in an anion column followed by 2-3 cation columns to remove Al and Ti. The purity of samples was confirmed using the ICPMS lab at the MRL facilities at UC Santa Barbara before BeOH was precipitated in NH4OH and dehydrated in a furnace to form BeO. The BeO was mixed with four parts of Nb, loaded into targets, and sent to the Purdue Rare Isotope Measurement (PRIME) Laboratory. There, the $^{10}Be/^{9}Be$ ratio was determined and calibrated against a 07KNSTD standard (Nishiizumi et al., 2007). A mean blank $^{10}Be/^{9}Be$ ratio of $13.82 \pm 1.30 \times 10^{-15}$ measured from two laboratory blanks ($^{10}Be/^{9}Be$ of $11.10 \pm 1.62 \times 10^{-15}$ and $16.53 \pm 2.00 \times 10^{-15}$), was subtracted from the

measured $^{10}Be/^{9}Be$ ratio of each sample. We applied a Monte Carlo depth-profile simulator (Hidy et al., 2010) to obtain the best-fit surface age, best-fit inheritance of ^{10}Be, and best-fit paleo-erosion rate, using a ^{10}Be half live of 1.387 Ma (Chmeleff et al., 2010; Korschinek et al., 2010), the reference ^{10}Be production rates of Borchers et al. (2016), and an atmospheric model based on the ERA40 climate reanalysis (Lifton et al., 2014) (Table A7, Fig. S5). We also updated the muon cross section in the Monte Carlo simulator based on new results from Borchers et al. (2016).

The Monte Carlo depth-profile simulator (Hidy et al., 2010) uses the time-independent scaling scheme by Stone (2000) based on (Lal, 1991) and does not take uncertainties in the reference production rates into account. Following Schildgen et al. (2016) and Dey et al. (2016), we therefore converted the best-fit age from the Monte Carlo simulations back into a best-fit ^{10}Be surface concentration using a site-specific ^{10}Be surface production rate in quartz of 12.8752 a/g/y and a ^{10}Be half-life of 1.387 Ma (Table A7). This hypothetical surface sample (and its 1σ uncertainty) was then input into the CRONUS-Earth-2008-v2.3 exposure age calculator to get the best-fit surface exposure age (Balco et al., 2008) (Table A8). Note that we modified the scripts of the CRONUS-Earth-2008-v2.3 exposure age calculator to include the ERA40 climate model (Lifton et al., 2014) instead of the default NCEP2 climate model.

2 Additional Discussions

2.1 OSL dating

Three OSL samples fall out of the stratigraphic order expected for samples preserved at different heights by yielding anomalously young ages (Fig. S6). Two of the samples are on

the T4 terrace of southern Mutule (sample SMT-7, SMT-8; Table 5) and one is on eastern Atushi (sample EA-2). SMT-7 was sampled on a steep slope rising up to the top of the terrace (Figs. S7a, S7b). Whereas the gravel below the sampled silt lens is horizontal, the gravel above the silt lens is inclined in the down-slope direction consistent with downward movement of grains that could cause mixing and introduction of younger grains (Figs. S7a, S7b). We note that this sample does have old grains, and, if the central age model is taken, it has an age similar to the other T4 terrace ages from south Mutule (Table 5). SMT-8 lies 1.4 m below the terrace surface along a convex-up hillslope edge and could have been reworked by bioturbation, inflation by windblown sand, or movement along the slope (Figs. S7c-d). Finally, the very young age of the terrace on the high surface on eastern Atushi (sample EA-2) is unlikely to represent the primary time of strath formation. This sample came from the sole, thin (< 1.5 m) remnant of gravel that was found on any of the surfaces on eastern Atushi (Fig. 6, Fig. S7e). Preserved along a narrow, elongate ridge, the ill-defined beds did not show clear fluvial genesis. Given its extensive erosion, the deposits could have been slumped or otherwise reworked, leading to further bleaching of the grains.

2.2 Preservation of fluvial deposits

During beveling, a veneer of gravel likely covered the entire fold surface; similar to the barely incised northern Mutule and northern central Atushi fold (Figs. 6, 7). Once the planation surface is abandoned and uplifted, incision drives hillslope retreat and stripping of the fluvial cover. Scattered and loose gravel on the western-central Atushi fold (Fig. S4a) is a testament to this process. Only where deposits are thick enough (> 0.5-1 m), do they get cemented, preserved, and, thereby, shield the underlying bedrock from erosion. Thus, we hypothesize, that thickness variations in the gravel cover at the time of beveling are the

primary cause of the variable preservation of deposits on the different parts of the folds (Table 1).

2.3 Planation surfaces and wind-erosion

The landscape flattening described in this paper might also be envisioned to have happened through efficient wind erosion (Rohrmann et al., 2013). Indeed, the Atushi Formation is easily weathered and, on many of the beveled platforms, bedrock slopes are covered by a thick veneer of silt that is readily washed away during rainstorms. Moreover, remnant beveled surfaces (now tilted to the north) on east-central Atushi show large depressions and ridges aligned in what is likely the general direction of the wind. Nonetheless, 1) fluvial deposits are preserved on nearly all beveled surfaces, and 2) the lithology, tectonic forcing, and local climate (rainfall and wind) are similar on the Kashi, Atushi, and Mutule folds, whereas the preservation of beveled surfaces is highly variable. Therefore, we deduce that planation by rivers is clearly the dominant process causing the formation of these surfaces.

References for supporting material of Chapter 2

Balco, G., Stone, J. O., Lifton, N. A., and Dunai, T. J., 2008, A complete and easily accessible means of calculating surface exposure ages or erosion rates from 10Be and 26Al measurements: Quaternary Geochronology, v. 3, no. 3, p. 174-195.

Borchers, B., Marrero, S., Balco, G., Caffee, M., Goehring, B., Lifton, N., Nishiizumi, K., Phillips, F., Schaefer, J., and Stone, J., 2016, Geological calibration of spallation production rates in the CRONUS-Earth project: Quaternary Geochronology, v. 31, p. 188-198.

Chmeleff, J., von Blanckenburg, F., Kossert, K., and Jakob, D., 2010, Determination of the 10Be half-life by multicollector ICP-MS and liquid scintillation counting: Nuclear Instruments and Methods in Physics Research Section B: Beam Interactions with Materials and Atoms, v. 268, no. 2, p. 192-199.

Dey, S., Thiede, R. C., Schildgen, T. F., Wittmann, H., Bookhagen, B., Scherler, D., Jain, V., and Strecker, M. R., 2016, Climate-driven sediment aggradation and incision since the late Pleistocene in the NW Himalaya, India: Earth and Planetary Science Letters, v. 449, p. 321-331.

Heermance, R. V., Chen, J., Burbank, D. W., and Miao, J., 2008, Temporal constraints and pulsed Late Cenozoic deformation during the structural disruption of the active Kashi foreland, northwest China: Tectonics, v. 27, no. 6, p. TC6012.

Hidy, A. J., Gosse, J. C., Pederson, J. L., Mattern, J. P., and Finkel, R. C., 2010, A geologically constrained Monte Carlo approach to modeling exposure ages from profiles of cosmogenic nuclides: An example from Lees Ferry, Arizona: Geochemistry, Geophysics, Geosystems, v. 11, no. 9.

Korschinek, G., Bergmaier, A., Faestermann, T., Gerstmann, U. C., Knie, K., Rugel, G., Wallner, A., Dillmann, I., Dollinger, G., von Gostomski, C. L., Kossert, K., Maiti, M., Poutivtsev, M., and Remmert, A., 2010, A new value for the half-life of 10Be by Heavy-Ion Elastic Recoil Detection and liquid scintillation counting: Nuclear Instruments and Methods in Physics Research Section B: Beam Interactions with Materials and Atoms, v. 268, no. 2, p. 187-191.

Lal, D., 1991, Cosmic ray labeling of erosion surfaces: in situ nuclide production rates and erosion models: Earth and Planetary Science Letters, v. 104, no. 2–4, p. 424-439.

Lifton, N., Sato, T., and Dunai, T. J., 2014, Scaling in situ cosmogenic nuclide production rates using analytical approximations to atmospheric cosmic-ray fluxes: Earth and Planetary Science Letters, v. 386, no. 0, p. 149-160.

Murray, A. S., and Wintle, A. G., 2000, Luminescence dating of quartz using an improved single-aliquot regenerative-dose protocol: Radiation Measurements, v. 32, no. 1, p. 57-73.

Nathan, R. P., 2010, Numerical modelling of environmental dose rate and its application to trapped-charge dating: University of Oxford.

Nelson, M. S., Gray, H. J., Johnson, J. A., Rittenour, T. M., Feathers, J. K., and Mahan, S. A., 2015, User Guide for Luminescence Sampling in Archaeological and Geological Contexts: Advances in Archaeological Practice, v. 3, no. 2, p. 166-177.

Nishiizumi, K., Imamura, M., Caffee, M. W., Southon, J. R., Finkel, R. C., and McAninch, J., 2007, Absolute calibration of 10Be AMS standards: Nuclear Instruments and

Methods in Physics Research Section B: Beam Interactions with Materials and Atoms, v. 258, no. 2, p. 403-413.
Olley, J. M., Murray, A., and Roberts, R. G., 1996, The effects of disequilibria in the uranium and thorium decay chains on burial dose rates in fluvial sediments: Quaternary Science Reviews, v. 15, no. 7, p. 751-760.
Olley, J. M., Roberts, R. G., and Murray, A. S., 1997, Disequilibria in the uranium decay series in sedimentary deposits at Allen's cave, nullarbor plain, Australia: Implications for dose rate determinations: Radiation Measurements, v. 27, no. 2, p. 433-443.
Petit, J. R., Jouzel, J., Raynaud, D., Barkov, N. I., Barnola, J. M., Basile, I., Bender, M., Chappellaz, J., Davis, M., Delaygue, G., Delmotte, M., Kotlyakov, V. M., Legrand, M., Lipenkov, V. Y., Lorius, C., Pepin, L., Ritz, C., Saltzman, E., and Stievenard, M., 1999, Climate and atmospheric history of the past 420,000 years from the Vostok ice core, Antarctica: Nature, v. 399, no. 6735, p. 429-436.
Prescott, J., and Hutton, J., 1988, Cosmic ray and gamma ray dosimetry for TL and ESR: International Journal of Radiation Applications and Instrumentation. Part D. Nuclear Tracks and Radiation Measurements, v. 14, no. 1-2, p. 223-227.
Prescott, J. R., and Hutton, J. T., 1994, Cosmic ray contributions to dose rates for luminescence and ESR dating: Large depths and long-term time variations: Radiation Measurements, v. 23, no. 2–3, p. 497-500.
Rohrmann, A., Heermance, R., Kapp, P., and Cai, F., 2013, Wind as the primary driver of erosion in the Qaidam Basin, China: Earth and Planetary Science Letters, v. 374, p. 1-10.
Scharer, K. M., Burbank, D. W., Chen, J., Weldon, R. J., Rubin, C., Zhao, R., and Shen, J., 2004, Detachment folding in the Southwestern Tian Shan–Tarim foreland, China: shortening estimates and rates: Journal of Structural Geology, v. 26, no. 11, p. 2119-2137.
Schildgen, T. F., Robinson, R. A. J., Savi, S., Phillips, W. M., Spencer, J. Q. G., Bookhagen, B., Scherler, D., Tofelde, S., Alonso, R. N., Kubik, P. W., Binnie, S. A., and Strecker, M. R., 2016, Landscape response to late Pleistocene climate change in NW Argentina: Sediment flux modulated by basin geometry and connectivity: Journal of Geophysical Research: Earth Surface, p. 392-414.
Stone, J. O., 2000, Air pressure and cosmogenic isotope production: Journal of Geophysical Research: Solid Earth, v. 105, no. B10, p. 23753-23759.
Thompson, J. A., Chen, J., Yang, H., Li, T., Bookhagen, B., and Burbank, D. W., in review, Coarse- versus fine-grain OSL and cosmogenic 10Be dating of deformed fluvial terraces on the northeast Pamir margin, northwest China: Quaternary Geochronology.
Wintle, A. G., and Murray, A. S., 2006, A review of quartz optically stimulated luminescence characteristics and their relevance in single-aliquot regeneration dating protocols: Radiation Measurements, v. 41, no. 4, p. 369-391.
Zander, A., Degering, D., Preusser, F., Kasper, H. U., and Brückner, H., 2007, Optically stimulated luminescence dating of sublittoral and intertidal sediments from Dubai, UAE: Radioactive disequilibria in the uranium decay series: Quaternary Geochronology, v. 2, no. 1–4, p. 123-128.

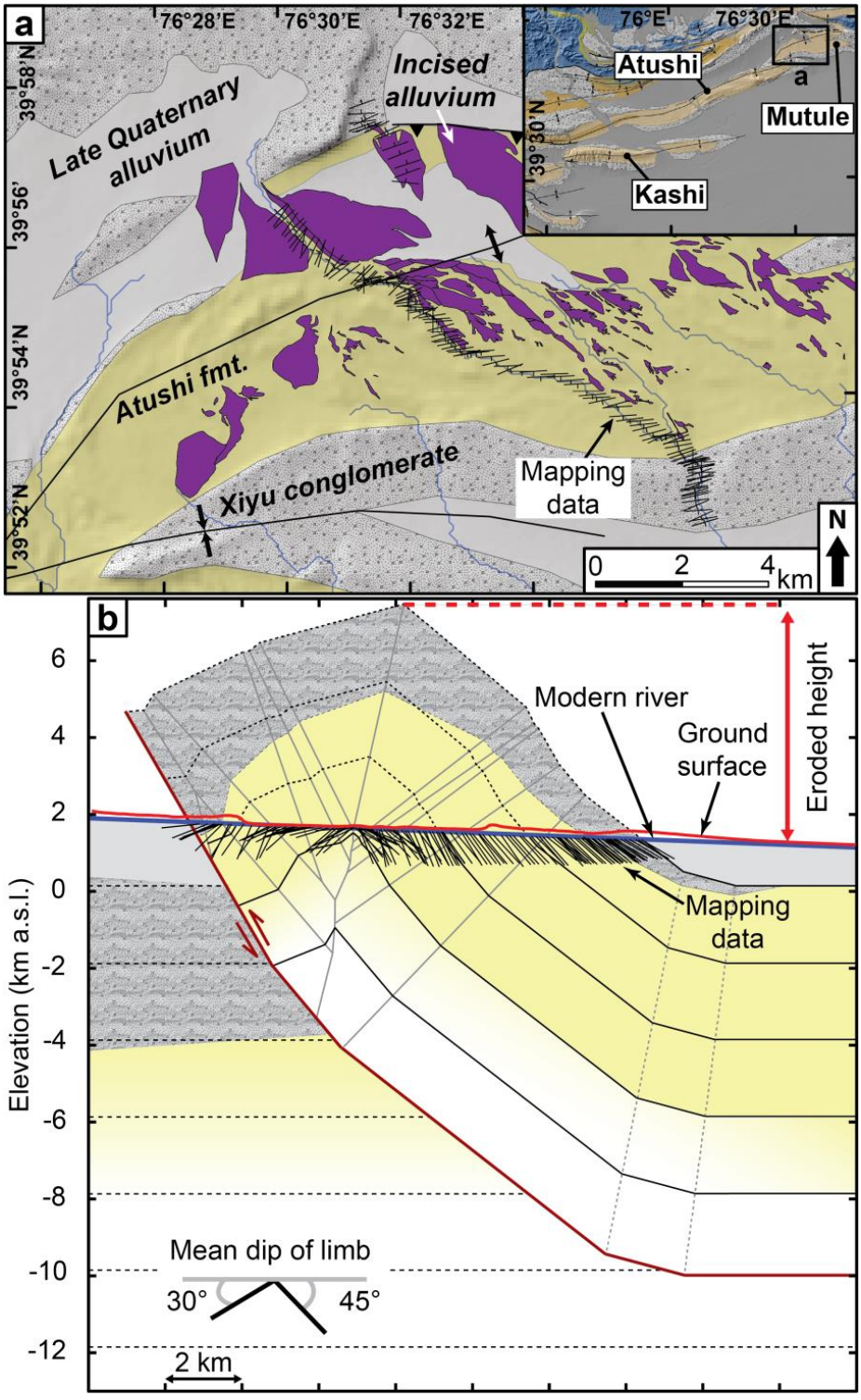

Figure S1: Structural mapping of the Mutule fold. (a) Location of mapped section on the Mutule fold and geologic map of the fold. The units are the same as in Fig. 3. (b) Structural cross section of the Mutule fold as in Fig. 4c.

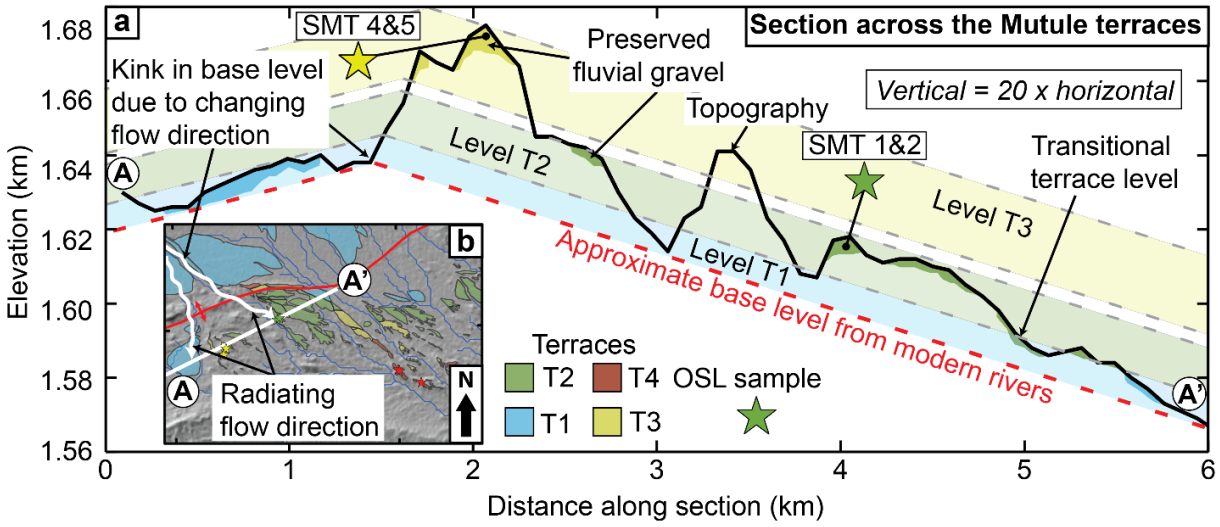

Figure S2: Map and section of the terraces on the Mutule fold showing the large range of elevations at which terraces are preserved. (a) Topographic cross section along the line marked in (b). Preserved fluvial gravels are shown according to mapped terrace levels. Because the section is not perpendicular to the flow direction of rivers, the base level is not flat. On the bases of troughs in the topography, an approximate local base-level is shown (dashed red line). Because the flow direction is changing across the section (cf. (b)), the trend of the base-level is, too, illustrating challenges in correlating terrace levels across the kilometer-wide surface of the Mutule fold. The transparent color bands mark the range of elevation across which terrace levels are preserved. (b) Map of the terraces on central Mutule (same as in Fig. 9b) with preserved fluvial terraces. Radiating flow direction of rivers, marked with white squiggly lines, are reminiscent of an alluvial fan.

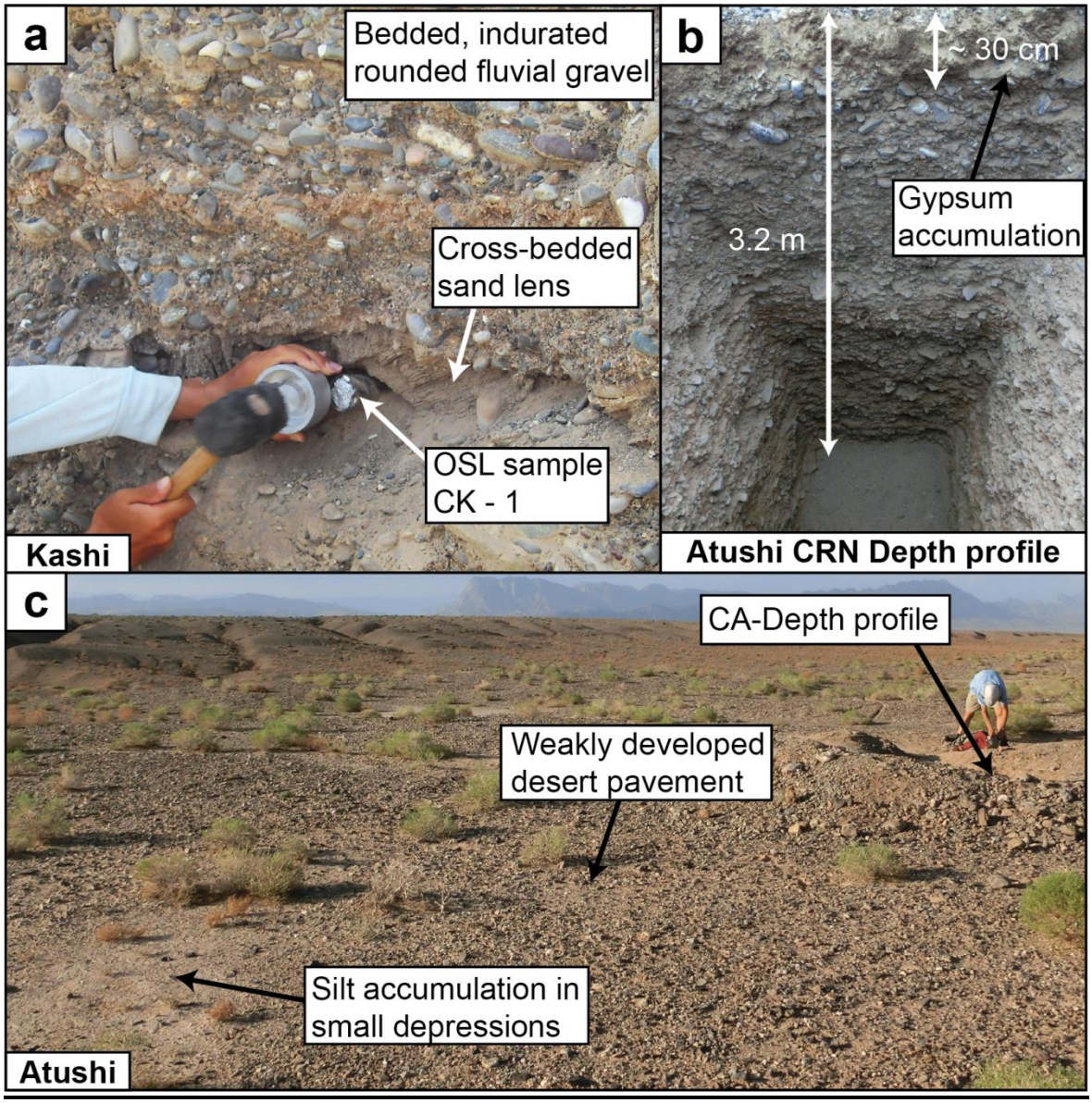

Figure S3: Field photographs showing typical structures of the gravel stratigraphy and the gravel terrace surface. (a) Close-up of typical terrace cover deposits around OSL sample CK-1 (location cf. Fig. 6) showing imbricated pebble conglomerate with a cross-bedded sand lens. (b) Depth profile on central Atushi (location cf. Fig. 6). (c) Smooth terrace top and desert pavement development close to the depth profile on central Atushi (location cf. Fig. 6).

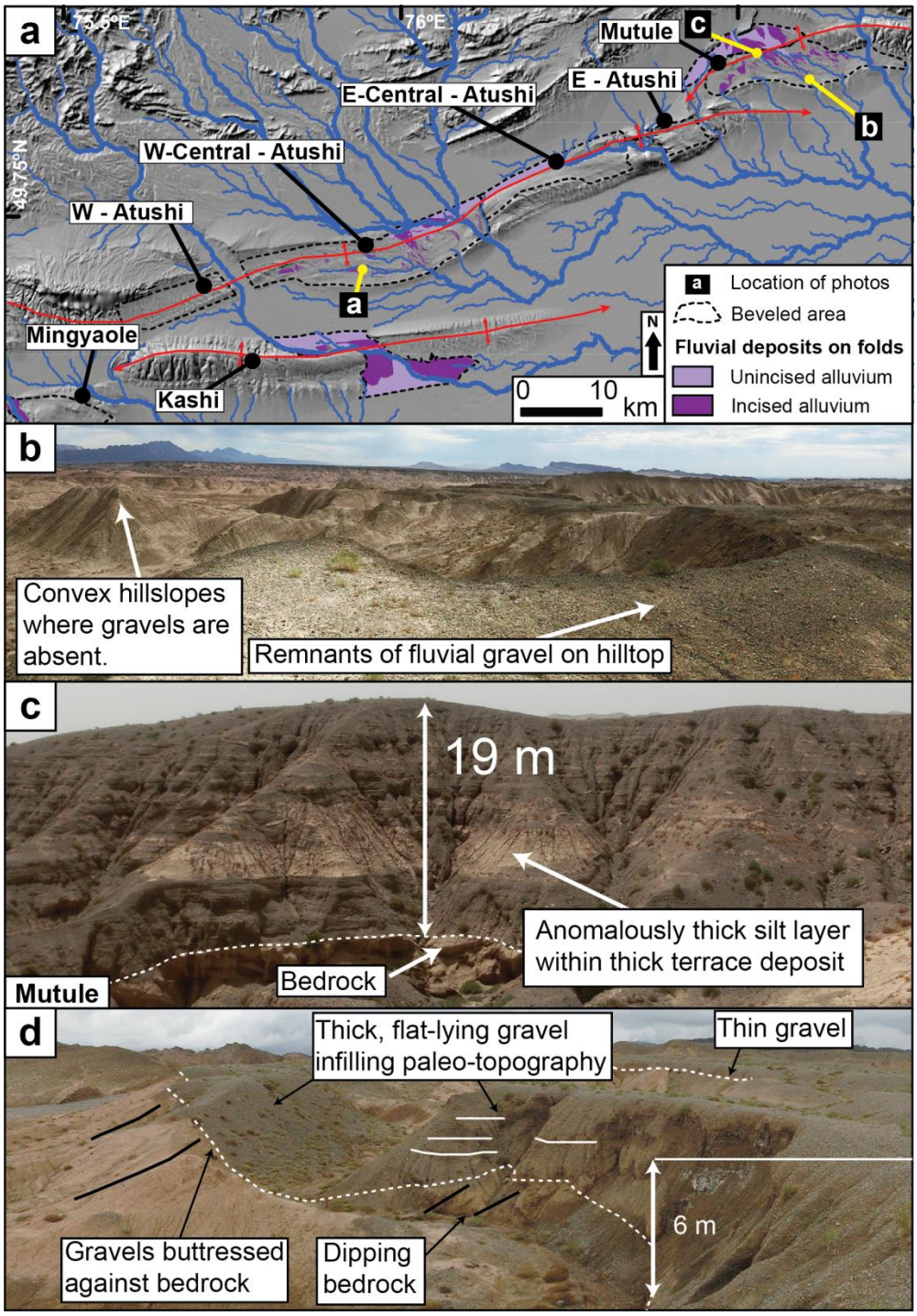

Figure S4: Field photographs of terraces in the study area. (a) Overview with locations of photographs. (b) Panorama of the incised planation surface on Atushi showing remnants of fluvial cover on otherwise bare hillslopes. (b) Terrace on Mutule showing thick fluvial gravel deposits with an anomalously thick silt layer. (c) Thick, gravels buttressed against steeply dipping bedrock on the northern Mutule fold.

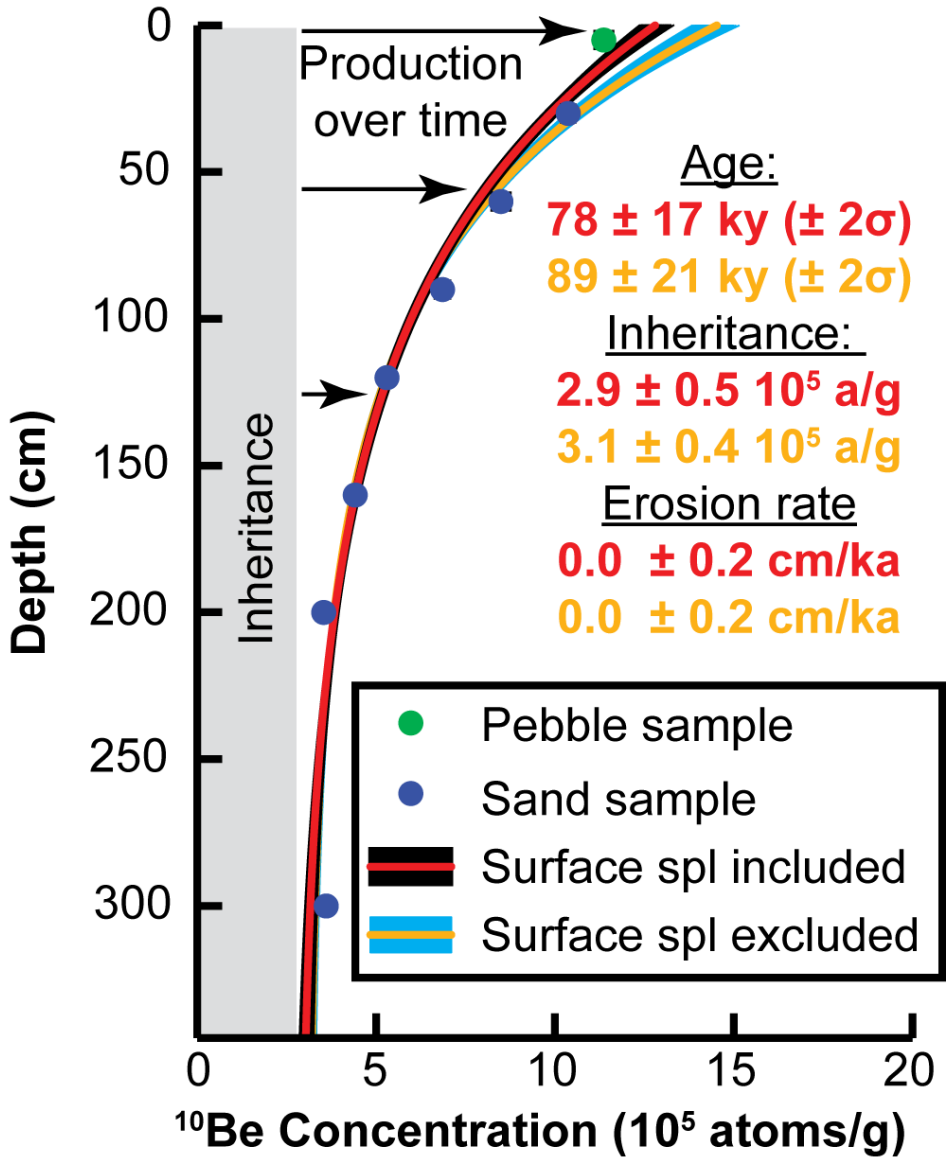

Figure S5: Fluvial terrace (T4) age on central Atushi fold based on Monte Carlo simulation (Hidy et al., 2010) of a cosmogenic nuclide depth profile (CA-DP1). For profile location, see Fig. 6. The data points are larger than the 2σ analytical uncertainties. Two simulations, either including the surface pebble sample (red line and black shading) or excluding it (orange line and blue shading) are shown. The central lines (red and orange) mark the best fit, whereas the bars (black and blue) show the range of fitted profiles from 2 x 10^5 simulations (Table A7). The ages shown are for the time-independent scaling scheme of Stone (2000), based on Lal (1991). They are obtained using the best-fit surface concentration of ^{10}Be atoms from the Monte-Carlo simulation as an input to the CRONUS-Earth-2008-v2.3 exposure age calculator (Balco et al., 2008) (cf. Table 6). Uncertainties (±2σ) are external uncertainties as described by Balco et al. (2008). Inheritance and erosion rates (±2σ) are outputs from the Monte Carlo simulations.

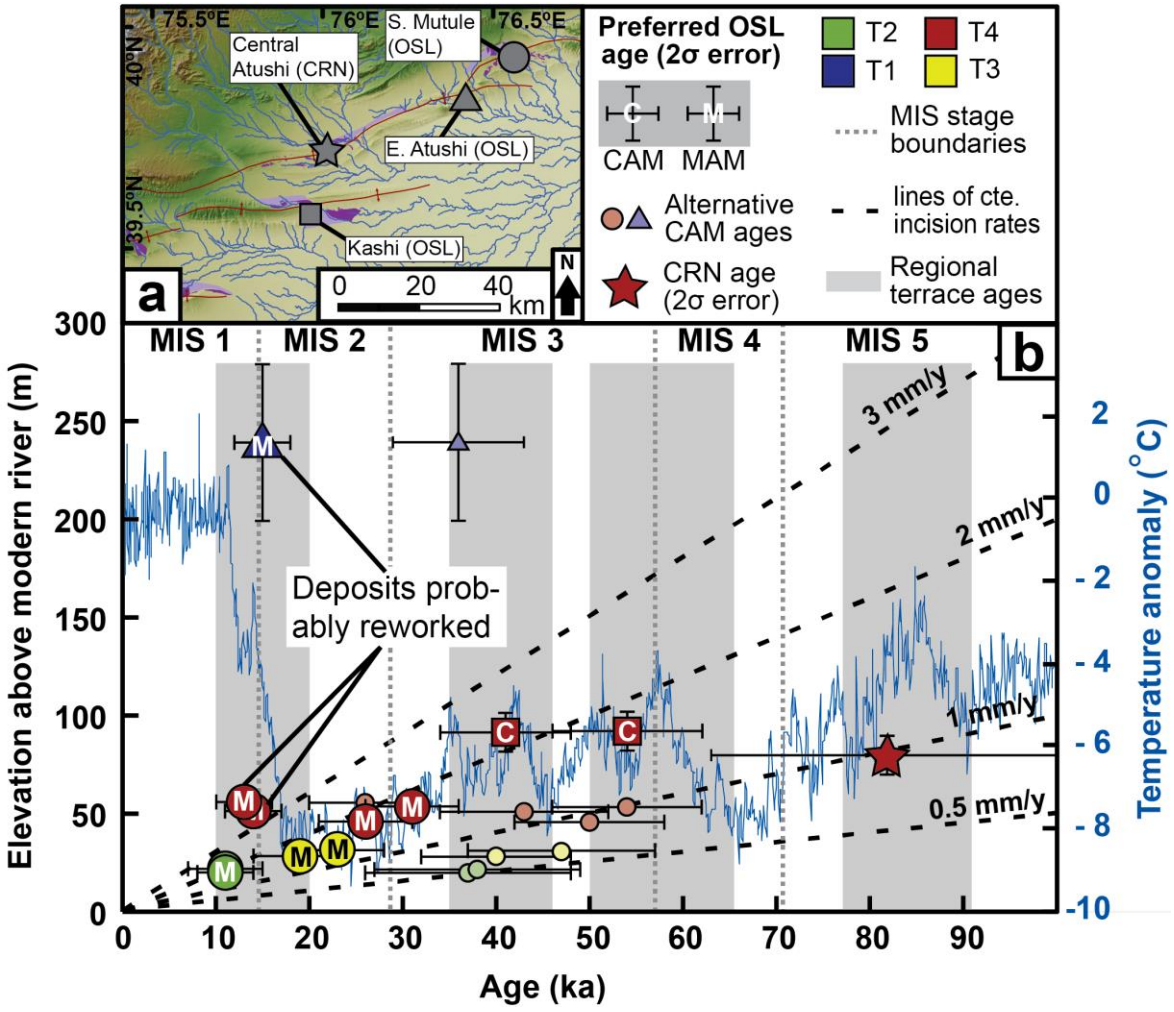

Figure S6: Terrace ages as a function of height as in Fig. 14 but including the outlier EA-2. The symbology is the same as in Figure 14. In addition, the blue data curve in the background shows the global temperature anomaly deduced from a $\delta^{18}O$ record in the Vostok ice core (Petit et al., 1999).

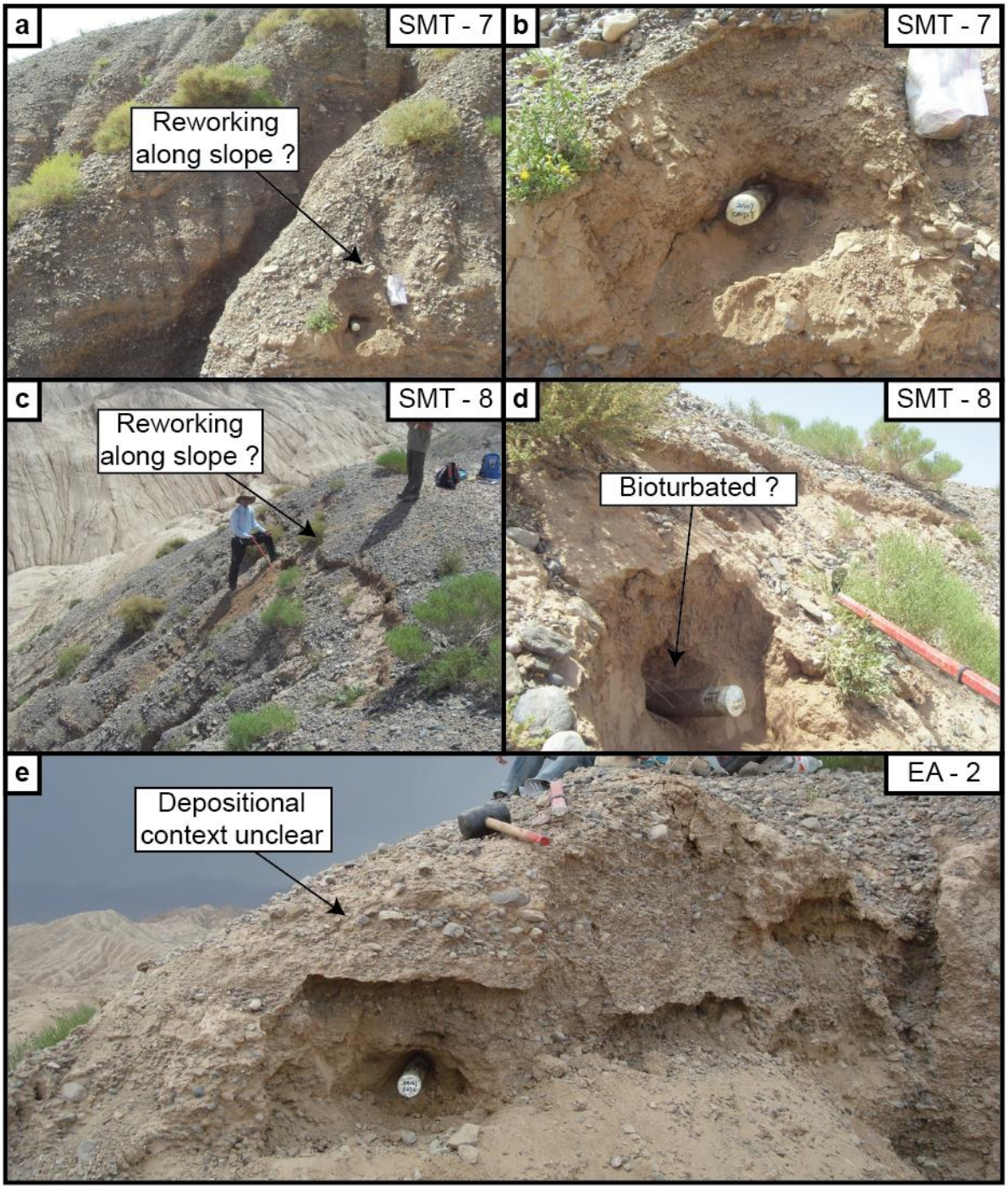

Figure S7: Field photographs of the three OSL samples that yielded ages outside of stratigraphic sequence.

Chapter 3: Spatial and temporal dynamics of folds in the foreland of the Tian Shan from geodetic and geologic rock-uplift rates[c]

Aaron Bufe[1,2], David Bekaert[3], Ekbal Hussain[4], Bodo Bookhagen[2,5], Douglas W. Burbank[1,2], Jessica A. Thompson[6], Chen Jie[7], Li Tao[8], Liu Langtao[9], Weijun Gan[7]

[1]Department of Earth Sciences, University of California, Santa Barbara, California, 93106, USA

[2]Earth Research Institute, University of California, Santa Barbara, California, 93106, USA

[3]Jet Propulsion Laboratory, California Institute of Technology, Pasadena, California, USA.

[4]School of Earth and Environment, University of Leeds, Leeds, UK.

[5]Institute of Earth and Environmental Science, University of Potsdam, Potsdam-Golm, Germany.

[6]Institute of Tectonic Studies, Department of Geological Sciences, University of Texas, El Paso, Texas, 79902, USA

[7]State Key Laboratory of Earthquake Dynamics, Institute of Geology, China Earthquake Administration, Beijing China.

[8]Department of Earth Sciences, San Yat-Sen University, Guangzhou, 510275, China

[9]Department of Earth Science and Engineering, Hebei University of Engineering, Handan, China

[c]Adapted from: Bufe et al., (in preparation for Geophysical Research Letters), Spatial and temporal dynamics of folds in the foreland of the Tian Shan from geodetic and geologic rock-uplift rates

Abstract

A major challenge in understanding the evolution of continental deformation zones lies in quantifying spatial and temporal changes in deformation rates of tectonic structures. Here, along the eastern boundary of the Pamir-Tian Shan collision zone, we constrain the probable evolution of rock-uplift rates for a series of five Quaternary detachment- and fault-related folds from their initiation to the modern day. A decomposition of interferometric synthetic aperture radar time-series and GPS data constrains the spatial pattern of surface- and rock-uplift on the folds deforming at decadal rates of 1-5 mm/y. Along strike of two major detachment folds, these rates culminate close to their centers and drop to zero across their tips which span 10-25% of the length of the structure. Such spatially varying deformation rates, together with geologic evidence for coeval fold propagation, suggest that uplift rates on geologic (10^5-10^6 yr) timescales vary gradually as opposed to by step-wise changes. This supposition motivates a simple, three-phase model of uplift-rate evolution, with an acceleration of rates after fold initiation, followed by steady uplift rates, and then a subsequent phase of acceleration or deceleration. Using a Monte Carlo simulation to fit our geodetic and previously published geologic uplift rates, we find that, where average uplift rates calculated across different time intervals are relatively similar, the most probable uplift-rate evolution of the structure is a rapid acceleration of uplift after fold initiation, followed by constant uplift rates. In contrast, where those average uplift rates change by more than a 1 mm/y, smoothly varying velocities are more likely.

1 Introduction

Deformation rates across individual tectonic structures underpin an understanding of the dynamics of continental deformation zones and their seismic hazards. Whereas the mechanics for many types of folds and faults are well-understood (Allmendinger, 1998; Epard and Groshong Jr, 1995; Hubert-Ferrari et al., 2007; Li et al., 2013; Poblet and McClay, 1996; Suppe, 1983; Suppe and Medwedeff, 1990; Suppe et al., 1997; Yan et al., 2016), commonly unknown temporal and spatial differences in deformation rates complicate the reconstruction of the kinematic history of deformation zones. After initiation, faults and folds commonly lengthen with annual rates of lateral propagation ranging from a few millimeters to several centimeters (Burbank et al., 1996; Chen et al., 2007; Jackson et al., 2002), until they encounter barriers that pin the tips of the structure (Amos et al., 2010; Dawers et al., 1993; Manighetti et al., 2001). Commonly, a near block-like pattern of incremental slip is assumed with constant slip rate along the structure, rapidly decreasing to zero at the tips (Amos et al., 2010; Manighetti et al., 2001). Such models produce spatially constant uplift rates, except at the tips. Nonetheless, block-like incremental slip is not necessary and spatially varying deformation rates have been shown to occur, for example, along laterally tilting (Li et al., 2013), propagating (Amos et al., 2010), or segmented (Anders and Schlische, 1994; Davis et al., 2005; Dawers et al., 1993) structures. In addition to spatial variations of slip rates, deformation varies temporally. Changes in the distribution of strain across fault zones and mountain ranges (Oskin et al., 2007; Thompson et al., 2002), foreland propagation of deformation (Heermance et al., 2008; Hubert-Ferrari et al., 2007), propagation of asperities along structures (Hilley and Arrowsmith, 2008), loading or unloading of the crust by water or ice (Hampel et al., 2007), or reorganization of strain

across plate boundaries (Allen et al., 2004; Clark, 2012; Friedrich et al., 2003; Molnar and Stock, 2009; Sobel et al., 2006) can cause decadal to million-year variations in slip rates. Moreover, stochastic or cyclic temporal variations in deformation rates due, for example, to the clustering of strain release (Chevalier et al., 2005; Friedrich et al., 2003; Grant and Sieh, 1994; Marco et al., 1996; Meade and Hager, 2004; Oskin et al., 2008), seasonal water loading (Bettinelli et al., 2008), or changes throughout a seismic cycle (Cattin and Avouac, 2000; Hilley et al., 2009; Thatcher, 1984) can contribute to such changes.

Slip-rate variations of single structures on geologic timescales are inferred from rate measurements across multiple time-intervals and, in the absence of additional evidence, are commonly described as step-like changes (Heermance et al., 2008; Hubert-Ferrari et al., 2007; Oskin et al., 2007). Measuring gradual rate-changes requires a density of data not commonly available, but rather assumes a functional form that can be fitted to the measurements (Gourmelen et al., 2011).

From a decomposition of interferometric synthetic aperture radar (InSAR) time-series and GPS data, we constrain the spatial pattern of surface-uplift rates for a series of Quaternary contractional structures along the rapidly deforming eastern boundary of the Pamir-Tian Shan collision zone. Assuming uplift of sparsely eroded surfaces to be equivalent to rock-uplift, these data are then compared with geologic rates. The spatial and temporal patterns on two, well-resolved detachment anticlines support a model of gradually changing rock-uplift rates. Therefore, in addition of fitting temporal changes in uplift rates with a simple step function, we use a Monte Carlo model to constrain the probable temporal evolution of the uplift rate. Step-changes in vertical velocities at the time of fold initiation are among the most probable fits to the data for folds where geologic samples (0.1-1.6 My

old) record similar average uplift rates. Where major changes in average uplift rates are measured over time, step functions are contained within the 95% confidence interval, but gradually varying uplift rates are more probable. With only three data points for uplift rates across a time interval of 0.5-1.6 My on a given fold, considerable uncertainties remain on a fold's uplift-rate evolution. However, our modeling framework yields ranges of probable temporal variations in uplift-rates that are distinct for different structures and can, therefore, constrain the range of likely kinematic evolution of contractional structures.

2 Geologic setting

The Pamir and Tian Shan jointly accommodate 20-25 mm/y (nearly 50%) of the total Indo-Asian shortening rate (Abdrakhmatov et al., 1996; Zubovich et al., 2010) (Fig. 1). About 11 ± 3 mm/y of shortening are taken up across the ~70 ± 10-km-wide boundary between the two orogens (Fig. 1a, b). At the eastern edge of the Pamir, deformation along the Main Pamir Thrust appears to have mostly ceased (Sobel et al., 2011; Thompson et al., 2015), and stepped northward, where it interferes with the southern Tian Shan (Fig. 1c). Here, the Pamir Frontal Thrust (PFT), the Mingyaole detachment fold, and the Mushi fault-tip fold have been accommodating a total Late Quaternary shortening of ~6-7 mm/y (Li et al., 2012; Li et al., 2015; Li et al., 2013). To the east of the PFT, deformation along the Tarim basin-Tian Shan boundary has stepped southward from the South Tian Shan thrust into the Kashi foreland basin over the past 25 My, causing the initiation, growth, and abandonment of a series of southward-younging structures (Fig. 1c) (Heermance et al., 2008). The most recent deformation occurs on a series of anticlines: the Kashi and Atushi detachment folds, and the Mutule fold (Fig. 1c) that have accommodated > 2-3 mm/y of shortening since their initiation 1-2 My ago (Heermance et al., 2008; Scharer et al., 2004).

Currently, structures to the north of these folds, such as the Keketamu and Tashipisake anticlines, appear to be mostly inactive (Heermance et al., 2008): an interpretation consistent with the absence of modern shallow seismicity in that region (Fig. 1c).

3 Methods and data

InSAR time-series analysis of Envisat-ASAR data from two ascending tracks (55 and 284) and two descending tracks (191 and 420) was performed using the Stanford Method for Persistent Scatterers (StaMPS) (Hooper et al., 2012; Hooper et al., 2004) (Fig. S1, Table S1). Topography was removed with a 90-m-resolution SRTM digital elevation model (Farr et al., 2007) and atmospheric phase delays were corrected with the Toolbox for Reducing Atmospheric InSAR Noise (TRAIN) (Bekaert et al., 2015). An interpolated northward velocity field from published GPS data (Zubovich et al., 2010), together with ascending and descending InSAR time-series, were then used to decompose the geodetic InSAR velocities into northward, eastward, and vertical components (Bürgmann et al., 2006; Wright et al., 2004; Yun et al., 2006). Additional information on the time-series analysis and decomposition can be found in the supporting material. In the remainder of the analysis, we use only the decomposed vertical velocity field as a measure of absolute decadal surface-uplift rates. Peak decadal surface-uplift rates were measured on 10-km-wide swath profiles plotted approximately perpendicular to the strike of thrust faults and/or the trend of fold axes (Figs. S5, S6, S7, Table S2). The weighted arithmetic means and corresponding standard errors were calculated in 1-by-10-km bins along the length of the 10-km-wide swath profiles. Decadal peak uplift rates were then specified as the maximum of the binned InSAR velocities across each structure. The resulting decadal surface-uplift rates of major tectonic

structures are assumed to largely reflect absolute rates of rock-uplift and can, therefore, be compared with geologic rock-uplift rates.

Published initiation ages and structural cross-sections for the Mingyaole (Chen et al., 2005; Li et al., 2015), Kashi (Chen et al., 2007), and Atushi (Heermance et al., 2008; Scharer et al., 2004) folds were used to calculate rock-uplift rates above the surrounding basin since initiation of the structures (Table 1, S3). For the Mutule fold, we estimated initiation on the basis of the interference of the structure with the Atushi fold to the west (Fig. 1c), and we used a published structural cross-section (Bufe et al., in review) to calculate a rock-uplift rate (Table 1). Finally, we compiled Late Quaternary surface-uplift rates of structures across the study area from ages on landforms uplifted with respect to either a river or the footwall of a thrust (Bufe et al., 2014; Li et al., 2012; Li et al., 2015; Li et al., 2013; Thompson et al., in review) (Tables 1, S3). Because all dated landforms are largely unaffected by erosion, these surface uplifts can be, again, assumed to be equivalent to rock-uplift. For two terraces with ages obtained through both optically stimulated luminescence and cosmogenic radionuclide (CRN) dating, we used the CRN dates because they have been shown to be more reliable in this region (Thompson et al., in review).

A comparison of uplift rates among multiple structures assumes a common base level. Vertical InSAR velocities are measured with respect to regional background uplift rates estimated from the swath profiles. Hanging-wall uplift of thrust faults on geologic timescales is also measured with respect to the local footwall. In contrast, surface uplift from elevated fluvial terraces is measured with respect to the level of the modern river. Therefore, a comparison of geologic with decadal rates requires that the local base level reliably approximates base-level changes in the modern river. Finally, the rock uplift since initiation

of folding was measured on structural cross-sections drawn perpendicular to the fold axes. In all cross-sections, the sloping beds of the outer limbs of the structures have to be projected into the subsurface, and the positions of the outermost hinges and, therefore, total stratal thickness, have to be estimated. Hence, we assign a 2σ uncertainty of $\pm$ 500 m to all measurements of cumulative uplift estimated from geologic cross-sections (Table 1).

4 Results

The decomposition of the InSAR time-series clearly resolves 10- to 20-km-wide zones of surface uplift centered above nearly all structures in the study area that are interpreted or known to have been active during the Quaternary (Fig. 2). These vertical velocities on active structures are smooth across track boundaries (Fig. 2). Apparent breaks across track boundaries, such as across track 284 along the eastern part of the Keketamu anticline north of Atushi (Figs 2, S2, S3), mark signals that are present in only one of the tracks and are most likely errors due to atmospheric disturbances. No correlation of the vertical InSAR velocities with topography is apparent (Figs. 3, S6, S7), thereby supporting the interpretation of a tectonic origin of the signal across Quaternary structures (Figs. 4, S6).

We find surface-uplift rates are highest in the west and in the center of the scene, along the Pamir Frontal Thrust (PFT), the Mushi anticline, and the Kashi anticline (Fig. 2). Whereas our data might show some recent uplift along the South Tian Shan Thrust, the Main Pamir Thrust, as well as the Tian Shan foreland north and east of the Atushi fold (including the Mutule fold), appear to be inactive (Fig. 2). It cannot be ruled out that a lack of surface uplift is associated with interseismic locking of structures (Harris and Segall, 1987) or to slip-rate variations during a seismic cycle (Cattin and Avouac, 2000; Hilley et al., 2009; Thatcher, 1984). Nevertheless, this pattern is consistent with inferred basinward

propagation of the deformation front over the past 25 My (Heermance et al., 2008; Thompson et al., 2015). The entire region covered by the InSAR data appears to be uplifting at a fairly consistent background rate of ~ 1.5 ± 0.5 mm/y (±2σ) as estimated from swath profiles drawn perpendicular to the strike of major structures (Figs. S6, S7).

Six-km-wide swaths aligned along the axis of each active structure reveal significant spatial variations in decadal surface-uplift rates (Fig. 3). The Kashi and Atushi detachment folds show a broad, bow-shaped pattern with peak rates close to their centers (Fig. 3). Surface-uplift rates drop sharply at the tips of the folds with a tip-zone length spanning 10-25% of the length of the structure. Such a tip-zone is consistent with commonly inferred incremental slip-rate distributions along folds and faults (Amos et al., 2010; Manighetti et al., 2001). Comparisons of rates for the propagating tip of eastern Kashi versus the pinned tips of Atushi and western Kashi show no clear differences. Similar to these two detachment folds, the Mushi fold also shows peak surface-uplift rates close to its center, but the peak is narrower and higher. Whereas post-seismic effects from the nearby 1985 M_s 7.4 Wuqia earthquake to the west of Mushi (Fig. 1c) cannot be ruled out, the gradual decrease of surface-uplift rates toward the eastern tip of the fold is consistent with observed lateral tilting of fluvial terraces since at least 130 ka (Li et al., 2013). In contrast to these well-defined patterns, spatial surface variations of uplift rate along the Pamir Frontal Thrust and the Mingyaole fold are more complex. Uncertainties in the InSAR data, interference of structures, and fault segmentation could cause these variations. Thus, possibly, the tips of the Mingyaole fold uplift faster due to interference with the Kashi fold (to the east) and the PFT (to the west).

Assuming that peak decadal surface-uplift rates on major structures are dominated by rock-uplift, as described above, we find that average rock-uplift rates measured (1) since fold-initiation, (2) across the last 10-80 ky, and (3) across a 7-year (InSAR) interval have either stayed constant or have slightly increased along frontal structures: the PFT and the Mushi and Kashi folds (Fig. 4). In contrast, rock-uplift rates on the more hinterland Mutule and Atushi folds have decreased (Fig. 4). Such spatial patterns are consistent with basinward propagation of peak strain rates (Heermance et al., 2008; Thompson et al., 2015).

5 Monte Carlo modeling of gradually changing rock-uplift rates

Although changes in rock-uplift rate measured across different time intervals (Fig. 4) can be easily fit by linearly connecting single measurements of cumulative displacements (Fig. 5a), this strategy results in step-changes of uplift rates at the times defined solely by dated samples (Fig. 5b). Sometimes such abrupt velocity changes can be linked to geologic triggers (Hampel et al., 2007). However, even if such abrupt changes occurred, their precise timing is unlikely to be captured, given the relative paucity of sample ages. Moreover, we argue here that gradual changes in velocity of a single structure are more likely than step-changes (Gourmelen et al., 2011). Imagine a fold with instantaneous rock-uplift rates that drop smoothly to zero toward the tip of the structure (Figs. 3a, c-d, 5c). If such a tip is propagating, the uplift rate in the migrating tip zone will increase through time (Fig. 5d). If the increase in rates is slow enough, a spatial difference in long-term uplift rates will also be seen in the long-term average uplift rates: a case for which the Kashi fold might be an example (points *g* and *i:* Fig. 3c). Even structures lacking propagating tips might accelerate after initiation and decelerate toward the cessation of deformation (Gourmelen et al., 2011). Slip rates can also vary in a more complex sequence of accelerations and decelerations

(Chevalier et al., 2005), but with constraints of rates across only three timescales, we are unable to resolve such intermediate fluctuations.

In order to understand the possible range of uplift-rate changes that fit our data, we explore a simple three-phase scenario with an initial phase of velocities increasing from zero ($v_3 = 0$) at the time of initiation (t_3) to an intermediate value (v_2) at some unknown time (t_2) (Fig. 6a). The velocity then remains steady ($v_1 = v_2$), until it increases or decreases at time (t_1) to the final velocity (v_0) at the modern day ($t_0 = 0$) (Fig. 6a). For each iteration of the Monte Carlo simulation, t_3 is picked from a normal distribution defined by the mean age (and its uncertainty) of the initial folding, and v_0 is picked from a normal distribution constrained by the peak InSAR velocity (Table S2). In turn, t_1, t_2, and v_1=v_2 are picked from uniform distributions with boundary conditions $0 \leq t_2 \leq t_3$, $0 \leq t_1 \leq t_2$, and $0 \leq v_1 \leq 10$ mm/y. We explicitly note here, that t_1 and t_2 are each allowed to be zero, equal to t_3, or equal to each other, which includes a range of scenarios, such as a steady increase of velocity, constant uplift rates across the entire lifecycle of the fold, or an instantaneous increase of uplift rate to a maximum value and followed by a steady decrease. For each randomly generated uplift-rate scenario, we calculate the cumulative uplift since the initiation time t_3, and since a time t_x. The latter time is picked from the normally distributed age of the Late Quaternary uplift-rate estimates (green points in Figs. 3 & 4). Finally, each uplift-rate scenario is assigned a likelihood value which is the product of 1) the probability of the chosen value of the initiation age (t_3) within the uncertainty of the geologic measurement (Table 1), 2) the probability of the final velocity in the model run (v_0) given the a normally distributed estimate of the peak decadal velocity, 3) the probability of t_x within the uncertainty of the Late Quaternary geologic sample age, 4) the probability of the predicted

cumulative uplift since t_3, and 5) the probability of the predicted cumulative uplift since t_x. Therefore, the likelihood of the fit represents both the probability of picking that particular scenario, as well as its goodness of fit to the geologic rock-uplift data.

Curves within 95% of the maximum probability for all folds show a variety of likely uplift-rate scenarios (Fig. 6). For structures with two separate averages of geologic uplift rates, e.g., derived from dated strath terraces and total rock uplift since fold initiation, that are similar in magnitude, a step-like function of instantaneous uplift appears probable (Mushi - Fig. 6c, Fig. 7a). In contrast, where average uplift rates measured across Late Quaternary timescales have increased compared to the rate since initiation of the structure, a more gradual change in uplift rate through time is predicted by a higher number of model solutions (Mingyaole - Fig. 6b, Fig. 7b). More intermediate patterns, with gradual uplift-rate changes for 10-50% of the structure's evolution, and with long plateaus in-between, occur where measured velocities across different time-intervals are similar (within a few fractions of a millimeter) (Kashi, Figs. 6d, e). Finally, where uplift rates have decreased significantly over time, gradual changes in rates are also likely (Atushi-Mutule, Figs. 6f-h, Fig. 7c). Such patterns appear fairly consistent along strike of the structures (Figs. 6d/e, 6f/g). We note that decreasing the maximum permitted velocity does not change the overall pattern of these results except by eliminating any solutions that extend beyond that maximum velocity.

6 Discussion

The careful decomposition of InSAR data presented in this study resolves surface-uplift rates of individual, ≤10-km-wide structures over the past decade in an unprecedented detail. The correlation of decadal surface-uplift rates with geologic outlines of the structures, the absence of a strong correlation between elevation and InSAR velocities, the consistency of

peak surface-uplift rates across track boundaries, and their smooth variation along the structure support the interpretation of a tectonic origin for the InSAR signal on the Pamir frontal thrust (PFT), and the Mushi, Mingyaole, Kashi, Atushi, and Mutule folds (Fig. 2). The consistency between the broad spatial patterns of geologic and geodetic uplift rates on the structures (Fig. 3) suggests that large-scale (> 10s of kms) patterns of decadal velocities can inform longer-term trends. Our data confirm previous findings of the basinward propagation of tectonic activity and lend further support to the assumed, but debated, inactivity of the Main Pamir Thrust (Sobel et al., 2011; Thompson et al., 2015) and the northern Tian Shan foreland (Heermance et al., 2008). The comparison of rock-uplift rates through time suggests slowing of deformation on the Atushi and Mutule folds, whereas the locus of high strain rates is presently concentrated on the PFT and the Mushi, Mingyaole, and Kashi folds (Fig. 4).

The apparent regional background surface uplift rate of 1.5 ± 0.5 mm/y (Figs. 2, S6, S7) may be surprising. Because this uplift rate is consistent across the entire study area and across track-boundaries, it seems unlikely to be an artefact contained in one of the InSAR tracks. Assuming conservation of volume, shortening of a crustal block ~52 ± 2 km-deep (Liu et al., 2006; Zheng et al., 2008), 70 ± 10 km long (N-S) (Fig. 1) at a rate of 11 ± 3 mm/y (Fig. 1) would result in crustal thickening at a rate of 8 ± 3 mm/y. Following isostatic compensation based on typical crustal and mantle densities, the corresponding surface uplift can be estimated to be 1.5 ± 0.6 mm/y. Given uncertainties in local crustal and mantle density and thickness, a more precise calculation is unwarranted. This simple approach, however, reproduces the observed regional surface uplift rates and suggests that crustal thickening is driving surface uplift throughout the study area.

The arc-shaped spatial pattern of decadal surface- and rock-uplift rates along the Kashi, Atushi, and Mushi folds with “tip zones” in which vertical velocities are smoothly dropping to zero is inconsistent with a pure block-shape model of incremental surface uplift (Manighetti et al., 2001). Instead, it favors interpretations in which uplift rates change more gradually along strike (Fig. 5). Such changes can be well-fitted with simple uplift-rate scenarios, especially where rock-uplift rates have markedly increased or decreased through time (Figs. 6, 7). Lateral propagation rates of ~40 and ~50 mm/y have been inferred for the tips of the Kashi and Atushi folds, respectively (Chen et al., 2007; Scharer et al., 2004). Thus, within a “tip zone” length of 10 ± 5 km, a point on the Kashi or Atushi fold would be expected to accelerate for at least 200 ± 100 ky or 250 ± 130 ky, respectively. Such time-scales of acceleration are consistent with the modeled uplift-rate scenarios, although the most probable fits for to the Atushi data predict slightly shorter periods of acceleration (Figs. 6f, g).

Where structures interfere (Mingyaole fold) or are segmented (Pamir Frontal Thrust) or tilt laterally (Mushi fold), the spatial pattern of decadal uplift rates is more complicated (Fig. 3). Such complexity makes the interpretation of a “representative” modern velocity challenging. However, when combined with the Late Quaternary rates, reasonable estimates of the recent development of these structures and distinct uplift-rate scenarios can be synthesized. Whereas our models cannot define a unique uplift-rate evolution with so few data, we find distributions of probable scenarios that inform the range of kinematic evolution of compressional structures.

7 Conclusions

With a careful decomposition of InSAR data, we obtain insights into the spatial patterns of decadal surface- and rock-uplift rates along rapidly deforming contractional structures along the Tian Shan-Pamir interface. Together with geologic estimates of uplift rates on these structures, we argue that gradual, rather than stepwise, changes in deformation rates on geologic timescales are common. Distinct patterns of probable fold growth can be predicted with just three measurements of cumulative uplift across different timescales. Where rates have changed through time, probabilistic models suggest gradual changes in velocity are more likely than step-wise changes.

References

Abdrakhmatov, K. Y., Aldazhanov, S. A., Hager, B. H., Hamburger, M. W., Herring, T. A., Kalabaev, K. B., Makarov, V. I., Molnar, P., Panasyuk, S. V., Prilepin, M. T., Reilinger, R. E., Sadybakasov, I. S., Souter, B. J., Trapeznikov, Y. A., Tsurkov, V. Y., and Zubovich, A. V., 1996, Relatively recent construction of the Tien Shan inferred from GPS measurements of present-day crustal deformation rates: Nature, v. 384, no. 6608, p. 450-453.

Allen, M., Jackson, J., and Walker, R., 2004, Late Cenozoic reorganization of the Arabia-Eurasia collision and the comparison of short-term and long-term deformation rates: Tectonics, v. 23, no. 2, p. n/a-n/a.

Allmendinger, R. W., 1998, Inverse and forward numerical modeling of trishear fault-propagation folds: Tectonics, v. 17, no. 4, p. 640-656.

Amos, C. B., Burbank, D. W., and Read, S. A. L., 2010, Along-strike growth of the Ostler fault, New Zealand: Consequences for drainage deflection above active thrusts: Tectonics, v. 29, no. 4, p. n/a-n/a.

Anders, M. H., and Schlische, R. W., 1994, Overlapping Faults, Intrabasin Highs, and the Growth of Normal Faults: The Journal of Geology, v. 102, no. 2, p. 165-179.

Bekaert, D. P. S., Walters, R. J., Wright, T. J., Hooper, A. J., and Parker, D. J., 2015, Statistical comparison of InSAR tropospheric correction techniques: Remote Sensing of Environment, v. 170, p. 40-47.

Bettinelli, P., Avouac, J.-P., Flouzat, M., Bollinger, L., Ramillien, G., Rajaure, S., and Sapkota, S., 2008, Seasonal variations of seismicity and geodetic strain in the Himalaya induced by surface hydrology: Earth and Planetary Science Letters, v. 266, no. 3–4, p. 332-344.

Bufe, A., Burbank, D., Chen, J., Liu, L., Li, T., and Thompson, J., Constraints on timing and rates of strath terrace formation on actively uplifting anticlines in the foreland of the Chinese Tien Shan, *in* Proceedings AGU Fall Meeting Abstracts2014, Volume 1, p. 04.

Burbank, D., Meigs, A., and Brozović, N., 1996, Interactions of growing folds and coeval depositional systems: Basin Research, v. 8, no. 3, p. 199-223.

Burbank, D. W., and Anderson, R. S., 2011, Tectonic geomorphology, John Wiley & Sons.

Bürgmann, R., Hilley, G., Ferretti, A., and Novali, F., 2006, Resolving vertical tectonics in the San Francisco Bay Area from permanent scatterer InSAR and GPS analysis: Geology, v. 34, no. 3, p. 221-224.

Cattin, R., and Avouac, J. P., 2000, Modeling mountain building and the seismic cycle in the Himalaya of Nepal: Journal of Geophysical Research: Solid Earth, v. 105, no. B6, p. 13389-13407.

Chen, J., Heermance, R., Burbank, D. W., Scharer, K. M., Miao, J., and Wang, C., 2007, Quantification of growth and lateral propagation of the Kashi anticline, southwest Chinese Tian Shan: Journal of Geophysical Research: Solid Earth, v. 112, no. B3, p. B03S16.

Chen, J., Scharer, K., Burbank, D., Heermance, R., and Wang, C.-S., 2005, Quaternary detachment folding of the Mingyaole anticline, southwestern Tian Shan: Dizhen Dizhi(Seismology and Geology), v. 27, no. 4, p. 530-547.

Chevalier, M.-L., Ryerson, F. J., Tapponnier, P., Finkel, R. C., Van Der Woerd, J., Haibing, L., and Qing, L., 2005, Slip-Rate Measurements on the Karakorum Fault May Imply Secular Variations in Fault Motion: Science, v. 307, no. 5708, p. 411-414.

Clark, M. K., 2012, Continental collision slowing due to viscous mantle lithosphere rather than topography: Nature, v. 483, no. 7387, p. 74-77.

Davis, K., Burbank, D. W., Fisher, D., Wallace, S., and Nobes, D., 2005, Thrust-fault growth and segment linkage in the active Ostler fault zone, New Zealand: Journal of Structural Geology, v. 27, no. 8, p. 1528-1546.

Dawers, N. H., Anders, M. H., and Scholz, C. H., 1993, Growth of normal faults: Displacement-length scaling: Geology, v. 21, no. 12, p. 1107-1110.

Epard, J. L., and Groshong Jr, R. H., 1995, Kinematic model of detachment folding including limb rotation, fixed hinges and layer-parallel strain: Tectonophysics, v. 247, no. 1–4, p. 85-103.

Farr, T. G., Rosen, P. A., Caro, E., Crippen, R., Duren, R., Hensley, S., Kobrick, M., Paller, M., Rodriguez, E., Roth, L., Seal, D., Shaffer, S., Shimada, J., Umland, J., Werner, M., Oskin, M., Burbank, D., and Alsdorf, D., 2007, The Shuttle Radar Topography Mission: Reviews of Geophysics, v. 45, no. 2, p. n/a-n/a.

Friedrich, A. M., Wernicke, B. P., Niemi, N. A., Bennett, R. A., and Davis, J. L., 2003, Comparison of geodetic and geologic data from the Wasatch region, Utah, and implications for the spectral character of Earth deformation at periods of 10 to 10 million years: Journal of Geophysical Research: Solid Earth, v. 108, no. B4, p. n/a-n/a.

Gourmelen, N., Dixon, T. H., Amelung, F., and Schmalzle, G., 2011, Acceleration and evolution of faults: An example from the Hunter Mountain–Panamint Valley fault zone, Eastern California: Earth and Planetary Science Letters, v. 301, no. 1–2, p. 337-344.

Grant, L. B., and Sieh, K., 1994, Paleoseismic evidence of clustered earthquakes on the San Andreas Fault in the Carrizo Plain, California: Journal of Geophysical Research: Solid Earth, v. 99, no. B4, p. 6819-6841.

Hampel, A., Hetzel, R., and Densmore, A. L., 2007, Postglacial slip-rate increase on the Teton normal fault, northern Basin and Range Province, caused by melting of the Yellowstone ice cap and deglaciation of the Teton Range?: Geology, v. 35, no. 12, p. 1107-1110.

Harris, R. A., and Segall, P., 1987, Detection of a locked zone at depth on the Parkfield, California, segment of the San Andreas Fault: Journal of Geophysical Research: Solid Earth, v. 92, no. B8, p. 7945-7962.

Heermance, R. V., Chen, J., Burbank, D. W., and Miao, J., 2008, Temporal constraints and pulsed Late Cenozoic deformation during the structural disruption of the active Kashi foreland, northwest China: Tectonics, v. 27, no. 6, p. TC6012.

Hilley, G. E., and Arrowsmith, J. R., 2008, Geomorphic response to uplift along the Dragon's Back pressure ridge, Carrizo Plain, California: Geology, v. 36, no. 5, p. 367-370.

Hilley, G. E., Johnson, K. M., Wang, M., Shen, Z.-K., and Bürgmann, R., 2009, Earthquake-cycle deformation and fault slip rates in northern Tibet: Geology, v. 37, no. 1, p. 31-34.

Hooper, A., Bekaert, D., Spaans, K., and Arıkan, M., 2012, Recent advances in SAR interferometry time series analysis for measuring crustal deformation: Tectonophysics, v. 514–517, no. 0, p. 1-13.

Hooper, A., Zebker, H., Segall, P., and Kampes, B., 2004, A new method for measuring deformation on volcanoes and other natural terrains using InSAR persistent scatterers: Geophysical Research Letters, v. 31, no. 23, p. n/a-n/a.

Hubert-Ferrari, A., Suppe, J., Gonzalez-Mieres, R., and Wang, X., 2007, Mechanisms of active folding of the landscape (southern Tian Shan, China): Journal of Geophysical Research: Solid Earth, v. 112, no. B3, p. n/a-n/a.

Jackson, J., Ritz, J.-F., Siame, L., Raisbeck, G., Yiou, F., Norris, R., Youngson, J., and Bennett, E., 2002, Fault growth and landscape development rates in Otago, New Zealand, using in situ cosmogenic 10Be: Earth and Planetary Science Letters, v. 195, no. 3–4, p. 185-193.

Li, T., Chen, J., Thompson, J. A., Burbank, D. W., and Xiao, W., 2012, Equivalency of geologic and geodetic rates in contractional orogens: New insights from the Pamir Frontal Thrust: Geophysical Research Letters, v. 39, no. 15, p. L15305.

Li, T., Chen, J., Thompson, J. A., Burbank, D. W., and Yang, H., 2015, Hinge-migrated fold-scarp model based on an analysis of bed geometry: A study from the Mingyaole anticline, southern foreland of Chinese Tian Shan: Journal of Geophysical Research: Solid Earth, v. 120, no. 9, p. 6592-6613.

Li, T., Chen, J., Thompson, J. A., Burbank, D. W., and Yang, X., 2013, Quantification of three-dimensional folding using fluvial terraces: A case study from the Mushi anticline, northern margin of the Chinese Pamir: Journal of Geophysical Research: Solid Earth, v. 118, no. 8, p. 4628-4647.

Liu, M., Mooney, W. D., Li, S., Okaya, N., and Detweiler, S., 2006, Crustal structure of the northeastern margin of the Tibetan plateau from the Songpan-Ganzi terrane to the Ordos basin: Tectonophysics, v. 420, no. 1–2, p. 253-266.

Manighetti, I., King, G. C. P., Gaudemer, Y., Scholz, C. H., and Doubre, C., 2001, Slip accumulation and lateral propagation of active normal faults in Afar: Journal of Geophysical Research: Solid Earth, v. 106, no. B7, p. 13667-13696.

Marco, S., Stein, M., Agnon, A., and Ron, H., 1996, Long-term earthquake clustering: A 50,000-year paleoseismic record in the Dead Sea Graben: Journal of Geophysical Research: Solid Earth, v. 101, no. B3, p. 6179-6191.

Meade, B. J., and Hager, B. H., 2004, Viscoelastic deformation for a clustered earthquake cycle: Geophysical Research Letters, v. 31, no. 10, p. n/a-n/a.

Molnar, P., and Stock, J. M., 2009, Slowing of India's convergence with Eurasia since 20 Ma and its implications for Tibetan mantle dynamics: Tectonics, v. 28, no. 3, p. n/a-n/a.

Oskin, M., Perg, L., Blumentritt, D., Mukhopadhyay, S., and Iriondo, A., 2007, Slip rate of the Calico fault: Implications for geologic versus geodetic rate discrepancy in the Eastern California Shear Zone: Journal of Geophysical Research: Solid Earth, v. 112, no. B3, p. n/a-n/a.

Oskin, M., Perg, L., Shelef, E., Strane, M., Gurney, E., Singer, B., and Zhang, X., 2008, Elevated shear zone loading rate during an earthquake cluster in eastern California: Geology, v. 36, no. 6, p. 507-510.

Poblet, J., and McClay, K., 1996, Geometry and kinematics of single-layer detachment folds: AAPG Bulletin, v. 80, no. 7, p. 1085-1109.
Scharer, K. M., Burbank, D. W., Chen, J., Weldon, R. J., Rubin, C., Zhao, R., and Shen, J., 2004, Detachment folding in the Southwestern Tian Shan–Tarim foreland, China: shortening estimates and rates: Journal of Structural Geology, v. 26, no. 11, p. 2119-2137.
Sobel, E. R., Chen, J., and Heermance, R. V., 2006, Late Oligocene–Early Miocene initiation of shortening in the Southwestern Chinese Tian Shan: Implications for Neogene shortening rate variations: Earth and Planetary Science Letters, v. 247, no. 1–2, p. 70-81.
Sobel, E. R., Schoenbohm, L. M., Chen, J., Thiede, R., Stockli, D. F., Sudo, M., and Strecker, M. R., 2011, Late Miocene–Pliocene deceleration of dextral slip between Pamir and Tarim: Implications for Pamir orogenesis: Earth and Planetary Science Letters, v. 304, no. 3–4, p. 369-378.
Suppe, J., 1983, Geometry and kinematics of fault-bend folding: American Journal of science, v. 283, no. 7, p. 684-721.
Suppe, J., and Medwedeff, D. A., 1990, Geometry and kinematics of fault-propagation folding: Eclogae Geologicae Helvetiae, v. 83, no. 3, p. 409-454.
Suppe, J., Sàbat, F., Anton Muñoz, J., Poblet, J., Roca, E., and Vergés, J., 1997, Bed-by-bed fold growth by kink-band migration: Sant llorenç de Morunys, eastern Pyrenees: Journal of Structural Geology, v. 19, no. 3–4, p. 443-461.
Thatcher, W., 1984, The earthquake deformation cycle, recurrence, and the time-predictable model: Journal of Geophysical Research: Solid Earth, v. 89, no. B7, p. 5674-5680.
Thompson, J. A., Burbank, D. W., Li, T., Chen, J., and Bookhagen, B., 2015, Late Miocene northward propagation of the northeast Pamir thrust system, northwest China: Tectonics, p. 2014TC003690.
Thompson, J. A., Chen, J., Yang, H., Li, T., Bookhagen, B., and Burbank, D. W., in review, Coarse- versus fine-grain OSL and cosmogenic 10Be dating of deformed fluvial terraces on the northeast Pamir margin, northwest China: Quaternary Geochronology.
Thompson, S. C., Weldon, R. J., Rubin, C. M., Abdrakhmatov, K., Molnar, P., and Berger, G. W., 2002, Late Quaternary slip rates across the central Tien Shan, Kyrgyzstan, central Asia: Journal of Geophysical Research: Solid Earth, v. 107, no. B9, p. 2203.
Wright, T. J., Parsons, B. E., and Lu, Z., 2004, Toward mapping surface deformation in three dimensions using InSAR: Geophysical Research Letters, v. 31, no. 1, p. n/a-n/a.
Yan, D.-P., Xu, Y.-B., Dong, Z.-B., Qiu, L., Zhang, S., and Wells, M., 2016, Fault-related fold styles and progressions in fold-thrust belts: Insights from sandbox modeling: Journal of Geophysical Research: Solid Earth, p. n/a-n/a.
Yun, S., Segall, P., and Zebker, H., 2006, Constraints on magma chamber geometry at Sierra Negra Volcano, Galápagos Islands, based on InSAR observations: Journal of Volcanology and Geothermal Research, v. 150, no. 1–3, p. 232-243.
Zheng, S., Sun, X., Song, X., Yang, Y., and Ritzwoller, M. H., 2008, Surface wave tomography of China from ambient seismic noise correlation: Geochemistry, Geophysics, Geosystems, v. 9, no. 5, p. Q05020.

Zubovich, A. V., Wang, X.-q., Scherba, Y. G., Schelochkov, G. G., Reilinger, R., Reigber, C., Mosienko, O. I., Molnar, P., Michajljow, W., Makarov, V. I., Li, J., Kuzikov, S. I., Herring, T. A., Hamburger, M. W., Hager, B. H., Dang, Y.-m., Bragin, V. D., and Beisenbaev, R. T., 2010, GPS velocity field for the Tien Shan and surrounding regions: Tectonics, v. 29, no. 6, p. TC6014.

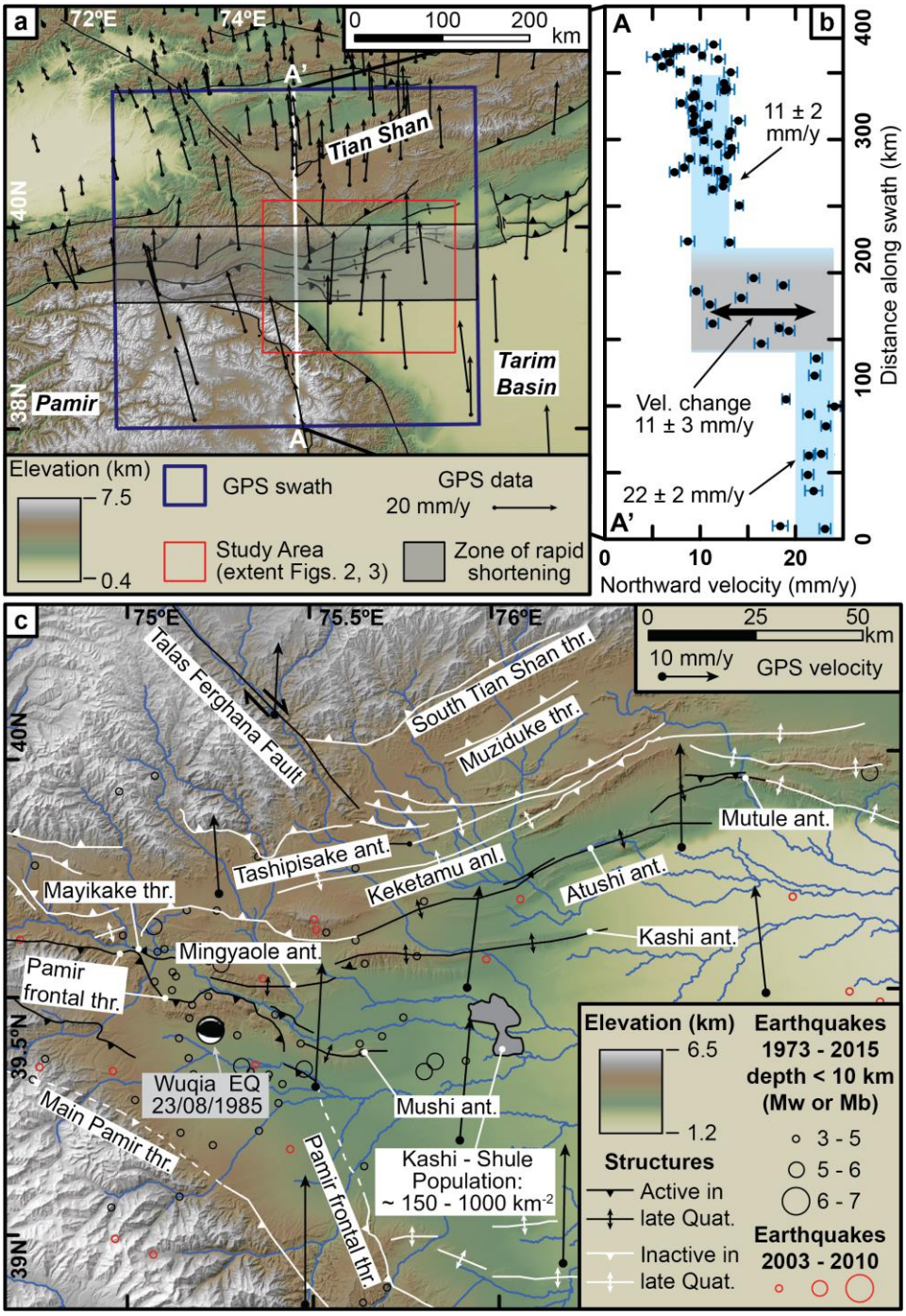

Figure 1: Overview of the study area. (a) Regional map of the Pamir and Tian Shan with horizontal GPS velocities (Zubovich et al., 2010). (b) Northward component of the GPS velocity in the 400 km-wide swath along A-A'. The grey area corresponds to the grey area in (a). (c) Digital elevation model of the study area showing a series of faults and folds in the foreland of the Tian Shan and Pamir. The Late Quaternary activity of structures (black and white lines) is based on geologic evidence published in previous studies (Chen et al., 2007; Heermance et al., 2008; Li et al., 2012; Li et al., 2015; Li et al., 2013; Thompson et al., 2015).

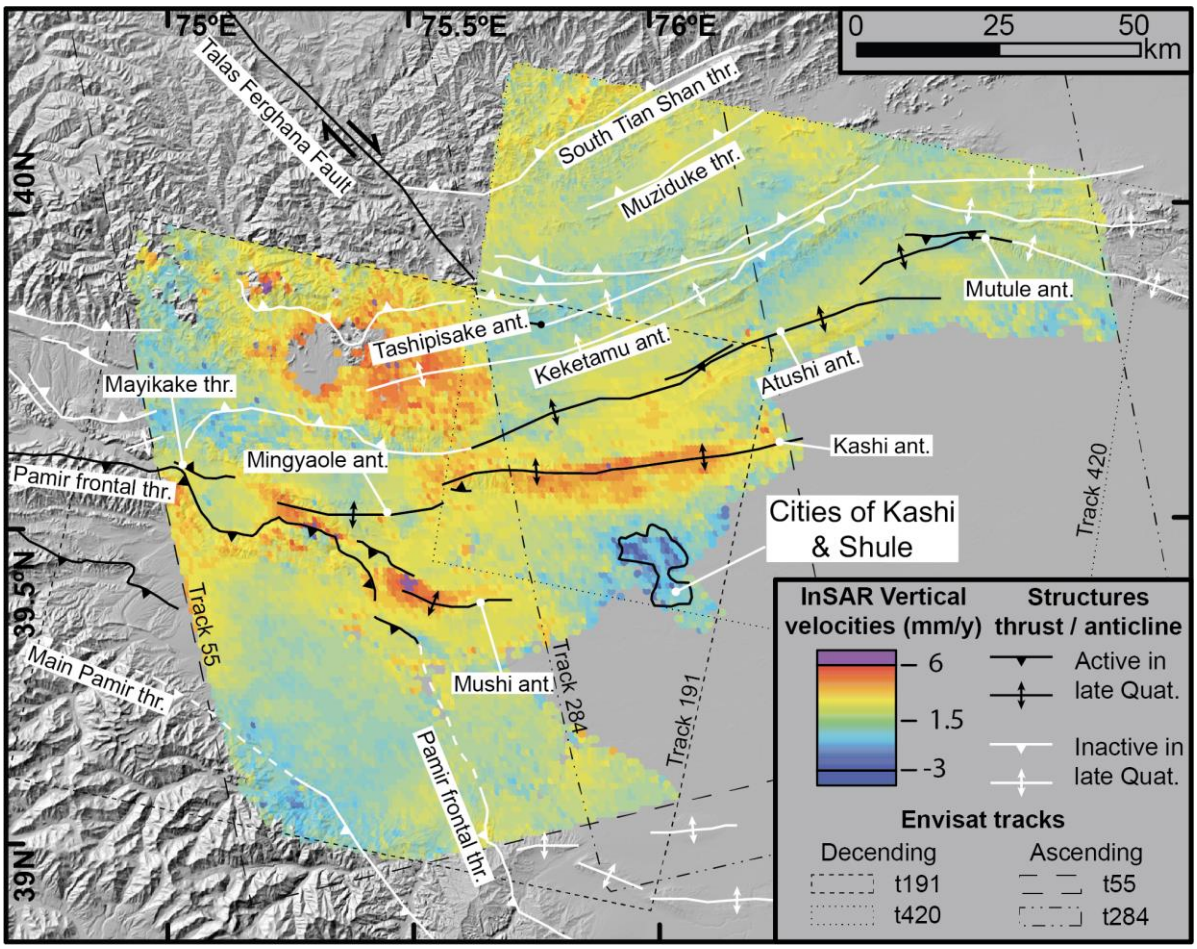

Figure 2: Decadal uplift rates from InSAR time-series analysis of Envisat data for two ascending tracks and two descending tracks. The activity of structures in the Late Quaternary (black and white structures) is based on geologic evidence published in previous studies (Chen et al., 2007; Heermance et al., 2008; Li et al., 2012; Li et al., 2015; Li et al., 2013; Thompson et al., 2015). Note significant subsidence near Kashgar which is probably due to groundwater withdrawal.

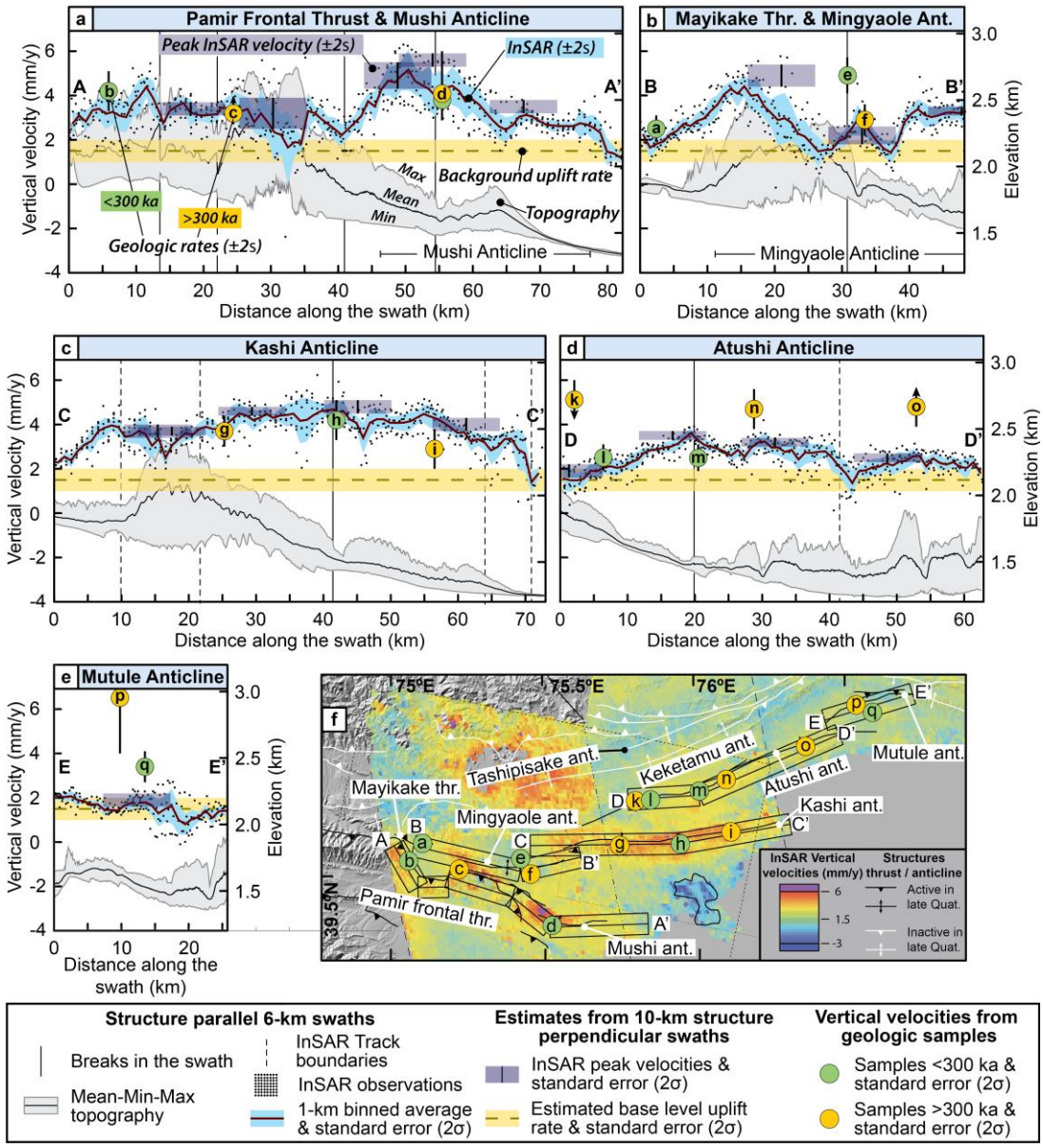

Figure 3: Along-strike changes in uplift rates and velocity. (a-e) Six-km-wide swath profiles along strike of the study area's major active structures show decadal vertical velocities and associated topography. Mean and standard error of the InSAR velocities are calculated in 1-km bins (approximate spacing of points in the InSAR velocity map). Yellow horizontal bar marks background uplift rate of 1.5 ± 0.5 mm/y deduced from 10-km-wide swaths perpendicular to the structures (Figs S6, S7). Peak geodetic uplift rates (2σ errors: vertical black lines) measured on 10-km-wide, structure-perpendicular profiles (blue bars). For reference, published uplift rates measured across geologic timescales (green and yellow circles) are shown where available. For comparison of decadal and geologic uplift rates, the background uplift rate in the InSAR velocity field is added to the geologic rates (Table 1). (f) Overview map with the locations of profiles and locations where geologic uplift rates were calculated.

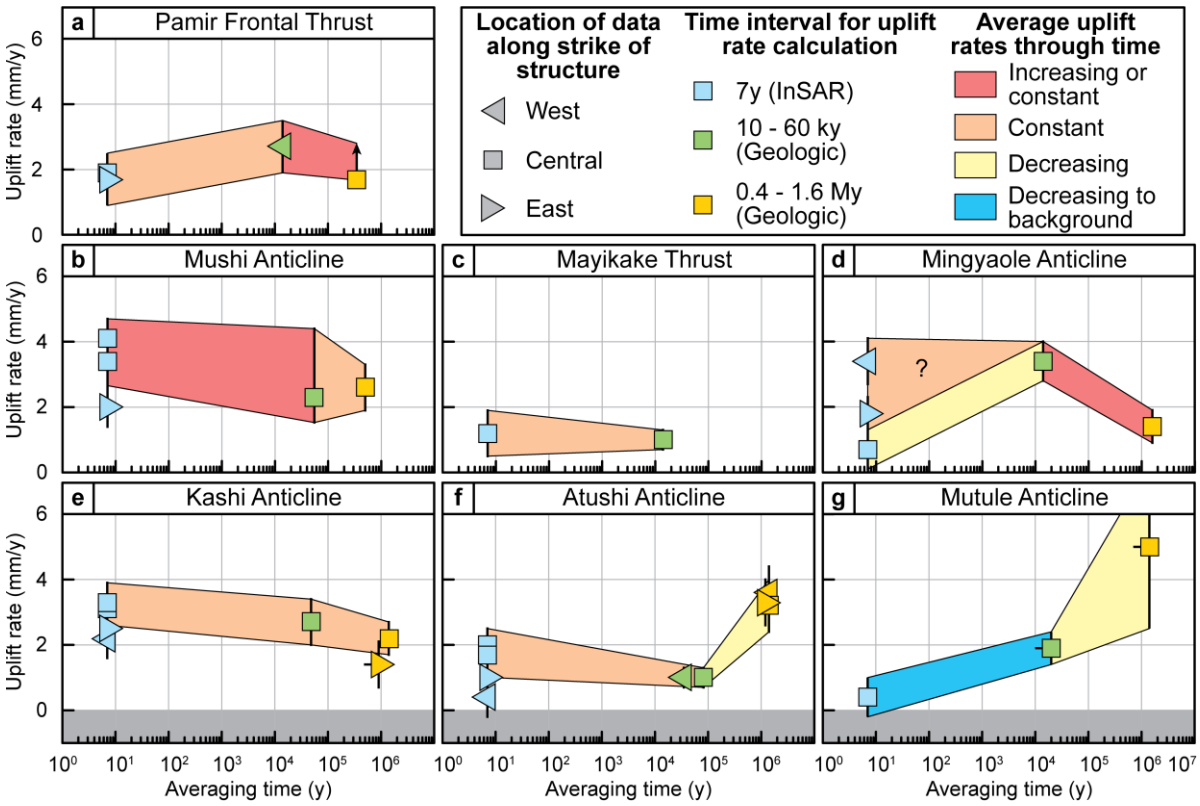

Figure 4: Temporal variations of uplift rate across all major structures. Peak uplift rates are from published geologic data (cf. Fig. 3) and from swath profiles drawn perpendicular to the strike of structures (Figs. 3, S6, S7).

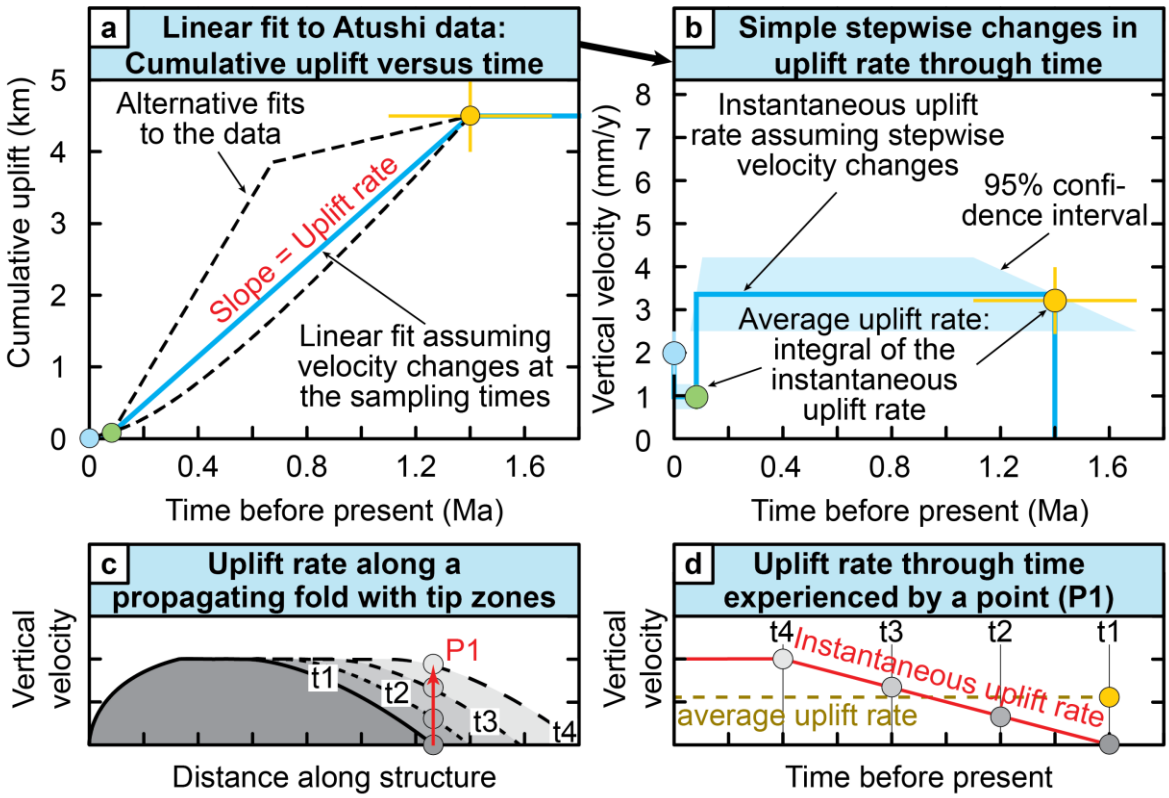

Figure 5: Conceptual sketch of scenarios of uplift-rate changes through time. (a) Cumulative uplift versus time for three datapoints on central Atushi. A linear fit is one possibility of deducing the uplift rate through time and results in the uplift rate scenario shown in b. (b) Instantaneous uplift rate through time converted from the fit to the central Atushi data shown in a. (c) Conceptual sketch of the along-strike uplift rate on a propagating fold tip at four different timesteps. (d) Instantaneous uplift rates experienced by the gray points sketched in (c).

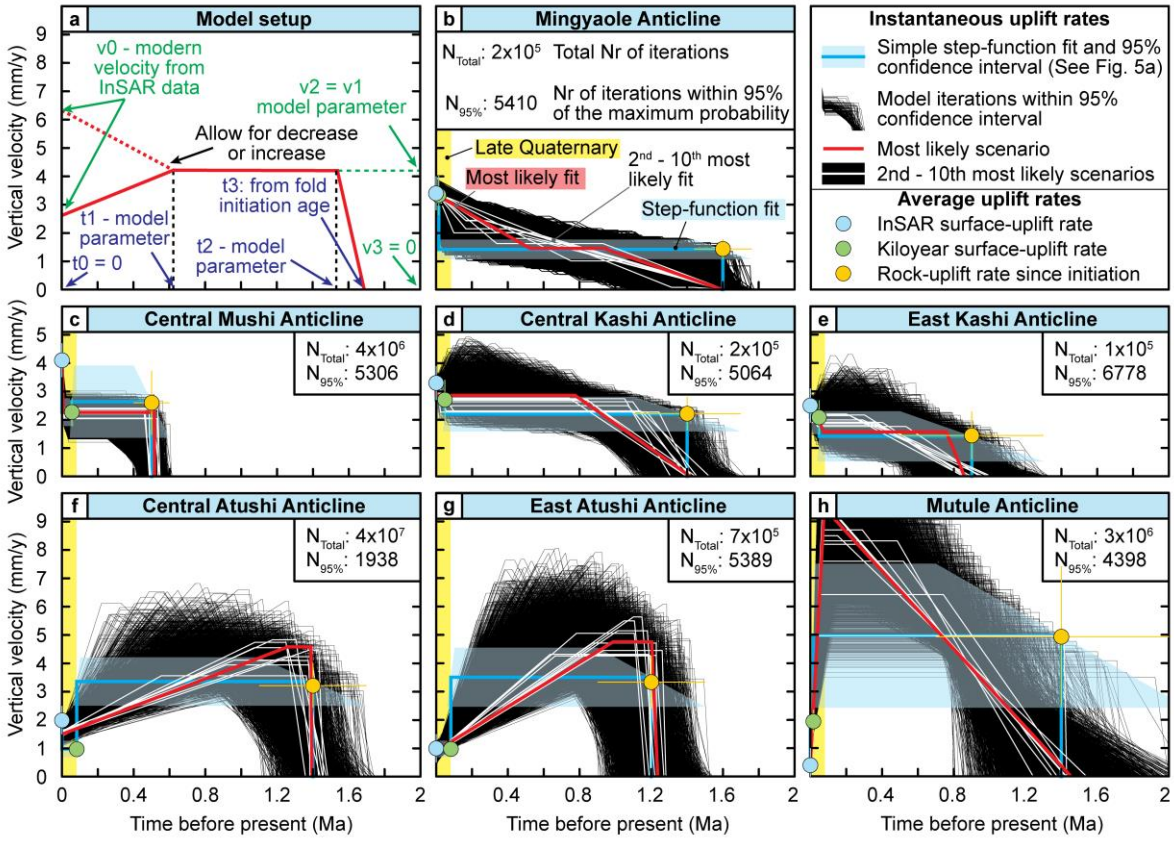

Figure 6: Uplift-rate modeling on Mingyaole, Mushi, Kashi, Atushi, and Mutule. (a) Conceptual sketch showing all model parameters. (b-h) Results from the modeling (black lines) showing all scenarios with probabilities within 5% of the maximum probability (95%-confidence interval). The single most likely scenario is shown in red, whereas the next nine most likely scenarios are shown in while. A step-function fit to the cumulative uplift data (similar to Figs. 5a-b) is shown in blue. Note: modeled uplift rates are instantaneous rates, whereas point-rates for geologic uplift are averaged across the entire time interval. Therefore, they do not have to fit to any of the curves, but rather have to fit the integral of the instantaneous uplift rates from the sample age to the present. Note also for the eastern sections of Atushi and Kashi folds, no geologic rates at intermediate timescales (green points) were available. These rates were, therefore, projected from the central section.

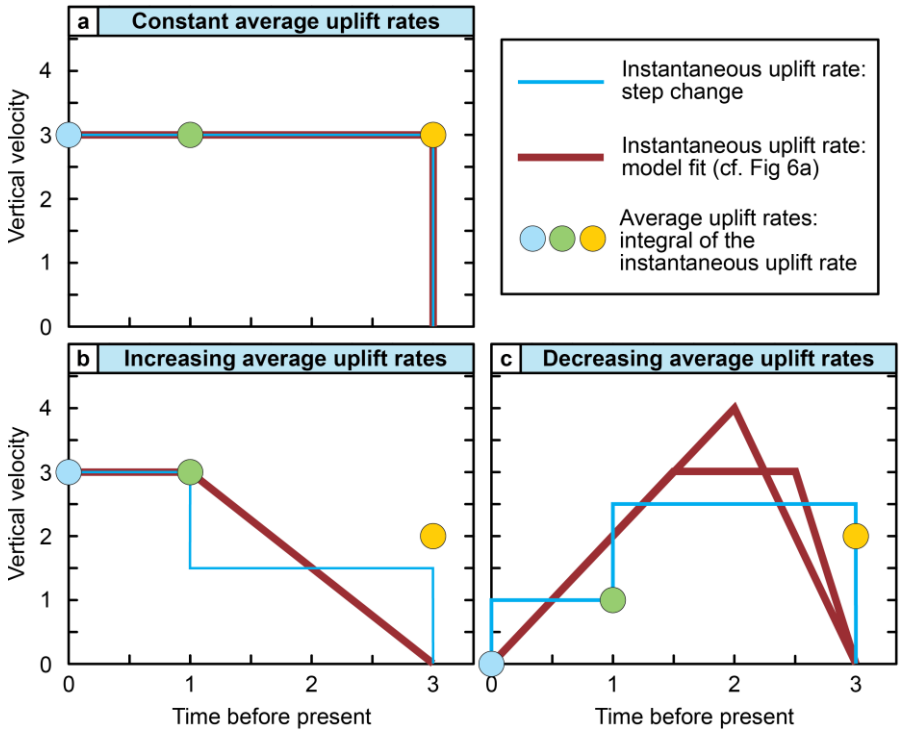

Figure 7: Changes in instantaneous uplift rates for three hypothetical scenarios of (a) constant average uplift rates, (b) increasing average uplift rates, (c) decreasing average uplift rates. Instantaneous uplift rates can be fitted with a step function (blue curves) but gradually varying uplift rates (red curves) are more likely.

Table 1: Quaternary and InSAR uplift rates

Structure	Location	Age of feature ±2σ (ka)	Total rock-uplift ±2σ (m)	Mean rock-uplift rates above base level ±2σ (mm/y)[a]	Background-corrected uplift rate ±2σ (mm/y)[b]
Mayikake Thrust	a	14 +3/-4	15 ± 1	1.0 ± 0.3	2.5 ± 0.6
PFT (Biertuokuoyi Thrust)[c]	b	14 +3/-4	38 ± 1	2.7 ± 0.8	4.2 ± 0.9
PFT (Tuomuluoan Thrust)[c]	c	< 350	600 ± 50	> 1.7	> 3.2 ± 0.5
Mushi Anticline	d-1	55 ± 11	~ 125	2.3 + 2.1/-0.8	3.8 + 2.2/-0.9
Mushi Anticline	d-2	500	1300 ± 500	2.6 ± 0.7	4.1 ± 0.9
Mingyaole Anticline	e	14.6 ± 2.6	50 ± 3	3.4 ± 0.6	4.9 ± 0.8
Mingyaole Anticline	f	1600	2300 ± 500	1.4 ± 0.5	2.9 ± 0.7
Kashi Anticline	g	1400 ± 300	3100 ± 500	2.2 ± 0.5	3.7 ± 0.7
Kashi Anticline	h	48 ± 10	130 ± 20	2.7 ± 0.7	4.2 ± 0.9
Kashi Anticline	i	900 ± 400	1300 ± 500	1.4 ± 0.7	2.9 ± 0.9
Atushi Anticline	k	> 1400 ± 300	5000 ± 500	< 3.6 ± 0.8	< 5.1 ± 0.9
Atushi Anticline	l	35 ± 7	35 ± 10	1.0 ± 0.3	2.5 ± 0.6
Atushi Anticline	m	82 ± 22	80 ± 10	1.0 ± 0.3	2.5 ± 0.6
Atushi Anticline	n	1400 ± 300	4500 ± 500	3.2 ± 0.8	4.7 ± 0.9
Atushi Anticline	o	< 1200 ± 300	4000 ± 500	> 3.3 ± 0.7	> 4.8 ± 0.9
Mutule Anticline[d]	p	1400 ± 700	6900 ± 500	5.0 ± 2.5	6.5 ± 2.5
Mutule Anticline	q	11 - 30	20 - 56	1.9 ± 0.5	3.4 ± 0.7

[a]Geologic rock-uplift rates calculated from published shortening rates and the thrust geometry (locations a-c), published surface-uplift rates assumed to correspond to rock-uplift (points d-1, e, g, k, l, p), or published ages of initiation of folding and structural profiles showing the total height of uplifted rock (points d-2, f, h, i, m-o). Uncertainties are reported at the 2σ-confidence level. A full table with references can be found in Table S3.
[b]A background uplift rate of 1.5 ± 0.5 (±2σ) mm/y was added to the geologic rate in order to directly compare geologic and InSAR rates (see Fig. 3). Reported uncertainties are propagated from errors in geologic rates and the base level.
[c]PFT = Pamir frontal thrust; names in brackets give the names of segments along the PFT that were used in other publications
[d]For the Mutule fold, a structural cross section exists, but no initiation age was published. We assign the initiation age of the Atushi fold to Mushi's east and added a larger uncertainty. Because the Atushi and Mutule folds interfere at their tips, the age of these tips is likely similar.

Supporting material for Chapter 3

We performed InSAR time-series analysis of Envisat data for two ascending tracks (55 and 284) and two descending tracks (191 and 420) spanning an interval from 2002-2011 (Fig. S1, Table S1). We used respectively 12 and 18 acquisitions for the ascending tracks 55 and 284, and 17 and 22 acquisitions for the descending tracks 191 and 420 (Table S1). We focused each raw acquisition using the ROI_PAC software (Rosen et al., 2004), generated our small baseline interferograms with the DORIS package (Kampes and Usai, 1999) and removed the topography using a 90-m resolution SRTM digital elevation model (DEM) (Farr et al., 2007). We used 31 interferograms for track 55, 38 for track 284, 58 for track 191, and 46 for track 420 as input to our time –series analysis using the Stanford Method for Persistent Scatterer (StaMPS) (Hooper et al., 2012; Hooper et al., 2004). StaMPS aims to reduce the number of noisy pixels by specifically selecting pixels with stable phase characteristics over time. Interferograms with unwrapping errors that could not be corrected manually were discarded (dashed lines in Fig. S1) (Hussain et al., in review). Moreover, the southeast of the study area, where unwrapping was consistently problematic, was masked out.

We reduce tropospheric noise in each interferogram by estimating a correction from the ERA-Interim (ERA-I) global weather model outputs published by the European Centre for Medium Range Weather Forecasting (ECWMF) (Dee et al., 2011) and computed with the Toolbox for Reducing Atmospheric InSAR Noise (TRAIN) (Bekaert et al., 2015b). Because our tectonic displacement signal in a single interferogram is smaller than the tropospheric noise, we can assume that the variance of any single interferogram will be strongly dominated by the tropospheric signal. We found that tropospheric correction decreases the

variance for interferograms of tracks 191, 55, and 284 on average by respectively 5.6%, 11.1%, and 17.7%, but increases the variance of interferograms in Track 420 by on average 4.3% (Fig. S2). From this result, we conclude that our correction does in general improve the data. Our resulting line-of-sight (LOS) rate maps are computed by calculating an average rate from 2002-2011, with the uncertainties estimated by boostrapping the time-series (Figs. S3, S4). Note that residual tropospheric noise is further reduced by this averaging approach (Bekaert et al., 2015a; Wright et al., 2001).

Decomposition of the LOS InSAR rates into north, east, and vertical components was done by combining InSAR and published GPS data (Zubovich et al., 2010). As a pre-processing step, we perform a long-wavelength (planar) correction to map each InSAR rate-map into the GPS reference frame (stable Eurasia) and resampled all tracks to a common 1-km grid. For the reference correction, we use only InSAR observations within a 1-km radius of the GPS station (Hussain et al., 2016) and estimate the plane correction from the residual rate between GPS and InSAR. As the InSAR sensitivity is limited in the north-south direction, we let the GPS constrain this component. We produced a 1-km-resolution regional northward velocity field interpolated from > 400 published horizontal GPS velocities acquired between 1994-2007 (Zubovich et al., 2010), and we remove the north component converted into the LOS for each rate map. This process results in InSAR LOS rate maps composed of east-west and up motions referenced to stable Eurasia on a fixed 1-km grid.

Now, for each pixel containing at least one observation from a descending and an ascending InSAR track, the observed InSAR LOS velocities for each track, ($d_{LOS}^{track_i}$) were decomposed into estimates of the eastward, (d_E), and vertical, (d_U), velocities by solving the following inverse problem:

$$\underline{d}_{obs} = A\underline{x} + \underline{e} \quad \text{(S1)}$$

$$E\left\{\begin{bmatrix} d_{LOS}^{track_1} \\ d_{LOS}^{track_2} \\ d_{LOS}^{track_3} \\ d_{LOS}^{track_4} \end{bmatrix}\right\} = \begin{bmatrix} \mathrm{E2LOS}^{track_1} & \mathrm{U2LOS}^{track_1} \\ \mathrm{E2LOS}^{track_2} & \mathrm{U2LOS}^{track_2} \\ \mathrm{E2LOS}^{track_3} & \mathrm{U2LOS}^{track_3} \\ \mathrm{E2LOS}^{track_4} & \mathrm{U2LOS}^{track_4} \end{bmatrix} \begin{bmatrix} d_E \\ d_U \end{bmatrix}, \quad \text{(S2)}$$

$$Q_d = \begin{bmatrix} \sigma_{track_1}^2 & 0 & 0 & 0 \\ 0 & \sigma_{track_2}^2 & 0 & 0 \\ 0 & 0 & \sigma_{track_3}^2 & 0 \\ 0 & 0 & 0 & \sigma_{track_4}^2 \end{bmatrix} \quad \text{(S3)}$$

where E2LOS and U2LOS are operators for converting the eastward and vertical velocity components into the line of sight of the satellite:

$$\mathrm{E2LOS} = \sin(\theta)\cos(\alpha) \quad \text{(S1)}$$

$$U2LOS = -\cos(\theta) \quad \text{(S1)}$$

based on the local radar incidence angle (θ) and the azimuth (α) of the satellite heading vector. Q_d is the covariance matrix with the variances of each pixel in a time series obtained from bootstrapping, as described above. This inverse problem is solved for each pixel by weighted linear least square minimization.

As mentioned above, uncertainties in LOS InSAR velocities of each time series are estimated from bootstrapping and reach up to > 12 mm/y (1σ) (Fig. S3, S4). These uncertainties are propagated through the decomposition and result in errors of 4-12 mm/y in the vertical velocities (Fig. S3, S4). Such large 1σ uncertainties on the order of 70-200% of the maximum signal, should, if random, result in a velocity map in which no patterns can be seen. However, our data appears to successfully resolve patterns and variations of uplift rates with a precision of ~1 mm/y. With the exception of some clearly atmospherically dominated features, such as the approximately elliptical 40 km-wide zone of apparent uplift

west of the Tashipishake anticline (Fig. 2), all major peaks of velocity occur along active Quaternary structures. Thus, it seems that bootstrapping severely overestimates the uncertainties. In the lack of an alternative method, we therefore estimate the error in the decomposed InSAR velocities from the scatter of datapoints measured along 10-km swath profiles.

References for supporting material of Chapter 3

Bekaert, D. P. S., Hooper, A., and Wright, T. J., 2015a, A spatially variable power law tropospheric correction technique for InSAR data: Journal of Geophysical Research: Solid Earth, v. 120, no. 2, p. 2014JB011558.

Bekaert, D. P. S., Walters, R. J., Wright, T. J., Hooper, A. J., and Parker, D. J., 2015b, Statistical comparison of InSAR tropospheric correction techniques: Remote Sensing of Environment, v. 170, p. 40-47.

Dee, D. P., Uppala, S. M., Simmons, A. J., Berrisford, P., Poli, P., Kobayashi, S., Andrae, U., Balmaseda, M. A., Balsamo, G., Bauer, P., Bechtold, P., Beljaars, A. C. M., van de Berg, L., Bidlot, J., Bormann, N., Delsol, C., Dragani, R., Fuentes, M., Geer, A. J., Haimberger, L., Healy, S. B., Hersbach, H., Hólm, E. V., Isaksen, L., Kållberg, P., Köhler, M., Matricardi, M., McNally, A. P., Monge-Sanz, B. M., Morcrette, J. J., Park, B. K., Peubey, C., de Rosnay, P., Tavolato, C., Thépaut, J. N., and Vitart, F., 2011, The ERA-Interim reanalysis: configuration and performance of the data assimilation system: Quarterly Journal of the Royal Meteorological Society, v. 137, no. 656, p. 553-597.

Farr, T. G., Rosen, P. A., Caro, E., Crippen, R., Duren, R., Hensley, S., Kobrick, M., Paller, M., Rodriguez, E., Roth, L., Seal, D., Shaffer, S., Shimada, J., Umland, J., Werner, M., Oskin, M., Burbank, D., and Alsdorf, D., 2007, The Shuttle Radar Topography Mission: Reviews of Geophysics, v. 45, no. 2, p. n/a-n/a.

Hooper, A., Bekaert, D., Spaans, K., and Arıkan, M., 2012, Recent advances in SAR interferometry time series analysis for measuring crustal deformation: Tectonophysics, v. 514–517, no. 0, p. 1-13.

Hooper, A., Zebker, H., Segall, P., and Kampes, B., 2004, A new method for measuring deformation on volcanoes and other natural terrains using InSAR persistent scatterers: Geophysical Research Letters, v. 31, no. 23, p. n/a-n/a.

Hussain, E., Hooper, A., Wright, T. J., Walters, R. J., and Bekaert, D., in review, Interseismic strain accumulation across the central North Anatolian Fault from iteratively unwrapped InSAR measurements: Journal of Geophysical Research.

Hussain, E., Wright, T. J., Walters, R. J., Bekaert, D., Hooper, A., and Houseman, G. A., 2016, Geodetic observations of postseismic creep in the decade after the 1999 Izmit earthquake, Turkey: Implications for a shallow slip deficit: Journal of Geophysical Research: Solid Earth, v. 121, no. 4, p. 2980-3001.

Kampes, B., and Usai, S., Doris: The delft object-oriented radar interferometric software, *in* Proceedings 2nd international symposium on operationalization of remote sensing, enschede, the netherlands1999, Volume 16, Citeseer, p. 20.

Rosen, P. A., Hensley, S., Peltzer, G., and Simons, M., 2004, Updated repeat orbit interferometry package released: Eos, Transactions American Geophysical Union, v. 85, no. 5, p. 47-47.

Thompson, J. A., Chen, J., Yang, H., Li, T., Bookhagen, B., and Burbank, D. W., in review, Coarse- versus fine-grain OSL and cosmogenic 10Be dating of deformed fluvial terraces on the northeast Pamir margin, northwest China: Quaternary Geochronology.

Wright, T., Parsons, B., and Fielding, E., 2001, Measurement of interseismic strain accumulation across the North Anatolian Fault by satellite radar interferometry: Geophysical Research Letters, v. 28, no. 10, p. 2117-2120.

Zubovich, A. V., Wang, X.-q., Scherba, Y. G., Schelochkov, G. G., Reilinger, R., Reigber, C., Mosienko, O. I., Molnar, P., Michajljow, W., Makarov, V. I., Li, J., Kuzikov, S. I., Herring, T. A., Hamburger, M. W., Hager, B. H., Dang, Y.-m., Bragin, V. D., and Beisenbaev, R. T., 2010, GPS velocity field for the Tien Shan and surrounding regions: Tectonics, v. 29, no. 6, p. TC6014.

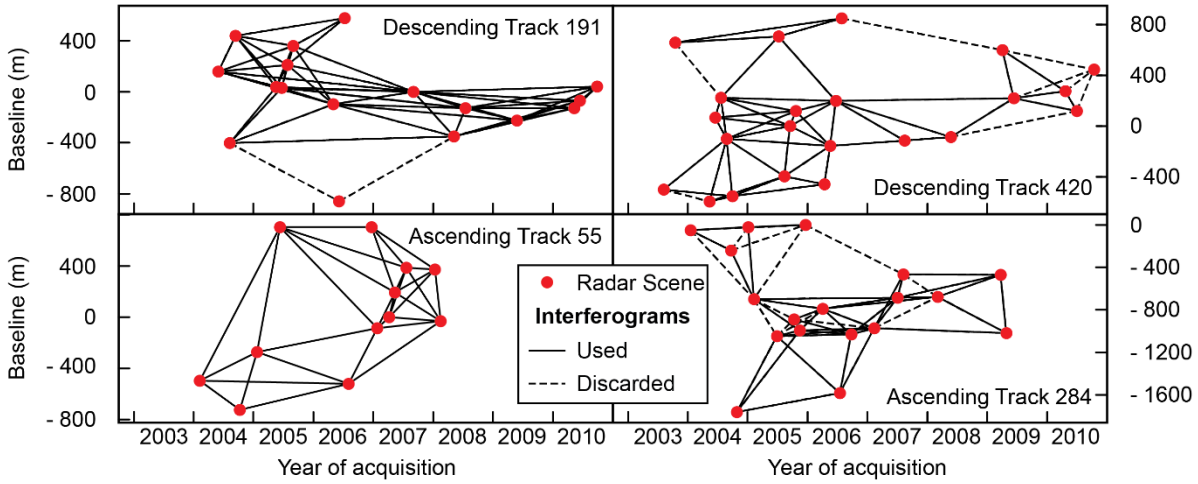

Figure S1: Baseline versus time plots for each of the tracks used in the study. Lines in-between radar acquisitions (red dots) mark all the interferograms that were created. Solid lines mark interferograms used for the time-series analysis, dashed lines mark interferograms discarded due to unwrapping errors.

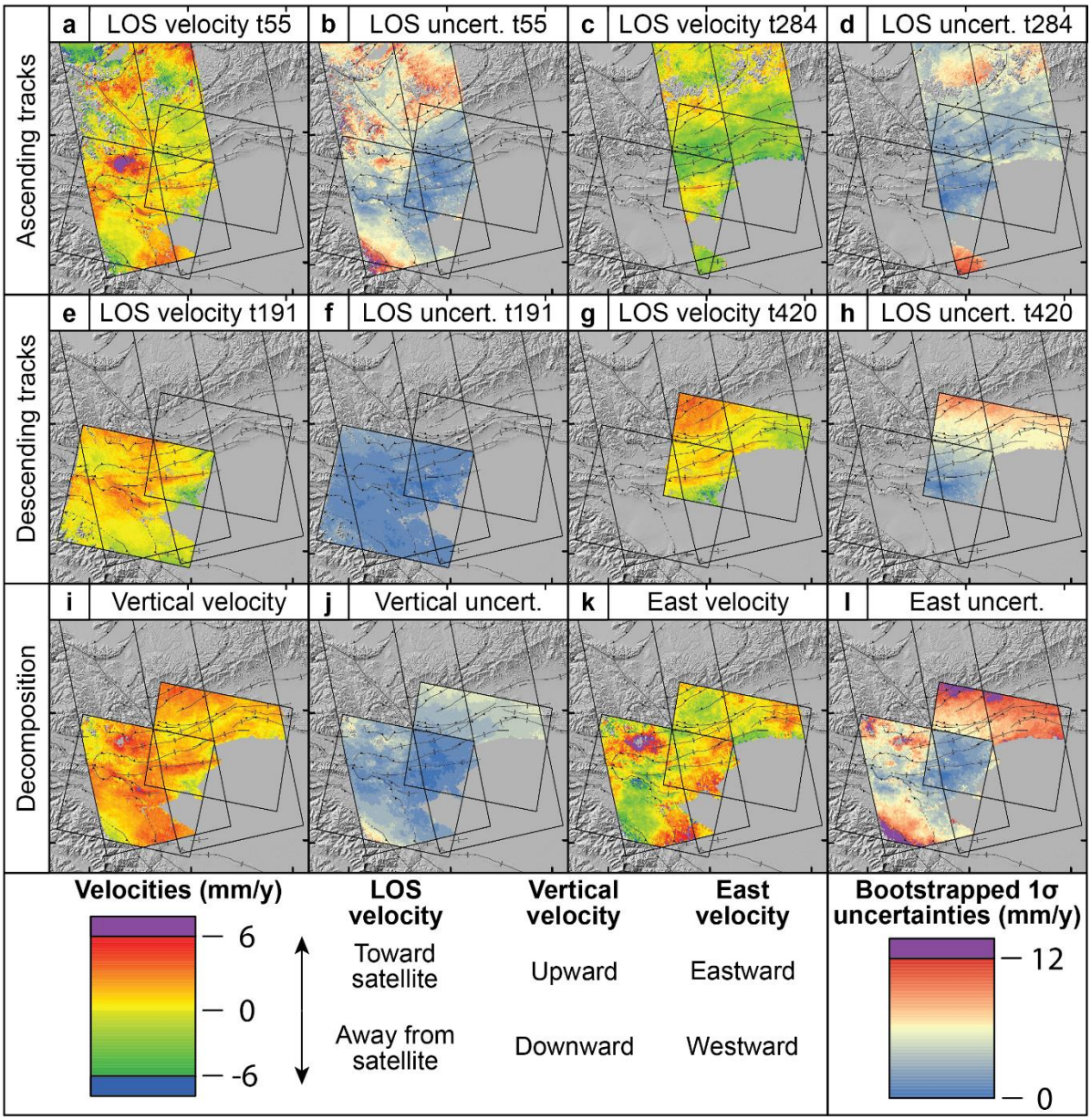

Figure S2: InSAR velocities and uncertainties for time series and decomposed scenes without atmospheric correction. For the sake of comparison, velocities of all time-series are plotted with respect to a common reference zone of 1-km radius and centered on 39.5161°N, 757714°E.

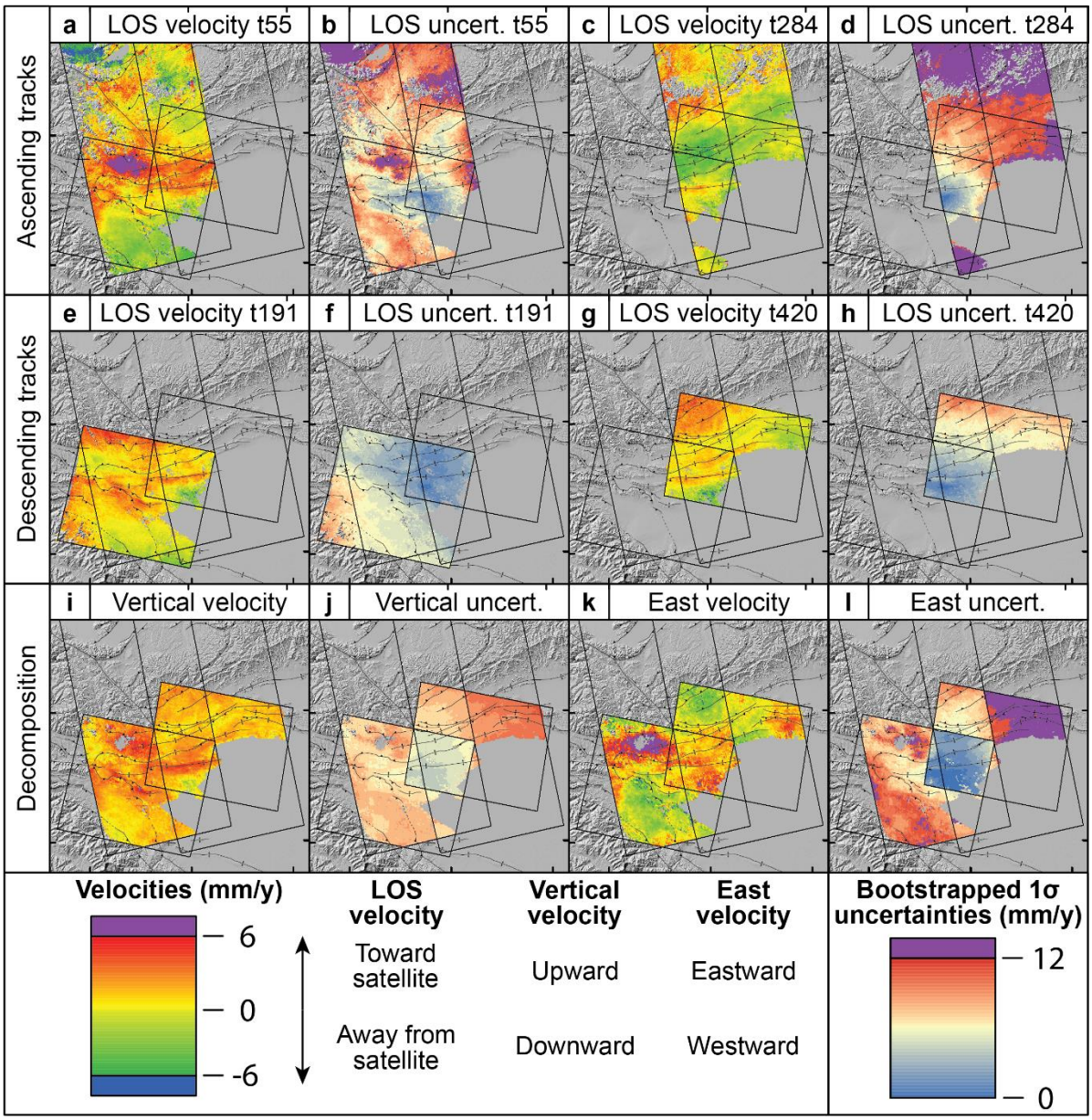

Figure S3: InSAR velocities and uncertainties for time series and decomposed scenes with atmospheric correction. For the sake of comparison, velocities of all time-series are plotted with respect to a common reference zone of 1-km radius and centered on 39.5161°N, 757714°E.

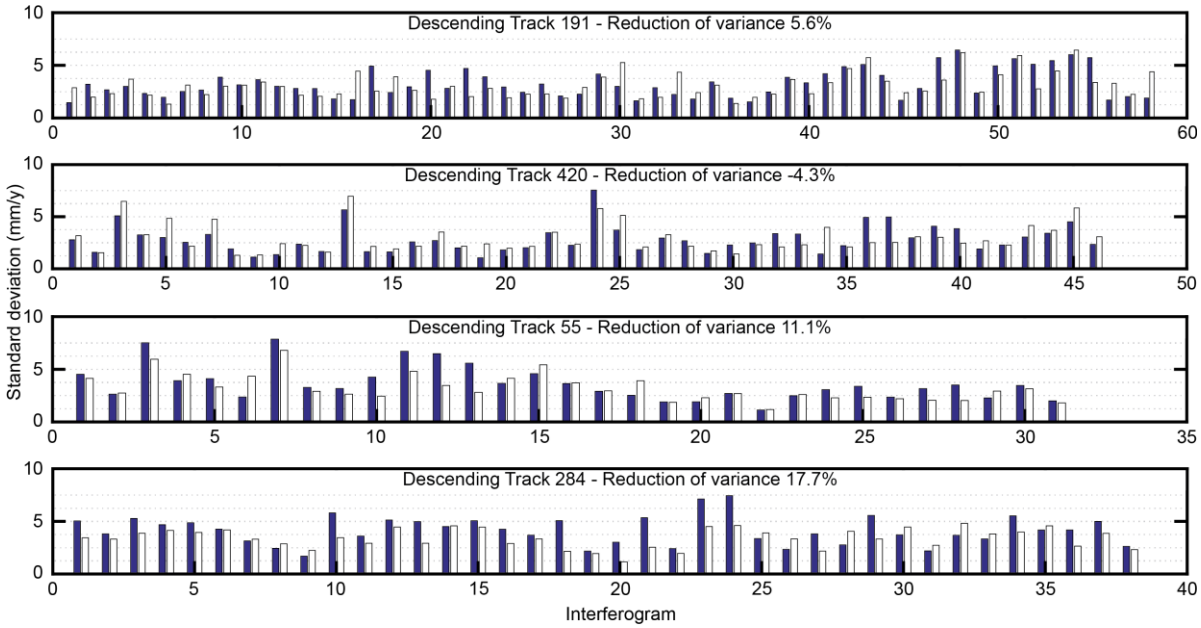

Figure S4: Reduction of variance in the InSAR data by atmospheric correction. The variance in a single interferogram is assumed to be dominated by atmospheric effects and the reduction of variance a measure for the performance of the atmospheric correction. For all tracks except Track 420, the variance is reduced by the atmospheric correction.

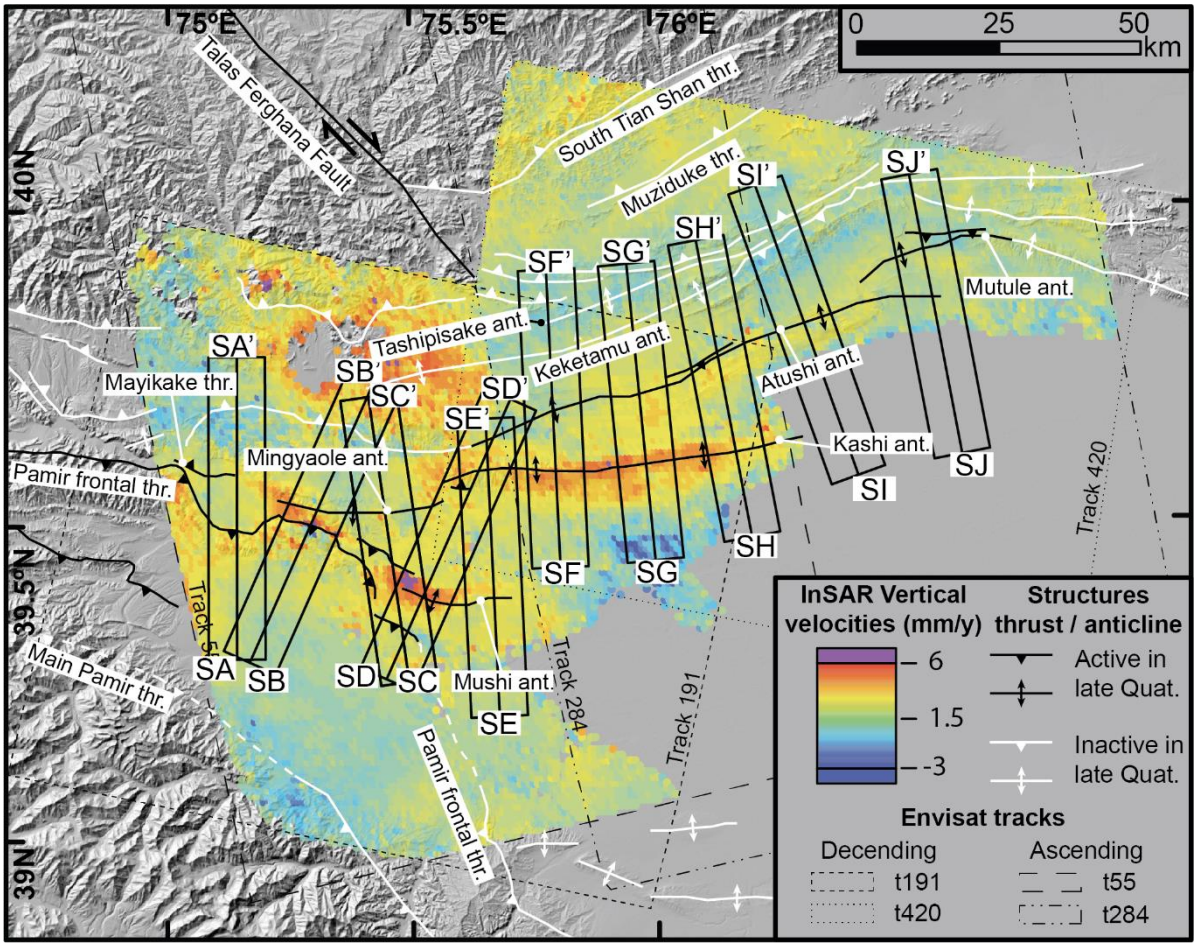

Figure S5: Location of 10-km wide swath profiles perpendicular to the strike of structures and shown in Figs S6, S7. The symbology is the same as in Figure 2.

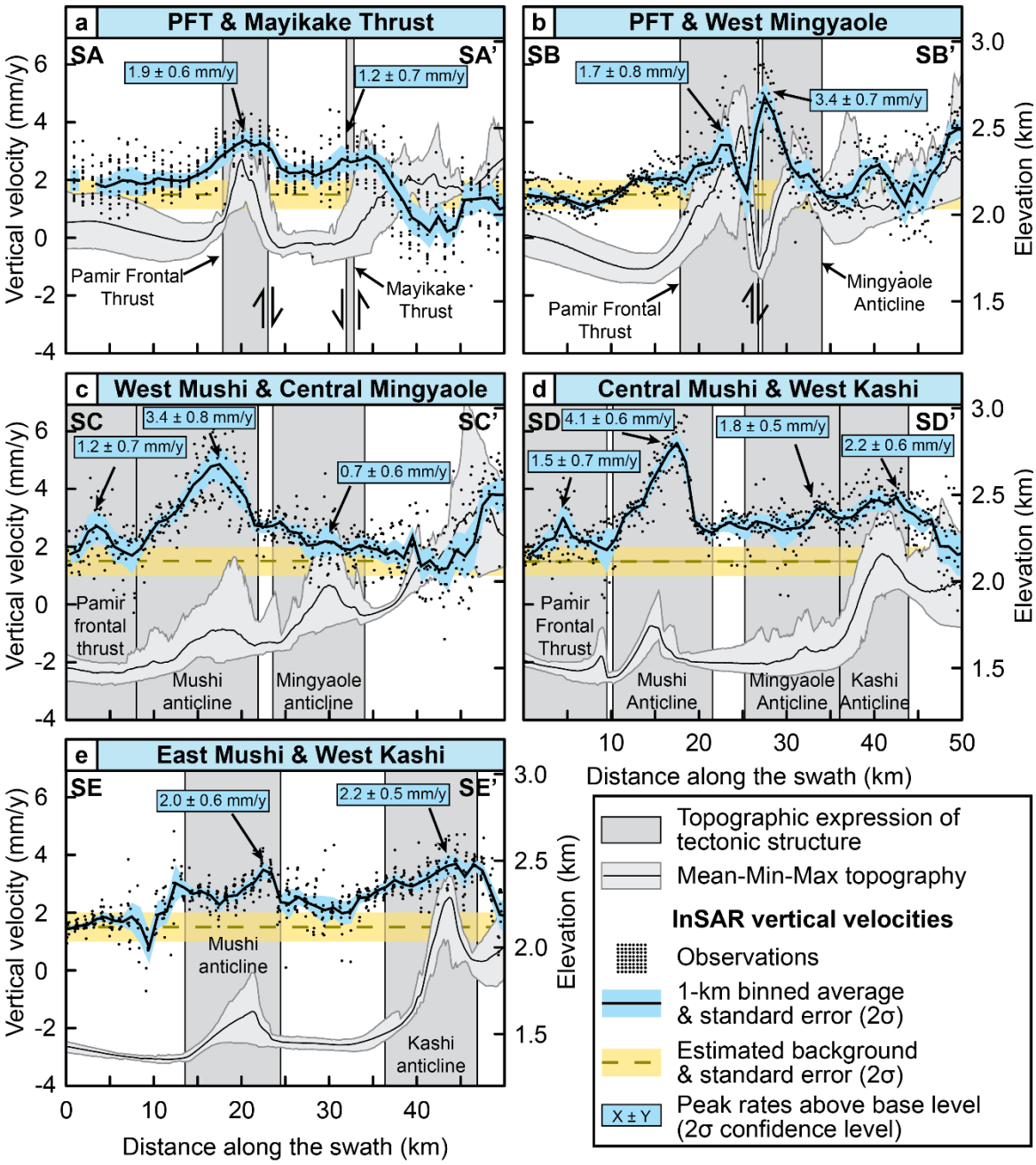

Figure S6: Ten-kilometer-wide swath profiles drawn approximately perpendicular to the strike of compressional structures in the study area. The mean and standard error of the InSAR velocities are calculated in 1-km bins (approximate spacing of points in the InSAR velocity map). Peak decadal uplift rates for all structures are taken as the peak mean value within the topographic expression of the tectonic structures. Location of all swath profiles is given in Fig. S5.

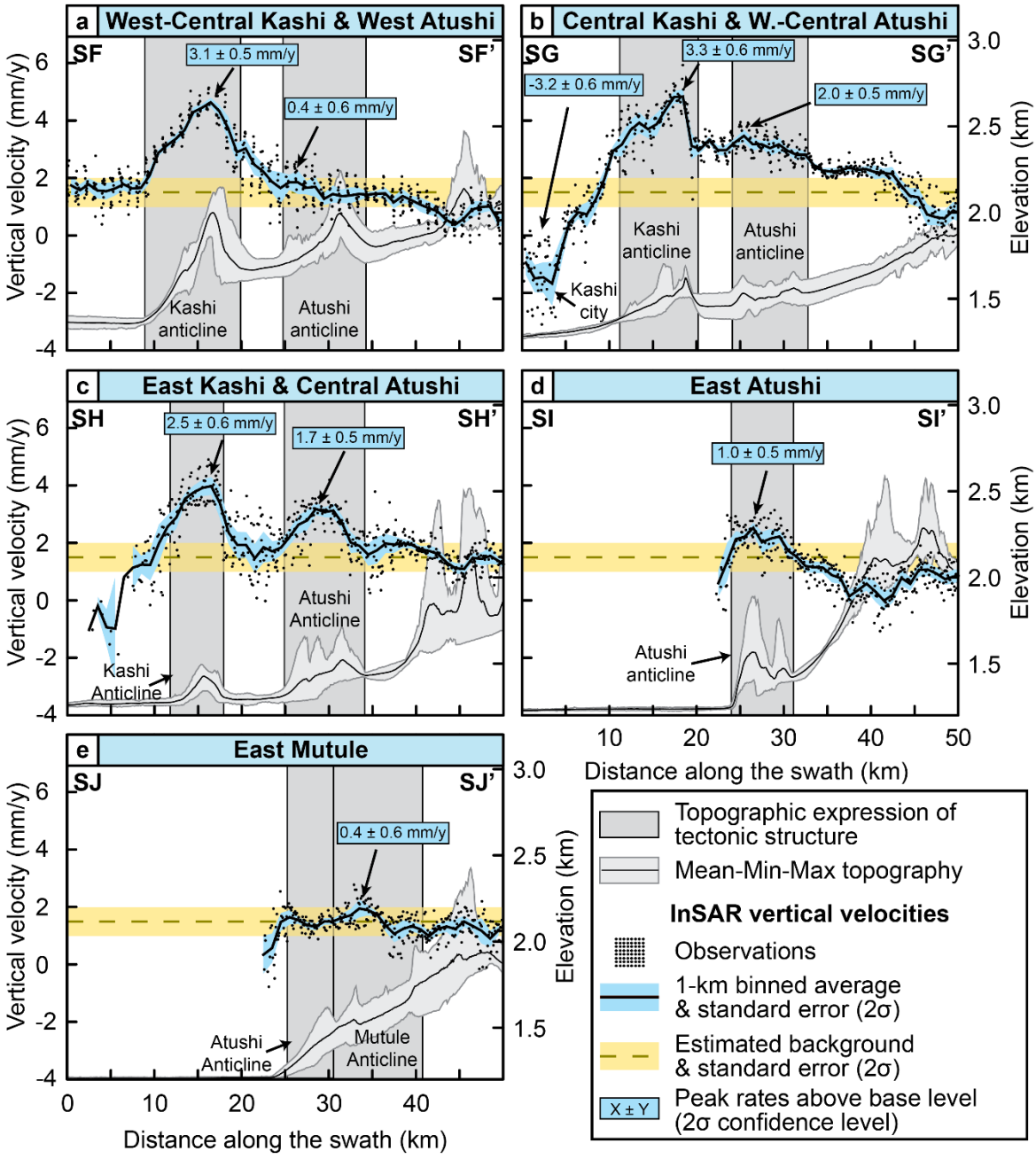

Figure S7: Additional Swath profiles across active structures. Symbology is the same as in Fig. S6. Location of all swath profiles is given in Fig. S5.

Table S1: Geometry and data coverage for the InSAR tracks used in this study

Track	Geometry	Time span	Number of images	Total interferograms created	Interferograms used
191	Descending	31 May 2004-27 Sep 2010	17	60	58
420	Descending	06 Aug 2003-30 Jun 2010	22	54	46
55	Ascending	06 Feb 2004-15 Feb 2008	12	31	31
284	Ascending	18 Jan 2004-26 Apr 2009	18	52	38

Table S2: InSAR peak uplift rates from swath profiles in Figs. S6, S7

Structure	Swath profile[a]	Total InSAR mean peak uplift rates ±2σ (mm/y)[b]	InSAR mean peak uplift rate above base level ±2σ (mm/y)[c]
Mayikake Thrust	SA - SA'	2.7 ± 0.5	1.2 ± 0.7
PFT (Biertuokuoyi Thrust)[d]	SA - SA'	3.4 ± 0.3	1.9 ± 0.6
PFT (Tuomuluoan Thrust)[d]	SB - SB'	3.2 ± 0.7	1.7 ± 0.8
West Mushi Anticline	SC - SC'	4.9 ± 0.6	3.4 ± 0.8
Central Mushi Anticline	SD - SD'	5.6 ± 0.3	4.1 ± 0.6
East Mushi Anticline	SE - SE'	3.5 ± 0.3	2.0 ± 0.6
West Mingyaole Anticline	SB - SB'	4.9 ± 0.5	3.4 ± 0.7
Central Mingyaole Anticline	SC - SC'	2.2 ± 0.4	0.7 ± 0.6
East Mingyaole Anticline	SD - SD'	3.3 ± 0.2	1.8 ± 0.5
West Kashi Anticline	SD - SD'	3.7 ± 0.3	2.2 ± 0.6
West Kashi Anticline	SE - SE'	3.7 ± 0.2	2.2 ± 0.5
Central Kashi Anticline	SF - SF'	4.6 ± 0.2	3.1 ± 0.5
Central Kashi Anticline	SG - SG'	4.8 ± 0.3	3.3 ± 0.6
East Kashi Anticline	SH - SH'	4.0 ± 0.3	2.5 ± 0.6
West - Atushi Anticline	SF - SF'	1.9 ± 0.3	0.4 ± 0.6
West-Central Atushi Anticline	SG - SG'	3.5 ± 0.2	2.0 ± 0.5
Central Atushi Anticline	SH - SH'	3.2 ± 0.2	1.7 ± 0.5
East Atushi Anticline	SI - SI'	2.5 ± 0.2	1.0 ± 0.5
West Mutule Anticline	SJ - SJ'	1.9 ± 0.3	0.4 ± 0.6
Kashi-Shule Cities	SG - SG'	-1.7 ± 0.8	-3.2 ± 0.9

[a]See Fig. S5 for locations of swath profiles.
[b]Peak rates for each structure obtained from the highest mean InSAR uplift rate on the structure measured along 10-km wide swath profiles (Figs. S6, S7). Reported uncertainties are 2-standard errors (standard deviations of the mean).
[c]A base uplift rate of 1.5 ± 0.5 (±2σ) mm/y was subtracted from the peak rate uplift rate to obtain uplift rates above the base level. Reported uncertainties are propagated from the standard error in the peak uplift rate and the uncertainty in the base level uplift rate.
[d]PFT = Pamir frontal thrust; names in brackets give the names of segments along the PFT that were used in other publications

Table S3-1: Geologic uplift rates and references-Part 1

Name of Structure	Latitude	Longitude	Point on Fig. 3	Landform dated	Dating technique[a]	Age of landform ±2σ (ka)[b]	Uplift of landform over time interval ±2σ (m)	Uplift rate averaged over landform age ±2σ (mm/y)[b]
Mayikake Thrust	39.5836	75.1046	a	Deformed terrace in Mayikake basin	CRN	14 +3/-4	15 ± 1	1.0 ± 0.3
Mayikake Thrust	39.5836	75.1046	a	Deformed terrace in Mayikake basin	OSL	18 ± 5	15 ± 1	0.8 ± 0.2
PFT (Biertuokuoyi Thrust)[c]	39.53910	75.05870	b	Deformed terrace in Mayikake basin	CRN	14 +3/-4	38 ± 1	2.7 ± 0.8
PFT (Biertuokuoyi Thrust)[c]	39.53910	75.05870	b	Deformed terrace in Mayikake basin	OSL	18 ± 5	38 ± 1	2.1 ± 0.5
Biertuokuoyi fold scarp	39.50540	75.02600		Deformed terrace	OSL	75 ± 10		1.0 ± 0.2
PFT (Tuomuluoan Thrust)[c]	39.51851	75.22313	c	Conglomerates underlying thrust fault	Paleomag	< 350	600 ± 50	> 1.7
PFT (Aismaola Anticline)[c]			d	Uplifted terrace	OSL	55 - 95		> 0.3
Mushi Anticline	39.37503	75.52915	d	Uplifted terrace	OSL	55 ± 11	~ 125	2.3 + 2.1/-0.8
Mushi anticline	39.37503	75.52915	d	growth strata	Paleomag	500.0	1300 ± 350	2.6 ± 0.7
Mingyaole Anticline	39.48945	75.47720	-	Dated fold scarp	CRN	8.5 + 4.3/-5	16 ± 1	1.9 ± 1.1
Mingyaole Anticline	39.54411	75.42379	e	Dated fold scarp	OSL	14.6 ± 2.6	50 ± 3	3.4 ± 0.6
Mingyaole anticline	39.50563	75.45713	f	growth strata	Paleomag	1600.0	~ 2300	1.4 ± 0.5
Kashi Anticline	39.57660	75.74893	g	growth strata	Paleomag	1400 ± 300	3100 ± 500	2.2 ± 0.5
Kashi Anticline	39.5785	75.9480	h	Incised & deformed terrace	OSL	48 ± 10	130 ± 20	2.7 ± 0.7

Kashi Anticline	39.60813	76.11352	i	growth strata	Paleomag	900 ± 400	1300 ± 500	1.4 ± 0.7
Atushi West	39.68892	75.80174	k	growth strata	Paleomag	> 1400 ± 300	5000 ± 500	< 3.6 ± 0.8
Atushi Anticline	39.712	76.0115	l	Incised & deformed terrace	CRN	82 ± 22	80 ± 10	1.0 ± 0.3
Atushi Anticline	39.6907	75.8513	m	Incised & deformed terrace	OSL	35 ± 7	35 ± 10	1.0 ± 0.3
Atushi Central	39.74068	76.09987	n	growth strata	Paleomag	1400 ± 300	4500 ± 500	3.2 ± 0.8
Atushi East	39.82239	76.36180	o	growth strata	Paleomag	< 1200 ± 300	4000 ± 500	> 3.3 ± 0.7
Mutule[d]	39.924839	76.529825	p	-	-	1400 ± 700	6900 ± 500	5.0 ± 2.5
Mutule Anticline	39.9046	76.5833	q	Series of incised and deformed terraces	OSL	11 - 30	21 - 59	1.9 ± 0.5

[a]CRN = cosmogenic nuclide dating; OSL = optically stimulated luminescence dating; Paleomag = paleomagnetic dating
[b]Where two different ages exist, preference was given to the CRN datess.
[c]PFT = Pamir frontal thrust. Names in brackets give name of the PFT segment used in the published literature
[d]For the Mutule fold, while a structural cross section exists, no initiation age was published. We therefore took the initiation age of the Atushi fold to the east and added a larger uncertainty. Since the Atushi and Mutule folds interfer at their tips, the age of these tips is likely similar.

Table S3-2: Geologic uplift rates and references-Part 2

Name of Structure	Uplift rate calculated from:	Reference
Mayikake Thrust	Published shortening rate & thrust geometry	Thompson et al., (2013)
Mayikake Thrust	Published shortening rate & thrust geometry	Li et al., (2012)
PFT (Biertuokuoyi Thrust)[c]	Published shortening rate & thrust geometry	Thompson et al., (2013)
PFT (Biertuokuoyi Thrust)[c]	Published shortening rate & thrust geometry	Li et al., (2012)
Biertuokuoyi fold scarp	yes	Thompson et al., (2013)
PFT (Tuomuluoan Thrust)[c]	Published shortening rate & thrust geometry	Li et al., (2012)
PFT (Aismaola Anticline)[c]	Published uplift rate	Thompson et al., (in prep)
Mushi Anticline	Published uplift rate	Li et al., (2013)
Mushi anticline	Published structural profile and published initiation age	Chen et al., 2005; Li et al., 2013,
Mingyaole Anticline	Age and elevation of T1	Li et al., (2015), Thompson et al., (2013)
Mingyaole Anticline	Age and elevation of T3	Li et al., (2015)
Mingyaole anticline	Published uplift rate	Chen et al., 2005; Li et al., 2015a&b,
Kashi Anticline	Extrapolated from published initiation age and structural cross section	Heermance et al., 2008; Scharer et al., 2004
Kashi Anticline	Published uplift rate	Bufe et al., (submitted)
Kashi Anticline	Extrapolated from published initiation age and structural cross section	Scharer et al., 2004, Chen et al., 2007
Atushi West	Extrapolated from published initiation age and structural cross section	Heermance et al., 2008 Scharer et al., 2004
Atushi Anticline	Published uplift rate	Bufe et al., (submitted) Heermance et al., (2008)
Atushi Anticline	Published uplift rate	Bufe et al., (submitted)
Atushi Central	Published initiation age and structural cross section	Heermance et al., 2008 Scharer et al., 2004
Atushi East	Extrapolated from published initiation age and structural cross section	Heermance et al., 2008 Scharer et al., 2004
Mutule[d]	Calculated from published Structural section, and estimated initiation age from initiation of Atushi fold	Heermance et al., 2008 Scharer et al., 2004, Bufe et al., in review
Mutule Anticline	Published uplift rate	Bufe et al., (in review)

Appendix-data tables for Chapter 2

Table A1: Imbrication measurements

Pont[a]	GPSTime (GMT)	Lat	Lon	MSL from GPS	Strike of imbrication (right hand rule)	Dip of imbrication	Strike of exposure face	Height below terace surace (m)	Paleoflow direction
AD1a	06/06/13 09:45:44am	39.74206	76.09841	1414.942	245	35	120		155
AD1b	06/06/13 09:45:44am	39.74206	76.09841	1414.942	254	34	120		164
AD1b	06/06/13 09:45:44am	39.74206	76.09841	1414.942	247	35	120		157
AD2a	06/06/13 09:45:44am	39.74206	76.09841	1414.942	240	37	120		150
AD2b	06/06/13 09:45:44am	39.74206	76.09841	1414.942	225	39	120		135
AD3a	06/06/13 09:45:44am	39.74206	76.09841	1414.942	56	40	120		326
AD3b	06/06/13 09:45:44am	39.74206	76.09841	1414.942	40	50	120		310
AD4	06/06/13 09:45:44am	39.74206	76.09841	1414.942	245	34	120		155
AD5	06/06/13 09:45:44am	39.74206	76.09841	1414.942	212	25	120		122
AD6	06/06/13 09:45:44am	39.74206	76.09841	1414.942	211	39	120		121
AQ1	06/06/13 11:42:38am	39.74646	76.08788	1391.714	194	36	125		104
AQ1b	06/06/13 11:42:38am	39.74646	76.08788	1391.714	214	37	125		124
AQ2a	06/06/13 11:42:38am	39.74646	76.08788	1391.714	171	48	86		81
AQ2b	06/06/13 11:42:38am	39.74646	76.08788	1391.714	166	39	86		76
AR1	06/06/13 12:05:18pm	39.74639	76.08838	1395.872	215	45	134		125
AR2	06/06/13 12:05:18pm	39.74639	76.08838	1395.872	76	24	130		346
AR3	06/06/13 12:05:18pm	39.74639	76.08838	1395.872	262	30	168		172
GA1	06/12/13 05:47:25am	39.71299	76.01116	1484.878	196	26	324	5.8	106
GA2	06/12/13 05:47:25am	39.71299	76.01116	1484.878	260	51	335	5.8	170
GA3	06/12/13 05:47:25am	39.71299	76.01116	1484.878	245	35	335	5.8	155
GA4	06/12/13 05:47:25am	39.71299	76.01116	1484.878	156	29	from below	6.1	66
GA5	06/12/13 05:47:25am	39.71299	76.01116	1484.878	260	24	335	5	170
GA6	06/12/13 05:47:25am	39.71299	76.01116	1484.878	215	30	235	5	125
GA7	06/12/13 05:47:25am	39.71299	76.01116	1484.878	204	24	355	4.9	114

GA8	06/12/13 05:47:25am	39.71299	76.01116	1484.878	190	20	355	4.9	100
GA9	06/12/13 05:47:25am	39.71299	76.01116	1484.878	226	33	355	4.9	136
GA10	06/12/13 05:47:25am	39.71299	76.01116	1484.878	233	40	355	4.9	143
GA11	06/12/13 05:47:25am	39.71299	76.01116	1484.878	237	50	330	5	147
GA12	06/12/13 05:47:25am	39.71299	76.01116	1484.878	220	29	330	5	130
GA13	06/12/13 05:47:25am	39.71299	76.01116	1484.878	23	50	335	4.6	293
GA14	06/12/13 05:47:25am	39.71299	76.01116	1484.878	40	60	335	4.6	310
GA15	06/12/13 05:47:25am	39.71299	76.01116	1484.878	289	35	340	4.6	199
GA16	06/12/13 05:47:25am	39.71299	76.01116	1484.878	41	34	325	5.3	311
GA17	06/12/13 05:47:25am	39.71299	76.01116	1484.878	241	30	320	4.5	151
GA18	06/12/13 05:47:25am	39.71299	76.01116	1484.878	215	25	329	5.3	125
GA19	06/12/13 05:47:25am	39.71299	76.01116	1484.878	225	40	329	5.3	135
GA20	06/12/13 05:47:25am	39.71299	76.01116	1484.878	35	25	329	5.3	305
GA21	06/12/13 05:47:25am	39.71299	76.01116	1484.878	225	40	310	4.8	135
GA22	06/12/13 05:47:25am	39.71299	76.01116	1484.878	223	40	320	4.9	133
GA23	06/12/13 05:47:25am	39.71299	76.01116	1484.878	224	46	310	5.5	134
IA1	06/13/13 02:32:42am	39.6922	76.0245	1421.822	123	26	50	2.9	33
IA2	06/13/13 02:32:42am	39.6922	76.0245	1421.822	105	33	71	2.9	15
IA3	06/13/13 02:32:42am	39.6922	76.0245	1421.822	130	35	55	2.9	40
IA4	06/13/13 02:32:42am	39.6922	76.0245	1421.822	189	37	55	2.8	99
IA5	06/13/13 02:32:42am	39.6922	76.0245	1421.822	144	44	40	2.8	54
IA6	06/13/13 02:32:42am	39.6922	76.0245	1421.822	195	31	79	2.7	105
IA7	06/13/13 02:32:42am	39.6922	76.0245	1421.822	115	20	45	2.8	25
IA8	06/13/13 02:32:42am	39.6922	76.0245	1421.822	164	41	84	2.8	74
IA9	06/13/13 02:32:42am	39.6922	76.0245	1421.822	155	34	94	2.8	65
IA10	06/13/13 02:32:42am	39.6922	76.0245	1421.822	190	33	86	2.6	100
IA11	06/13/13 02:32:42am	39.6922	76.0245	1421.822	152	20	86	2.6	62
IA12	06/13/13 02:32:42am	39.6922	76.0245	1421.822	0	39	89	2.5	270

IA13	06/13/13 02:32:42am	39.6922	76.0245	1421.822	193	32	89	2.5	103
IA14	06/13/13 02:32:42am	39.6922	76.0245	1421.822	146	31	116	2.7	56
IA15	06/13/13 02:32:42am	39.6922	76.0245	1421.822	156	34	116	2.7	66
IA16	06/13/13 02:32:42am	39.6922	76.0245	1421.822	170	34	102	2.8	80
IA17	06/13/13 02:32:42am	39.6922	76.0245	1421.822	171	25	102	2.8	81
IA18	06/13/13 02:32:42am	39.6922	76.0245	1421.822	174	20	100	2.8	84
IB1	06/13/13 03:03:52am	39.69213	76.02367	1419.053	198	16	22	4.6	108
IB2	06/13/13 03:03:52am	39.69213	76.02367	1419.053	209	30	22	4.6	119
IB3	06/13/13 03:03:52am	39.69213	76.02367	1419.053	181	45	22	4.6	91
IB4	06/13/13 03:03:52am	39.69213	76.02367	1419.053	135	35	39	4.7	45
IB5	06/13/13 03:03:52am	39.69213	76.02367	1419.053	173	34	16	4.9	83
IB6	06/13/13 03:03:52am	39.69213	76.02367	1419.053	119	26	16	4.9	29
IB7	06/13/13 03:03:52am	39.69213	76.02367	1419.053	185	51	303	5.4	95
IB8	06/13/13 03:03:52am	39.69213	76.02367	1419.053	134	31	285	5.9	44
IB9	06/13/13 03:03:52am	39.69213	76.02367	1419.053	174	48	271	5.9	84
IB10	06/13/13 03:03:52am	39.69213	76.02367	1419.053	245	44	316	5.6	155
IB11	06/13/13 03:03:52am	39.69213	76.02367	1419.053	130	30	276	6	40
IB12	06/13/13 03:03:52am	39.69213	76.02367	1419.053	123	34	179	5.7	33
IB13	06/13/13 03:03:52am	39.69213	76.02367	1419.053	90	42	179	5.7	0
IB14	06/13/13 03:03:52am	39.69213	76.02367	1419.053	115	43	179	5.7	25
IB15	06/13/13 03:03:52am	39.69213	76.02367	1419.053	188	42	280	5.5	98
IB16	06/13/13 03:03:52am	39.69213	76.02367	1419.053	164	45	250	4.9	74
IB17	06/13/13 03:03:52am	39.69213	76.02367	1419.053	194	46	276	4.2	104
IB18	06/13/13 03:03:52am	39.69213	76.02367	1419.053	90	32	318	5	0
IB19	06/13/13 03:03:52am	39.69213	76.02367	1419.053	180	36	275	3.6	90
IB20	06/13/13 03:03:52am	39.69213	76.02367	1419.053	156	27	280	3.5	66
IB21	06/13/13 03:03:52am	39.69213	76.02367	1419.053	160	41	280	3.5	70
IB22	06/13/13 03:03:52am	39.69213	76.02367	1419.053	135	39	241	1.2	45

IB23	06/13/13 03:03:52am	39.69213	76.02367	1419.053	150	40	226	1.2	60
IB24	06/13/13 03:59:44am	39.69216	76.02346	1421.982	171	50	65	3.4	81
IB25	06/13/13 04:00:43am	39.69228	76.02361	1418.962	80	47	355	2	350
IB26	06/13/13 04:00:43am	39.69228	76.02361	1418.962	75	35	350	2	345
IB27	06/13/13 04:00:43am	39.69228	76.02361	1418.962	255	36	356	2.3	165
IB28	06/13/13 04:00:43am	39.69228	76.02361	1418.962	94	49	347	2.3	4
IC1	06/13/13 04:20:20am	39.69511	76.01914	1449.386	200	32	105	0.3	110
IC2	06/13/13 04:20:20am	39.69511	76.01914	1449.386	212	35	104	0.2	122
IC3	06/13/13 04:20:20am	39.69511	76.01914	1449.386	190	24	80	0.2	100
IC4	06/13/13 04:20:20am	39.69511	76.01914	1449.386	183	31	270	2.3	93
IC5	06/13/13 04:20:20am	39.69511	76.01914	1449.386	204	45	279	2.3	114
IC6	06/13/13 04:20:20am	39.69511	76.01914	1449.386	150	57	260	2.3	60
ID1	06/13/13 04:34:54am	39.69668	76.01607	1455.261	240	24	330	3.5	150
ID2	06/13/13 04:34:54am	39.69668	76.01607	1455.261	250	32	330	3.5	160
ID3	06/13/13 04:34:54am	39.69668	76.01607	1455.261	216	23	320	3	126
ID4	06/13/13 04:34:54am	39.69668	76.01607	1455.261	186	36	320	3.2	96
IE1	06/13/13 04:51:21am	39.69696	76.01559	1453.334	324	35	195	2	234
IE2	06/13/13 04:51:21am	39.69696	76.01559	1453.334	280	42	25	2	190
IE3	06/13/13 04:51:21am	39.69696	76.01559	1453.334	275	30	160	2	185
IE4	06/13/13 04:51:21am	39.69696	76.01559	1453.334	156	37	83	2	66
IE5	06/13/13 04:51:21am	39.69696	76.01559	1453.334	256	44	155	6.1	166
IE6	06/13/13 04:51:21am	39.69696	76.01559	1453.334	261	39	175	5	171
IE7	06/13/13 04:51:21am	39.69696	76.01559	1453.334	30	55	175	5	300
IE8	06/13/13 04:51:21am	39.69696	76.01559	1453.334	203	44	285	4.7	113
IE9	06/13/13 04:51:21am	39.69696	76.01559	1453.334	190	51	285	4.7	100
IE10	06/13/13 04:51:21am	39.69696	76.01559	1453.334	199	25	285	4.7	109
IE11	06/13/13 04:51:21am	39.69696	76.01559	1453.334	41	39	290	4.1	311
IE12	06/13/13 04:51:21am	39.69696	76.01559	1453.334	216	46	310	4.1	126

IE13	06/13/13 04:51:21am	39.69696	76.01559	1453.334	300	27	190	3	210
IE14	06/13/13 04:51:21am	39.69696	76.01559	1453.334	295	26	190	3	205
IE15	06/13/13 04:51:21am	39.69696	76.01559	1453.334	262	40	191	2	172
IE16	06/13/13 04:51:21am	39.69696	76.01559	1453.334	280	60	187	2.5	190
IE17	06/13/13 04:51:21am	39.69696	76.01559	1453.334	90	56	210	2.5	0
IG1	06/13/13 05:48:55am	39.70376	76.01273	1470.955	184	41	306	2.2	94
IG2	Between top and bottom	Between top and bottom	Between top and bottom	Between top and bottom	200	40	306	2.2	110
IG3	Between top and bottom	Between top and bottom	Between top and bottom	Between top and bottom	175	21	270	2.4	85
IG4	Between top and bottom	Between top and bottom	Between top and bottom	Between top and bottom	173	41	300	2.3	83
IG5	Between top and bottom	Between top and bottom	Between top and bottom	Between top and bottom	44	56	290	2.3	314
IG6	Between top and bottom	Between top and bottom	Between top and bottom	Between top and bottom	140	34	274	2.7	50
IG7	Between top and bottom	Between top and bottom	Between top and bottom	Between top and bottom	131	35	210	3	41
IG8	Between top and bottom	Between top and bottom	Between top and bottom	Between top and bottom	115	39	210	3	25
IG9	Between top and bottom	Between top and bottom	Between top and bottom	Between top and bottom	130	60	210	3	40
IG10	Between top and bottom	Between top and bottom	Between top and bottom	Between top and bottom	295	34	210	3	205
IG11	Between top and bottom	Between top and bottom	Between top and bottom	Between top and bottom	301	31	210	2.8	211

IG12	Between top and bottom	Between top and bottom	Between top and bottom	Between top and bottom	291	53	210	2.8	201
IG13	Between top and bottom	Between top and bottom	Between top and bottom	Between top and bottom	276	46	193	3.2	186
IG14	Between top and bottom	Between top and bottom	Between top and bottom	Between top and bottom	106	31	193	3.2	16
IG15	Between top and bottom	Between top and bottom	Between top and bottom	Between top and bottom	170	35	305	4.2	80
IG16	Between top and bottom	Between top and bottom	Between top and bottom	Between top and bottom	254	26	329	4.6	164
IG17	Between top and bottom	Between top and bottom	Between top and bottom	Between top and bottom	256	38	180	4.1	166
IG18	Between top and bottom	Between top and bottom	Between top and bottom	Between top and bottom	73	37	180	3.9	343
IG19	Between top and bottom	Between top and bottom	Between top and bottom	Between top and bottom	96	40	180	3.9	6
IG20	Between top and bottom	Between top and bottom	Between top and bottom	Between top and bottom	305	31	188	3.1	215
IG21	Between top and bottom	Between top and bottom	Between top and bottom	Between top and bottom	310	40	195	3.1	220
IG22	Between top and bottom	Between top and bottom	Between top and bottom	Between top and bottom	295	62	195	3.1	205
IG23	Between top and bottom	Between top and bottom	Between top and bottom	Between top and bottom	259	36	170	4.5	169
IG24	Between top and bottom	Between top and	Between top and	Between top and	296	36	214	2.3	206

		bottom	bottom	bottom					
IG25	Between top and bottom	Between top and bottom	Between top and bottom	Between top and bottom	313	23	215	2.9	223
IG26	Between top and bottom	Between top and bottom	Between top and bottom	Between top and bottom	285	62	215	2.9	195
IG27	Between top and bottom	Between top and bottom	Between top and bottom	Between top and bottom	101	25	201	3.5	11
IG28	Between top and bottom	Between top and bottom	Between top and bottom	Between top and bottom	144	50	232	3.9	54
IG29	Between top and bottom	Between top and bottom	Between top and bottom	Between top and bottom	265	34	166	2.1	175
IG30	Between top and bottom	Between top and bottom	Between top and bottom	Between top and bottom	336	41	264	2.3	246
IG31	Between top and bottom	Between top and bottom	Between top and bottom	Between top and bottom	243	31	295	1.9	153
IG32	Between top and bottom	Between top and bottom	Between top and bottom	Between top and bottom	181	26	294	1.3	91
IG33	Between top and bottom	Between top and bottom	Between top and bottom	Between top and bottom	250	21	140	0.8	160
IG34	Between top and bottom	Between top and bottom	Between top and bottom	Between top and bottom	232	31	140	0.8	142
IG35	06/13/13 06:28:39am	39.70342	76.01332	1466.972	206	38	140	0.8	116
IH1	06/13/13 07:33:41am	39.70211	76.02095	1465.255	256	55	326	0.7	166
IH2	06/13/13 07:33:41am	39.70211	76.02095	1465.255	246	46	335	0.9	156
IH3	06/13/13 07:33:41am	39.70211	76.02095	1465.255	176	26	316	1.4	86
IH4	06/13/13 07:33:41am	39.70211	76.02095	1465.255	213	43	290	1.3	123

IH5	06/13/13 07:33:41am	39.70211	76.02095	1465.255	230	32	290	1.3	140
IH6	06/13/13 07:33:41am	39.70211	76.02095	1465.255	215	30	290	1.3	125
IH7	06/13/13 07:33:41am	39.70211	76.02095	1465.255	198	33	315	1.4	108
IH8	06/13/13 07:33:41am	39.70211	76.02095	1465.255	204	25	292	1.9	114
IH9	06/13/13 07:33:41am	39.70211	76.02095	1465.255	192	44	292	1.9	102
IH10	06/13/13 07:33:41am	39.70211	76.02095	1465.255	190	25	292	1.9	100
IH11	06/13/13 07:33:41am	39.70211	76.02095	1465.255	163	36	294	2.5	73
II1	06/13/13 07:57:31am	39.70308	76.02324	1462.805	325	28	243	2	235
II2	06/13/13 07:57:31am	39.70308	76.02324	1462.805	155	33	244	2	65
II3	06/13/13 07:57:31am	39.70308	76.02324	1462.805	111	28	244	2	21
II4	06/13/13 07:57:31am	39.70308	76.02324	1462.805	166	61	244	2	76
II5	06/13/13 07:57:31am	39.70308	76.02324	1462.805	118	56	215	2.8	28
II6	06/13/13 07:57:31am	39.70308	76.02324	1462.805	265	31	203	2.4	175
II7	06/13/13 07:57:31am	39.70308	76.02324	1462.805	144	40	238	3.1	54
II8	06/13/13 07:57:31am	39.70308	76.02324	1462.805	274	29	241	2.8	184
II9	06/13/13 07:57:31am	39.70308	76.02324	1462.805	340	33	246	2.5	250
II10	06/13/13 07:57:31am	39.70308	76.02324	1462.805	144	38	272	3.5	54
II11	06/13/13 07:57:31am	39.70308	76.02324	1462.805	166	22	272	3.5	76
II12	06/13/13 07:57:31am	39.70308	76.02324	1462.805	165	41	272	3.5	75
II13	06/13/13 07:57:31am	39.70308	76.02324	1462.805	176	72	272	3.5	86
II14	06/13/13 07:57:31am	39.70308	76.02324	1462.805	180	66	272	3.5	90
II15	06/13/13 07:57:31am	39.70308	76.02324	1462.805	139	38	250	3.4	49
II16	06/13/13 07:57:31am	39.70308	76.02324	1462.805	164	16	250	3.4	74
II17	06/13/13 07:57:31am	39.70308	76.02324	1462.805	128	41	257	2.7	38
II18	06/13/13 07:57:31am	39.70308	76.02324	1462.805	113	36	257	2.7	23
II19	06/13/13 07:57:31am	39.70308	76.02324	1462.805	145	31	257	2.7	55
II20	06/13/13 07:57:31am	39.70308	76.02324	1462.805	118	26	257	2.7	28
II21	06/13/13 07:57:31am	39.70308	76.02324	1462.805	148	34	257	2.7	58

II22	06/13/13 07:57:31am	39.70308	76.02324	1462.805	149	31	257	2.7	59
II23	06/13/13 07:57:31am	39.70308	76.02324	1462.805	137	34	257	2.7	47
II24	06/13/13 07:57:31am	39.70308	76.02324	1462.805	261	31	154	4.9	171
II25	06/13/13 07:57:31am	39.70308	76.02324	1462.805	258	69	154	4.9	168
IK1	06/14/13 03:15:19am	39.89122	76.60739	1362.629	353	50	231	12	263
IK2	06/14/13 03:15:19am	39.89122	76.60739	1362.629	327	36	231	12	237
IK3	06/14/13 03:15:19am	39.89122	76.60739	1362.629	337	41	231	12	247
IK4	06/14/13 03:15:19am	39.89122	76.60739	1362.629	323	32	231	12	233
IK5	06/14/13 03:15:19am	39.89122	76.60739	1362.629	202	45	274	12.2	112
IK6	06/14/13 03:15:19am	39.89122	76.60739	1362.629	213	46	312	11.9	123
IK7	06/14/13 03:15:19am	39.89122	76.60739	1362.629	186	39	282	11.5	96
IK8	06/14/13 03:15:19am	39.89122	76.60739	1362.629	183	41	273	11.3	93
IK9	06/14/13 03:15:19am	39.89122	76.60739	1362.629	300	53	220	6.7	210
IK10	06/14/13 03:15:19am	39.89122	76.60739	1362.629	245	42	292	4.5	155
IK11	06/14/13 03:15:19am	39.89122	76.60739	1362.629	222	44	140	1.5	132
IK12	06/14/13 03:15:19am	39.89122	76.60739	1362.629	166	30	291	12	76
IK13	06/14/13 03:15:19am	39.89122	76.60739	1362.629	175	57	309	10.7	85
IK14	06/14/13 03:15:19am	39.89122	76.60739	1362.629	184	65	309	10.7	94
IK15	06/14/13 03:15:19am	39.89122	76.60739	1362.629	185	34	299	10.9	95
IK16	06/14/13 03:15:19am	39.89122	76.60739	1362.629	188	35	282	9.9	98
IK17	06/14/13 03:15:19am	39.89122	76.60739	1362.629	306	36	221	11.5	216
IK18	06/14/13 03:15:19am	39.89122	76.60739	1362.629	314	55	226	6.4	224
IK19	06/14/13 03:15:19am	39.89122	76.60739	1362.629	219	37	296	8.5	129
IK20	06/14/13 03:15:19am	39.89122	76.60739	1362.629	168	48	255	7.5	78
IK21	06/14/13 03:15:19am	39.89122	76.60739	1362.629	157	51	255	7.5	67
IK22	06/14/13 03:15:19am	39.89122	76.60739	1362.629	174	36	255	7.6	84
IK23	06/14/13 03:15:19am	39.89122	76.60739	1362.629	356	46	255	7.8	266
IK24	06/14/13 03:15:19am	39.89122	76.60739	1362.629	131	47	223	7.2	41

IK25	06/14/13 03:15:19am	39.89122	76.60739	1362.629	136	49	246	6.7	46
IK26	06/14/13 03:15:19am	39.89122	76.60739	1362.629	205	41	309	5.3	115
IK27	06/14/13 03:15:19am	39.89122	76.60739	1362.629	209	46	309	5.3	119
IK28	06/14/13 03:15:19am	39.89122	76.60739	1362.629	203	46	282	4.7	113
IK29	06/14/13 03:15:19am	39.89122	76.60739	1362.629	211	35	321	5.1	121
IK30	06/14/13 03:15:19am	39.89122	76.60739	1362.629	265	46	1	4.7	175
IK31	06/14/13 03:15:19am	39.89122	76.60739	1362.629	301	37	225	4.2	211
IK32	06/14/13 03:15:19am	39.89122	76.60739	1362.629	192	36	300	3.9	102
IK33	06/14/13 03:15:19am	39.89122	76.60739	1362.629	275	36	194	1.4	185
IK34	06/14/13 03:15:19am	39.89122	76.60739	1362.629	246	56	335	3.2	156
IK35	06/14/13 03:15:19am	39.89122	76.60739	1362.629	237	34	311	3.8	147
JG1	06/14/13 07:18:20am	39.90508	76.58254	1487.305	284	42	267	3	194
JG2	06/14/13 07:18:20am	39.90508	76.58254	1487.305	262	26	267	3	172
JG3	06/14/13 07:18:20am	39.90508	76.58254	1487.305	276	33	215	1.8	186
JG4	06/14/13 07:18:20am	39.90508	76.58254	1487.305	261	43	215	2	171
JG5	06/14/13 07:18:20am	39.90508	76.58254	1487.305	284	27	215	2	194
JG6	06/14/13 07:18:20am	39.90508	76.58254	1487.305	145	35	270	3.7	55
JG7	06/14/13 07:18:20am	39.90508	76.58254	1487.305	147	37	270	3.7	57
JG8	06/14/13 07:18:20am	39.90508	76.58254	1487.305	295	30	145	3.7	205
JG9	06/14/13 07:18:20am	39.90508	76.58254	1487.305	248	45	145	3.7	158
JG10	06/14/13 07:18:20am	39.90508	76.58254	1487.305	290	57	145	3.7	200
JG11	06/14/13 07:18:20am	39.90508	76.58254	1487.305	259	29	190	2.5	169
JG12	06/14/13 07:18:20am	39.90508	76.58254	1487.305	285	54	196	2.5	195
JG13	06/14/13 07:18:20am	39.90508	76.58254	1487.305	109	45	196	2.5	19
JG14	06/14/13 07:18:20am	39.90508	76.58254	1487.305	166	68	215	1	76
JG15	06/14/13 07:18:20am	39.90508	76.58254	1487.305	196	49	270	4.9	106
JG16	06/14/13 07:18:20am	39.90508	76.58254	1487.305	210	38	139	5.7	120
JG17	06/14/13 07:18:20am	39.90508	76.58254	1487.305	230	49	139	5.7	140

JG18	06/14/13 07:18:20am	39.90508	76.58254	1487.305	237	55	139	5.7	147
JG19	06/14/13 07:18:20am	39.90508	76.58254	1487.305	225	46	139	5.7	135
JG20	06/14/13 07:18:20am	39.90508	76.58254	1487.305	256	32	142	5.3	166
JG21	06/14/13 07:18:20am	39.90508	76.58254	1487.305	254	38	180	5.7	164
JG22	06/14/13 07:18:20am	39.90508	76.58254	1487.305	149	31	275	4.4	59
JG23	06/14/13 07:18:20am	39.90508	76.58254	1487.305	306	29	250	4	216
JG24	06/14/13 07:18:20am	39.90508	76.58254	1487.305	174	49	275	3.3	84
JG25	06/14/13 07:18:20am	39.90508	76.58254	1487.305	191	51	275	3.3	101
JG26	06/14/13 07:18:20am	39.90508	76.58254	1487.305	187	53	268	6	97
JG27	06/14/13 07:18:20am	39.90508	76.58254	1487.305	186	58	268	6	96
JG28	06/14/13 07:18:20am	39.90508	76.58254	1487.305	179	61	268	6	89
JG29	06/14/13 07:18:20am	39.90508	76.58254	1487.305	145	31	268	6	55
JG30	06/14/13 07:18:20am	39.90508	76.58254	1487.305	143	40	268	6	53
JG31	06/14/13 07:18:20am	39.90508	76.58254	1487.305	165	55	268	6	75
JG32	06/14/13 07:18:20am	39.90508	76.58254	1487.305	186	57	268	5.8	96
JG33	06/14/13 07:18:20am	39.90508	76.58254	1487.305	161	32	254	4.8	71
JG34	06/14/13 07:18:20am	39.90508	76.58254	1487.305	145	38	251	5.4	55
JG35	06/14/13 07:18:20am	39.90508	76.58254	1487.305	136	49	249	5.9	46
JG36	06/14/13 07:18:20am	39.90508	76.58254	1487.305	155	80	249	5.9	65
JN1	06/14/13 08:28:02am	39.9018	76.58643	1451.024	225	45	310	23.7	135
JN2	Between top and bottom	Between top and bottom	Between top and bottom	Between top and bottom	190	44	270	23.4	100
JN3	Between top and bottom	Between top and bottom	Between top and bottom	Between top and bottom	195	54	285	22.9	105
JN4	Between top and bottom	Between top and bottom	Between top and bottom	Between top and bottom	182	55	271	21.5	92
JN5	Between top and bottom	Between top and	Between top and	Between top and	159	44	271	21.5	69

		bottom	bottom	bottom					
JN6	Between top and bottom	Between top and bottom	Between top and bottom	Between top and bottom	262	32	202	22.5	172
JN7	Between top and bottom	Between top and bottom	Between top and bottom	Between top and bottom	246	46	140	22.5	156
JN8	Between top and bottom	Between top and bottom	Between top and bottom	Between top and bottom	176	40	265	20	86
JN9	Between top and bottom	Between top and bottom	Between top and bottom	Between top and bottom	148	19	254	19.3	58
JN10	Between top and bottom	Between top and bottom	Between top and bottom	Between top and bottom	179	68	255	18.9	89
JN11	Between top and bottom	Between top and bottom	Between top and bottom	Between top and bottom	140	55	194	19.3	50
JN12	Between top and bottom	Between top and bottom	Between top and bottom	Between top and bottom	265	31	205	19.9	175
JN13	Between top and bottom	Between top and bottom	Between top and bottom	Between top and bottom	169	22	250	17.7	79
JN14	Between top and bottom	Between top and bottom	Between top and bottom	Between top and bottom	103	21	183	17.7	13
JN15	Between top and bottom	Between top and bottom	Between top and bottom	Between top and bottom	145	34	242	17.4	55
JN16	Between top and bottom	Between top and bottom	Between top and bottom	Between top and bottom	130	32	244	17.6	40
JN17	Between top and bottom	Between top and bottom	Between top and bottom	Between top and bottom	195	55	278	17.8	105

JN18	Between top and bottom	Between top and bottom	Between top and bottom	Between top and bottom	200	48	287	17.5	110
JN19	Between top and bottom	Between top and bottom	Between top and bottom	Between top and bottom	183	34	294	17.6	93
JN20	Between top and bottom	Between top and bottom	Between top and bottom	Between top and bottom	342	36	235	16	252
JN21	Between top and bottom	Between top and bottom	Between top and bottom	Between top and bottom	294	42	231	16.6	204
JN22	Between top and bottom	Between top and bottom	Between top and bottom	Between top and bottom	235	34	323	16	145
JN23	Between top and bottom	Between top and bottom	Between top and bottom	Between top and bottom	299	23	182	14.8	209
JN24	Between top and bottom	Between top and bottom	Between top and bottom	Between top and bottom	288	25	200	13.8	198
JN25	Between top and bottom	Between top and bottom	Between top and bottom	Between top and bottom	210	45	172	16.8	120
JN26	Between top and bottom	Between top and bottom	Between top and bottom	Between top and bottom	169	36	260	16.1	79
JN27	Between top and bottom	Between top and bottom	Between top and bottom	Between top and bottom	165	42	250	14.9	75
JN28	Between top and bottom	Between top and bottom	Between top and bottom	Between top and bottom	174	24	244	14.7	84
JN29	Between top and bottom	Between top and bottom	Between top and bottom	Between top and bottom	145	51	244	14.7	55
JN30	Between top and bottom	Between top and	Between top and	Between top and	216	33	314	12.5	126

		bottom	bottom	bottom					
JN31	Between top and bottom	Between top and bottom	Between top and bottom	Between top and bottom	261	52	344	11.9	171
JN32	06/14/13 09:57:58am	39.9025	76.58511	1460.538	192	40	280	11.9	102
KK1	06/15/13 08:35:50am	39.73838	76.09985	1397.145	220	46	311	0.8	130
KK2	06/15/13 08:35:50am	39.73838	76.09985	1397.145	214	48	311	0.8	124
KK3	06/15/13 08:35:50am	39.73838	76.09985	1397.145	222	39	205	1.2	132
KK4	06/15/13 08:35:50am	39.73838	76.09985	1397.145	207	49	300	1	117
KK5	06/15/13 08:35:50am	39.73838	76.09985	1397.145	218	46	300	1	128
KK6	06/15/13 08:35:50am	39.73838	76.09985	1397.145	195	36	110	0.9	105
KK7	06/15/13 08:35:50am	39.73838	76.09985	1397.145	199	37	303	1.2	109
KM1	06/15/13 08:35:50am	39.73838	76.09985	1397.145	252	37	339	0.9	162
KM2	06/15/13 08:35:50am	39.73838	76.09985	1397.145	169	51	276	0.6	79
KM3	06/15/13 08:35:50am	39.73838	76.09985	1397.145	240	36	306	0.9	150
KM4	06/15/13 08:35:50am	39.73838	76.09985	1397.145	251	61	301	0.7	161
KM5	06/15/13 08:35:50am	39.73838	76.09985	1397.145	164	44	286	0.8	74
KN1	06/15/13 08:35:50am	39.73838	76.09985	1397.145	206	14			116
KN2	06/15/13 08:35:50am	39.73838	76.09985	1397.145	215	20	281	1.6	125
KN3	06/15/13 08:35:50am	39.73838	76.09985	1397.145	165	24	75	0.9	75
KN4	06/15/13 08:35:50am	39.73838	76.09985	1397.145	211	41	315	1.4	121
KN5	06/15/13 08:35:50am	39.73838	76.09985	1397.145	226	64	315	1.4	136
KU1	06/15/13 09:48:23am	39.73783	76.10118	1388.426	179	44	260	0.7	89
KU2	06/15/13 09:48:23am	39.73783	76.10118	1388.426	184	41	270	0.7	94
KU3	06/15/13 09:48:23am	39.73783	76.10118	1388.426	270	31	242	0.6	180
KV1	06/15/13 09:59:08am	39.738	76.10138	1381.847	332	29	60	1.1	242
KV2	06/15/13 09:59:08am	39.738	76.10138	1381.847	30	41	284	1.3	300
KV3	06/15/13 09:59:08am	39.738	76.10138	1381.847	135	40	210	1.3	45
KV4	06/15/13 09:59:08am	39.738	76.10138	1381.847	144	60	210	1.4	54

KV5	06/15/13 09:59:08am	39.738	76.10138	1381.847	179	41	240	1.4	89
KV6	06/15/13 09:59:08am	39.738	76.10138	1381.847	1	31	260	1.6	271
KW1	06/15/13 10:23:45am	39.73862	76.10086	1388.996	320	61	249	0.5	230
KW2	06/15/13 10:23:45am	39.73862	76.10086	1388.996	271	52	181	1.4	181
KW3	06/15/13 10:23:45am	39.73862	76.10086	1388.996	254	34	172	1.4	164
KW4	06/15/13 10:23:45am	39.73862	76.10086	1388.996	254	38	172	1.4	164
PN1	06/23/13 08:03:44am	39.71949	76.0124	1490.69	273	31	349	2.4	183
PN2	06/23/13 08:03:44am	39.71949	76.0124	1490.69	256	30	349	2.6	166
PN3	06/23/13 08:03:44am	39.71949	76.0124	1490.69	274	41	349	2.4	184
PN4	06/23/13 08:03:44am	39.71949	76.0124	1490.69	239	29	349	2.3	149
PN5	06/23/13 08:03:44am	39.71949	76.0124	1490.69	243	33	349	2.3	153
PN6	06/23/13 08:03:44am	39.71949	76.0124	1490.69	256	32	349	2	166
PO1	06/23/13 08:11:13am	39.71978	76.01253	1479.794	271	39	140	2.9	181
PO2	06/23/13 08:11:13am	39.71978	76.01253	1479.794	259	45	140	2.9	169
PO3	06/23/13 08:11:13am	39.71978	76.01253	1479.794	268	37	140	2.9	178
PO4	06/23/13 08:11:13am	39.71978	76.01253	1479.794	269	60	145	2.8	179
PO5	06/23/13 08:11:13am	39.71978	76.01253	1479.794	305	49	145	2.7	215
PO6	06/23/13 08:11:13am	39.71978	76.01253	1479.794	48	36	145	2.7	318
PO7	06/23/13 08:11:13am	39.71978	76.01253	1479.794	351	35	100	2.9	261
PP1	06/23/13 08:21:15am	39.72013	76.01231	1477.359	300	41	23	2.8	210
PP2	06/23/13 08:21:15am	39.72013	76.01231	1477.359	115	22	10	2.5	25
PP3	06/23/13 08:21:15am	39.72013	76.01231	1477.359	266	38	10	2.6	176
PP4	06/23/13 08:21:15am	39.72013	76.01231	1477.359	115	29	10	2.6	25
PP5	06/23/13 08:21:15am	39.72013	76.01231	1477.359	295	39	15	2.7	205
PP6	06/23/13 08:21:15am	39.72013	76.01231	1477.359	242	48	15	2.7	152
PP7	06/23/13 08:21:15am	39.72013	76.01231	1477.359	242	42	20	3	152
PP8	06/23/13 08:21:15am	39.72013	76.01231	1477.359	135	34	20	2.3	45
PP9	06/23/13 08:21:15am	39.72013	76.01231	1477.359	262	34	25	3.1	172

PP10	06/23/13 08:21:15am	39.72013	76.01231	1477.359	113	40	25	2.3	23
PP11	06/23/13 08:21:15am	39.72013	76.01231	1477.359	287	58	45	3.1	197
PQ1	06/23/13 08:35:16am	39.72032	76.01234	1478.789	355	45	284	3.3	265
PQ2	06/23/13 08:35:16am	39.72032	76.01234	1478.789	14	59	284	3.3	284
PQ3	06/23/13 08:35:16am	39.72032	76.01234	1478.789	66	61	334	3.1	336
PQ4	06/23/13 08:35:16am	39.72032	76.01234	1478.789	279	36	359	2.9	189
PQ5	06/23/13 08:35:16am	39.72032	76.01234	1478.789	263	32	326	2.8	173
PQ6	06/23/13 08:35:16am	39.72032	76.01234	1478.789	245	49	335	2.5	155
PQ7	06/23/13 08:35:16am	39.72032	76.01234	1478.789	237	23	40	2.8	147
PQ8	06/23/13 08:35:16am	39.72032	76.01234	1478.789	266	45	336	3	176
PR1	06/23/13 09:21:33am	39.71033	76.02166	1472.433	223	41	305	3.5	133
PR2	06/23/13 09:21:33am	39.71033	76.02166	1472.433	355	38	251	3.5	265
PR3	06/23/13 09:21:33am	39.71033	76.02166	1472.433	253	41	305	3.4	163
PS1	06/23/13 09:31:57am	39.7104	76.02176	1485.718	283	44	216	3.1	193
PS2	06/23/13 09:31:57am	39.7104	76.02176	1485.718	277	37	216	2.9	187
PS3	06/23/13 09:31:57am	39.7104	76.02176	1485.718	89	35	216	2.9	359
PS4	06/23/13 09:31:57am	39.7104	76.02176	1485.718	275	28	185	2.8	185
PT1	06/23/13 09:45:40am	39.71064	76.02167	1477.935	251	39	168	3.4	161
PT2	06/23/13 09:45:40am	39.71064	76.02167	1477.935	291	40	201	3.6	201
PT3	06/23/13 09:45:40am	39.71064	76.02167	1477.935	272	40	185	2.9	182
PT4	06/23/13 09:45:40am	39.71064	76.02167	1477.935	287	31	199	2.9	197
PT5	06/23/13 09:45:40am	39.71064	76.02167	1477.935	281	39	198	2.2	191
PT6	06/23/13 09:45:40am	39.71064	76.02167	1477.935	334	19	214	3.1	244
PU1	06/23/13 10:03:32am	39.71082	76.02144	1480.142	180	35	70	2.2	90
PU2	06/23/13 10:03:32am	39.71082	76.02144	1480.142	187	31	60	2.1	97
PU3	06/23/13 10:03:32am	39.71082	76.02144	1480.142	210	48	65	2.2	120
PU4	06/23/13 10:03:32am	39.71082	76.02144	1480.142	354	41	70	1.2	264
PU5	06/23/13 10:03:32am	39.71082	76.02144	1480.142	155	26	60	1.2	65

PU6	06/23/13 10:03:32am	39.71082	76.02144	1480.142	314	45	65	1.2	224
PU7	06/23/13 10:03:32am	39.71082	76.02144	1480.142	305	29	40	1.2	215
PU8	06/23/13 10:03:32am	39.71082	76.02144	1480.142	7	20	90	0.5	277
PU9	06/23/13 10:03:32am	39.71082	76.02144	1480.142	213	29	115	0.4	123
PV1	06/23/13 10:17:33am	39.7108	76.02133	1480.828	173	40	281	1.8	83
PV2	06/23/13 10:17:33am	39.7108	76.02133	1480.828	191	45	286	0.6	101
PV3	06/23/13 10:17:33am	39.7108	76.02133	1480.828	175	31	280	1.2	85
PV4	06/23/13 10:17:33am	39.7108	76.02133	1480.828	25	20	260	1.3	295
PV5	06/23/13 10:17:33am	39.7108	76.02133	1480.828	215	43	320	0.6	125
PV6	06/23/13 10:17:33am	39.7108	76.02133	1480.828	211	43	310	0.7	121
PW1	06/23/13 10:27:58am	39.71088	76.02133	1477.153	285	31	190	1.3	195
PW2	06/23/13 10:27:58am	39.71088	76.02133	1477.153	285	34	190	1.6	195
PW3	06/23/13 10:27:58am	39.71088	76.02133	1477.153	268	32	185	1.1	178
PW4	06/23/13 10:27:58am	39.71088	76.02133	1477.153	266	36	185	1.1	176
PW5	06/23/13 10:27:58am	39.71088	76.02133	1477.153	290	34	199	1.3	200
PX1	06/23/13 10:36:55am	39.71098	76.02126	1484.497	285	39	170	0.5	195
PX2	06/23/13 10:36:55am	39.71098	76.02126	1484.497	270	34	135	0.6	180
PX3	06/23/13 10:36:55am	39.71098	76.02126	1484.497	310	31	165	0.5	220
PX4	06/23/13 10:36:55am	39.71098	76.02126	1484.497	75	31	155	0.4	345
PY1	06/23/13 10:57:55am	39.7134	76.0124	1479.909	182	33	75	0.9	92
PY2	06/23/13 10:57:55am	39.7134	76.0124	1479.909	210	29	75	1	120
PY3	06/23/13 10:57:55am	39.7134	76.0124	1479.909	185	36	75	0.9	95
PY4	06/23/13 10:57:55am	39.7134	76.0124	1479.909	285	36	75	0.9	195
PY5	06/23/13 10:57:55am	39.7134	76.0124	1479.909	182	31	75	0.9	92
PY6	06/23/13 10:57:55am	39.7134	76.0124	1479.909	303	42	85	0.7	213
PY7	06/23/13 10:57:55am	39.7134	76.0124	1479.909	220	28	85	0.9	130
PY8	06/23/13 10:57:55am	39.7134	76.0124	1479.909	216	19	84	0.6	126
PZ1	06/23/13 11:10:43am	39.71314	76.01192	1485.628	165	29	290	2.7	75

PZ2	06/23/13 11:10:43am	39.71314	76.01192	1485.628	164	20	268	2.7	74
PZ3	06/23/13 11:10:43am	39.71314	76.01192	1485.628	206	26	283	2.1	116
PZ4	06/23/13 11:10:43am	39.71314	76.01192	1485.628	190	27	304	1.8	100
PZ5	06/23/13 11:10:43am	39.71314	76.01192	1485.628	202	28	290	2	112
QG1	06/24/13 03:34:18am	39.91409	76.5547	1535.209	205	54	124	0.3	115
QG2	06/24/13 03:34:18am	39.91409	76.5547	1535.209	226	36	124	0.4	136
QG3	06/24/13 03:34:18am	39.91409	76.5547	1535.209	252	41	115	0.3	162
QG4	06/24/13 03:34:18am	39.91409	76.5547	1535.209	166	44	70	0.3	76
QG5	06/24/13 03:34:18am	39.91409	76.5547	1535.209	220	31	141	0.2	130
QG6	06/24/13 03:34:18am	39.91409	76.5547	1535.209	262	39	166	0.4	172
QG7	06/24/13 03:34:18am	39.91409	76.5547	1535.209	224	38	174	0.3	134
QG8	06/24/13 03:34:18am	39.91409	76.5547	1535.209	255	56	174	0.4	165
QG9	06/24/13 03:34:18am	39.91409	76.5547	1535.209	243	48	171	0.5	153
QG10	06/24/13 03:34:18am	39.91409	76.5547	1535.209	232	40	171	0.3	142
QG11	06/24/13 03:34:18am	39.91409	76.5547	1535.209	243	46	171	0.5	153
QG12	06/24/13 03:34:18am	39.91409	76.5547	1535.209	248	29	171	0.4	158
QG13	06/24/13 03:34:18am	39.91409	76.5547	1535.209	288	49	171	0.6	198
QG14	06/24/13 03:34:18am	39.91409	76.5547	1535.209	273	42	171	0.6	183
QG15	06/24/13 03:34:18am	39.91409	76.5547	1535.209	264	33	185	0.4	174
QH1	06/24/13 03:53:18am	39.91392	76.55507	1531.806	235	26	89	2.5	145
QH2	06/24/13 03:53:18am	39.91392	76.55507	1531.806	199	46	89	2.5	109
QH3	06/24/13 03:53:18am	39.91392	76.55507	1531.806	214	34	70	2.5	124
QH4	06/24/13 03:53:18am	39.91392	76.55507	1531.806	258	31	87	2.5	168
QH5	06/24/13 03:53:18am	39.91392	76.55507	1531.806	242	33	87	2.5	152
QH6	06/24/13 03:53:18am	39.91392	76.55507	1531.806	260	19	115	2.5	170
QH7	06/24/13 03:53:18am	39.91392	76.55507	1531.806	226	37	130	2.6	136
QH8	06/24/13 03:53:18am	39.91392	76.55507	1531.806	187	35	125	1.9	97
QH9	06/24/13 03:53:18am	39.91392	76.55507	1531.806	242	29	130	1.2	152

QH10	06/24/13 03:53:18am	39.91392	76.55507	1531.806	221	37	125	1.3	131
QI1	06/24/13 04:11:53am	39.91369	76.55522	1526.179	140	34	255	2.3	50
QI2	06/24/13 04:11:53am	39.91369	76.55522	1526.179	208	25	255	2.3	118
QI3	06/24/13 04:11:53am	39.91369	76.55522	1526.179	189	26	242	2.3	99
QI4	06/24/13 04:11:53am	39.91369	76.55522	1526.179	23	25	242	2.4	293
QI5	06/24/13 04:11:53am	39.91369	76.55522	1526.179	191	49	251	2.3	101
QI6	06/24/13 04:11:53am	39.91369	76.55522	1526.179	179	58	260	1.8	89
QI7	06/24/13 04:11:53am	39.91369	76.55522	1526.179	169	53	270	1.8	79
QI9	06/24/13 04:11:53am	39.91369	76.55522	1526.179	166	39	255	2.1	76
QI10	06/24/13 04:11:53am	39.91369	76.55522	1526.179	344	27	260	2	254
QI11	06/24/13 04:11:53am	39.91369	76.55522	1526.179	161	46	260	2	71
QJ1	06/24/13 04:27:11am	39.91361	76.55539	1529.802	254	36	330	2	164
QJ2	06/24/13 04:27:11am	39.91361	76.55539	1529.802	234	46	330	2.4	144
QJ3	06/24/13 04:27:11am	39.91361	76.55539	1529.802	218	31	320	2.4	128
QJ4	06/24/13 04:27:11am	39.91361	76.55539	1529.802	176	39	310	2.5	86
QJ5	06/24/13 04:27:11am	39.91361	76.55539	1529.802	210	30	296	2.6	120
SL1	06/24/13 09:22:44am	39.92463	76.54847	1549.071	206	72	286	2.2	116
SL2a	06/24/13 09:22:44am	39.92463	76.54847	1549.071	179	69	90	1.9	89
SL3	06/24/13 09:22:44am	39.92463	76.54847	1549.071	190	58	90	1.9	100
SL4	06/24/13 09:22:44am	39.92463	76.54847	1549.071	211	31	315	1.8	121
SL5	06/24/13 09:22:44am	39.92463	76.54847	1549.071	196	32	340	1.7	106
SL6	06/24/13 09:22:44am	39.92463	76.54847	1549.071	215	61	340	1.9	125
SL7	06/24/13 09:22:44am	39.92463	76.54847	1549.071	243	33	345	1.6	153
SL8	06/24/13 09:22:44am	39.92463	76.54847	1549.071	164	34	255	2.2	74
SL9	06/24/13 09:22:44am	39.92463	76.54847	1549.071	205	30	290	1.8	115
SM-N1	06/24/13 09:41:11am	39.92458	76.54733	1552.999	227	35	340	1.9	137
SM-N2	Between top and bottom	Between top and bottom	Between top and bottom	Between top and bottom	120	58	230	1.5	30

SM-N3	Between top and bottom	Between top and bottom	Between top and bottom	Between top and bottom	234	39	330	1.9	144
SM-N4	Between top and bottom	Between top and bottom	Between top and bottom	Between top and bottom	159	41	250	1.9	69
SM-N5	Between top and bottom	Between top and bottom	Between top and bottom	Between top and bottom	187	38	355	2.1	97
SM-N6	Between top and bottom	Between top and bottom	Between top and bottom	Between top and bottom	250	38	335	1.9	160
SM-N7	Between top and bottom	Between top and bottom	Between top and bottom	Between top and bottom	150	51	280	0.3	60
SM-N8	Between top and bottom	Between top and bottom	Between top and bottom	Between top and bottom	196	39	285	0.5	106
SM-N9	Between top and bottom	Between top and bottom	Between top and bottom	Between top and bottom	286	30	185	0.6	196
SM-N10	Between top and bottom	Between top and bottom	Between top and bottom	Between top and bottom	278	30	185	0.6	188
SM-N11	Between top and bottom	Between top and bottom	Between top and bottom	Between top and bottom	177	37	260	5.8	87
SM-N12	Between top and bottom	Between top and bottom	Between top and bottom	Between top and bottom	165	41	275	5.6	75
SM-N13	Between top and bottom	Between top and bottom	Between top and bottom	Between top and bottom	231	27	345	2.3	141
SM-N14	Between top and bottom	Between top and bottom	Between top and bottom	Between top and bottom	267	47	180	2.3	177
SM-N15	Between top and bottom	Between top and	Between top and	Between top and	184	41	315	2.2	94

		bottom	bottom	bottom					
SM-N16	Between top and bottom	Between top and bottom	Between top and bottom	Between top and bottom	146	47	275	3.4	56
SM-N17	Between top and bottom	Between top and bottom	Between top and bottom	Between top and bottom	346	34	250	2.9	256
SM-N18	Between top and bottom	Between top and bottom	Between top and bottom	Between top and bottom	175	45	295	2.9	85
SM-N19	06/24/13 09:42:19am	39.9246	76.54719	1553.439	172	57	270	3.8	82
SO1	06/24/13 10:19:54am	39.92481	76.54658	1552.342	153	40	275	1.2	63
SO2	06/24/13 10:19:54am	39.92481	76.54658	1552.342	203	28	275	1.3	113
SO3	06/24/13 10:19:54am	39.92481	76.54658	1552.342	167	59	270	1.2	77
SO4	06/24/13 10:19:54am	39.92481	76.54658	1552.342	166	44	275	1.4	76
SO5	06/24/13 10:19:54am	39.92481	76.54658	1552.342	237	39	160	1.9	147
SO6	06/24/13 10:19:54am	39.92481	76.54658	1552.342	295	38	190	1.4	205
SR1	06/24/13 10:49:41am	39.92199	76.53895	1576.228	171	36	330	2.8	81
SR2	06/24/13 10:49:41am	39.92199	76.53895	1576.228	274	16	330	2.8	184
SR3	06/24/13 10:49:41am	39.92199	76.53895	1576.228	220	34	330	2.9	130
SR4	06/24/13 10:49:41am	39.92199	76.53895	1576.228	194	28	340	2.9	104
SR5	06/24/13 10:49:41am	39.92199	76.53895	1576.228	227	25	340	3	137
SR6	06/24/13 10:49:41am	39.92199	76.53895	1576.228	240	27	45	2.7	150
SR7	06/24/13 10:49:41am	39.92199	76.53895	1576.228	210	25	45	2.7	120
SR8	06/24/13 10:49:41am	39.92199	76.53895	1576.228	266	32	45	2.7	176
SR9	06/24/13 10:49:41am	39.92199	76.53895	1576.228	261	36	45	2.7	171
SS1	06/24/13 11:00:05am	39.92188	76.53946	1576.547	286	31	30	0.9	196
SS2	06/24/13 11:00:05am	39.92188	76.53946	1576.547	268	45	30	0.8	178
ST1	06/24/13 11:04:17am	39.92151	76.53952	1573.521	186	63	300	3.7	96
ST2	06/24/13 11:04:17am	39.92151	76.53952	1573.521	185	56	290	2.6	95
ST3	06/24/13 11:04:17am	39.92151	76.53952	1573.521	187	51	300	3.7	97

ST4	06/24/13 11:04:17am	39.92151	76.53952	1573.521	174	29	290	3.7	84
ST5	06/24/13 11:04:17am	39.92151	76.53952	1573.521	151	65	255	3.7	61
ST6	06/24/13 11:04:17am	39.92151	76.53952	1573.521	179	43	250	3.7	89
ST7	06/24/13 11:04:17am	39.92151	76.53952	1573.521	130	26	250	3.7	40
ST8	06/24/13 11:04:17am	39.92151	76.53952	1573.521	155	58	250	3.7	65
ST9	06/24/13 11:04:17am	39.92151	76.53952	1573.521	189	46	250	3.3	99
ST10	06/24/13 11:04:17am	39.92151	76.53952	1573.521	215	38	130	2.9	125
ST11	06/24/13 11:04:17am	39.92151	76.53952	1573.521	191	54	130	2.8	101
ST12	06/24/13 11:04:17am	39.92151	76.53952	1573.521	236	36	130	3.1	146
SY1	06/26/13 03:07:02am	39.91274	76.57551	1502.703	201	36	190	4.7	111
SY2	06/26/13 03:07:02am	39.91274	76.57551	1502.703	285	43	202	4.7	195
SY3	06/26/13 03:07:02am	39.91274	76.57551	1502.703	294	54	202	4.7	204
SY4	06/26/13 03:07:02am	39.91274	76.57551	1502.703	261	32	201	4.7	171
SY5	06/26/13 03:07:02am	39.91274	76.57551	1502.703	262	34	210	4.7	172
SY6	06/26/13 03:07:02am	39.91274	76.57551	1502.703	198	34	305	5	108
SY7	06/26/13 03:07:02am	39.91274	76.57551	1502.703	187	26	305	5	97
SY8	06/26/13 03:07:02am	39.91274	76.57551	1502.703	221	54	305	5	131
SY9	06/26/13 03:07:02am	39.91274	76.57551	1502.703	176	21	285	5	86
SY10	06/26/13 03:07:02am	39.91274	76.57551	1502.703	195	22	305	5	105
SY11	06/26/13 03:07:02am	39.91274	76.57551	1502.703	258	27	310	5.4	168
SY12	06/26/13 03:07:02am	39.91274	76.57551	1502.703	248	34	320	5.4	158
SY13	06/26/13 03:07:02am	39.91274	76.57551	1502.703	223	34	320	5.4	133
SY14	06/26/13 03:07:02am	39.91274	76.57551	1502.703	217	31	150	4.9	127
SY15	06/26/13 03:07:02am	39.91274	76.57551	1502.703	225	62	320	5.2	135
SY16	06/26/13 03:07:02am	39.91274	76.57551	1502.703	218	30	320	5.1	128
SY17	06/26/13 03:07:02am	39.91274	76.57551	1502.703	178	31	310	4.7	88
SY18	06/26/13 03:07:02am	39.91274	76.57551	1502.703	201	47	325	4.7	111
SY19	06/26/13 03:07:02am	39.91274	76.57551	1502.703	202	38	150	4.6	112

SY20	06/26/13 03:07:02am	39.91274	76.57551	1502.703	241	36	300	4.7	151
SY21	06/26/13 03:07:02am	39.91274	76.57551	1502.703	162	21	295	4.7	72
SY22	06/26/13 03:07:02am	39.91274	76.57551	1502.703	200	41	295	4.9	110
SY23	06/26/13 03:07:02am	39.91274	76.57551	1502.703	159	35	300	5.4	69
SZ1	06/26/13 03:49:25am	39.91261	76.57566	1503.814	146	33	255	7	56
SZ2	06/26/13 03:49:25am	39.91261	76.57566	1503.814	158	42	255	7	68
SZ3	06/26/13 03:49:25am	39.91261	76.57566	1503.814	149	48	250	7	59
SZ4	06/26/13 03:49:25am	39.91261	76.57566	1503.814	156	49	250	7	66
SZ5	06/26/13 03:49:25am	39.91261	76.57566	1503.814	115	42	210	7	25
SZ6	06/26/13 03:49:25am	39.91261	76.57566	1503.814	141	56	215	6.9	51
SZ7	06/26/13 03:49:25am	39.91261	76.57566	1503.814	157	20	225	6.7	67
SZ8	06/26/13 03:49:25am	39.91261	76.57566	1503.814	161	53	230	6.7	71
SZ9	06/26/13 03:49:25am	39.91261	76.57566	1503.814	166	54	230	6.7	76
SZ10	06/26/13 03:49:25am	39.91261	76.57566	1503.814	154	58	230	6.7	64
SZ11	06/26/13 03:49:25am	39.91261	76.57566	1503.814	130	34	25	6.6	40
SZ12	06/26/13 03:49:25am	39.91261	76.57566	1503.814	169	28	25	6.8	79
SZ13	06/26/13 03:49:25am	39.91261	76.57566	1503.814	153	37	245	6.4	63
SZ14	06/26/13 03:49:25am	39.91261	76.57566	1503.814	103	33	250	6.4	13
SZ15	06/26/13 03:49:25am	39.91261	76.57566	1503.814	192	44	220	6.4	102
SZ16	06/26/13 03:49:25am	39.91261	76.57566	1503.814	138	25	230	6.3	48
SZ17	06/26/13 03:49:25am	39.91261	76.57566	1503.814	305	54	240	6	215
TA1	06/26/13 04:07:23am	39.91223	76.57619	1493.547	212	27	300	13.6	122
TA2	06/26/13 04:07:23am	39.91223	76.57619	1493.547	254	29	305	13.6	164
TA3	06/26/13 04:07:23am	39.91223	76.57619	1493.547	202	14	265	14	112
TA4	06/26/13 04:07:23am	39.91223	76.57619	1493.547	218	31	265	13.3	128
TA5	06/26/13 04:07:23am	39.91223	76.57619	1493.547	181	26	295	14	91
TA6	06/26/13 04:07:23am	39.91223	76.57619	1493.547	239	35	165	8.5	149
TA7	06/26/13 04:07:23am	39.91223	76.57619	1493.547	273	31	160	8.1	183

TA8	06/26/13 04:07:23am	39.91223	76.57619	1493.547	242	52	155	7.9	152
TB1	06/26/13 04:18:12am	39.91207	76.5764	1485.322	111	59	190	101	21
TB2	06/26/13 04:18:12am	39.91207	76.5764	1485.322	119	21	190	101	29
TB3	06/26/13 04:18:12am	39.91207	76.5764	1485.322	202	22	260	9.9	112
TB4	06/26/13 04:18:12am	39.91207	76.5764	1485.322	291	60	200	10.1	201
TB5	06/26/13 04:18:12am	39.91207	76.5764	1485.322	166	24	190	10.1	76
TB6	06/26/13 04:18:12am	39.91207	76.5764	1485.322	278	36	175	9.9	188
TB7	06/26/13 04:18:12am	39.91207	76.5764	1485.322	105	34	175	9.9	15
TB8	06/26/13 04:18:12am	39.91207	76.5764	1485.322	132	36	240	9.8	42
TB9	06/26/13 04:18:12am	39.91207	76.5764	1485.322	186	43	206	9.1	96
TB10	06/26/13 04:18:12am	39.91207	76.5764	1485.322	171	43	240	9.1	81
TB11	06/26/13 04:18:12am	39.91207	76.5764	1485.322	278	32	195	9.1	188
UO1	06/26/13 07:08:47am	39.91602	76.56953	1510.544	205	32	305	12	115
UO2	06/26/13 07:08:47am	39.91602	76.56953	1510.544	215	64	305	12	125
UO3	06/26/13 07:08:47am	39.91602	76.56953	1510.544	176	38	159	12	86
UO4	06/26/13 07:08:47am	39.91602	76.56953	1510.544	154	51	300	13	64
UO5	06/26/13 07:08:47am	39.91602	76.56953	1510.544	199	37	305	13	109
UO6	06/26/13 07:08:47am	39.91602	76.56953	1510.544	104	33	220	12.3	14
UO7	06/26/13 07:08:47am	39.91602	76.56953	1510.544	161	49	305	12	71
UO8	06/26/13 07:08:47am	39.91602	76.56953	1510.544	146	30	209	13	56
UO9	06/26/13 07:08:47am	39.91602	76.56953	1510.544	198	39	290	12.5	108
UO10	06/26/13 07:08:47am	39.91602	76.56953	1510.544	164	25	275	12.5	74
UO11	06/26/13 07:08:47am	39.91602	76.56953	1510.544	187	38	290	12	97
UO12	06/26/13 07:08:47am	39.91602	76.56953	1510.544	116	41	215	12.2	26
UO13	06/26/13 07:08:47am	39.91602	76.56953	1510.544	155	37	235	10.5	65
UO14	06/26/13 07:08:47am	39.91602	76.56953	1510.544	204	48	295	11.7	114
UO15	06/26/13 07:08:47am	39.91602	76.56953	1510.544	139	34	300	11.7	49
UO16	06/26/13 07:08:47am	39.91602	76.56953	1510.544	177	29	300	11.7	87

UO17	06/26/13 07:08:47am	39.91602	76.56953	1510.544	143	50	225	11.8	53
UO18	06/26/13 07:08:47am	39.91602	76.56953	1510.544	163	52	235	12	73
UO19	06/26/13 07:08:47am	39.91602	76.56953	1510.544	146	44	240	11.2	56
UO20	06/26/13 07:08:47am	39.91602	76.56953	1510.544	164	39	245	11.3	74
UO21	06/26/13 07:08:47am	39.91602	76.56953	1510.544	260	52	20	12.5	170
UO22	06/26/13 07:08:47am	39.91602	76.56953	1510.544	189	44	295	12.3	99
UO23	06/26/13 07:08:47am	39.91602	76.56953	1510.544	206	44	310	12.5	116
UO24	06/26/13 07:08:47am	39.91602	76.56953	1510.544	208	43	300	12.2	118
UO25	06/26/13 07:08:47am	39.91602	76.56953	1510.544	202	35	300	12.2	112
UO26	06/26/13 07:08:47am	39.91602	76.56953	1510.544	174	43	285	10.9	84
UO27	06/26/13 07:08:47am	39.91602	76.56953	1510.544	162	45	285	11.1	72
UO28	06/26/13 07:08:47am	39.91602	76.56953	1510.544	157	50	290	11.2	67
UO29	06/26/13 07:08:47am	39.91602	76.56953	1510.544	148	42	245	10.8	58
UO30	06/26/13 07:08:47am	39.91602	76.56953	1510.544	313	37	245	10.8	223
UO31	06/26/13 07:08:47am	39.91602	76.56953	1510.544	145	55	245	10.7	55
UO32	06/26/13 07:08:47am	39.91602	76.56953	1510.544	191	22	265	9.1	101
UO33	06/26/13 07:08:47am	39.91602	76.56953	1510.544	225	39	285	9.1	135
UO34	06/26/13 07:08:47am	39.91602	76.56953	1510.544	137	48	260	9.5	47
UO35	06/26/13 07:08:47am	39.91602	76.56953	1510.544	2	39	260	9.5	272
UO36	06/26/13 07:08:47am	39.91602	76.56953	1510.544	334	34	260	9.5	244
UO37	06/26/13 07:08:47am	39.91602	76.56953	1510.544	168	64	265	9.5	78
UO38	06/26/13 07:08:47am	39.91602	76.56953	1510.544	146	50	270	9.3	56
UO39	06/26/13 07:08:47am	39.91602	76.56953	1510.544	152	50	70	9.5	62
UO40	06/26/13 07:08:47am	39.91602	76.56953	1510.544	229	23	305	7.6	139
UO41	06/26/13 07:08:47am	39.91602	76.56953	1510.544	134	49	50	6	44
UO42	06/26/13 07:08:47am	39.91602	76.56953	1510.544	161	16	255	5.9	71
UO43	06/26/13 07:08:47am	39.91602	76.56953	1510.544	184	26	260	1.9	94
UO44	06/26/13 07:08:47am	39.91602	76.56953	1510.544	154	40	255	2	64

UO45	06/26/13 07:08:47am	39.91602	76.56953	1510.544	162	36	265	2.1	72
UO46	06/26/13 07:08:47am	39.91602	76.56953	1510.544	229	28	5	7.7	139
UO47	06/26/13 07:08:47am	39.91602	76.56953	1510.544	230	46	45	7.8	140
UO48	06/26/13 07:08:47am	39.91602	76.56953	1510.544	196	49	305	6.5	106
UO49	06/26/13 07:08:47am	39.91602	76.56953	1510.544	208	46	310	6.3	118
UO50	06/26/13 07:08:47am	39.91602	76.56953	1510.544	268	52	359	6.2	178
UO51	06/26/13 07:08:47am	39.91602	76.56953	1510.544	278	42	10	6.2	188
UO52	06/26/13 07:08:47am	39.91602	76.56953	1510.544	250	34	310	5.3	160
UO53	06/26/13 07:08:47am	39.91602	76.56953	1510.544	262	41	355	5.3	172
UO54	06/26/13 07:08:47am	39.91602	76.56953	1510.544	280	36	90	6.1	190
UO55	06/26/13 07:08:47am	39.91602	76.56953	1510.544	270	39	170	4	180
UO56	06/26/13 07:08:47am	39.91602	76.56953	1510.544	266	39	170	3.8	176
UP1	06/26/13 08:20:39am	39.91603	76.56856	1493.416	235	44	330	5.5	145
UP2	06/26/13 08:20:39am	39.91603	76.56856	1493.416	257	33	20	5.5	167
UW1	06/30/13 05:24:56am	39.71318	76.0116	1482.57	233	46	5	4.1	143
UW2	06/30/13 05:24:56am	39.71318	76.0116	1482.57	224	40	10	4.1	134
UW3	06/30/13 05:24:56am	39.71318	76.0116	1482.57	225	24	10	4.1	135
UW4	06/30/13 05:24:56am	39.71318	76.0116	1482.57	86	46	350	4.8	356
UW5	06/30/13 05:24:56am	39.71318	76.0116	1482.57	265	25	355	4.9	175
UW6	06/30/13 05:24:56am	39.71318	76.0116	1482.57	273	39	355	4.9	183
UW7	06/30/13 05:24:56am	39.71318	76.0116	1482.57	260	46	355	4.5	170
UW8	06/30/13 05:24:56am	39.71318	76.0116	1482.57	224	33	0	4.3	134
UW9	06/30/13 05:24:56am	39.71318	76.0116	1482.57	321	42	40	4.3	231
UW10	06/30/13 05:24:56am	39.71318	76.0116	1482.57	145	26	30	4.3	55
UW11	06/30/13 05:24:56am	39.71318	76.0116	1482.57	275	31	5	3.9	185
UW12	06/30/13 05:24:56am	39.71318	76.0116	1482.57	266	55	10	3.9	176
UX1	06/30/13 06:00:28am	39.71293	76.01165	1479.83	176	26	235	4.7	86
UX2	06/30/13 06:00:28am	39.71293	76.01165	1479.83	308	26	230	5.1	218

UX3	06/30/13 06:00:28am	39.71293	76.01165	1479.83	-	47	24	5.1	-
UX4	06/30/13 06:00:28am	39.71293	76.01165	1479.83	281	45	240	5	191
UX5	06/30/13 06:00:28am	39.71293	76.01165	1479.83	223	33	245	5.4	133
UX6	06/30/13 06:00:28am	39.71293	76.01165	1479.83	210	39	245	5.4	120
UX7	06/30/13 06:00:28am	39.71293	76.01165	1479.83	175	32	245	5.4	85
UX8	06/30/13 06:00:28am	39.71293	76.01165	1479.83	230	23	235	5.3	140
UX9	06/30/13 06:00:28am	39.71293	76.01165	1479.83	0	45	240	5.1	270
UY1	06/30/13 11:02:01am	39.71877	76.01392	1494.687	301	32	230	0.8	211
UY2	06/30/13 11:02:01am	39.71877	76.01392	1494.687	175	28	265	0.8	85
UY3	06/30/13 11:02:01am	39.71877	76.01392	1494.687	340	32	220	0.8	250
UY4	06/30/13 11:02:01am	39.71877	76.01392	1494.687	299	28	210	0.8	209
UY5	06/30/13 11:02:01am	39.71877	76.01392	1494.687	335	41	215	0.8	245
UY6	06/30/13 11:02:01am	39.71877	76.01392	1494.687	325	35	225	0.8	235
UY7	06/30/13 11:02:01am	39.71877	76.01392	1494.687	281	44	160	0.6	191
UY8	06/30/13 11:02:01am	39.71877	76.01392	1494.687	290	32	180	0.8	200
UY9	06/30/13 11:02:01am	39.71877	76.01392	1494.687	310	25	190	1.1	220
UY10	06/30/13 11:02:01am	39.71877	76.01392	1494.687	107	39	195	1.5	17
UY11	06/30/13 11:02:01am	39.71877	76.01392	1494.687	274	46	180	1.1	184
UY12	06/30/13 11:02:01am	39.71877	76.01392	1494.687	271	34	45	1.7	181
UZ1	06/30/13 11:17:21am	39.71896	76.0141	1489.185	103	32	210	2.4	13
UZ2	06/30/13 11:17:21am	39.71896	76.0141	1489.185	43	31	180	2	313
UZ3	06/30/13 11:17:21am	39.71896	76.0141	1489.185	243	44	340	1.7	153
UZ4	06/30/13 11:17:21am	39.71896	76.0141	1489.185	45	35	145	3.1	315
UZ5	06/30/13 11:17:21am	39.71896	76.0141	1489.185	214	36	125	3.6	124
UZ6	06/30/13 11:17:21am	39.71896	76.0141	1489.185	299	52	210	3.2	209
UZ7	06/30/13 11:17:21am	39.71896	76.0141	1489.185	151	33	220	3.2	61
UZ8	06/30/13 11:17:21am	39.71896	76.0141	1489.185	196	49	19	1.6	106
UZ9	06/30/13 11:17:21am	39.71896	76.0141	1489.185	156	40	260	1.3	66

UZ10	06/30/13 11:17:21am	39.71896	76.0141	1489.185	196	33	300	1.2	106
UZ11	06/30/13 11:17:21am	39.71896	76.0141	1489.185	286	36	210	4.9	196
UZ12	06/30/13 11:17:21am	39.71896	76.0141	1489.185	228	54	165	4.7	138
UZ13	06/30/13 11:17:21am	39.71896	76.0141	1489.185	215	50	155	4.1	125
UZ14	06/30/13 11:17:21am	39.71896	76.0141	1489.185	190	44	320	2.4	100
UZ15	06/30/13 11:17:21am	39.71896	76.0141	1489.185	256	22	335	2.1	166
UZ16	06/30/13 11:17:21am	39.71896	76.0141	1489.185	226	39	345	1.9	136
VA1	06/30/13 11:48:40am	39.71937	76.01461	1488.23	289	31	210	2.7	199
VA2	06/30/13 11:48:40am	39.71937	76.01461	1488.23	263	43	175	1.9	173
VA3	06/30/13 11:48:40am	39.71937	76.01461	1488.23	289	49	185	1	199
VA4	06/30/13 11:48:40am	39.71937	76.01461	1488.23	263	3	185	1.1	173

[a]Lumped measurements of several clasts are marked in grey.

Table A2: Statistics for lithologic clast counts

Sample Name (West to East)	1	2	3	4	5	6	7	8	9	10	11	12	13	14	15	16
Bai1	0	14	36	52	40	28	32	72	58	54	59	62	58	59	59	46
Bai2	14	0	44	48	42	28	32	82	68	62	68	72	67	69	69	52
Bog3	36	44	0	40	22	26	25	38	23	19	23	29	22	25	25	12
Bog2	52	48	40	0	18	24	20	68	53	42	51	62	52	56	56	34
Bog1	40	42	22	18	0	14	10	54	38	28	36	46	37	41	41	18
CA_north	28	28	26	24	14	0	4	63	47	39	46	54	46	49	49	28
CA_south	32	32	25	20	10	4	0	61	45	36	44	52	44	47	47	26
EA_R1	72	82	38	68	54	63	61	0	16	26	18	10	17	14	14	36
MUT_R1	58	68	23	53	38	47	45	16	0	11	4	8	1	3	3	20
MUT_R2	54	62	19	42	28	39	36	26	11	0	8	19	10	14	14	10
SMT_north	59	68	23	51	36	46	44	18	4	8	0	12	3	7	7	18
SMT_south_lower 4m	62	72	29	62	46	54	52	10	8	19	12	0	9	5	5	28
SMT_south_upper 4m	58	67	22	52	37	46	44	17	1	10	3	9	0	4	4	19
SMT_south_surface	59	69	25	56	41	49	47	14	3	14	7	5	4	0	0	23
SMT_south_mean	59	69	25	56	41	49	47	14	3	14	7	5	4	0	0	23
MUT_R3	46	52	12	34	18	28	26	36	20	10	18	28	19	23	23	0

See Chapter 2, Supplementary material, Section 1,2 for how the statistics were calculated

Table A3: All clast-size counts on Mutule

CMTriv1	CMTriv2	CMTriv3	CMTter1	CMTter2	CMTter3	CMTter4	CMTter5	CMTter6	CMTter7
Number of silt-sized counts									
197	6	72	1	3	1	3	3	2	6
Length of b-axis measured with a tape measure (cm)									
<0.5	<0.5	<0.5	<0.5	<0.5	<0.5	<0.5	<0.5	<0.5	<0.5
<0.5	<0.5	<0.5	<0.5	<0.5	<0.5	<0.5	<0.5	<0.5	<0.5
<0.5	<0.5	<0.5	<0.5	<0.5	<0.5	<0.5	<0.5	<0.5	<0.5
<0.5	<0.5	<0.5	<0.5	<0.5	<0.5	<0.5	<0.5	<0.5	<0.5
<0.5	<0.5	<0.5	<0.5	<0.5	<0.5	<0.5	<0.5	<0.5	<0.5
<0.5	<0.5	<0.5	<0.5	<0.5	<0.5	<0.5	<0.5	<0.5	<0.5
<0.5	<0.5	<0.5	<0.5	<0.5	<0.5	0.5	<0.5	<0.5	<0.5
<0.5	<0.5	<0.5	<0.5	0.5	<0.5	0.5	<0.5	<0.5	<0.5
<0.5	<0.5	<0.5	<0.5	0.6	<0.5	0.6	<0.5	<0.5	<0.5
<0.5	<0.5	<0.5	8.4	0.6	<0.5	0.7	<0.5	0.6	<0.5
<0.5	<0.5	<0.5	0.5	0.6	<0.5	0.7	0.5	0.6	<0.5
<0.5	<0.5	<0.5	0.5	0.6	<0.5	0.8	0.7	0.7	<0.5
<0.5	<0.5	<0.5	0.7	0.7	<0.5	0.9	0.7	0.7	0.5
<0.5	<0.5	<0.5	0.7	0.9	<0.5	0.9	0.7	0.8	0.5
<0.5	<0.5	<0.5	0.7	1.0	<0.5	0.9	0.7	0.9	0.5
<0.5	<0.5	<0.5	0.7	1.1	0.5	1.0	1.0	1.0	0.6
<0.5	<0.5	<0.5	0.8	1.1	0.5	1.0	1.0	1.1	0.6
<0.5	<0.5	<0.5	1.0	1.2	0.5	1.1	1.0	1.2	0.6
<0.5	<0.5	<0.5	1.0	1.4	0.5	1.2	1.1	1.4	0.7
<0.5	<0.5	<0.5	1.2	1.6	0.6	1.5	1.3	1.8	0.7
<0.5	<0.5	<0.5	1.5	1.9	0.6	1.6	1.3	1.8	0.8
<0.5	<0.5	<0.5	1.5	2.1	0.6	1.7	1.8	1.8	0.8
<0.5	<0.5	<0.5	1.8	2.2	0.7	1.7	1.8	1.9	0.9

<0.5	<0.5	<0.5	2.0	2.4	0.7	1.8	2.0	2.6	0.9
<0.5	<0.5	0.5	2.5	2.8	0.7	1.8	2.5	2.7	1.0
<0.5	<0.5	0.5	3.8	3.7	0.7	1.9	2.9	4.0	1.3
<0.5	<0.5	0.5	8.0	-	0.8	2.0	3.5	11.9	1.4
<0.5	<0.5	0.5	-	-	0.8	2.1	4.0	14.5	1.4
0.5	0.5	0.6	-	-	0.8	2.2	4.3	-	1.4
0.6	0.5	0.6	-	-	0.9	2.2	4.7	-	1.5
0.6	0.5	0.6	-	-	0.9	2.7	7.6	-	1.6
0.6	0.5	0.6	-	-	0.9	2.8	8.0	-	1.6
0.6	0.5	0.6	-	-	1.0	2.8	-	-	1.7
0.6	0.5	0.6	-	-	1.0	3.5	-	-	1.7
0.6	0.6	0.6	-	-	1.0	7.0	-	-	1.7
0.7	0.6	0.7	-	-	1.0	9.1	-	-	2.1
0.7	0.6	0.7	-	-	1.0	-	-	-	2.2
0.7	0.7	0.7	-	-	1.0	-	-	-	2.3
0.7	0.7	0.8	-	-	1.1	-	-	-	2.5
0.7	0.7	0.8	-	-	1.2	-	-	-	2.8
0.7	0.7	0.8	-	-	1.2	-	-	-	3.3
0.8	0.8	0.8	-	-	1.2	-	-	-	7.7
0.8	0.8	0.8	-	-	1.3	-	-	-	-
0.8	0.8	0.8	-	-	1.3	-	-	-	-
0.8	0.9	0.9	-	-	1.4	-	-	-	-
0.9	0.9	0.9	-	-	1.4	-	-	-	-
0.9	0.9	0.9	-	-	1.4	-	-	-	-
0.9	0.9	1.0	-	-	1.4	-	-	-	-
0.9	0.9	1.0	-	-	1.4	-	-	-	-
0.9	0.9	1.0	-	-	1.7	-	-	-	-
0.9	0.9	1.0	-	-	1.8	-	-	-	-

0.9	0.9	1.0	-	-	1.9	-	-	-	-
0.9	1.0	1.0	-	-	1.9	-	-	-	-
0.9	1.0	1.0	-	-	2.7	-	-	-	-
1.0	1.1	1.1	-	-	3.4	-	-	-	-
1.0	1.2	1.1	-	-	3.4	-	-	-	-
1.0	1.2	1.1	-	-	3.9	-	-	-	-
1.0	1.3	1.2	-	-	4.2	-	-	-	-
1.0	1.3	1.2	-	-	5.0	-	-	-	-
1.1	1.3	1.3	-	-	6.7	-	-	-	-
1.1	1.4	1.3	-	-	-	-	-	-	-
1.1	1.4	1.4	-	-	-	-	-	-	-
1.2	1.5	1.4	-	-	-	-	-	-	-
1.2	1.5	1.5	-	-	-	-	-	-	-
1.2	1.5	1.5	-	-	-	-	-	-	-
1.2	1.5	1.5	-	-	-	-	-	-	-
1.2	1.5	1.5	-	-	-	-	-	-	-
1.2	1.5	1.6	-	-	-	-	-	-	-
1.3	1.6	1.6	-	-	-	-	-	-	-
1.3	1.6	1.7	-	-	-	-	-	-	-
1.3	1.7	1.7	-	-	-	-	-	-	-
1.4	1.7	1.7	-	-	-	-	-	-	-
1.4	1.7	1.8	-	-	-	-	-	-	-
1.4	1.7	1.8	-	-	-	-	-	-	-
1.5	1.7	1.8	-	-	-	-	-	-	-
1.5	1.8	1.9	-	-	-	-	-	-	-
1.5	1.8	1.9	-	-	-	-	-	-	-
1.5	1.8	1.9	-	-	-	-	-	-	-
1.6	1.9	1.9	-	-	-	-	-	-	-

1.6	1.9	1.9	-	-	-	-	-	-	-
1.6	1.9	2.0	-	-	-	-	-	-	-
1.8	1.9	2.0	-	-	-	-	-	-	-
2.1	1.9	2.0	-	-	-	-	-	-	-
2.1	1.9	2.1	-	-	-	-	-	-	-
2.2	1.9	2.2	-	-	-	-	-	-	-
2.2	1.9	2.3	-	-	-	-	-	-	-
2.3	2.0	2.3	-	-	-	-	-	-	-
2.3	2.0	2.3	-	-	-	-	-	-	-
2.3	2.0	2.6	-	-	-	-	-	-	-
2.4	2.0	2.6	-	-	-	-	-	-	-
2.4	2.1	2.7	-	-	-	-	-	-	-
2.4	2.1	2.7	-	-	-	-	-	-	-
2.4	2.1	2.8	-	-	-	-	-	-	-
2.4	2.2	2.8	-	-	-	-	-	-	-
2.5	2.3	2.8	-	-	-	-	-	-	-
2.5	2.4	2.9	-	-	-	-	-	-	-
2.6	2.5	3.1	-	-	-	-	-	-	-
2.7	2.5	3.2	-	-	-	-	-	-	-
2.7	2.7	3.2	-	-	-	-	-	-	-
2.8	2.8	3.3	-	-	-	-	-	-	-
2.8	2.8	3.4	-	-	-	-	-	-	-
2.8	2.9	3.4	-	-	-	-	-	-	-
3.0	2.9	3.5	-	-	-	-	-	-	-
3.1	3.0	3.5	-	-	-	-	-	-	-
3.1	3.0	3.5	-	-	-	-	-	-	-
3.1	3.0	3.5	-	-	-	-	-	-	-
3.3	3.0	3.8	-	-	-	-	-	-	-

3.4	3.1	3.8	-	-	-	-	-	-	-
3.4	3.1	3.9	-	-	-	-	-	-	-
3.5	3.1	4.0	-	-	-	-	-	-	-
3.7	3.2	4.3	-	-	-	-	-	-	-
3.8	3.2	4.4	-	-	-	-	-	-	-
3.8	3.4	4.5	-	-	-	-	-	-	-
3.9	3.8	4.5	-	-	-	-	-	-	-
4.4	3.9	4.5	-	-	-	-	-	-	-
4.8	4.4	4.7	-	-	-	-	-	-	-
5.2	4.5	4.9	-	-	-	-	-	-	-
5.3	4.5	6.5	-	-	-	-	-	-	-
5.6	4.7	8.0	-	-	-	-	-	-	-
5.8	5.1	8.0	-	-	-	-	-	-	-
5.8	5.8	8.0	-	-	-	-	-	-	-
5.9	6.8	8.3	-	-	-	-	-	-	-
6.4	7.9	8.5	-	-	-	-	-	-	-
9.0	8.0	9.8	-	-	-	-	-	-	-
-	-	14.5	-	-	-	-	-	-	-

Table A4: Structural data for the eastern Mutule fold

Northing	Easting	Lat	Long	strike	dip	Dip direction	Date	Comment
4422179	628046.8	39.94005	76.49874	228	29	318	23-Jun-12	ripples
4422102	628123.4	39.93935	76.49963	215	31	305	23-Jun-12	
4422021	628202.6	39.9386	76.50054	227	29	317	23-Jun-12	
4421906	628322.8	39.93755	76.50192	215	27	305	23-Jun-12	
4421835	628429.9	39.93689	76.50316	226	30	316	23-Jun-12	
4421729	628486.8	39.93594	76.5038	221	47	311	23-Jun-12	
4421600	628511.7	39.93477	76.50407	220	22	310	23-Jun-12	
4421528	628560.7	39.93411	76.50463	213	24	303	23-Jun-12	
4421476	628625.9	39.93364	76.50538	189	22	279	23-Jun-12	
4421368	628727	39.93265	76.50654	213	18	303	23-Jun-12	fine bedded. Maybe a little kink?
4421280	628858.3	39.93183	76.50806	205	19	295	23-Jun-12	ripples
4421240	629020.9	39.93145	76.50996	204	19	294	23-Jun-12	
4421196	629053.8	39.93105	76.51033	195	20	285	23-Jun-12	N2a,siltstone,285/20
4421051	629228.4	39.92972	76.51235	200	23	290	23-Jun-12	N2a,290/23
4420937	629361.3	39.92867	76.51388	217	21	307	23-Jun-12	N2a,307/21
4420881	629383.4	39.92816	76.51413	235	42	325	23-Jun-12	N2a,325/42
4420830	629485.6	39.92768	76.51531	233	45	323	23-Jun-12	N2a,323/45
4420798	629701.3	39.92736	76.51783	232	51	322	23-Jun-12	N2a,322/51
4420739	629957.9	39.92679	76.52082	225	33	315	23-Jun-12	N2a,315/33
4420717	630034.4	39.92658	76.52171	225	32	315	23-Jun-12	N2a,315/32
4420608	630092.4	39.92559	76.52237	225	45	315	23-Jun-12	N2a,315/45
4420587	630113.8	39.9254	76.52261				23-Jun-12	kink band
4420579	630127.9	39.92533	76.52278	225	5	315	23-Jun-12	N2a,315/5
4420568	630161.8	39.92522	76.52317	253	25	343	23-Jun-12	N2a,343/25
4420566	630174.2	39.9252	76.52332	80	30	170	23-Jun-12	N2a,170/30
4420552	630246.1	39.92506	76.52415	78	45	168	23-Jun-12	N2a,168/45

4420520	630368.9	39.92475	76.52558	80	50	170	23-Jun-12	N2a,170/50
4420532	630515.6	39.92484	76.5273	64	69	154	23-Jun-12	N2a,154/69
4420536	630613.8	39.92486	76.52845	80	33	170	23-Jun-12	N2a,170/33
4420533	630587.6	39.92484	76.52814	74	61	164	23-Jun-12	N2a,164/61
4420478	630647.6	39.92433	76.52883	88	26	178	23-Jun-12	N2a,178/26
4420453	630770	39.92409	76.53026	93	26	183	23-Jun-12	N2a,183/26
4420419	630903.6	39.92376	76.53182	45	25	135	23-Jun-12	
4420349	631020	39.92312	76.53317	106	47	196	23-Jun-12	
4420331	631112.7	39.92294	76.53425	62	61	152	23-Jun-12	
4420240	631139.2	39.92212	76.53454	67	71	157	23-Jun-12	
4420150	631110.9	39.92131	76.53419	68	80	158	23-Jun-12	
4420102	631094.6	39.92088	76.53399	73	67	163	23-Jun-12	
4420024	631092.9	39.92018	76.53395	83	47	173	23-Jun-12	
4419958	631153.5	39.91958	76.53465	85	39	175	23-Jun-12	
4419916	631268.6	39.91918	76.53599	93	33	183	23-Jun-12	
4419853	631365	39.91859	76.5371	85	38	175	23-Jun-12	ripples
4419832	631451.5	39.91839	76.53811	80	51	170	23-Jun-12	
4419776	631514.6	39.91788	76.53884	65	70	155	23-Jun-12	
4419701	631658	39.91718	76.5405	81	48	171	23-Jun-12	
4419634	631754.5	39.91656	76.54161	87	60	177	23-Jun-12	ripples
4419574	631804.6	39.91601	76.54219	85	62	175	23-Jun-12	
4419442	631859.8	39.91481	76.54281	75	67	165	23-Jun-12	
4419337	631928.2	39.91386	76.54358	90	53	180	23-Jun-12	not perfect surface
4419303	631951.3	39.91355	76.54385	75	68	165	23-Jun-12	
4419196	631959.3	39.91258	76.54392	75	61	165	23-Jun-12	
4419149	632020.8	39.91216	76.54463	80	69	170	23-Jun-12	
4419070	632091.4	39.91143	76.54544	78	60	168	23-Jun-12	
4419008	632188.2	39.91086	76.54656	77	64	167	23-Jun-12	

4418934	632304.5	39.91017	76.5479	82	64	172	23-Jun-12	
4418883	632335.9	39.90971	76.54826	87	62	177	23-Jun-12	
4418844	632462.5	39.90934	76.54973	77	62	167	23-Jun-12	
4418844	632553.3	39.90933	76.5508	80	58	170	23-Jun-12	
4418848	632672.4	39.90934	76.55219	83	56	173	23-Jun-12	
4418890	632782.7	39.9097	76.55349	85	55	175	23-Jun-12	N2a,175/55
4418761	633026.2	39.9085	76.55631	86	55	176	23-Jun-12	N2a,176/55
4418641	633135.9	39.90741	76.55757	76	50	166	23-Jun-12	N2a,166/50
4418540	633404.8	39.90645	76.56069	88	59	178	23-Jun-12	N2a,178/59
4418474	633478.4	39.90584	76.56154	67	55	157	23-Jun-12	N2a,157/55
4418419	633725.1	39.90531	76.56441	90	56	180	23-Jun-12	N2a,180/56
4418413	634001.1	39.90521	76.56764	86	52	176	23-Jun-12	N2a,176/52
4418299	634166.8	39.90416	76.56955	87	55	177	23-Jun-12	N2a,177/55
4418360	634489.6	39.90466	76.57334	88	50	178	23-Jun-12	N2a,178/50
4418311	634631.1	39.9042	76.57499	87	51	177	23-Jun-12	N2a,177/51
4418212	634862.5	39.90327	76.57767	86	50	176	23-Jun-12	N2a,176/50
4418123	635023.9	39.90244	76.57954	87	48	177	23-Jun-12	N2a,177/48
4417966	635224.4	39.90099	76.58185	90	56	180	23-Jun-12	N2a,180/56
4417880	635366.6	39.90019	76.5835	85	50	175	23-Jun-12	N2a,175/50
4417810	635461.4	39.89955	76.58459	87	49	177	23-Jun-12	N2a,177/49
4417745	635601.8	39.89894	76.58622	78	48	168	23-Jun-12	N2a,168/48
4417657	635924.6	39.8981	76.58998	74	48	164	23-Jun-12	N2a,164/48
4417600	635967.2	39.89758	76.59046	87	46	177	23-Jun-12	N2a,177/46
4417388	636077.5	39.89565	76.59171	86	48	176	23-Jun-12	N2a,176/48
4417306	636236.6	39.89489	76.59355	83	45	173	23-Jun-12	N2a,173/45
4417275	636471.9	39.89457	76.5963	84	49	174	23-Jun-12	
4417197	636551.1	39.89385	76.59721	84	49	174	23-Jun-12	
4417113	636613.6	39.89308	76.59792	77	38	167	23-Jun-12	

4417005	636772	39.89209	76.59975	75	40	165	23-Jun-12	
4416906	636838	39.89119	76.6005	75	42	165	23-Jun-12	
4416894	636953	39.89106	76.60184	65	38	155	23-Jun-12	pebbly beds
4416938	637053.3	39.89144	76.60302	87	49	177	23-Jun-12	
4416935	637072.2	39.89141	76.60324	80	43	170	23-Jun-12	
4416932	637283.3	39.89135	76.60571	72	43	162	23-Jun-12	
4416846	637314.8	39.89057	76.60606	69	44	159	23-Jun-12	
4416799	637332.6	39.89015	76.60626	81	42	171	23-Jun-12	
4416695	637368.6	39.8892	76.60666	80	44	170	23-Jun-12	
4416576	637409.6	39.88812	76.60711	73	42	163	23-Jun-12	
4416512	637469	39.88754	76.60779	72	42	162	23-Jun-12	not perfect surface
4416425	637501	39.88674	76.60815	73	40	163	23-Jun-12	
4416379	637635	39.88631	76.60971	71	43	161	23-Jun-12	
4416364	637678.3	39.88617	76.61021	78	40	168	23-Jun-12	N2a,168/40
4416323	637796.1	39.88578	76.61158	76	38	166	23-Jun-12	N2a,166/38
4416237	637891.3	39.88499	76.61267	81	42	171	23-Jun-12	Q1x,171/42
4416197	637881.6	39.88463	76.61255	76	40	166	23-Jun-12	Q1x,166/40
4416081	637898.7	39.88358	76.61273	88	40	178	23-Jun-12	Q1x,178/40
4415960	637873.9	39.8825	76.61241	81	28	171	23-Jun-12	Q1x,171/28
4415951	637879.2	39.88242	76.61247	80	40	170	23-Jun-12	Q1x,170/40
4415850	637828.3	39.88152	76.61186	75	37	165	23-Jun-12	Q1x,165/37
4415728	637725.9	39.88043	76.61063	82	39	172	23-Jun-12	Q1x,172/39
4415635	637748.4	39.87959	76.61088	75	34	165	23-Jun-12	Q1x,165/34
4415545	637744.4	39.87878	76.61081	78	35	168	23-Jun-12	Q1x,168/35
4414927	637974.9	39.87318	76.61337	74	30	164	02-Jul-12	Xiyu
4415003	637944.5	39.87387	76.61303	81	34	171	02-Jul-12	
4415064	637891.1	39.87443	76.61242	65	30	155	02-Jul-12	
4415205	637821.3	39.87571	76.61164	86	31	176	02-Jul-12	

4415325	637785.8	39.87679	76.61125	67	31	157	02-Jul-12	
4415424	637757.2	39.87769	76.61093	82	30	172	02-Jul-12	
4415589	637748.3	39.87917	76.61086	79	30	169	02-Jul-12	
4415693	637741	39.88011	76.6108	82	37	172	02-Jul-12	
4415796	637796	39.88104	76.61147	67	37	157	02-Jul-12	
4415963	637880	39.88253	76.61248	72	30	162	02-Jul-12	
4416075	637846.2	39.88354	76.61211	71	39	161	02-Jul-12	start to see Atushi fmt
4416199	637886.6	39.88465	76.61261	80	38	170	02-Jul-12	
4416338	637883.3	39.8859	76.6126	90	40	180	02-Jul-12	
4416327	637790	39.88582	76.61151	70	38	160	02-Jul-12	
4416356	637730.3	39.88608	76.61082	??	??		02-Jul-12	???
4416356	637730.2	39.88608	76.61082	76	41	166	02-Jul-12	
4428899	647089.2	39.99748	76.72306	260	78	350	23-Oct-15	NE Mutule
4429123	647108.8	39.99949	76.72334	279	46	9	23-Oct-15	NE Mutule
4429325	647111.7	40.00131	76.72342	268	54	358	23-Oct-15	NE Mutule
4429665	647115.4	40.00437	76.72354	272	52	2	23-Oct-15	NE Mutule
4429627	646795	40.00408	76.71978	270	53	0	23-Oct-15	NE Mutule
4422887	631048.6	39.94597	76.53401	276	64	6	23-Oct-15	N Central Mutule
4423103	631068.8	39.94791	76.53429	250	70	340	23-Oct-15	N Central Mutule
4423310	631066.1	39.94978	76.5343	252	54	342	23-Oct-15	N Central Mutule
4423525	630908.6	39.95174	76.5325	248	67	338	23-Oct-15	N Central Mutule
4423717	630789	39.95349	76.53114	251	55	341	23-Oct-15	N Central Mutule
4424000	630622.7	39.95606	76.52925	250	58	340	23-Oct-15	N Central Mutule
4424059	630587.5	39.9566	76.52885	245	64	335	23-Oct-15	N Central Mutule
4424174	630353.1	39.95767	76.52613	245	45	335	23-Oct-15	uncertain if longitude copied correctly
4424161	630186.7	39.95758	76.52418	248	20	338	23-Oct-15	N Central Mutule
4424135	630097.5	39.95736	76.52313	253	20	343	23-Oct-15	N Central Mutule
4424188	630027.4	39.95785	76.52232	250	20	340	23-Oct-15	N Central Mutule

4424287	630036.8	39.95874	76.52245	262	25	352	23-Oct-15	N Central Mutule
4424332	630098.4	39.95913	76.52318	245	24	335	23-Oct-15	N Central Mutule
4424478	630010.5	39.96046	76.52218	267	22	357	23-Oct-15	N Central Mutule
4424698	630016.9	39.96244	76.5223	250	6	340	23-Oct-15	N Central Mutule

Table A5-1: All OSL small aliquot data for samples CK-1-2, and CMTL-1-5

13-75		14-152		14-153		13-76		13-77		13-78		13-79	
2012-07-CK-1		2012-07-CK-2		2012-07-CK-3		2012-07-CMTL-1		2012-07-CMTL-2		2012-07-CMTL-4		2012-07-CMTL-5	
De (Gy)	% Error ±1σ [a]	De (Gy)	% Error ±1σ [a]	De (Gy)	% Error ±1σ [a]	De (Gy)	% Error ±1σ [a]	De (Gy)	% Error ±1σ [a]	De (Gy)	% Error ±1σ [a]	De (Gy)	% Error ±1σ [a]
23.5	7.66	49.82	2.18	58.02	3.19	17.27	2.95	19.15	3.19	33.03	7.78	13.61	2.13
27.24	1.36	54.95	3.85	71.87	5.19	21.36	4.09	28.94	6.17	41.38	6.26	51.89	12.76
41.55	10.39	61.12	6.81	71.87	5.86	22.72	2.95	36.6	11.7	41.38	5.5	56.57	5.53
42.23	3.92	67.54	5.26	73.2	5.32	29.99	3.41	37.88	5.96	43.28	18.41	69.32	9.57
55.9	3.19	67.79	7.45	77.72	6.92	34.09	8.63	42.13	12.13	43.28	9.3	73.15	16.37
66.07	7.15	67.79	6.81	77.99	5.32	36.36	8.41	53.62	10.43	47.45	12.34	73.58	8.72
68.45	24.86	71.9	3.72	87.04	6.65	52.26	9.54	58.31	8.09	56.56	11.96	77.83	15.52
81.39	8.68	73.44	6.42	87.57	4.79	61.35	5.68	59.16	6.81	56.94	7.97	86.34	9.57
82.65	8.54	82.17	4.49	90.5	8.52	61.81	7.95	82.99	19.79	58.08	14.05	86.76	13.61
89.57	7.15	92.96	5.39	100.88	10.38	70.9	9.32	84.69	11.07	59.98	15.75	109.73	12.76
96.04	10.73	95.78	6.29	125.9	7.72	73.62	5.23	110.65	17.24	60.74	16.7	114.83	15.31
103.73	25.24	101.18	4.11	126.7	8.38	74.99	14.32	118.31	14.9	61.12	43.84	116.96	13.4
112.04	24.18	106.31	6.29	127.49	7.99	75.9	7.27	118.74	16.6	65.67	11.58	125.04	23.82
114.77	20.94	112.99	4.49	145.06	5.99	81.35	6.36	124.27	14.9	71.75	7.4	125.04	17.65
132.73	8.93	116.33	6.55	153.58	13.04	83.17	15.68	130.65	19.36	71.75	5.69	138.22	21.48
134.52	11.58	119.64	3.96	166.35	7.19	90.89	26.81	133.1	15.48	76.3	8.73	155.23	31.9
140.62	5.96	121.46	5.26	167.15	7.59	94.98	10.91	134.91	13.19	77.82	26.95	157.36	32.54
146.43	8.57	125.31	7.32	168.75	7.05	105.44	21.13	158.32	30.85	92.25	10.82	179.48	20.63
148.09	12.85	128.65	9.89	180.99	16.77	111.34	14.09	164.06	14.04	98.7	14.05	188.83	21.48
148.14	10.05	135.33	8.47	201.22	15.84	161.79	39.99	174.49	14.9	102.49	8.54	195.21	17.44
208.42	16.86	150.22	14.12			168.04	12.27	267.27	27.45	119.58	13.1	214.78	25.52
215.02	20.28	168.71	13.74			207.24	12.04			132.1	17.27	230.94	68.05
224.68	14.32					214.05	16.53			132.86	17.46	258.58	33.6

239.41	71.86									135.52	19.17	281.97	35.3
253.03	23.33									146.1	11.4		
										156.4	34.92		
										157.92	28.28		
										160.2	27.9		
										176.14	19.36		
										178.42	45.55		
										196.64	46.31		
										244.47	80.67		
										282.43	23.16		

[a]Uncertainties are estimated from the goodness of fit of the theoretical saturation curve to the regenerative data.

Table A5-2: All OSL small aliquot data for samples CMTL-1-5, EAT-2, and WA1-2

13-80		13-81		14-154		13-82		13-85		13-83		13-84	
2012-07-CMTL-6		2012-07-CMTL-7		2012-07-CMTL-8		2012-07-CMTL-9		2012-07-EAT-2		2012-07-WA-1		2012-07-WA-3	
De (Gy)	% Error ±1σ[a]	De (Gy)	% Error ±1σ[a]	De (Gy)	% Error ±1σ[a]	De (Gy)	% Error ±1σ[a]	De (Gy)	% Error ±1σ[a]	De (Gy)	% Error ±1σ[a]	De (Gy)	% Error ±1σ[a]
69.48	7.38	39.55	3.62	30.29	5.3	54.42	5.53	25.98	8.09	72.65	7.43	47.22	6.38
81.59	7.71	41.27	4.8	40.33	1.18	56.97	6.59	28.96	4.47	83.27	16.14	53.6	4.04
87.08	14.54	50.87	5.04	44.53	5	68.45	7.86	29.24	3.16	84.12	9.13	61.26	6.38
88.41	12.57	66.7	12.72	47.56	5.6	69.93	13.47	29.81	4.68	89.22	8.28	67.64	10
89.5	8.56	72.94	14.16	52.11	5.45	71.35	8.5	45.14	3.83	100.69	12.75	72.32	7.66
97.85	9.71	81.1	8.88	53.92	6.36	81.74	5.91	49.8	3.91	106.21	30.38	88.48	11.7
99.42	15.61	83.98	14.4	62.71	7.57	82.21	17.72	49.82	10.65	108.34	12.53	91.46	7.66
105.2	14.54	90.22	23.99	63.18	5.71	83.16	25.28	60.04	4.26	112.16	10.2	95.29	16.8
107.62	27.06	91.66	8.88	64.22	8.63	84.1	9.69	62.17	10.22	124.48	24	99.54	9.36
113.35	11.54	99.34	13.68	65.54	6.72	87.41	12.28	73.41	7.8	127.45	6.37	109.32	18.72
114.45	10.18	101.26	13.92	72.93	4.71	89.3	12.28	73.98	15.32	133.4	48.64	115.28	17.65
118.27	15.64	106.05	34.55	75.96	6.39	90.98	9.14	75.14	8.38	134.25	8.07	123.79	13.19
123	15.28	107.97	9.84	83.61	7.73	104.16	12.97	78.61	9.83	151.24	15.08	130.59	18.5
128.89	16.92	110.85	16.08	92.09	7.06	106.78	16.54	81.33	8.52	161.23	11.63	144.63	18.5
132.15	17.79	114.69	17.28	96.03	6.82	107.25	19.61	82.75	42.34	169.51	18.91	147.18	15.53
138.58	16.82	122.37	18	125.02	5.38	109.62	7.8	89.42	9.15	172.06	19.76	148.03	24.03
143.85	23.76	127.17	19.2	140.15	6.89	112.23	20.41	91.98	15.33	175.25	11.79	157.82	17.23
152.38	15.75	135.33	15.6	147.88	7.56	123.32	17.25	94.53	12.56	215.4	19.76	158.67	28.08
153.67	15.82	137.25	15.12	177.22	15.15	131.82	10.16	95.38	8.09	248.11	20.39	160.37	20.84
164.64	33.91	138.69	27.59	185.09	21.66	140.8	22.92	96.66	10.86	294.42	32.93	161.65	19.99
165.73	21.83	176.12	29.51			142.22	27.17	97.68	25.43	351.35	48.22	162.07	15.74
173.66	20.87	193.87	30.47			142.22	27.17	99.42	8.67			163.77	14.89
184.89	18.29	194.35	22.79			143.16	20.79	101.34	9.37			184.4	13.24

186.56	23.5	215.2	26.79			153.56	32.37	113.69	18.52			192.7	26.8
187.08	26.94	217.75	40.19			163.48	27.4	114.54	14.9			196.1	23.61
204.85	29.2	220.75	44.39			169.62	13.47	130.05	17.63			223.75	139.53
211.42	33.59	231.78	51.35			180.02	42.76	140.94	22.36			240.87	14.2
237.56	61.26	243.78	55.43			197.5	36.62	161.81	20.01			256.93	32.97
253.9	57.68	321.53	61.19			219.71	61.19	197.68	27.74			333.5	32.54
256.54	42.11	358.1	105.05			237.22	30.18					404.97	42.33
256.99	59.01	435.74	85.9			240.49	41.81						
342.02	70.26					245.22	68.98						
349.58	93.74					300.03	45.36						
						308.53	107.96						

[a]Uncertainties are estimated from the goodness of fit of the theoretical saturation curve to the regenerative data.

Table A6-1: Full results from optically stimulated luminescence dating-Part 1

Sample Name	Latitude	Longitude	Elevation of terrace from SRTM ±2σ (m)[a]	Elevation of terrace above modern river ±2σ (m)[a]	Depth of sample below surface ±2σ (m)[a]	Measured water content (%)	Water content used for dose rate calculation ±2σ (%)[a]	Density of sediment ±2σ (g/cm^3)[a]
CK-1	39.5643	75.9505	1478 ± 5	60 ± 10	1.4 ± 0.2	1	5 ± 5	2.0 ± 0.6
CK-2	39.5776	75.9480	1539 ± 5	95 ± 10	3.3 ± 0.2	0.1	5 ± 5	2.0 ± 0.6
CK-3	39.5785	75.9480	1540 ± 5	95 ± 10	3.9 ± 0.2	0.5	5 ± 5	2.0 ± 0.6
SMT-1	39.9195	76.5384	1617 ± 5	21 ± 1	1.3 ± 0.2	1	5 ± 5	2.0 ± 0.6
SMT-2	39.9200	76.5393	1618 ± 5	23 ± 1	1.4 ± 0.2	7	5 ± 5	2.0 ± 0.6
SMT-4	39.9114	76.5191	1667 ± 5	34 ± 2	6.0 ± 0.2	10	5 ± 5	2.0 ± 0.6
SMT-5[f]	39.9096	76.5183	1665 ± 5	34 ± 2	3.0 ± 0.2	9	5 ± 5	2.0 ± 0.6
SMT-6	39.9046	76.5833	1511 ± 5	59 ± 1	5.7 ± 0.2	4	5 ± 5	2.0 ± 0.6
SMT-7	39.9043	76.5838	1509 ± 5	58 ± 1	7.0 ± 0.2	6	5 ± 5	2.0 ± 0.6
SMT-8	39.9008	76.5918	1485 ± 5	57 ± 1	1.4 ± 0.2	1.4	5 ± 5	2.0 ± 0.6
SMT-9	39.8907	76.6082	1426 ± 5	51 ± 1	5.3 ± 0.2	2	5 ± 5	2.0 ± 0.6
EA-2	39.8439	76.4201	1627 ± 5	240 ± 40	0.9 ± 0.2	1	5 ± 5	2.0 ± 0.6
WCA-1	39.6907	75.8513	1719 ± 5	35 ± 10	1.0 ± 0.2	4	5 ± 5	2.0 ± 0.6
WCA-3	39.6907	75.8513	1719 ± 5	35 ± 10	2.3 ± 0.2	5	5 ± 5	2.0 ± 0.6

[a]Uncertainties are estimated.
[f]discarded one additional aliquot

Table A6-2: Full results from optically stimulated luminescence dating-Part 2

Sample Name	^{238}U ±2σ (Bq/kg)[b]	^{226}Ra ±2σ (Bq/kg)[b]	^{228}Ra ±2σ (Bq/kg)[b]	^{228}Th ±2σ (Bq/kg)[b]	^{232}Th ±2σ (Bq/kg)[b]	^{40}K ±2σ (Bg/Kg)[b]	^{238}U/^{226}Ra ±2σ [b]
CK-1	19.9 ± 3.6	10.1 ± 0.3	16.8 ± 0.5	15.6 ± 0.4	16.0 ± 0.3	353 ± 7	2.0 ± 0.2
CK-2	9.5 ± 2.6	14.1 ± 0.2	18.1 ± 0.4	17.3 ± 0.3	17.6 ± 0.2	317 ± 5	0.7 ± 0.3
CK-3	26.0 ± 3.3	22.4 ± 0.3	31.9 ± 0.5	32.3 ± 0.5	32.1 ± 0.3	477 ± 8	1.2 ± 0.1
SMT-1	24.4 ± 6.6	15.6 ± 5.2	19.9 ± 0.5	19.1 ± 0.4	19.1 ± 0.4	297 ± 6	1.6 ± 0.4
SMT-2	22.0 ± 4.1	18.2 ± 0.3	26.0 ± 0.6	24.5 ± 0.5	25.1 ± 0.4	384 ± 7	1.2 ± 0.2
SMT-4	22.0 ± 4.4	23.1 ± 0.4	26.8 ± 0.6	25.9 ± 0.5	26.3 ± 0.4	395 ± 8	1.0 ± 0.2
SMT-5[f]	29.7 ± 4.4	23.9 ± 0.4	30.1 ± 0.6	28.7 ± 0.5	29.2 ± 0.4	453 ± 8	1.2 ± 0.1
SMT-6	25.1 ± 4.3	21.8 ± 0.4	29.7 ± 0.6	27.4 ± 0.5	28.2 ± 0.4	519 ± 9	1.2 ± 0.2
SMT-7	29.4 ± 4.7	25.3 ± 0.4	34.9 ± 0.7	32.9 ± 0.6	33.7 ± 0.4	564 ± 10	1.2 ± 0.2
SMT-8	18.5 ± 3.3	24.8 ± 0.3	31.6 ± 0.5	31.1 ± 0.5	31.3 ± 0.3	560 ± 9	0.7 ± 0.2
SMT-9	25.4 ± 4.2	18.5 ± 0.3	26.0 ± 0.6	24.8 ± 0.5	25.3 ± 0.4	461 ± 8	1.4 ± 0.2
EA-2	14.2 ± 4.1	21.6 ± 0.4	24.3 ± 0.6	22.7 ± 0.4	23.3 ± 0.3	340 ± 7	0.7 ± 0.3
WCA-1	24.7 ± 4.3	19.8 ± 0.4	26.1 ± 0.6	24.8 ± 0.5	25.3 ± 0.4	389 ± 7	1.2 ± 0.2
WCA-3	84.9 ± 5.0	27.4 ± 0.4	29.8 ± 0.6	27.5 ± 0.5	28.4 ± 0.4	473 ± 9	3.1 ± 0.1

[b]Uncertainties are standard deviations from the gamma ray spectrometry.
[f]discarded one additional aliquot

Table A6-3: Full results from optically stimulated luminescence dating-Part 3

Sample Name	Number of aliquots (accepted / total)	Over-dispersion (%)	Skew	Kurtosis	Dose Rate ±2σ (Gy/ky)[c]	MAM Equivalent dose ±2σ (Gy)[d]	CAM Equivalent dose ±2σ (Gy)[d]	MAM Age ±2σ (ka)[e]	CAM Age ±2σ (ka)[e]
CK-1	25/33	61	0.5	-0.6	1.8 ± 0.1	28 ± 4	102 ± 25	15 ± 2	55 ± 14
CK-2	22/29	32	0.3	-0.7	1.7 ± 0.1	51 ± 5	94 ± 13	30 ± 4	54 ± 8
CK-3	20/27	36	0.4	-1.2	2.7 ± 0.1	61 ± 8	110 ± 18	23 ± 3	41 ± 7
SMT-1	23/42	67	1.1	0.6	1.8 ± 0.1	21 ± 6	69 ± 20	11 ± 3	37 ± 11
SMT-2	21/35	64	0.8	1.1	2.2 ± 0.1	24 ± 8	85 ± 25	11 ± 4	38 ± 11
SMT-4	33/64	52	1.1	0.7	2.3 ± 0.1	44 ± 10	91 ± 18	19 ± 5	40 ± 8
SMT-5[f]	23/38	45	0.5	-0.4	2.6 ± 0.1	61 ± 13	123 ± 25	23 ± 5	47 ± 10
SMT-6	33/47	36	1.1	0.9	2.7 ± 0.2	82 ± 13	144 ± 20	31 ± 5	54 ± 8
SMT-7	31/55	56	1.4	1.8	3.0 ± 0.2	43 ± 8	127 ± 27	14 ± 3	43 ± 9
SMT-8	20/27	48	1.0	0.1	3.0 ± 0.2	40 ± 10	77 ± 17	13 ± 3	26 ± 6
SMT-9	34/58	42	1.0	0.3	2.4 ± 0.1	63 ± 11	121 ± 19	26 ± 5	50 ± 8
EA-2	29/44	48	0.8	1.1	2.1 ± 0.1	32 ± 6	76 ± 14	15 ± 3	36 ± 7
WCA-1	21/49	40	1.4	1.9	2.3 ± 0.1	80 ± 15	141 ± 26	35 ± 7	61 ± 12
WCA-3	30/38	49	1.4	2.5	3.0 ± 0.2	55 ± 9	134 ± 25	18 ± 3	45 ± 9

[c]The dose rate is calculated from radionuclide activities in representative samples measured through gamma ray spectroscopy and an estimated water content of 5 ± 5% (±2σ). Uncertainties are propagated from the standard deviations of radionuclide activities and the estimated uncertainties of the water contents.
[d]Equivalent dose distributions are obtained by applying the minimum age model and the central age model (Galbraith, 2005; Galbraith and Roberts, 2012; Galbraith et al., 1999) to the single aliquot equivalent dose data.
[e]Ages by dividing the equivalent doses by the dose rate. Uncertainties are propagated from the dose rate uncertainty and equivalent dose standard error.
[f]discarded one additional aliquot

Table A7: Results from depth-profile modeling for CA-DP1 using a Monte Carlo calculator (Hidy et al., 2010)

CA-DP1							
Iputs to the Hidy et al., (2010) Monte Carlo simulator		**Results from the Monte Carlo simulator**		**Age (ka)**	**Inheritance (10^4 atoms/g)**	**Erosion rate (cm/ky)**	**Best fit concentration assuming no erosion (atoms/g)**
Latitude	39.712	**Including the surface sample**	Mean	78.2	29.2	-0.04	987421
Longitude	76.0115		Median	78.1	29.3	-0.03	986183
Altitude (m)	1534		Mode	76.4	29.5	0.09	965124
Shielding	0.999		Min χ^2	76.8	29.3	-0.07	970080
Reference production rate (atoms/g/y)[b]	4.1		Maximum	88.3	32.1	0.12	1112161
Depth of muon fit (m)	5		Minimum	69.1	26.1	-0.22	874490
% error in total prod rate	10		Bayesian most probable	77.1	29.7	0.10	973797
Chi Squared cutoff value[c]	15/10		Bayesian 2-sigma upper	88.1	33.8	0.11	1109697
Number of profiles	200000		Bayesian 2-sigma lower	68.0	23.3	-0.22	860805
Density lower bound (g/cm^3)	1.4		Average 2-sigma error used	10.1	5.2	0.2	129071
Density upper bound (g/cm^3)	2.3	**Excluding the surface sample**	Mean	89.1	31.4	-0.03	1122015
Age lower bound (ka)	40		Median	88.9	31.4	-0.03	1119552
Age upper bound (ka)	140		Mode	89.3	31.3	0.09	1124478
Erosion rate lower bound (cm/ky)	-1		Min χ^2	82.4	31.9	-0.18	1039369
Erosion rate upper bound (cm/ky)	1		Maximum	103.2	33.6	0.11	1295039
Total erosion lower bound (cm)	-15		Minimum	77.9	29.5	-0.19	983706
Total erosion upper bound (cm)	10		Bayesian most probable	86.6	31.2	0.09	1091209
Inheritance lower bound (10^5 atoms/g)	1		Bayesian 2-sigma upper	101.3	33.8	0.10	1271794
Inheritance upper bound (10^5 atoms/g)	4		Bayesian 2-sigma lower	74.8	26.2	-0.20	945287
Neutron attenuation (g/cm^2)	160 ± 5		Average 2-sigma error used	13.3	3.8	0.2	170033

[a]The half live is based on Chmeleff et al., (2010) and Korschinek et al., (2010)

[b]Production rates are based on the reference 10Be production rates of Borchers et al., (2016), an atmospheric model based on the ERA40 climate reanalysis (Lifton et al., 2014), and the scaling scheme of Stone, (2000) based on Lal, (1991)
cUsed 15 for the profile including the surface sample and 10 for the profile without the surface sample

Table A8: Exposure ages for different scaling schemes

Scaling schemes	**Lal, (1991) & Stone, (2000)**	**Time dependent Lal & Stone (Balco et al., 2008)**
Reference production rate ±1σ (atoms/g/y)[a]	4.1 ± 0.4	4.0 ± 0.4
Site specific spallation prod. rate ±1σ (atoms/g/y)	12.7516	time varying
Site specific muogenic prod. rate at surface (atoms/g/y)	0.1236	
Best fit age including the surface sample ±2σ (ka)[b]	78 ± 17	74 ± 17
Best fit age excluding the surface sample ±2σ (ka)[b]	89 ± 21	85 ± 21

All values are outputs from the CRONUS-Earth-2008-v2.3 exposure age calculator assuming a sample density of 2 g/cm3, a sample thickness of 0 and a shielding factor of 0.999.
[a]Uncertainties in the production rate are standard deviations of the calibration data estimated by Greg Balco in the CRONUS-Earth-2008-v2.3 exposure age calculator.
[b]Uncertainties are external uncertainties taking into account the error in the production rate and in the 10Be concentration of the sample as described by Balco et al., (2008).